/
Article / Book Information

( )	
Title(English)	Experimental and numerical study on dynamic behavior of double concave friction pendulum bearing for base-isolated buildings
( )	LiJiaxi
Author(English)	Jiaxi Li
( )	: ( ), : , : 12237 , :2022 9 22 , : , : , , , ,
Citation(English)	Degree:Doctor (Engineering), Conferring organization: Tokyo Institute of Technology, Report number: 12237 , Conferred date:2022/9/22, Degree Type:Course doctor, Examiner:,,,,,
( )	
Type(English)	Doctoral Thesis

Doctor Thesis, 2022

Experimental and numerical study on dynamic behavior of double concave friction pendulum bearing for base-isolated buildings

（実験および数値解析による免震建物用球面すべり支承の動的挙動に関する研究）

Li Jiaxi

Academic Advisor: Prof. Kishiki Shoichi

Department of Architecture and Building Engineering

Tokyo Institute of Technology

ABSTRACT

An isolation system can significantly reduce the deformation of the superstructure by focusing the deformation on the isolation layer. When friction pendulum bearings (FPBs) are applied, this deformation will be highly related to the friction coefficient. Therefore, the influence of the friction dependencies on the maximum displacement is of vital importance. However, the reliability of proposed friction dependencies under real earthquakes and the effect of friction dependencies on the maximum response displacement remain unclear. Thus, the friction dependencies were combined in friction models and further validated by full-scale dynamic tests under unidirectional and bidirectional orbits. Further, the contribution of friction dependencies to the maximum displacement and superstructure acceleration was assessed under various earthquake excitations and various base isolation systems.

Contents

1. Introduction

Since the first applications of the base isolation system (BIS) in the earthquake-prone countries, many destructive earthquakes have occurred, such as Northbridge in 1994, Kobe in 1995, and Tohoku in 2011 [1-1]. During these earthquakes, BIS has been validated as the most effective method to mitigate seismic hazards [1-2][1-3] and consequently, its use in earthquake-prone countries has witnessed a remarkable increase [1-4][1-5]. A BIS can significantly reduce the deformation of the superstructure by concentrating the deformation on the isolation layer. Therefore, determining the maximum displacement of the isolation layer is one of the most important target through the design procedure [1-6][1-7]. Also, as the mechanical properties of the isolation system depend on various factors [1-8], the influence of the dependencies of these factors on the maximum displacement is of vital significance and cannot be ignored.

Moreover, the destructive earthquakes occurred in recent decades have led to increased demand for larger response displacements and larger isolation periods in the seismic isolation design [1-9]. Compared to other bearings, friction pendulum bearings (FPBs) offer advantages such as the ability to conveniently change the maximum displacement and its independence of natural period on mass. However, their application in seismic isolation remains minimal[1-9]. Therefore, the effectiveness of FPBs has not been tested comprehensively by earthquakes. Nowadays, FPBs are most popular in the US, therefore, Japan followed US and developed similar devices. The devices considered in this study is based on a double concave FPB (DCFPB) developed by Nippon Steel Engineering in 2019 (NS-SSB) [1-10].

1.1 Development and early application history of base isolation systems

In order to mitigate the seismic response of structures, various devices have been developed and applied in the base isolation system (BIS). For example, rubber bearings (RB), sliders with elastomer and friction pendulum bearings (FPB).

The first modern seismic isolation building in the world is the Heinrich Pestalozzi School constructed in Skopje in 1969, applying laminated rubber bearings [1-11]. However, the main construction of the modern base isolation structures started in early 1980s, which were mainly applications of RBs. In 1981, the first application of BIS in New Zealand, the William Clayton building, was constructed using lead-rubber bearings [1-12]. The first application in Japan is the Yachiyodai House erected in 1983 using laminated rubber bearings [1-13]. From 1977 to 1984, Electricity de France (EDF) constructed the first nuclear power plant in South Africa (Koeberg) and in France (Cruas), using laminated neoprene bearings with and without sliding plates [1-1] [1-14]. As for the USA, the first utilization is the Foothill Communities Law and Justice Centre in San Bernardino completed in 1985, using high damping rubber bearings [1-15]. Compared with RBs, the applications of friction pendulum system (FPS) occur a few decades later. According to the authors' knowledge, the first application of the FPS for retrofitting the "Marine Apartment" was conducted in San Francisco in 1991 after the Loma Prieta earthquake [1-16].

Thereafter, the destructive earthquakes, such as Northbridge in 1994, Kobe in 1995, and Tohoku in 2011, lead to demands of larger response displacements (increase from 100mm to 650mm) and larger isolation period (increase from 2s to 10s) in the seismic isolation design [1-17]. Comparing with RBs, FPB's ability of conveniently changing the maximum displacement by adjusting the diameter of the concave plate and its independency of natural period on mass give it more advantages. Also, based on FPB, the demand of larger displacement facilitates the application of double concave friction pendulum bearings (DCFP bearings), whose concept was already proposed in US [1-18][1-19] and European countries [1-20] more than one hundred years ago. Based on the authors' knowledge, the first application of DCFP Bearings in Japan was described by Hyakuda etc. in 2001 [1-21]. To

date, DCFP bearings are becoming more and more popular due to its advantage in fulfilling the pre-mentioned demands in nowadays BIS design. One of the types of DCFP bearings used in this study is shown in Figure. 1.1, which is the Nippon steel product of SSB (Spherical Sliding Bearing).
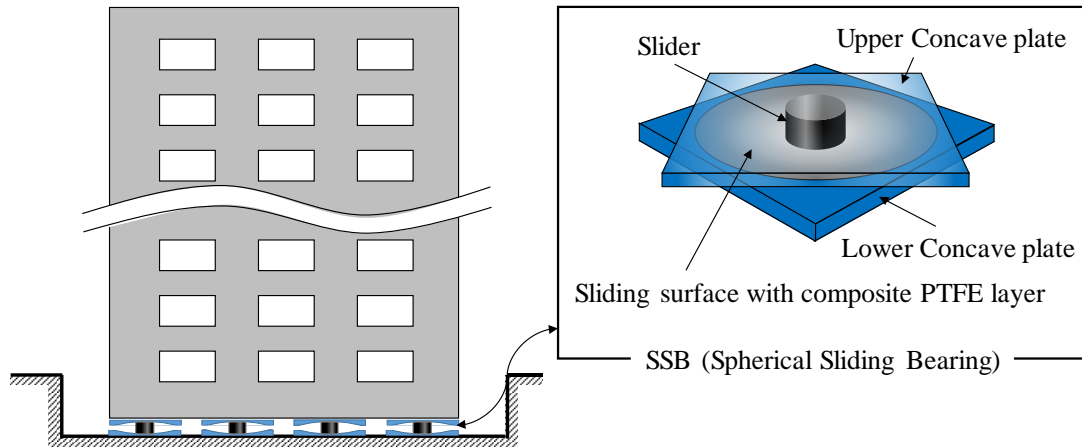
Figure 1.1. Base isolated buildings installed with SSBs

1.2 Dependencies of base isolation systems

Dependencies of the mechanical properties of the BIS on pressure, velocity, temperature, aging, etc. were studied for sliding, lead rubber, and elastomeric bearings by Constantinou MC et al. [1-8]. Among which, the mechanical properties of sliding bearings (SBs) depend mainly on the effect of pressure, velocity and temperature on the friction coefficient [1-22]. These dependencies differ by the sliding materials. Low friction materials applied to build isolation devices are mainly based on polytetrafluoroethylene (PTFE), polyethylene (PE) and polyamide (PA). Among which, PTFE-based material has relatively lower friction coefficient and higher melting temperature [1-23], and is used as the sliding interface of the DCFPB considered in this study. In previous studies, pressure, velocity, and temperature dependencies of FPBs were mainly obtained by small-scale material friction tests [1-8][1-24][1-25]. Full-scale dynamic tests in a large region of speed and displacement conducted to validate the applicability of the obtained dependency equations under real size is still insufficient. Further, to understand the behavior of FPBs and validate the credibility of the friction dependencies under real earthquakes, full-scale experiments under bidirectional artificial graphics and earthquake response orbits are still necessary.

1.3 Influence of dependencies on the maximum displacement of FPBs

Simplified prediction methods were generally introduced in various structural codes, such as ASCE (American Society of Civil Engineering) [1-26], AASHTO (American Association State and Highway Transportation Officials) [1-27], Euro Code [1-28] and AIJ (Architectural Institute of Japan) [1-29], to obtain the design displacement of the isolation system, which were considered under unidirectional excitations with constant friction coefficients. However, Warn GP et al. proposed that the influence of bidirectional excitation and coupling on the maximum displacement cannot be ignored [1-30]. The coupling effect exists between the responses of the FPBs in each orthogonal direction, which if ignored results in an underestimation of the maximum isolator displacement by approximately 20% [1-30][1-31][1-32]. Moreover, Manish Kumar et al. demonstrate that a friction model of a FPB that ignores the effects of temperature rise may underestimate the median maximum displacement by 10% and 30%, for static axial pressures of 10 and 50MPa, respectively, based on 30 sets of three-component ground motions (GMs). And the effects of changes in velocity and axial pressure on the friction coefficient are small and may not need to be included in a friction model [1-22]. Li Jiaxi et al. did similar response analysis of a different DCFPB under 48 sets of three-component GMs, and concluded that the effect of bearing stress and velocity dependency on the maximum displacement is less than 10%, for static axial pressures of 60MPa. And, in most situation, the larger the intensity of the earthquake the less the effect [1-33].

As most existing codes and the determination of mechanical properties (mainly refer to the friction coefficient of the bearing in this study) were considered under unidirectional excitations, the effect of the velocity and temperature change caused by the additional perpendicular excitation (bidirectional effect) on the friction coefficient and further on the maximum response displacement needs to be clarified. Therefore, an approach to determine the design displacement in preliminary design that considers these effects remains a research topic [1-8].

1.4 Earthquake response spectra of FPBs

There are many parameters in simulating the earthquake response of a structure isolated by FPBs. R.S. Jangid proposed that, in the design of a BIS, the selection of the friction coefficient of the FPB (μ) and the natural period of the BIS (T_b) is of vital importance [1-34]. Manish Kumar et al. demonstrate that the effects of changes in velocity and axial pressure on the friction coefficient are small and may not need to be included in a friction model. And the effect of temperature rise cannot be ignored [1-22]. Warn GP et al. proposed that the influence of bidirectional excitation and coupling on the maximum displacement cannot be ignored [1-30]. Midorikawa et al. proposed that the characteristics of ground motion is affected by the source characteristics (Magnitude and fault type of the earthquake), path (distance to fault), and site condition (Soil type) [1-35]. All these parameters were listed in Table 1.1. However, in the existing studies of the response spectra of structures isolated with FPBs, the friction coefficient is always considered as constant (the pressure, velocity, and temperature dependencies were rarely considered in conducting the response spectra). Moreover, the earthquakes were generally classified by distance to fault, the influence of other earthquake characteristics on the response of FPBs were rarely considered [1-34][1-36][1-37]. Therefore, the significance of each parameter and how each parameter affect the earthquake response still need to be further studied.

Table 1.1 Parameters in the earthquake response analysis of DCFP bearings

BIS	Analysis Model	Earthquake Selection
μ (friction coefficient)	Pressure dependency	Distance to fault
T_b (Isolation Period)	Velocity dependency	Magnitude
	Temperature dependency	Soil type
	Coupling effect	Fault type
	Second Component	

1.5 Objectives of this study and structure of this dissertation

This paper has five chapters. The subject of research is the Double Concave Friction Pendulum (DCFP) bearing used for seismic isolated buildings, and the dynamic behavior of it is discussed by full-scale experiments and numerical analysis.

In Chapter 1, "Introduction", as a background of the research, we investigated the DCFP bearings in general and pointed out that the influence of friction coefficient and various friction dependencies on the dynamic response when using DCFP bearings are important. From the above background, it is stated that the purpose is to understand the dynamic behavior the DCFP bearing under one-directional and two-directional horizontal excitations, to grasp the influence of various dependencies, and to propose the optimum design under various GMs.

Chapter 2, "Behavior of DCFP bearings under unidirectional excitations (1D)", conducted full-scale dynamic experiments and numerical analysis of DCFP bearings in 1D. The specimens are full-scale DCFP bearings and the parameters are slider diameter, surface pressure, velocity, and number of cycles. From the experimental results, various dependencies of surface pressure, velocity, and temperature on the coefficient of friction are clarified. In addition, we conducted seismic response analysis using a 1D single-degree-of-freedom (SDOF) shear system model, examined the effects of velocity and temperature dependencies on the maximum response, and concluded that the effect of temperature dependency is particularly large.

In Chapter 3, "Behavior of DCFP bearings under bidirectional excitations (2D)", following Chapter 2, full-scale dynamic experiments and numerical analysis of DCFP bearings in 2D were conducted. We proposed analysis models that consider 2D deformation, and verified its validity by comparing it with the results of full-scale experiments. In addition, seismic response analysis was performed using a 2D SDOF shear system model to clarify the effects of an additional perpendicular ground motion component on temperature and velocity, and in turn, on friction coefficient and maximum response displacement. Further, the influence of characteristic parameters of GMs and BISs on the response increase from 1D to 2D was discussed.

In Chapter 4, "Response spectra of various DCFP bearings under various GM classifications", parametric study of DCFP systems under various GMs using the analysis model constructed in Chapter 3 is conducted and a preliminary design method is proposed. In the analysis, the parameters are the classification of input GMs (based on magnitude and

distance to fault), the friction coefficient of the DCFP bearing, and the isolation period. The analysis results are represented as response spectra, and the selection of the optimal isolation period and friction coefficient of the seismic isolation layer using DCFP bearing was discussed under various GM classifications based on response displacement and response acceleration. Also, the effect of bidirectional behavior and temperature change on the response was studied. Based on these parametric studies, some general rules and notes about the optimal preliminary design were summarized

Chapter 5, "Conclusions", summarized the findings obtained in each chapter. In short, this paper clarified various dependencies of the friction coefficient by full-scale experiments of real-size DCFP bearings, and discussed the selection of the optimum seismic isolation period and friction coefficient of DCFP bearings under various ground motion classifications based on the bidirectional model that applies these dependencies.

References.

[1-1].   Makris N. Seismic isolation: Early history. Earthq Eng Struct Dyn, 2019;48(2):269-283.

[1-2].   Nakashima M, Pan P, Zamfirescu D, Weitzmann R. Post-Kobe approach for design and construction of base-isolated buildings. J Japan Assoc Earthq Eng 2004;4:259–64. http://dx.doi.org/10.5610/jaee.4.3_259

[1-3].   Bertero VV, Bozorgnia Y. The early years of Earthquake engineering and its modern goal, Earthquake Engineering. From engineering seismology to Performance-Based engineering. Boca Raton CRC Press; 2006. p. 676–715.

[1-4].   Japan Society of Seismic Isolation (JSSI), https://www.jssi.or.jp/index.html.

[1-5].   Earthquake Protection Systems (EPS), https://www.earthquakeprotection.com/.

[1-6].   Shimazaki D, Nakagawa K. Seismic Isolation System Incorporating with RC Core Walls and Precast Concrete Perimeter Frames. Int J High-Rise Build 2015;4(3):181–9.

[1-7].   Calvi GM, Spaziante V. Reconstruction between temporary and definitive: the CASE project. Progettazione Sismica. 03/English; 2009. p. 221-50.

[1-8].   Constantinou MC, Whittaker AS, Kalpakidis Y, Fenz DM, Warn GP. Performance of seismic isolation hardware under service and seismic loading. Multidisciplinary Center for Earthquake Engineering Research: Buffalo, NY, USA, 2007;Report No. MCEER-07-0012.

[1-9].   De Luca A, Guidi L G. State of art in the worldwide evolution of base isolation design. Soil Dyn Earthq Eng 2019;125:105722. https://doi.org/10.1016/j.soildyn.2019.105722

[1-10]. NS-SSB, https://www.eng.nipponsteel.com/steelstructures/product/base_isolation/nsssb/

[1-11]. Coladant C. V-2 base isolation and aseismic bearings[M]//Recent advances in earthquake engineering and structural dynamics. 1992.

[1-12]. Skinner R I, Robinson W H, McVerry G H. An introduction to seismic isolation[M]. Wiley, 1993.

[1-13]. Atwater B F, Musumi-Rokkaku S, Satake K, etc.. The orphan tsunami of 1700: Japanese clues to a parent earthquake in North America[M]. University of Washington Press, 2016.

[1-14]. Coladant C. Seismic isolation of nuclear power plants—EDF's philosophy[J]. Nuclear Engineering and Design, 1991, 127(3): 243-251.

[1-15]. Tarics AG, Way D, Kelly JM. The implementation of base isolation for the Foothill Communities Law and Justice center, county of Bernardino, California. A report to the national Science foundation and the county of san Bernardino- national technical information service U.S.A. Department of Commerce Springfield; 1984. Report No. NSF/CEE – 84041. PB85 – 152155.

[1-16]. Naeim F, Brzev S. Advanced technologies in housing construction[J]. British Columbia Institute of Technology, Canada, 2011.

[1-17]. De Luca A, Guidi L G. State of art in the worldwide evolution of base isolation design[J]. Soil Dynamics and Earthquake Engineering, 2019, 125: 105722.

[1-18]. Touaillon J. Improvement in buildings. US patent 99973; Feb. 15, 1870.

[1-19]. Bechtold J. Earthquake proof building. US patent 845046A; Feb. 26, 1907.

[1-20]. Barucci C. La casa antisismica [The antiseismic house]. Gangemi, Rome (In Italian); 1990.

[1-21]. Hyakuda T, Saito K, Matsushita T, Tanaka N, Yoneki S, Yasuda M, Miyazaki M, Suzuki A, Sawada T. The structural design and earthquake observation of a seismic

isolation building using friction pendulum system. In: Proceedings, 7th international seminar on seismic isolation, passive energy dissipation and active control of vibrations of structures. Assisi, Italy; 2001.

[1-22]. Kumar M, Whittaker AS, Constantinou MC. Characterizing friction in sliding isolation bearings. Earthq Eng Struct Dyn 2015;44:1409–1425. https://doi.org/10.1002/eqe.2524

[1-23]. Calvi, Paolo M., and Gian Michele Calvi. "Historical development of friction-based seismic isolation systems." Soil Dynamics and Earthquake Engineering 106 (2018): 14-30.

[1-24]. Nakamura, H.; Nishimoto, K.; Hasegawa, H.; Nakamura, H. Predictive Method of a Temperature Rise and the Friction Coefficient of Spherical Sliding Bearing (Part 3), Paper No. 21232. AIJ, Kanto, Japan, 4–6 September 2015.

[1-25]. Nishimoto, K.; Nakamura, H.; Hasegawa, H.; Wakita, N. Bearing Stress and Velocity Dependency of Spherical Sliding Bearing through Full-scale tests, Paper No. 21223. AIJ, Fukuoka, Japan, 24–26 August 2016.

[1-26]. ASCE/SEI 7-16. Minimum Design Loads and Associated Criteria for Buildings and Other Structures; American Society of Civil Engineers (ASCE): Reston, VA, USA, 2016.

[1-27]. Transportation Officials. AASHTO Guide for Design of Pavement Structures, 1993; Aashto.

[1-28]. General rules, Eurocode 8. Design provisions for earthquake resistance of structures; Part 1: seismic actions and rules for buildings. BS EN 1998-1; European Committee for Standardization, Brussels, Belgium, 2004.

[1-29]. Design Recommendations for Seismically Isolated Buildings; ISBN 978-4-8189-5000-9, Architectural Institute of Japan: Tokyo, Japan, 2016.

[1-30]. Warn G P, Whittaker A S. Performance estimates in seismically isolated bridge structures. Eng Struct, 2004;26(9):1261-1278.

[1-31]. Mosqueda G, Whittaker A S, Fenves G L. Characterization and modeling of friction pendulum bearings subjected to multiple components of excitation. J Struct Eng 2004;130(3):433-442. https://doi.org/10.1061/(ASCE)0733-9445(2004)130:3(433)

[1-32]. Lomiento G, Bonessio N, Benzoni G. Concave sliding isolator's performance under multi-directional excitation. Ingegneria Sismica, 2013;30(3):17-32.

[1-33]. Li Jiaxi, Nitawaki Masashi, Kishiki Shoichi, Ishida Takanori, Nishimoto Koji, Watanabe Atsushi and Yamada Satoshi, Analytical Study on Spherical Sliding Bearing (SSB) Subjected to Tri-directional Excitation ---- Effect of Bearing Stress and Velocity dependency of SSB on the response of isolation system, Summaries of Technical Papers of Annual Meeting, Architectural Institute of Japan, Paper No. 21490, Tohoku, Japan, 4-6 September 2018.

[1-34]. Jangid RS. Optimum friction pendulum system for near-fault motions. Engineering structures. 2005 Feb 1;27(3):349-59.

[1-35]. Si H, Midorikawa S. New attenuation relations for peak ground acceleration and velocity considering effects of fault type and site condition. In Proceedings of 12th World Conference on Earthquake Engineering 2000 Jan 30 (No. 0532).

[1-36]. Panchal VR, Jangid RS. Seismic behavior of variable frequency pendulum isolator. Earthquake Engineering and Engineering Vibration. 2008 Jun;7(2):193-205.

[1-37]. Providakis CP. Effect of supplemental damping on LRB and FPS seismic isolators under near-fault ground motions. Soil Dynamics and Earthquake Engineering. 2009 Jan 1;29(1):80-90.

2. Behavior of DCFP bearings under unidirectional excitations (1D)

2.1 Introduction

Friction pendulum bearings (FPBs), which are a type of base isolation technique that detaches structures from the ground to help stabilize buildings from earthquakes, are widely used in earthquake-prone regions. This article focuses on double concave FCBs (DCFPBs), which consist of a slider in between two concave plates, as shown in figure 2-1. For the specimen we used in this study, the material on the upper and lower surfaces of the slider is a composite polytetrafluoroethylene (PTFE) material, and the sliding plates on the two concave plates are composed of stainless steel.
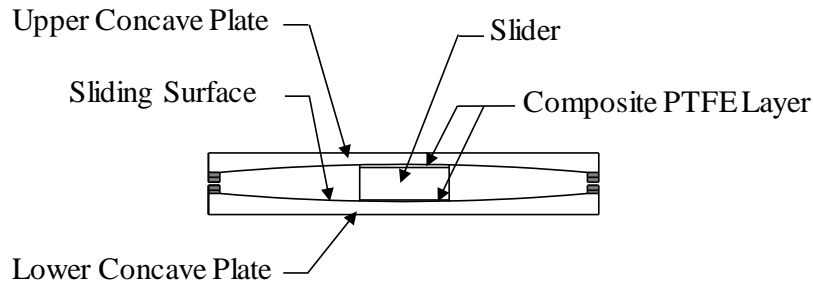
Figure 2-1. Composition of a DCFPB

Figure 2-2 shows the free body diagram of a DCFPB during motion. u_L is the displacement of the slider on the lower concave plate, u_U is the displacement of the slider on the upper concave plate and d is the displacement of the bearing. *VL* is the vertical load and *Fh* is the horizontal force acting on the bearing. In this study, the spherical radiuses of the upper and lower concave plates are the same and the slider and the concave plates are assumed to be rigid bodies. Also, the friction coefficients of the upper and lower contact surfaces between the slider and the concave plates are the same and static friction coefficient is not considered. Therefore, the motion of the upper and lower concave plates is considered to be symmetrical about the center of the slider, and u_L equals u_U equals $d/2$.
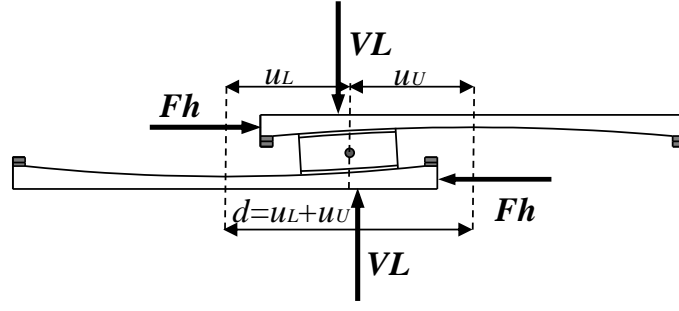
Figure 2-2. Free body diagram of a DCFPB during motion

In order to obtain the force-displacement relationship of DCFPB, the free body diagram of the slider on the lower concave plate is shown in figure 2-3. The forces acting on the slider are vertical load, *VL*, and horizontal force, *Fh*, from the upper concave plate and friction force, Ff_L, and resultant force, *SL*, from the lower concave plate. R_S is the spherical radius of both upper and lower sliding surface and *h* is the thickness of the slider.
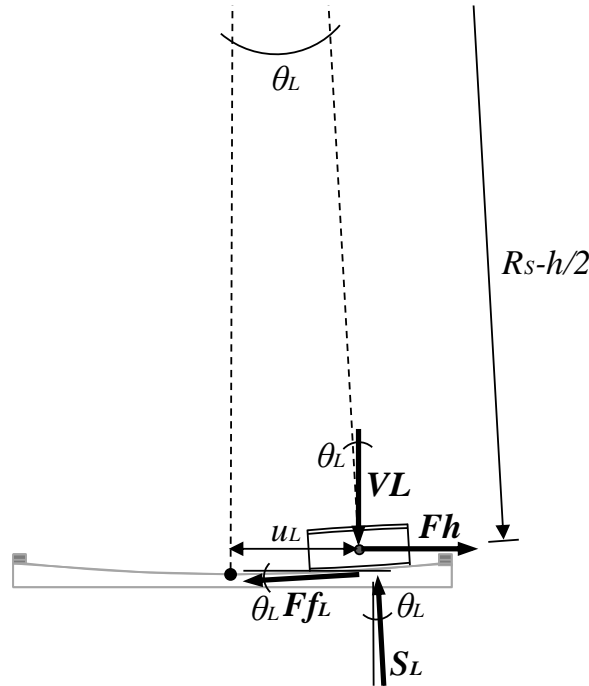
Figure 2-3. Free body diagram of the slider on the lower concave plate

According to geometry and equilibriums in horizontal and vertical directions, the horizontal force, *Fh*, can be expressed as:

$$Fh = \frac{VL}{(R_S - h/2)\cos\theta_L} u_L + \frac{Ff_L}{\cos\theta_L} \tag{2-1}$$

19

Since R_S is very large compared with u_L and h, $\cos\theta_L$ is taken as 1 and h is neglected. In this case, since the motion of the upper and lower concave plates are considered to be symmetrical about the center of the slider, the amplitudes of the friction force between the slider and the upper and the lower concave plates (Ff_U and Ff_L) are the same. Taking Ff equals Ff_L equals Ff_U and u_L equals $d/2$, Fh can be obtained as:

$$Fh = \frac{VL}{2R_S}d + Ff \tag{2-2}$$

The clear force–displacement relationship of friction pendulum bearings (FPBs) makes numerical analysis one of the best ways in which to study and predict their performance. The main focus is on the calculation of the friction force. This is because the friction coefficient's dependence on pressure, velocity and temperature is the most important characteristic for the performance of a FPB (Friction Pendulum Bearing). Therefore, the lubricant material used in an FPB and the characteristics of this material are very important. Quaglini et al. (2012) proposed an experimental methodology for the characterization of self-lubricating materials based on pressure, velocity, external temperature and displacement through small-scale specimens [2-1]. In addition to external temperature, particular attention was paid to the temperature increase on the sliding surface caused by friction heating because this increase in temperature had a significant influence on the behavior of the FPB during an earthquake event. Moreover, the measurement of this temperature increase is very difficult to perform during dynamic excitation. To confront this difficulty, Lomiento et al. (2013) proposed a friction model that takes into account the vertical load, velocity and cycling effect (degradation of friction characteristics due to the repetition of cycles and consequent temperature rise) by performing 1D prototype dynamic tests on single concave friction pendulum (SCFP) bearings [2-2]. Quaglini et al. (2014) proposed a 3D finite element model (FEM) of an SCFP bearing to estimate friction heating, and the estimated temperature was validated with experimental data measured by thermocouples embedded in the concave

sliding plate [2-3]. Following this work, some studies proposed simplified temperature simulation methods. Kumar et al. (2015) proposed a simplified model to calculate the representative temperature of the sliding surface in thermal calculations (Method 2 in the article) and considered pressure, velocity and temperature dependency. The analysis results were verified by 2D prototype dynamic tests of the SCFP bearings [2-4]. The distributions of the maximum displacement under 30 sets of ground motions in the original model (Method 1 in the article) and the simplified model were compared, and a relatively small difference was found between the models; thus, the simplified model could be applied instead of the original model. Furthermore, with the appearance of multiple concave friction pendulum bearings (MCFP bearings), Bianco et al. (2018) proposed a simplified rheological model to simulate the temperature rise in the MCFP bearings [2-5].

Most of these studies proposed new methods for obtaining dependency equations or simulating temperature caused by friction heating and new friction models that combine dependency equations together, but few of these friction models were comprehensively validated with a sufficient number of experiments containing various loading conditions. Most of the models were checked under only one or two types of seismic load. Although the pressure, velocity and temperature dependency equations were individually determined under their own range by controlling the other factors as constant, it is still necessary to validate the accuracy of the friction model (combined by all the friction dependencies) under a sufficient number of loading conditions because of the interaction between the dependencies.

In the previous study of the considered DCFP bearing, the pressure, velocity, and temperature dependencies were obtained individually [2-6][2-7]. In this Chapter, to validate the applicability of the obtained dependency equations under real size and a large range of dynamic loads, the dependencies were combined in a friction model and validated by full-scale unidirectional dynamic tests in a large range of speed and displacement.

2.2 Performed experiments

Two series of full-scale unidirectional dynamic tests were conducted. The dependency test was conducted to verify the applicability of the dependency equations of pressure and velocity proposed in the previous study on $\varphi300$ and $\varphi400$ specimens. The ASCE test, which complied with the provisions of ASCE/SEI 7-16 [2-8], was performed for the validation of the friction models.R_S

2.2.1 Specimens and test setup

Two types of DCFPBs were tested. The dimensions of these specimens are shown in Figure 2-4 and Table 2-1, where φ is the diameter of the slider, Φ is the diameter of the spherical surface, W is the width of the concave plate and H is the thickness of the specimen.
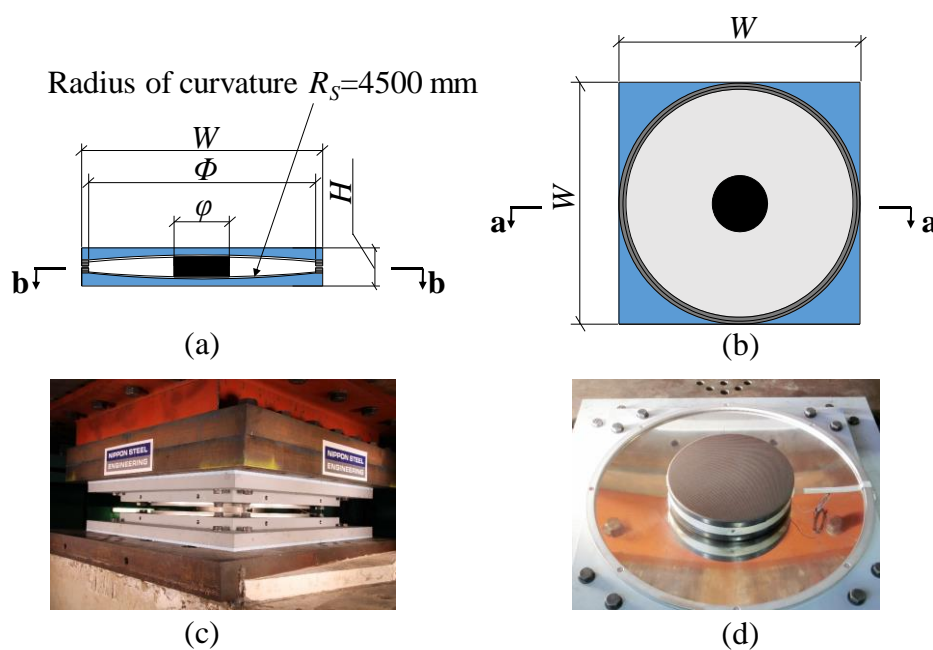
Figure 2-4. Specimen configuration: (a) a-a cross section, (b) b-b cross section, (c) outward appearance and (d) concave plate and slider

Table 2-1. Specimen dimensions

Specimen	φ (mm)	Φ (mm)	W (mm)	H (mm)
φ200	200	670	720	140.1
φ300	300	770	820	152.0
φ400	400	870	920	162.9

The experiments were conducted at the University of California, San Diego, in the Caltrans Seismic Response Modification Device (SRMD) Test Facility **Error! Reference source not found.** as shown in Figure 2-5, because the testing system must accomplish the following two primary tasks for testing the dynamic behavior of full-scale DCFP bearings.

① Simulate the relative seismic motion at the interface of a full-scale DCFP bearing specimen by applying large horizontal shearing displacements in real- time (large Num. of cycle and Velocity in unidirectional dynamic tests).

② Simulate the superstructure's dead weight by applying large, static, vertical compressive loads (large Pressure).
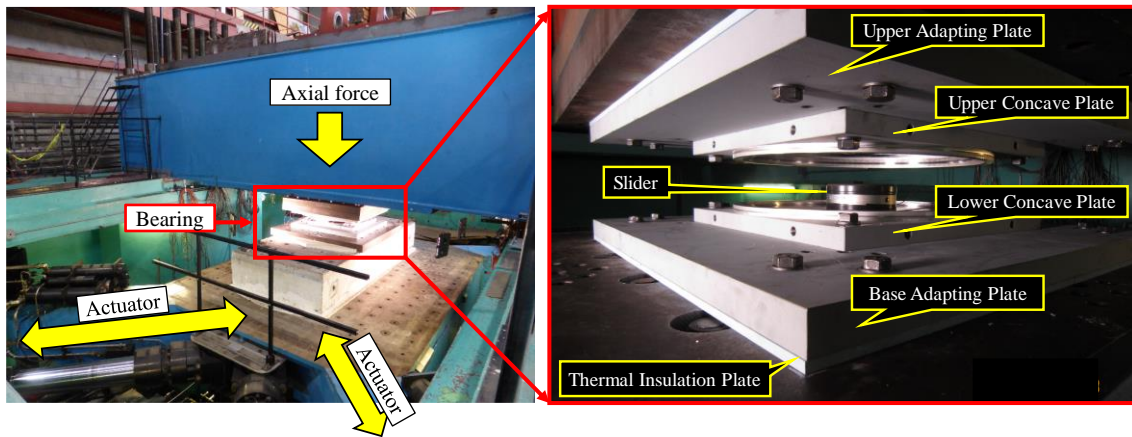
Figure 2-5. Test setup

After the specimen is placed inside the facility, four horizontal actuators can make the lower concave plate of the DCFP bearing move in the horizontal plane to control the velocity and loading path. Additionally, a vertical force can be added by the reaction beam and four vertical actuators under the platform to control the contact pressure between the slider and the concave plates. Figure 2-6 shows the loading system in detail.

Figure 2-6 (a) shows a perspective view of the SRMD test system, while more detailed plan and section views are shown in figure 2-6 (b) and (c). The system consists of a pre-stressed concrete box or frame, a removable steel cross-beam and a movable steel-concrete composite platen. A total of 12 hydraulic actuators connect the concrete frame and the movable platen. DCFP bearing specimens are installed between the movable platen and the steel cross-beam. The relative bearing shear displacements are accomplished by moving the platen and the lower concave plate of the bearing specimen. The upper concave plate of the specimen is attached to the cross-beam and remains fixed during testing.
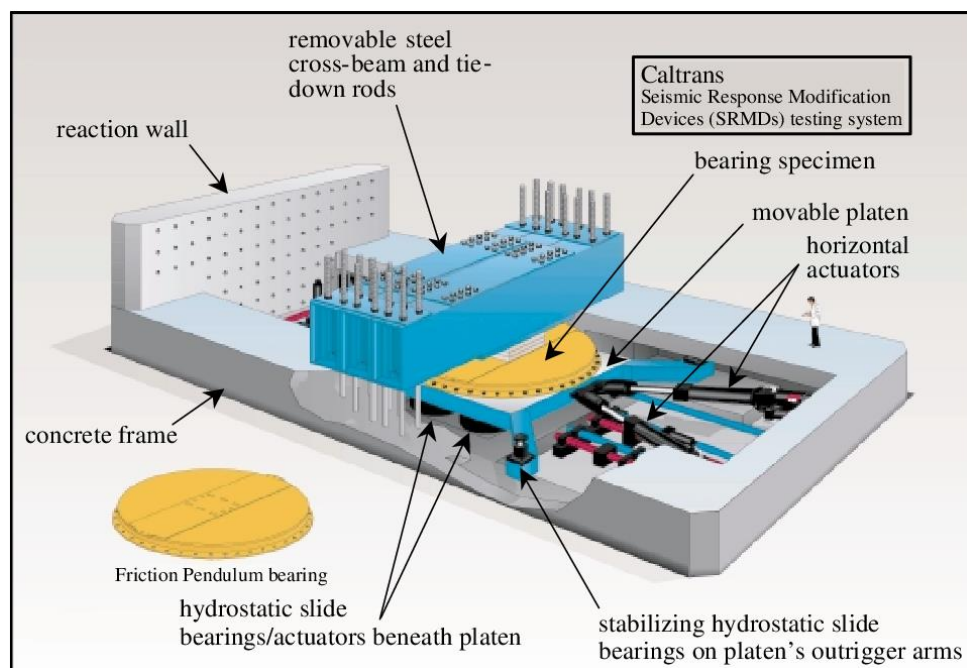
(a) Perspective view [2-9]
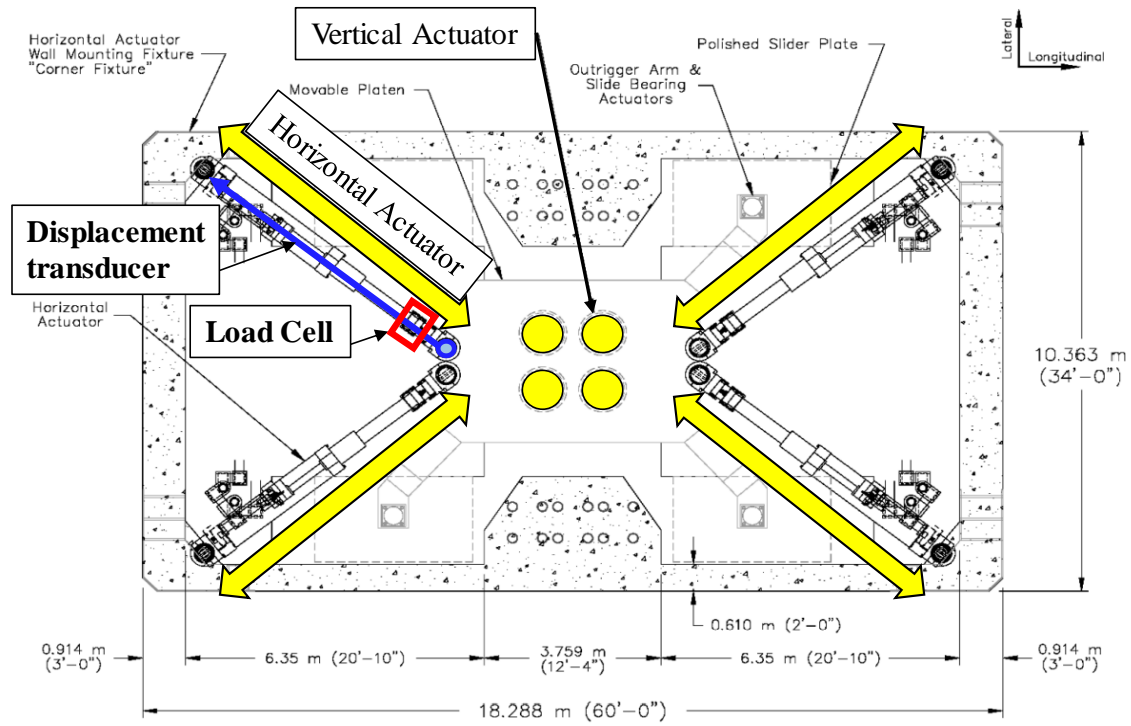
(b) Plan View
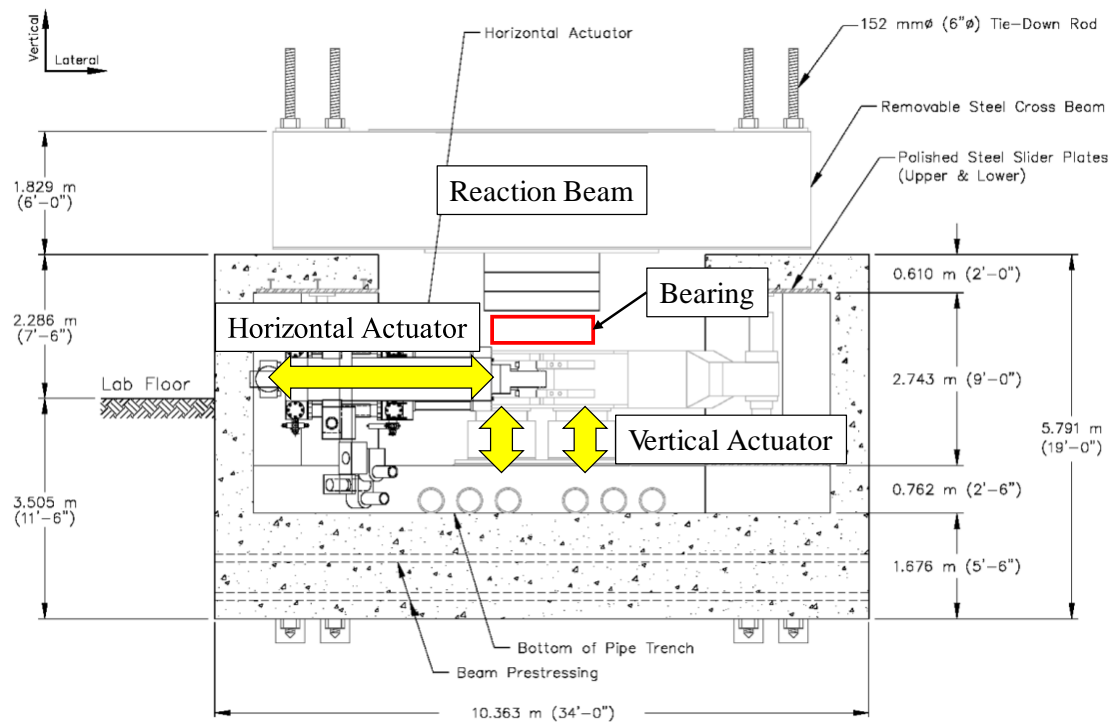
(c) Lateral Cross-Section View

Figure 2-6. Loading system [2-9]

The large lateral displacements required of the platen are accomplished via four horizontal actuators, extending from the corners of the concrete frame to the platen. These four actuators can accommodate a very large range of combined longitudinal and transverse motion. The horizontal forces from these actuators are resisted by the post-tensioned walls of the concrete frame. The concrete frame transfers the net horizontal force to the steel cross-beam, which in turn reacts against the top of the bearing specimen. Hence, the system forms a completely self-reacting horizontal frame, as seen in Figure 2-7. Inertial loads associated with dynamic testing are transmitted into the surrounding foundation.
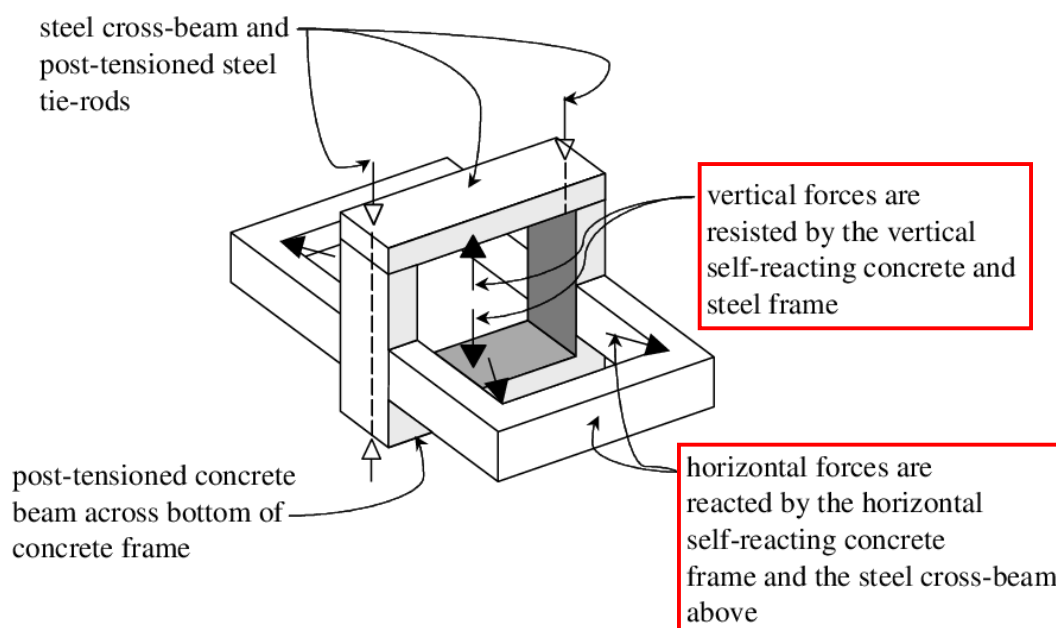
Figure 2-7. Schematic of horizontal and vertical self-reacting frames [2-9]

Simultaneously, large vertical compressive loads must be applied to the bearing specimen. The system's platen slides over a group of four stationary hydrostatic sliding bearings/actuators, fixed to the concrete frame beneath the platen. The polished underside of the steel platen slides over these four hydrostatic actuators with very little frictional resistance. Beneath these actuators, the vertical load is resisted by a post-tensioned concrete beam extending to the sides of the concrete frame. Above the platen, the vertical force is transmitted through the bearing specimen and into the removable steel cross-beam. Hence, the system forms a second self-reacting frame in the vertical plane, as illustrated in Figure 2-7.

Figure 2-8 shows a simplified free-body diagram of the platen. For simplicity, the four horizontal actuator forces have been lumped into a single horizontal force (F_a), and the eight distributed outrigger and vertical actuator forces have been lumped into a single vertical force ($N + W$), where N is the applied vertical force; W is the weight of the platen and specimen; F_a is the horizontal vector sum of actuator forces read by load cells; F_I is the inertia force of the platen; F_m is the machine friction force; and F_b is the shear force across the specimen.
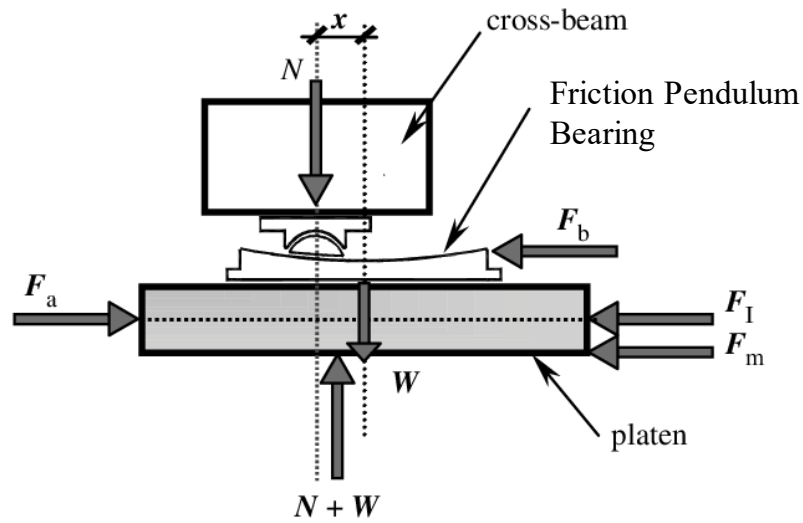
Figure 2-8. Simplified free-body diagram of platen with FPB specimen [2-9]

2.2.2 Installation plan

Installation plan is shown in Figure 2-9. Different size of specimens, base plates, and heat insulation plates were attached to the jigs by connection bolts.
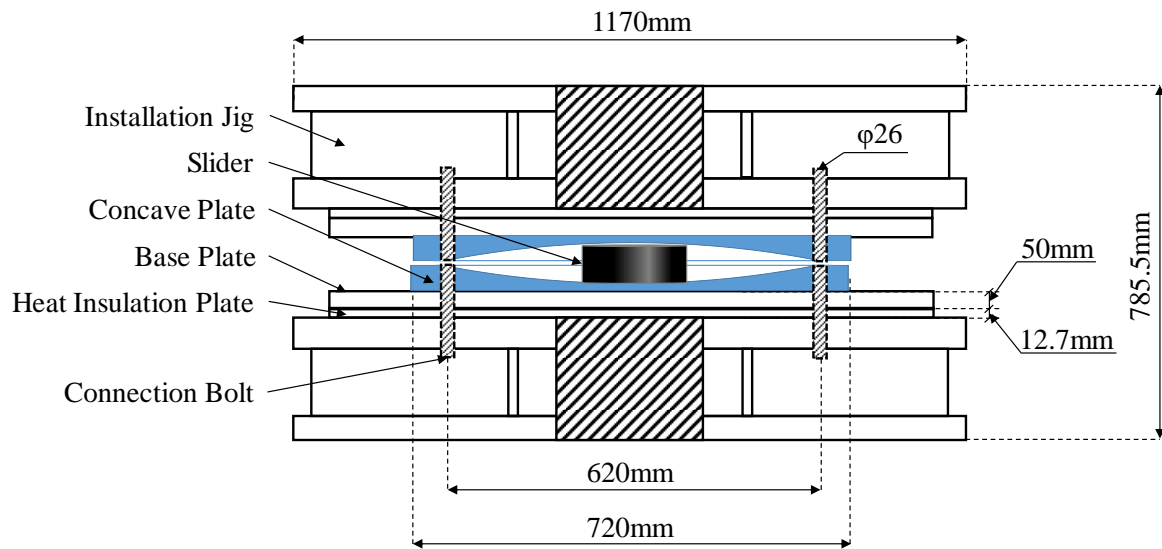
Figure 2-9. Installation plan

2.2.3 Measurement plan

The SRMD test system monitors forces on the platen via load cells on each of the four horizontal actuators and pressure transducers in each of the eight vertical actuators. And the displacements were measured by displacement transducers installed along the actuators. Figure 2-6 (b) shows that the horizontal actuator's load cells are located adjacent to the platen. Then the shear force across the specimen can be calculated by [2-9]:

$$F_b = F_a - F_I - F_m \tag{2-3}$$

And the procedure of calculating F_b under an event of this study is illustrated in Figure 2-10.
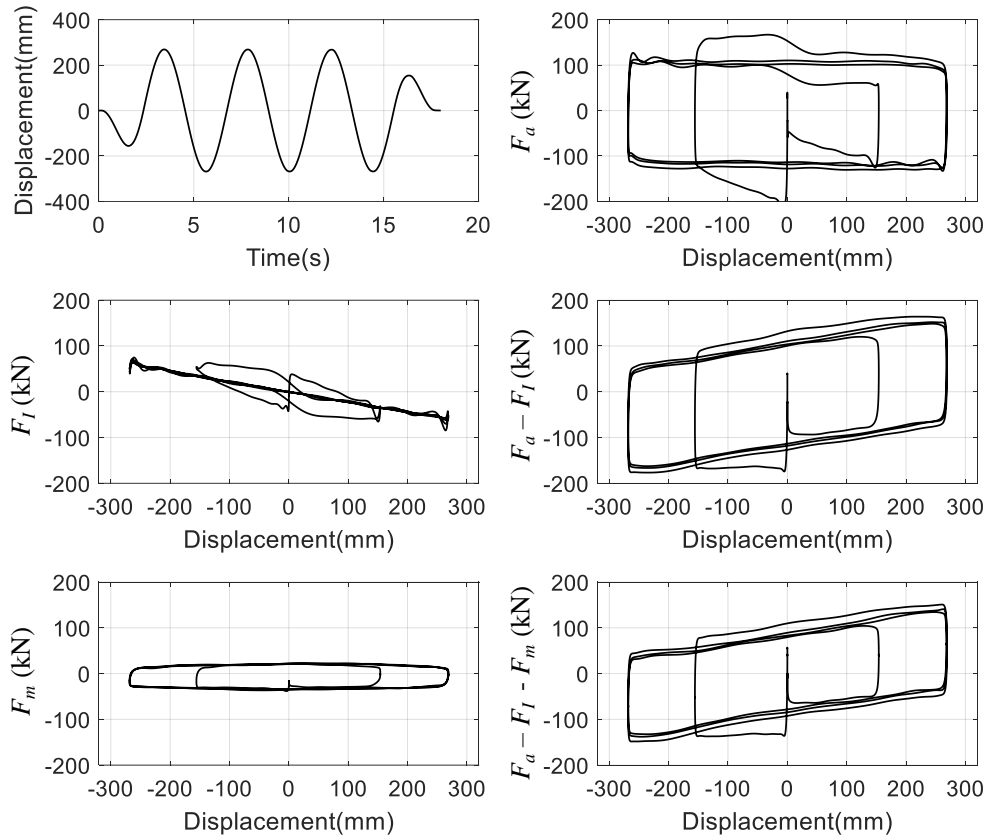
Figure 2-10 Example of force correction procedure for a ASCE φ200-T01 test

Where the vector sum of the forces read by these 4 load cells (F_a) represents only the inertia and friction applied to the platen. Hence, the load cells should not measure any of the inertia of the horizontal actuators. Accelerometers mounted at the center of the platen provide the acceleration measurements. Then the inertia force of the platen (F_I) can be obtained. By replacing the DCFP bearing with a sliding bearing with very little frictional resistance and

doing the same loading path, the friction force of the machine (F_m) can also be obtained by directly subtracting the inertia force of the platen from the vector sum of the forces read by the 4 load cells on the horizontal actuators.

Thermocouples were also installed on the specimen as shown in Figure 2-11 (a) to measure the temperature during the conducted dynamic tests and the experimental results under a sine wave with a maximum velocity of 400 mm/s are shown in Figure 2-11 (b) as an example. Where, T1, T2, T3, and T4 are the temperature of the atmosphere, surface of the concave plate, back of the lower concave plate, and side of the slider respectively.

(a) Position of thermocouples   (b) Experimental results of temperature
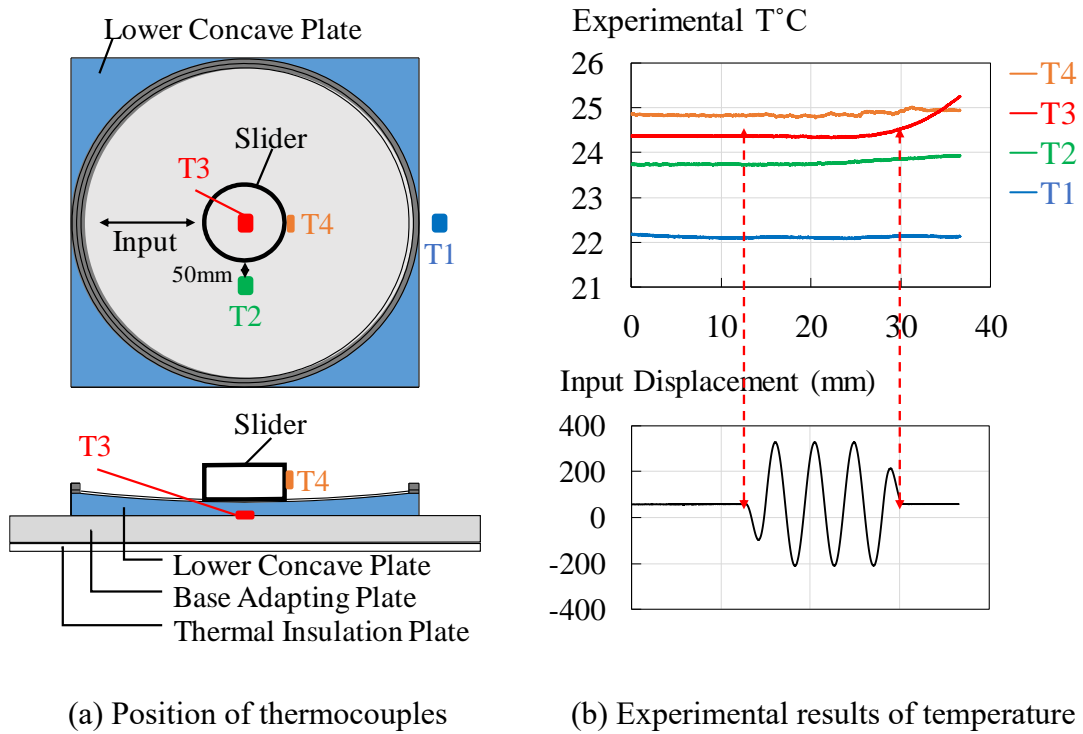
Figure 2-11. Temperature measurement

As the thermocouple cannot be placed directly on the contact surface between the slider and the concave plate, it is installed on the back of the lower concave plate instead as T3. However, the thickness of the concave plate will cause a significant measurement delay as shown in Figure 2-11 (b). Therefore, the experimental results are not reliable, and analytical results will be applied to simulate the temperature instead. Hence, only the experimental data at the beginning of the tests can be considered to be useful as initial temperature, and initial temperature of T3 were considered as the initial temperature of the contact surface (T_0). The

method to simulate the temperature increase caused by friction heating during the test ("heat transfer model") will be introduced later. This method is proposed and experimentally validated by M.C. Constantinou et al. in 2007, which can simulate the temperature based on the orbit of the bearing [2-11].

The analytical temperature history of the point at the center of the surface of the lower concave plate (above T3) under the same sine wave is shown in Figure 2-12 (a) as an example. Compared with the experimental results shown in Figure 2-12 (b), the analytical results are much higher and show much better synchronicity with the input wave.

(a) Analytical results   (b) Experimental results
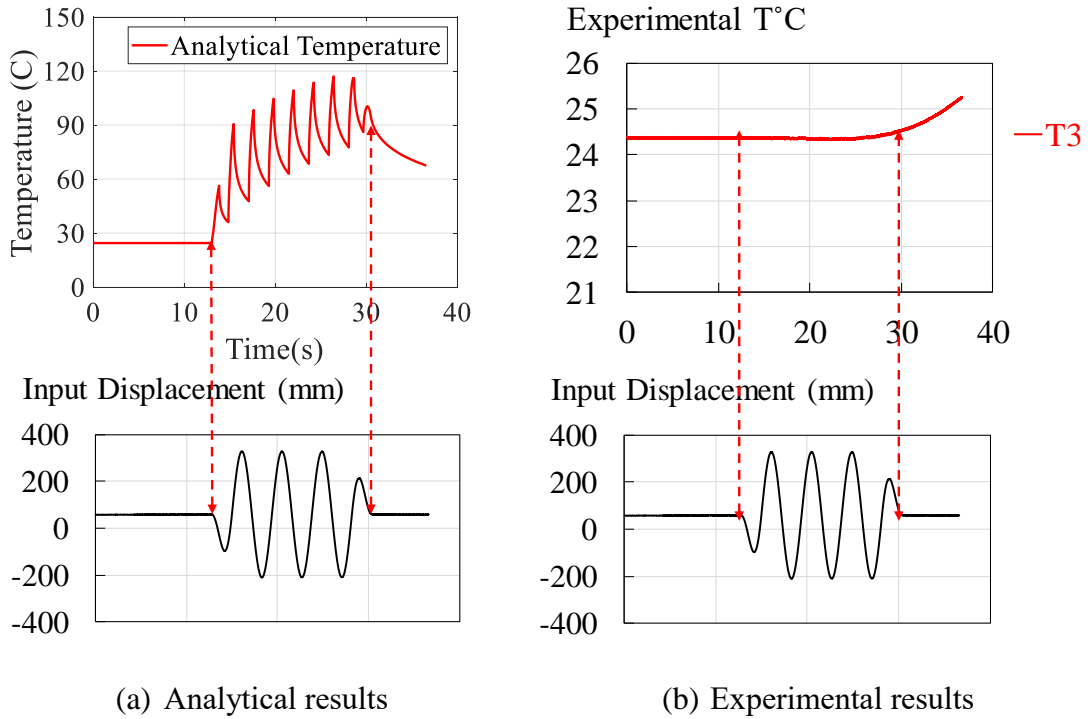
Figure 2-12. Temperature history under corresponding input displacement wave

2.2.4 Test procedure

The loading of both the dependency test and the ASCE test are controlled by horizontal displacement. The loading protocol of the dependency test is a 4-cycle sinusoidal displacement variation with a 200 mm amplitude, as shown in Figure 2-13 (a), and the test procedure is shown in Fable 2-2. Additionally, the loading protocol of a 3-cycle ASCE test is shown in Figure 2-13 (b), and the test procedure is determined based on 17.8.2.2 in standard ASCE/SEI 7-16 [2-8], as shown in Fable 2-3. In Fables 2-2 and 2-3, spec. num. shows the diameter of the slider, pressure is the contact pressure between the slider and the concave plate, amplitude is shown as Amp in Figure 2-13 (b), velocity is the maximum velocity of the loading protocol, period is the effective period of the DCFPB (shown as T in Figure 2-13 (a)) and the accumulated displacement is counted after each test. Three different specimens with identical sizes were used for each slider size for the velocity dependency test, pressure dependency test and ASCE test.
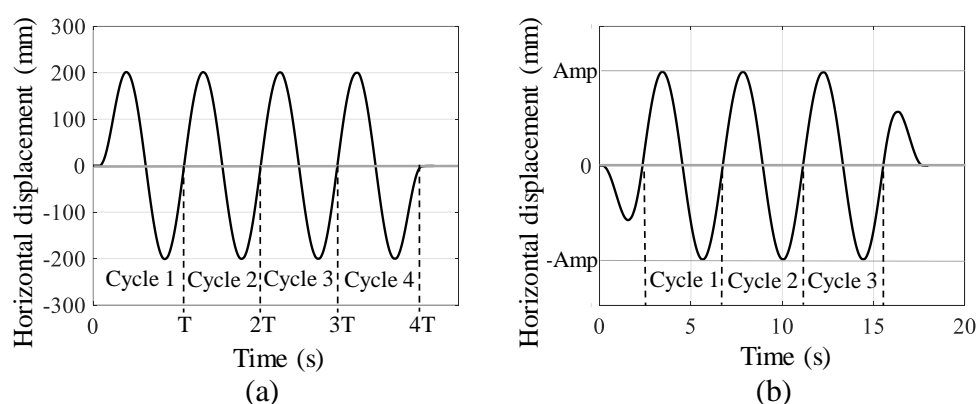
Figure 2-13. Loading protocol: (a) dependency test and (b) ASCE test (3 cycles)

Table 2-2. Test procedure (dependency test)

Spec. Num.	Test Num.	Pressure MPa	Amplitude ±mm	Velocity mm/sec	Period sec	Cycle Num.	T_0 (φ200) °C
			1) Test for Velocity Dependency				
	T01			20	62.83	4	19.81
	T02			50	25.13	4	21.42
	T03			100	12.57	4	22.67
φ200;	T04	60	200	200	6.28	4	23.34
&	T05			400	3.14	4	23.82
φ300;	T06			600	2.09	4	19.98
&	T07			800	1.57	4	22.48
φ400.			2) Test for Pressure Dependency				
	T08	40		20	62.83	4	20.39
	T09		200	400	3.14	4	22.21
	T10	80		20	62.83	4	22.76
	T11			400	3.14	4	23.04

Table 2-3. Test procedure (ASCE test)

Spec. num.	Test num.	Pressure N\mm²	Amplitude ±mm	Velocity mm/s	Period s	Cycle num.	Accumulated displacement m	T_0 (φ300) °C
	T01		268	392	4.26	3	3.84	22.67
	T02		10	14.646	4.26	20	4.66	26.64
	T03		100	146.369	4.26	3	6.09	25.73
	T04	60	200	292.738	4.26	3	8.96	26.27
	T05		268	392.269	4.26	3	12.79	26.28
φ200	T06		400	585.476	4.26	3	18.52	26.28
&	T07		400	585.476	4.26	3	24.25	22.03
φ300	T08	40	400	585.476	4.26	3	29.98	25.32
&	T09	80	400	585.476	4.26	3	35.71	25.74
φ400	T10	30	440	644.024	4.26	1	38.49	26.04
	T11	90	440	644.024	4.26	1	41.27	26.13
	T12a					7	50.36	25.67
	T12b	60	300	439.107	4.26	7	59.46	30.36
	T12c					6	67.36	30.59
	T13		268	392.269	4.26	3	71.20	26.16

In Table 2-3, two tests with identical loading protocols, T01 and T13, are placed at the beginning and the end of the test to consider the influence of accumulated displacement on the isolator properties. The lateral force of T02 is designed corresponding to wind design, whereas T03~T11 are designed to consider the influence of the rate of loading (velocity and pressure). Test 12 is designed to consider the influence of long duration excitation (for a DCFPB, the influence is mainly determined by the temperature increase caused by friction heating) and is separated into 3 parts because of the limit of the testing machine.

2.3 Validation of friction dependencies

Pressure, velocity and temperature dependency equations from previous studies [2-6][2-7] [2-10]are introduced in this section, and the applicability of the pressure and velocity dependency equations for φ300 and φ400 specimens are verified by the experimental results of the dependency test. Since the temperature is difficult to accurately measure during testing, a numerical method proposed by MC. Constantinou et al. [2-4][2-11] was also introduced to simulate the temperature. Based on these equations, three friction models are described: precise, simplified and constant models.

2.3.1 Friction dependencies

The pressure dependency of the friction coefficient can be considered by a pressure dependency factor γ, which is related to the bearing stress σ at the contact area of the concave plate and slider. The pressure dependency equation is shown as follows:

$$\gamma(\sigma) = 2.03 \times \sigma^{-0.19} + 0.068 \tag{2-4}$$

This equation was obtained by a previous experimental study on the pressure dependency of DCFPBs with slider diameters equal 350mm [2-7], as shown in Figure 2-14 (a). The equation was determined based on the average value of the ±y-intercept in the 3rd cycle of friction coefficient-displacement figures from prototype tests. These tests were loaded by a unidirectional sinusoidal displacement input with a maximum velocity of 20 mm/s and various pressures. The 3rd cycle was selected because the behavior of the bearing at the 3rd cycle was stable.

The dependency of the friction coefficient on velocity is considered by a velocity dependency factor α. This factor is related to the velocity of the upper concave plate relative to the lower concave plate v, which can be described by the following equation:

$$\alpha(v) = 1 - 0.55 \times e^{-0.019v} \tag{2-5}$$

This equation was obtained by a previous experimental study on the velocity dependency of SCFPBs with slider diameters equal 200mm [2-7] , as shown in Figure 2-14 (b). The equation was determined based on the experimental value of the friction coefficient at different velocities in the 3rd cycle of the friction coefficient-displacement figures from prototype tests. These tests were loaded by a unidirectional sinusoidal displacement input with a constant pressure of 60 N/mm^2 and a maximum velocity of 300 mm/s (same as 600mm/s for DCFPB).

(a) Pressure dependency (b) Velocity dependency (c) T°C dependency
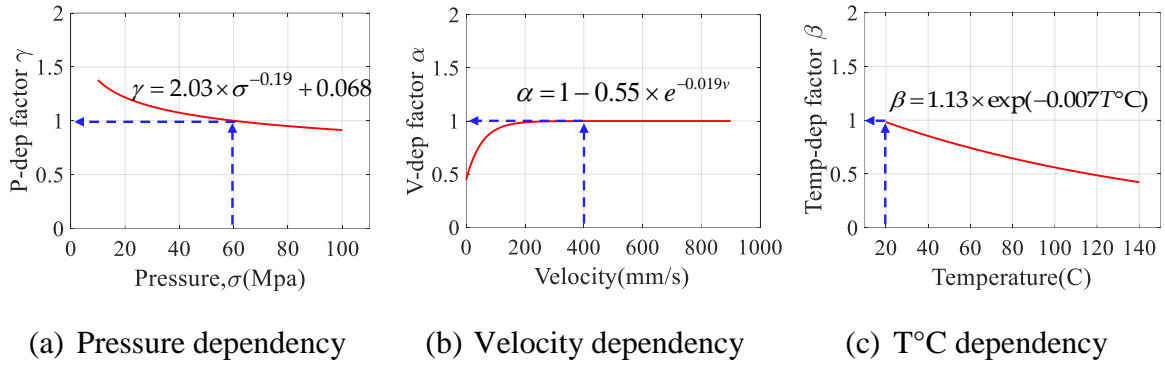
Figure 2-14. Friction dependencies obtained by previous experiments

The temperature dependency equation is shown as follows:

$$\beta(T°C) = 1.13 \times \exp(-0.007T°C) \tag{2-6}$$

where β is the temperature dependency factor and $T°C$ is the temperature of the contact area between the slider and the concave plate in Celsius [2-10]. The temperature $T°C$ during the test consists of the initial temperature and the temperature increase caused by friction heating. However, during the test, it is very difficult to correctly measure the temperature increase, as introduced in section 2.2.3. In this case, to obtain the temperature dependency, the temperature increase must be sufficiently small that it can be neglected, and the temperature will be controlled by the initial temperature. To achieve this objective, a unidirectional repeat test (material test) was conducted in a previous study, in which the velocity between PTFE and stainless steel was constant at 20 mm/s, the contact pressure was constant at 1 MPa, the contact area was 19.6 mm^2 and the number of cycles was 3 [2-6]. In these loading conditions, the temperature increase can be considered ignorable, and the initial temperature is controlled

by a heater. Based on this test, the temperature dependency equation was first obtained based on the friction coefficient calculated at the 3rd testing at the 50mm distance point of 100mm sliding test with initial temperatures of 20˚C, 40˚C, 60˚C, 90˚C, 150˚C and 200˚C [2-6]. Then, after conducting the prototype tests of DCFPBs, this equation was revised to Equation (2-6) based on the experimental results so that the behavior of the specimen in the experiment can be reproduced [2-10].

The accuracy of the friction dependencies was validated by the dependency test shown in Table 2-2. First, basic knowledge about friction dependencies will be introduced: The value of friction coefficient (μ) between two materials is affected by pressure, velocity and temperature. Therefore, when a μ is obtained by dividing the friction force with the vertical load based on Equation (2-2), it represents the μ under a certain pressure (σ), a certain velocity (v) and a certain temperature ($T°C$). The procedure of getting the friction coefficient from the experimental results is shown in Figure 2-15.

(a) Horizontal force (*Fh*)   (b) Friction force (*Ff*)   (c) Friction coefficient (μ)
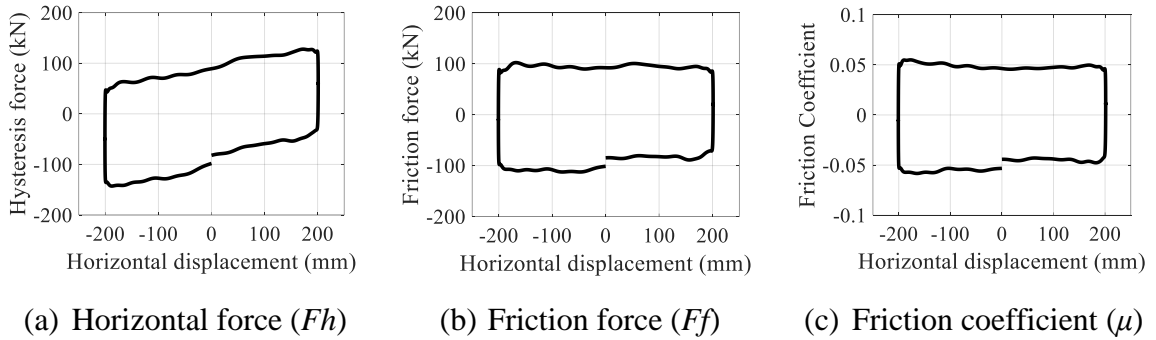
Figure 2-15. Procedure of getting the friction coefficient from the experimental results (taking φ200-T05 in dependency test as an example)

In order to describe the value of μ, we need to clarify its relation with *P*, *V*, and *T°C* respectively, and a friction coefficient under a specific pressure, velocity, and temperature (μ_0) should be selected as reference. In this study, this reference condition is selected as: 60MPa, 400mm/s and 20°C. Then, μ under various condition can be expressed as:

$$\mu(\sigma,v,T°C) = \mu_0 \times \gamma(\sigma) \times \alpha(v) \times \beta(T°C) \tag{2-7}$$

Where μ is the friction coefficient under a certain condition (σ, *v*, $T°C$), μ_0 is the reference friction coefficient under the reference condition (60MPa, 400mm/s and 20°C), γ is the

pressure dependency factor, α is the velocity dependency factor, and β is the temperature dependency factor.

As for the calculation of dependency factors, velocity dependency is taken as an example. Since the reference velocity is 400mm/s, the velocity dependency factor at 50mm/s can be calculated by:

$$\alpha(50mm/s) = \frac{\mu(50mm/s)}{\mu(400mm/s)} \tag{2-8}$$

As shown in Equation (2-7), except for velocity, pressure and temperature will also affect the value of μ. Therefore, in Equation (2-8), in order to eliminate these effects, the μ at the numerator and the denominator should share the same pressure and temperature. Similar procedure can also be used for calculating pressure and temperature dependencies.

2.3.2 Validation of temperature dependency

As introduced in Section 2.2.2, the temperature measured from the thermocouples are not accurate and the analytical temperature will be used to validate the temperature dependency equation. φ200-T05 in dependency test was taken as an example. The displacement input of it shown in Figure 2-16 (a). The points which are used to calculate the temperature dependency factor (β) is marked in the displacement input. These points have the same pressure as 60Mpa and the same velocity as 400mm/s, under which the pressure dependency factor (γ) and the velocity dependency factor (α) are both 1. The position of point a and b is also shown in friction coefficient – displacement curve as shown in Figure 2-16 (b), from which the friction coefficient of these points can be obtained.

(a) Displacement input   (b) Points used to calculate β
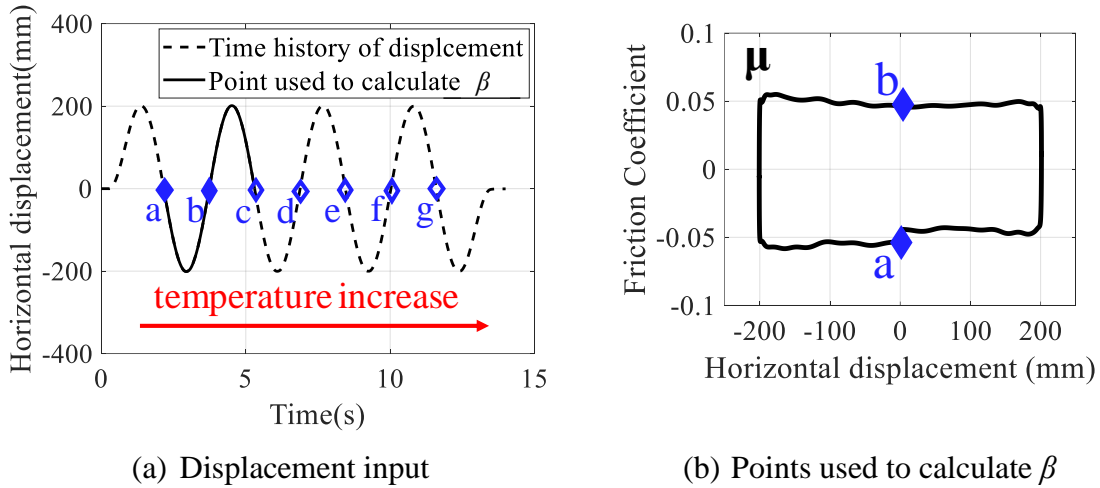
Figure 2-16. Displacement input and points used to calculate β of φ200-T05 in dependency test

Then, using a similar equation as Equation (2-8) for calculating the temperature dependency factor (β), the experimental values of β at points a ~ g can be obtained:

$$\beta(T°C_{a\sim g}) = \frac{\mu(T°C_{a\sim g})}{\mu(20°C)} \qquad (2\text{-}9)$$

Where T°C$_{a\sim g}$ is the temperature at points a ~ g. Together with corresponding analytical temperature results, they can be plotted in the β – temperature figure as shown in Figure 2-17. It can be seen that the temperature dependency equation shows high consistency with the

experimental results. Based on this procedure, the applicability of the temperature dependency equation under real-size DCFP bearings and dynamic excitations is verified.
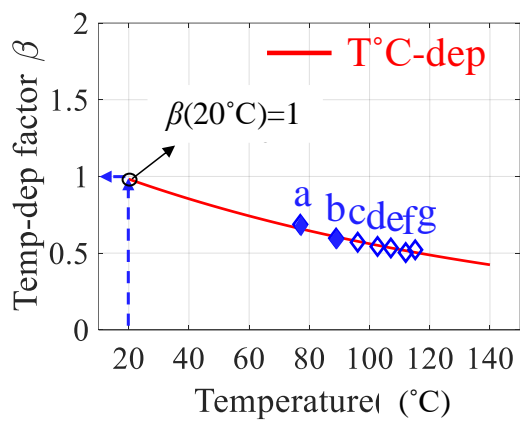
Figure 2-17. Validation of temperature dependency equation under φ200-T05 in dependency test

2.3.3 Validation of pressure and velocity dependencies

When validating the velocity dependency equation, experiments of sine displacement inputs with various maximum velocities were conducted (T01~T07 in Table 2.2). As for the pressure dependency equation, various pressures were considered (T05, T09, T11 with the maximum velocity as 400mm/s and T01, T08, T10 with the maximum velocity as 20mm/s). Also, taking φ200-T05 in dependency test as an example, the experimental value of pressure dependency factor γ and velocity dependency factor α of points a ~ g is shown in Figure 2-18. The blue diamond markers are obtained from experimental results: First, the friction coefficients at zero displacements (a ~ g in Figure 2-16 (a)) calculated by dividing the friction force with the vertical load were obtained at each point. Then, as shown in Equation (2-8), in order to obtain the velocity dependency factor (α), the friction coefficients under various velocities should be divided by the friction coefficient under 400mm/s. As the points a ~ g in φ200-T05 (Figure 2-16 (a)) are all under 400mm/s, the experimental friction coefficient under 400mm/s, μ(400mm/s), is determined by taking the average of a ~ g in φ200-T05. Therefore, the experimental velocity dependency factor at point a ~ g under various velocities considered in Table 2.2 can be expressed as:

$$\alpha(v_{a\sim g}) = \frac{\mu(v_{a\sim g})}{\mu(400mm/s)} \tag{2-10}$$

Where $v_{a\sim g}$ is the velocity at points a ~ g. Similarly, the experimental pressure dependency factor under 400mm/s and 20mm/s at point a ~ g under various pressure considered in Table 2.2 can be expressed as:

$$\gamma(\sigma_{a\sim g}) = \frac{\mu(\sigma_{a\sim g})}{\mu(60MPa)} \tag{2-11}$$

Where $\sigma_{a\sim g}$ is the pressure at points a ~ g. Then, the experimental data of γ and α under φ200-T05 calculated by Equation (2-10) and (2-11) respectively is shown in Figure 2-18 as an example. Where the line in Figure 2-18(a) is the pressure dependency equation, the line in Figure 2-18(b) is the velocity dependency equation, and the markers are the experimental

data. Based on Section 2.3.1, it clear that the difference between the value of a ~g is caused by the effect of temperature on the friction coefficient.

(a) Pressure dependency factor (γ) (b) Velocity dependency factor (α)
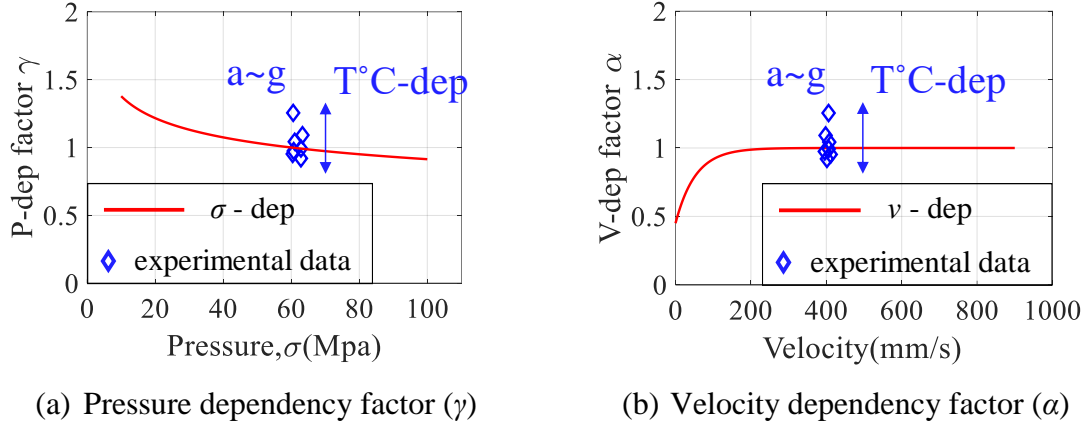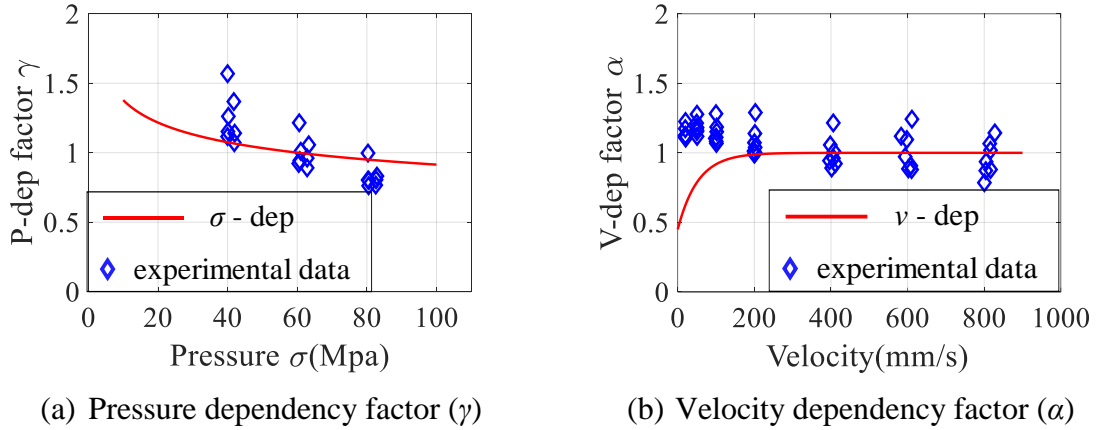
Figure 2-18. Experimental data of γ and α under φ200-T05 in dependency test

To validate the pressure and velocity dependencies, the experimental data of γ and α under various pressures and velocities were shown in Figure 2-19 (a) and (b) respectively.

(a) Pressure dependency factor (γ) (b) Velocity dependency factor (α)

Figure 2-19. Experimental data of γ and α under various pressures and velocities

From Figure 2-19. It can be seen that the experimental results under small velocity (e.g. 50 mm/s) are very different from the velocity dependency equation proposed. This is caused by the effect of temperature dependency. Based on the basic knowledge about friction dependencies, the reason can be explained:

In the experiment, the pressure and velocity at the contact surface can be measured and the temperature of the contact surface at each moment can be simulated based on the study of Constantinou et al. [2-11] as shown in Figure 2-20, which shows the sine displacement input of two unidirectional dynamic tests with the maximum velocity equals 50 mm/s and

400 mm/s respectively. Further, based on Equation (2-6), the temperature dependency factor of the considered specimen can be calculated from the simulated temperature. In Figure 2-20, a ~ g are the points with zero displacement, which means the velocity of these points equals to the maximum velocity and the restoring force provided by the curvature of the concave plate at these points is zero. T is the period of the sine wave. With the same amplitude, smaller T will lead to larger velocity.

(a) Max. velocity equals 50 mm/s   (b) Max. velocity equals 400 mm/s
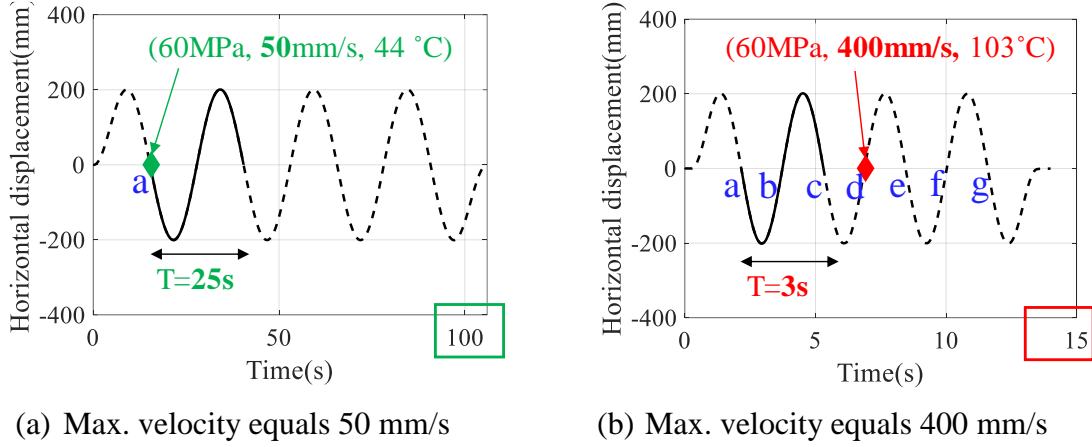
Figure 2-20. Input displacement of T02 and T05 of the dependency test

(a) Experimental results of V-dep factor   (b) T˚C-dependency
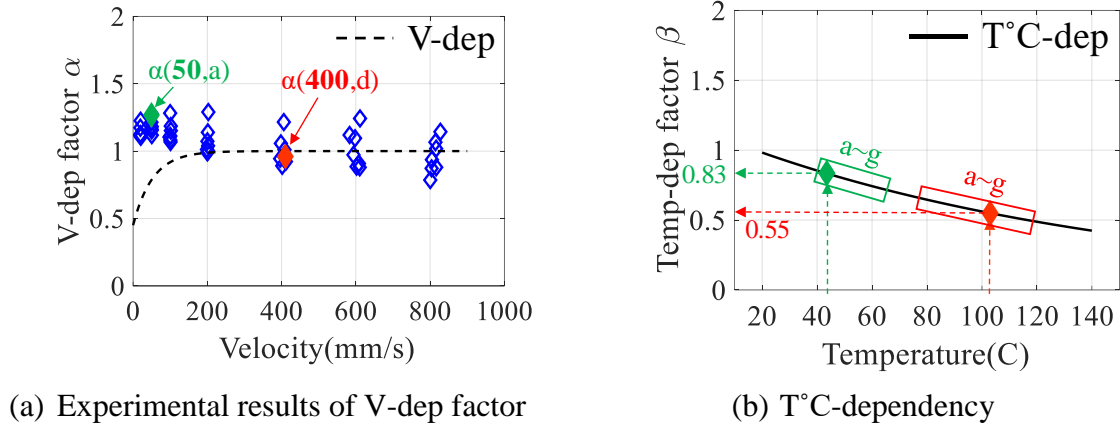
Figure 2-21. Effect of T˚C-dependency on experimental results of V-dependency factor

Figure 2-21 (a) shows the experimental results and the previously proposed velocity dependency equation. The blue diamond markers shown in Figure 2-21 (a) are obtained from experimental results: First, the friction coefficients at zero displacements (a ~ g in Figure 2-20) calculated by dividing the horizontal force with the vertical load were obtained for various velocities. Then, as shown in Equation (2-8), in order to obtain the velocity dependency factor (α), the friction coefficients under various velocities should be divided by

43

the friction coefficient under 400mm/s. As the points a ~ g in Figure 2-20 (b) are all under 400mm/s, the experimental friction coefficient under 400mm/s is determined by taking the average of a ~ g in Figure 2-20 (b). Therefore, the velocity dependency factor at point a in Figure 2-20 (a) (50 mm/s) can be expressed by the experimental results:

$$\alpha(50mm/s, a) = \frac{\mu(50mm/s, a)}{ave(\mu(400mm/s, a \sim g))} \qquad (2\text{-}12)$$

In can be seen from Figure 2-21 (a) that, the average experimental μ under 400 mm/s (a~g) is similar to the μ at point d. Therefore, μ at point d is used instead of the average value for easier explanation of why large difference exists at low velocity:

$$\alpha(50mm/s, a) \approx \frac{\mu(50mm/s, a)}{\mu(400mm/s, d)} \qquad (2\text{-}13)$$

To explain why the experimental results under 50mm/s are so different from the velocity dependency equation, we need to consider it in an analytical form: Based on Equation (2-7), by considering all the friction dependencies at point a in Figure 2-20 (a) (50 mm/s), the friction coefficient at this point can be expressed as:

$$\mu(50mm/s, a) \approx \mu_0 \times \gamma(60MPa) \times \alpha(50mm/s) \times \beta(44^\circ C) = \mu_0 \times 1 \times 0.79 \times 0.83 \qquad (2\text{-}14)$$

The friction coefficient at point d in Figure 2-20 (b) (400 mm/s) can be expressed as:

$$\mu(400mm/s, d) \approx \mu_0 \times \gamma(60MPa) \times \alpha(400mm/s) \times \beta(103^\circ C) = \mu_0 \times 1 \times 1 \times 0.55 \qquad (2\text{-}15)$$

If the temperature dependency is not eliminated, the velocity dependency factor α will be obtained by directly dividing the experimental results, like:

$$\alpha(50mm/s, a) \approx \frac{\mu(50mm/s, a)}{\mu(400mm/s, d)} = \frac{\mu_0 \times 1 \times 0.79 \times 0.83}{\mu_0 \times 1 \times 1 \times 0.55} = 1.19 \qquad (2\text{-}16)$$

However, to obtain velocity dependency, the pressure and temperature dependencies need to be eliminated by dividing the pressure and temperature dependency factors:

$$\alpha(50mm/s, a) \approx \frac{\mu(50mm/s, a)/\gamma(60MPa)/\beta(44^\circ C)}{\mu(400mm/s, d)/\gamma(60MPa)/\beta(103^\circ C)}$$
$$= \frac{\mu_0 \times 1 \times 0.79 \times 0.83/1/0.83}{\mu_0 \times 1 \times 1 \times 0.55/1/0.55} = 0.79 \qquad (2\text{-}17)$$

In Figure 2-21 (a), 1.19 represents the experimental result (blue diamond maker) which contains the effect of temperature dependency, and 0.79 represents the corresponding point on the velocity dependency equation which eliminated the temperature dependency. Therefore, the difference is caused by the effect of the temperature dependency factor, β.

Based on this procedure, red circle markers in Figure 2-22 (b) shows the results of velocity dependency factor after eliminating the effect of temperature dependency as shown in Equation (2-17). It shows that after eliminating the temperature dependency, all the points (a ~ g) at the same velocity will have similar value. Based on Equation (2-17), it implies that the effect of temperature dependency is successfully eliminated. Moreover, the experimental data after eliminating the temperature effect fits well with the velocity dependency equation proposed by the previous study. Therefore, it can be concluded that the velocity dependency equation obtained from small-scale element tests is also suitable for the real case (full-scale tests conducted in this study).

(a) T°C dependency not eliminated   (b) T°C dependency eliminated
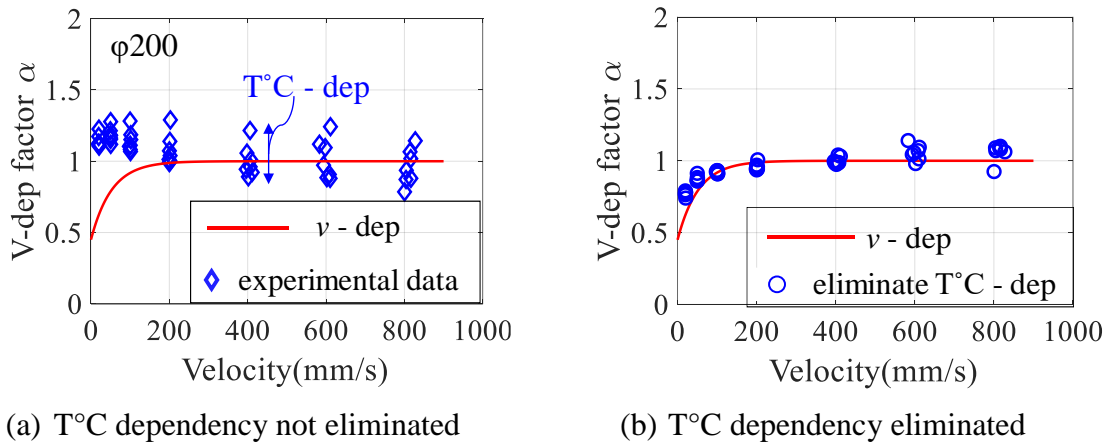
Figure 2-22. Validation of velocity dependency equation by prototype dynamic test (φ200)

The same procedure was also conducted on validating the pressure dependency. Figure 2-23 shows the results of φ200 under the inputs whose maximum velocity was set as 400mm/s, where Figure 2-23 (a) and (b) show the experimental results of γ and the results of γ eliminating the effect of temperature dependency respectively. Moreover, Figure 2-24 shows the results of φ200 under the inputs whose maximum velocity was set as 20mm/s, where Figure 2-24 (a) and (b) show the experimental results of γ and the results of γ eliminating the effect of temperature dependency respectively. It can be seen that, compared

with the experimental data with the maximum velocity set as 400mm/s (Figure 2-23 (a)), the experimental data with 20mm/s (Figure 2-24 (a)) is more consistent with the pressure dependency equation. This is because that the friction heating under 20mm/s is much weaker than that under 400mm/s, which means the effect of temperature dependency on the friction coefficient under 20mm/s is much less. Combining Figure 2-23 and 2-24, it can be concluded that the pressure dependency equation obtained from small-scale element tests is also suitable for the real case (full-scale tests conducted in this study).
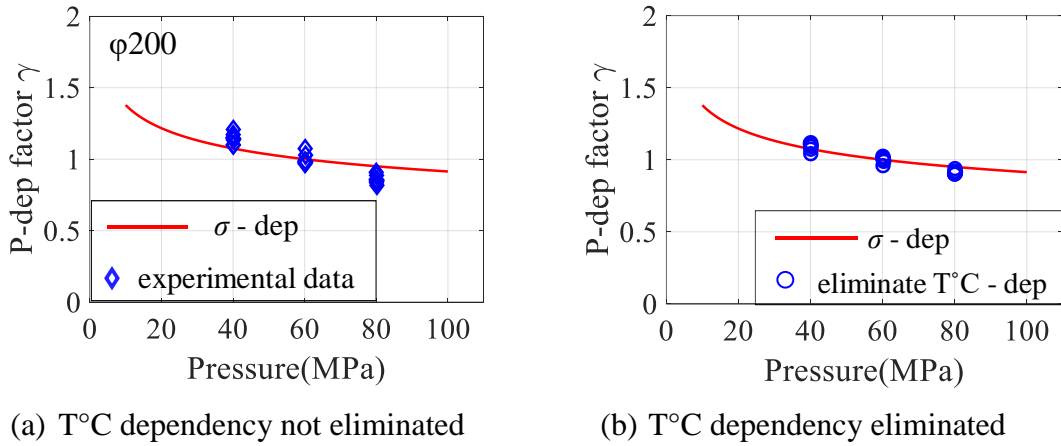

(a) T°C dependency not eliminated   (b) T°C dependency eliminated
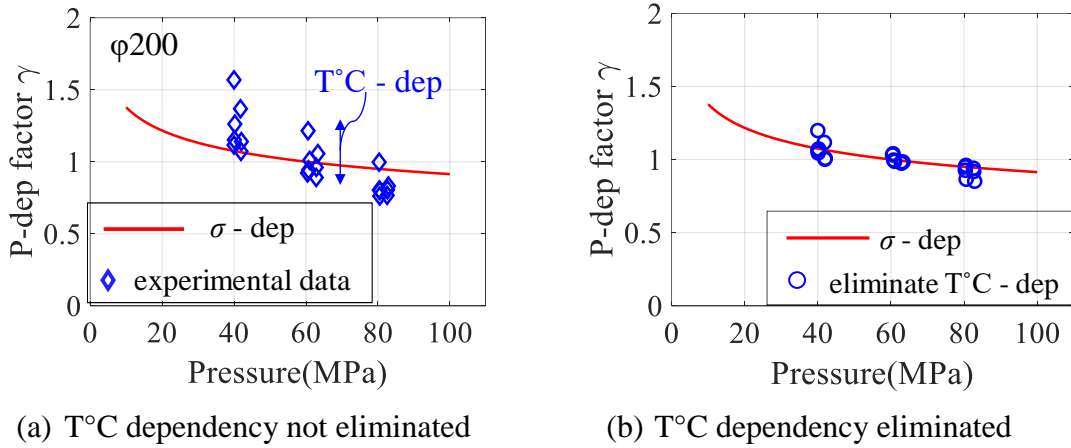
Figure 2-23. Validation of the pressure dependency equation by full-scale dynamic tests with the maximum velocity set as 400mm/s (φ200)

(a) T°C dependency not eliminated   (b) T°C dependency eliminated

Figure 2-24. Validation of the pressure dependency equation by full-scale dynamic tests with the maximum velocity set as 20mm/s (φ200)

The validation of the velocity and the pressure dependencies are also validated by DCFP bearings with φ400 slider. The results are shown in Figure 2-25 ~ 2-27. The experimental results of α and γ after eliminating the temperature dependency also show high consistence

with the dependency equations. Therefore, it can be concluded that the accuracy of the friction dependencies is not related to the size of the slider.

(a) T°C dependency not eliminated (b) T°C dependency eliminated

Figure 2-25. Validation of the velocity dependency by prototype dynamic test (φ400)
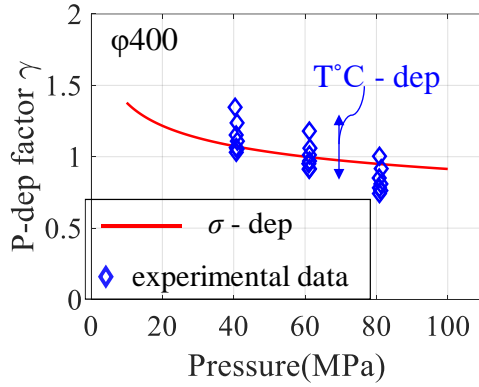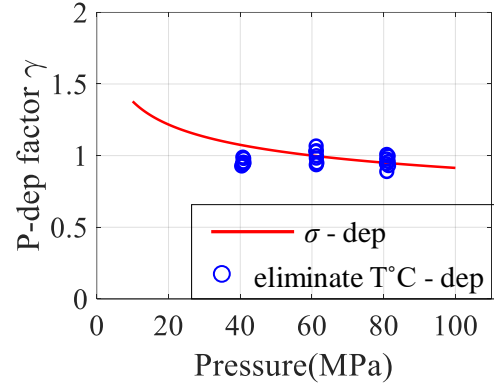
(a) T°C dependency not eliminated (b) T°C dependency eliminated
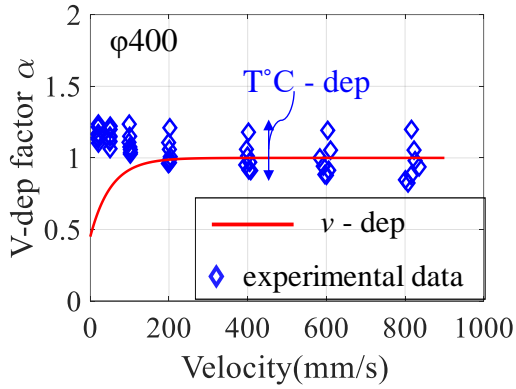
Figure 2-26. Validation of the pressure dependency equation by full-scale dynamic tests with the maximum velocity set as 400mm/s (φ400)

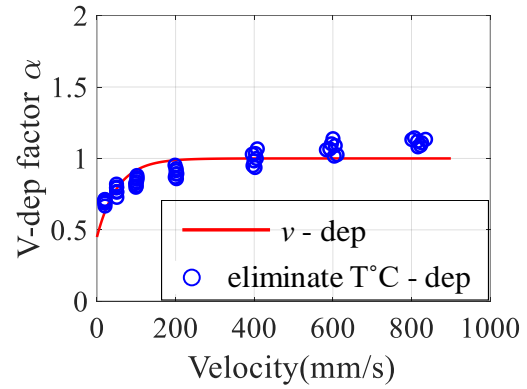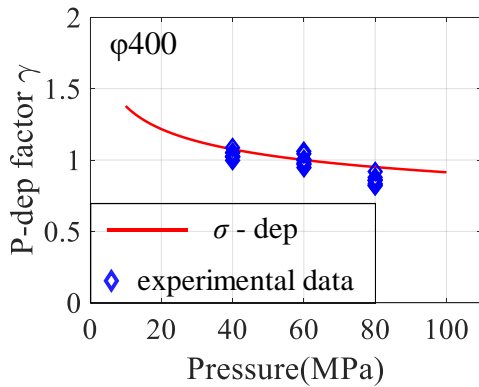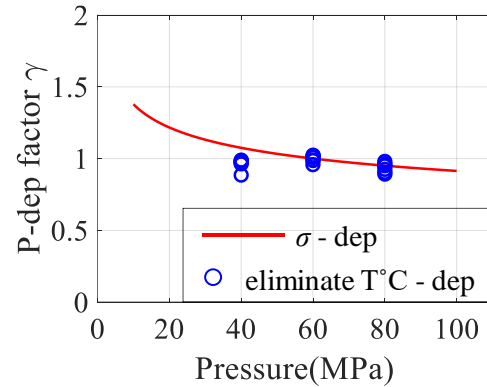(a) T°C dependency not eliminated (b) T°C dependency eliminated

Figure 2-27. Validation of the pressure dependency equation by full-scale dynamic tests with the maximum velocity set as 20mm/s (φ400)

2.4 Friction models

Pressure, velocity and temperature dependency equations from previous studies were validated by the experimental results of the dependency test in the last section. To simulate the behavior of the DCFP bearing, a numerical method proposed by MC. Constantinou et al. was also introduced in this section to simulate the temperature of the contact surface of the bearing under excitations. Based on these equations, three friction models are described as the precise, simplified and constant models.

2.4.1 Temperature computation of friction heating

A general computation of temperature at the surface of a semi-infinite solid (Figure 2-28) at x=0 with heat flux $q(t)$ that varies with time is shown as follows:

$$\Delta T(t) = \frac{\sqrt{D}}{k\sqrt{\pi}} \int_0^t \frac{q(t-\tau)d\tau}{\sqrt{\tau}} \tag{2-18}$$

where $q(t)$ is the heat flux at the surface of the solid, $\Delta T(t)$ is the temperature change at time t compared with the temperature at t=0, τ is a time parameter that varies between 0 and t, D is the thermal diffusivity of the solid, and k is the thermal conductivity of the solid [2-11]. In this study, the values of k and D are adopted from the "JSME Data Book: Heat Transfer", which are 0.016 W/(mm·°C) and 4.07 mm^2/s, respectively [2-12]. Equation (2-18) is for a semi-infinite solid with infinite plan dimensions and depth, as shown in Figure 2-28.
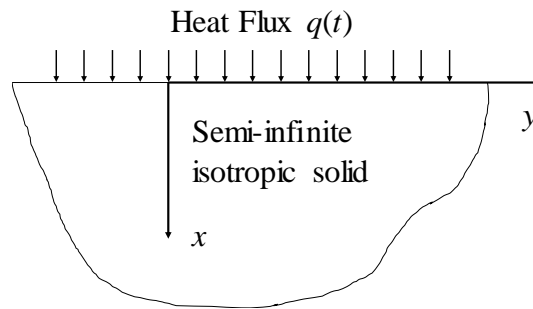
Figure 2-28. Semi-infinite solid with heat Flux at x=0

Based on the studies of MC. Constantinou et al., wherein this equation for the friction heating problem of FPBs was recognized [2-4][2-11], the following conclusions can be

drawn: (1) The friction heating problem of an FPB is not about an infinite solid; however, when considering the temperature of one point at the contact area of the slider and concave plate, the infinite solid assumption is valid because a point is relatively small compared with the dimensions of the bearing. (2) For PTFE-stainless steel interfaces, it is appropriate to assume that all of the generated heat flux from friction heating enters the steel part because the stainless steel has greater thermal conductivity and thermal diffusivity than the PTFE. (3) The instantaneous heat flux at a point on the concave plate is nonzero as the slider passes over it, whereas this heat flux remains zero otherwise. Therefore, for DCFPBs, the instantaneous heat flux, $q(t)$, is defined as follows:

$$q(t) = \begin{cases} \mu(t)p(t)\dfrac{v(t)}{2} & \text{if } \delta \leq \sqrt{\pi \cdot r_{contact}^{2}}/2 \\ 0 & \text{otherwise} \end{cases} \tag{2-19}$$

where $\mu(t)$, $p(t)$ and $v(t)$ are the coefficient of friction, the pressure at the contact area and the relative velocity between the upper and lower concave plates at time t, respectively; δ is the lateral distance from the center of the slider to the point of interest; and $r_{contact}$ is the contact radius. (4) To address the uneven heat flux distribution generated by friction, the estimation for the temperature increase will be taken as an average over the contact area.

2.4.2 Friction models that combines pressure, velocity and temperature dependencies (precise model and simplified model)

Two friction models are proposed as precise and simplified models, and both considered the pressure, velocity and temperature dependency introduced in Section 2.3.1. Meanwhile, the precise model applies the precise temperature simulation model shown in Figure 2-29 (a) and the simplified model applies the simplified temperature simulation model shown in Figure 2-29 (b), where $r_{contact}$ is the radius of the bearing and the monitor points are virtual points in the model used for temperature simulation, which is proposed by Constantinou, M.C. et al. [2-4][2-11]. The temperatures at these points can be calculated by the method introduced in section 2.4.1 at any time during excitation. In the excitation, heat will be generated at the points within the contact surface of the slider and the contact plates, and the effective temperature of the contact surface will also be calculated based on these points. As the precise model has a lot of monitor points along the sliding direction, the simulation results are more precise. However, for the simplified model, which only applies one monitor point, the calculation speed is much faster. Therefore, the validation of the simplified model is very important in judging whether it can be used instead of the precise model. Figure 2-29 (a) shows the monitor point distribution for the precise model (the number of monitor points shown in the figure is much less than that used in the model). The temperature is tracked on a line of uniformly distributed points along the sliding direction across the center of the slider on the sliding surface with an interval of 5 mm. The average value of the temperatures at the points within the contact area is used for $T°C$ in Equation (2-6). Here, the section of the slider is assumed as a square with an area equal to the area of the slider (contact area). Because the contact area is assumed to be a square, one line of monitor points in the direction of sliding shown in figure 2-29 (a) can give the same result as a grid of monitor points.Figure 2-29 (b) shows a simplified method proposed by M. Kumar et al., in which only the temperature at the center of the sliding surface is used to compute $T°C$ in Equation (2-6) [2-4]. In this case, when the slider is above the center point, $T°C$ in Equation (2-6) will increase, and when the slider moves away, the temperature will decrease.
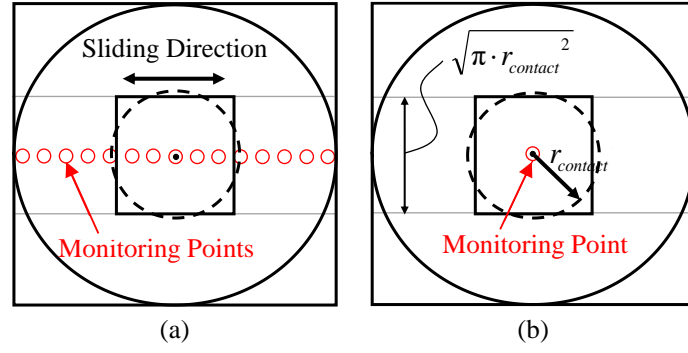
Figure 2-29. Simulation models of the representative temperature used in the (a) precise model and (b) simplified model.

After obtaining the representative temperature of the contact surface, the coefficient of friction of the precise and simplified model at each time during excitation can be calculated by Equation (2-7) introduced in Section 2.3.1:

$$\mu(\sigma, v, T^\circ C) = \mu_0 \times \gamma(\sigma) \times \alpha(v) \times \beta(T^\circ C) \tag{2-7}$$

where μ, γ, α and β are the friction coefficient, pressure dependency factor, velocity dependency factor and temperature dependency factor at each time, respectively, and μ_o is the friction coefficient at 60 N/mm^2 ($\gamma = 1$), 400 mm/s ($\alpha = 1$) and an atmosphere temperature of around 20°C ($\beta = 1$), which was selected as 0.075 for all the specimens in this study. μ_o was calculated from the trend line of the friction coefficient versus the time from the dependency test – φ300 – T05 in Table 2-2, which was when the time was approaching zero, as shown in Figure 2-30. The experimental values in this figure represent the friction coefficients near zero displacement where the velocity was 400 mm/s and the pressure was 60 N/mm^2.
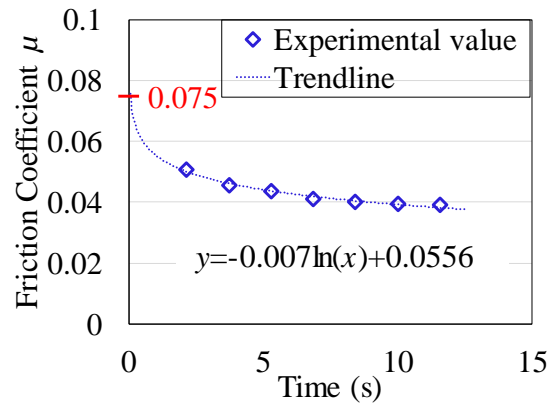
Figure 2-30. Determination of μ_o.

51

2.4.3 Numerical results using the precise and simplified model

The comparison of the first hysteresis curve between the friction models and the experimental results of the DCFP bearings with 400 mm-diameter sliders under both strong and weak excitations are shown in Figure 2-31, and show high accuracy for both friction models. The input excitations in Figure 2-31 (a) and (b) are the first cycles in T01 and T02 of the ASCE test as shown in Table 2-3, respectively. In all of the ASCE tests, the simplified model shows a similar accuracy to the precise model, with both models showing high accuracy in the simulation of the behaviors of the DCFP bearings.
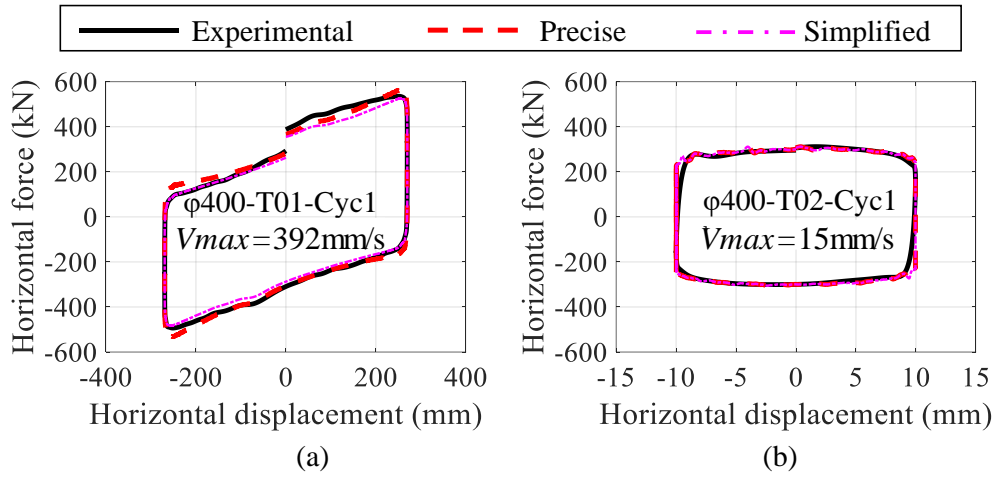
Figure 2-31. Accuracy of the precise and simplified models under (a) strong excitation (seismic) and (b) weak excitation.

2.4.4 Numerical results using a constant friction coefficient (constant model)

In order to find the constant friction coefficient that was suitable for the most amount of time during most seismic situations, a nominal friction coefficient, μ_n, was defined. The value of μ_n was 0.043 for all considered sizes of the sliders based on experimental results, and it represented the nominal friction coefficient under seismic load conditions. This value was determined by taking the average of the friction coefficient of the DCFPB at zero displacement points in the third cycle (points e and f in Figure 2-32) of the input sine wave with a constant pressure of 60 N/mm², a maximum velocity of 400 mm/s, and an amplitude of 200 mm (T05 of the dependency test in Table 2-2).

(a) displacement history   (b) experimental friction coefficient
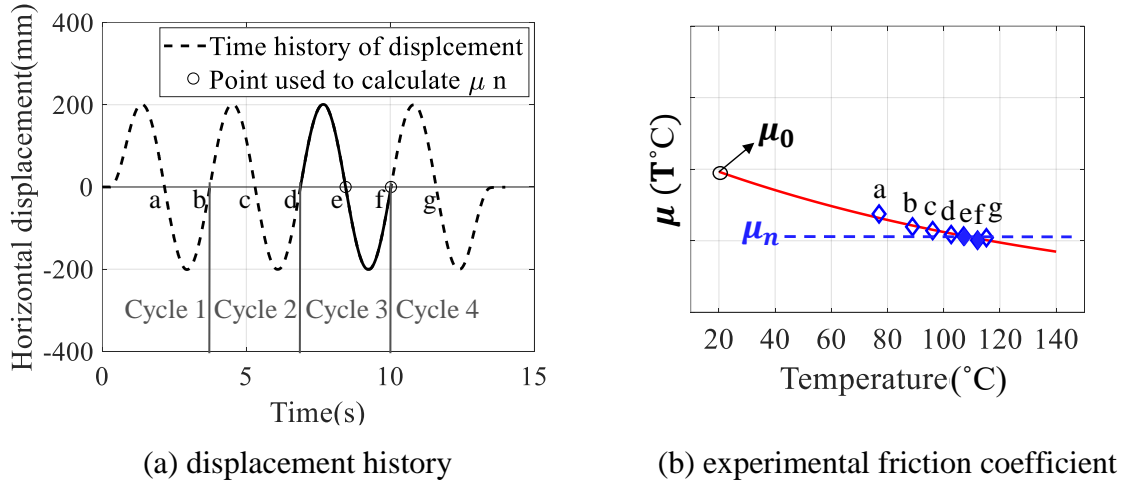
Figure 2-32. Experimental data used to obtain μ_n.

The accuracy of using μ_n under strong excitation and weak excitation is shown in Figure 2-32. The results showed that μ_n was suitable for strong excitations but could not be used under weak excitations. In the other tests in Table 2-3, which can all be considered to be strong excitations, the simulations using μ_n all showed that the force–deflection relations of the DCFP bearings had no large differences. Therefore, the constant friction coefficient, μ_n, could be applied for the rough behavior estimation of DCFP bearings under seismic loads.
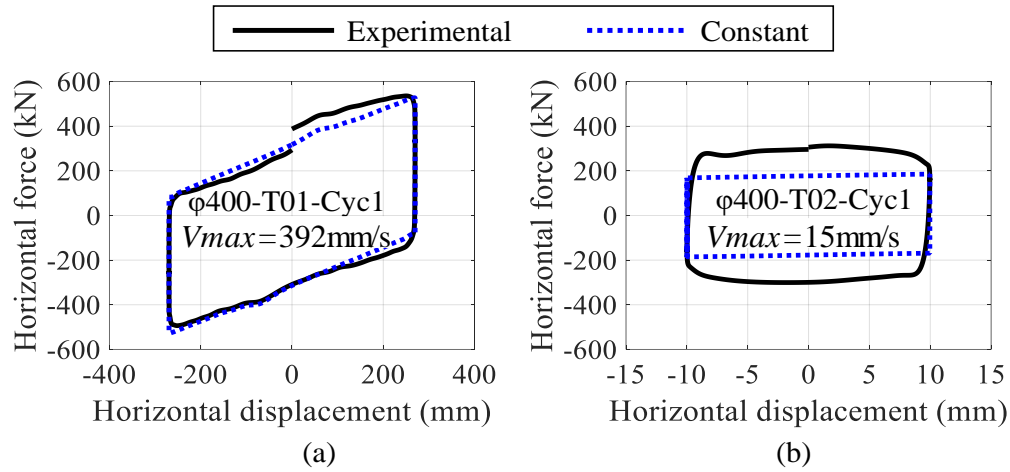
Figure 2-33. Accuracy of using μ_n under (a) strong excitation (seismic) and (b) weak excitation (wind-like).

In the numerical simulation of DCFP bearings, pressure, velocity and temperature dependencies all have influence on the behavior of the bearings. However, for DCFP bearings under stable pressure, the temperature variation caused by friction heating will dominate the influence. This influence is more obvious when the temperature is relatively low (e.g., 20–100 °C), meaning that it is under weak excitations, as shown in Figures 2-31 (b) and 2-33 (b). However, when the temperature is higher, the influence will ease up, as shown in Figures 2-31 (a) and 2-33 (a), and this is the reason why the constant friction coefficient can be applied for rough estimation under strong excitations such as seismic loads. The same trend can also be seen in Figure 2-27.

2.5 Influence of velocity and temperature dependencies on the earthquake response

It has been clarified that the value of friction coefficient is also highly related to pressure, velocity and temperature. Therefore, in the seismic isolation system design, it is important for the designers to know whether certain dependency of friction can be ignored and if it is ignored, how much will be the influence. Therefore, another purpose of this study is to clarify the influence of pressure, velocity and temperature dependency on the seismic response of DCFPBs installed beneath isolated structures. In this section, the vertical component of the earthquake is not considered, therefore, the pressure is considered as a constant of 60Mpa. Then, a parametric study was held on the unidirectional response analysis using the precise model in order to investigate the influence of the velocity and temperature dependency on the behavior of DCFPBs under earthquakes.

2.5.1 Unidirectional mechanical model of a rigid-body structure isolated with DCFP bearings

Double concave friction pendulum bearings are commonly used in isolated structures and the accuracy of the proposed friction models of them are usually validated by displacement controlled tests. However, the validation of the accuracy of their response displacement under earthquakes, which is very important for isolation system design, is always neglected during the validation of their friction models. Especially for using a constant friction coefficient in response analysis, whether it is applicable and how much will be the error of response displacement are still unknown.

In order to investigate the accuracy of the simplified model and the constant model on estimating the behavior of a DCFPB under a structure during earthquakes, as well as to investigate the influence of velocity and temperature dependency on the behavior of the DCFPB, a unidirectional mechanical model of a rigid-body structure with DCFPB is introduced in this part as shown in Figure 2-34.
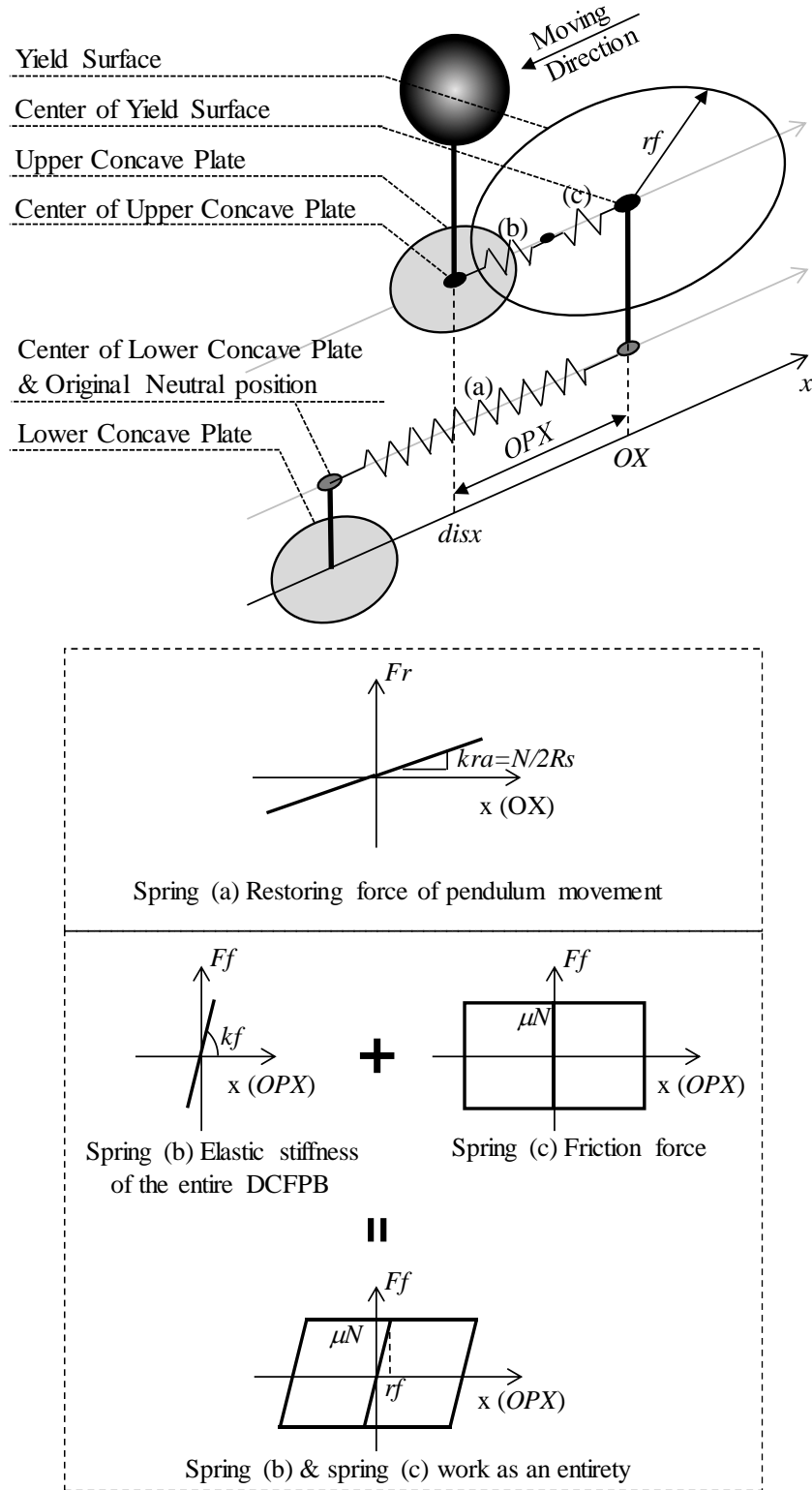
Figure 2-34 Unidirectional mechanical model of a rigid-body structure with DCFPB

In Figure 2-34, the center of the lower concave plate is taken as the original neutral position. The stiffness of the upper structure is considered as infinite in order to make the behavior of the DCFPB clearer. The boundary of whether the sliding between the slider and

the concave plate will happen or not is considered as a yield surface with a radius r_f [2-13][2-14]. Only when the displacement between the upper structure and the center of the yield surface is larger than the radius of the yield surface, the bearing will slide. *OX* is the center of the yield surface, *disx* is the displacement of the upper structure relatives to the center of the lower concave plate and OPX is the distance in between. The internal forces of the DCFPB are considered as three springs: spring (a), spring (b) and spring (c). Spring (a) represents the restoring force of the pendulum movement. k_{ra} is the stiffness, N is the vertical force acts on the DCFPB and R_s is the spherical radius of the upper and lower concave plates. In this study, a DCFPB with the slider diameter equals 400mm is set and a vertical load that can provide 60MPa pressure on the slider surface is applied, therefore k_{ra} equals 0.838kN/mm. *OX* is considered to be the plastic displacement between the upper and lower concave plate, which is the displacement removing elastic displacement of the bearing. Spring (b) represents the elastic stiffness of the entire DCFPB with a value k_f=1900kN/mm based on experimental results. Spring (c) represents the friction force between the slider and two concave plates. Spring (b) and spring (c) work as an entirety to simulate the friction force. When there is no sliding, the friction force is represented by the spring (b) and by the friction models introduced in Section 2.4 during sliding.

2.5.2 Response analysis under gound motions

8 earthquakes with different peak ground velocity (PGV), duration time and distance to fault were selected as shown in Table 2-4 as input earthquake motion. The PGV in the table is obtained from the component with the largest PGV in the horizontal direction of each earthquake record. In the analysis, the PGV of the input ground motions were amplified to 0.25, 0.50, 0.75, and 1.00 m/s to consider various intensities.

Table 2-4. Input ground motions

Abv.	Earthquake	Station	PGV (m/s)	Duration (s)	Field
JKB	Kobe	JMA Kobe	0.893	30	Far
KNA	Kobe	Nishi-Akashi	0.373	41	Near
TC1	Chi-Chi	TCU129	0.554	90	Near
NCC	Northridge	Canyon Country-WLC	0.449	20	Far
LPG	Loma Prieta	Gilroy Array	0.447	40	Near
IVD	Imperial Valley	Delta	0.330	100	Near
TSD	Tohoku	JMA Sendai	0.545	180	Near
TIM	Tohoku	JMA Ishinomaki	0.376	300	Near

In addition, equations of motion at step i which release the unbalanced force is used:

$$accx(i) = -\frac{gaccx(i) + \frac{QFX(i-1)}{mass} + c \times (velx(i-1) + 0.5 \times accx(i-1) \times dt) + \frac{k(i-1)}{mass} \times (velx(i-1) \times dt + (0.5 - \beta_c) \times accx(i-1) \times dt^2)}{1 + 0.5 \times c \times dt + \frac{\beta_c \times k(i-1) \times dt^2}{mass}} \quad (2\text{-}20)$$

$$velx(i) = velx(i-1) + 0.5 \times (accx(i-1) + accx(i)) \times dt \quad (2\text{-}21)$$

$$disx(i) = disx(i-1) + velx(i-1) \times dt + (0.5 - \beta_c) \times accx(i-1) \times dt^2 + \beta_c \times accx(i) \times dt^2 \quad (2\text{-}22)$$

In which $accx(i)$ is the acceleration of the upper structure relatives to the lower concave plate, $gaccx(i)$ is the ground acceleration at step i, $QFX(i)$ is the total restoring force of the DCFPB, $mass$ is the mass of the rigid body which equals the mass that can provide 60MPa pressure on the slider surface, c is the damping coefficient which is set as 0, $velx(i)$ is the

velocity of the upper structure relatives to the lower concave plate, dt is the time interval of each step which equals 0.0025s (this value is selected based on the error validation and the time consumption), $k(i)$ is the stiffness of the system at step i and β_c is the constant value which equals 0.25.

A flow chart of the response analysis a SDOF (single degree of freedom) system based on precise model is shown in Figure 2-35 for a rigid-body structure with DCFPB. In which, n is the serial number of the monitor points, $mp(n)$ is the coordinate of monitor point n on the lower concave plate, r is the side length of a square that has the same area as the slider surface, $q(i,n)$ is the heat flux generated by friction heating at monitor point n at step i and σ is the average pressure at the slider surface which is set as 60 Mpa during excitation. For each step, firstly, the motion of the system is calculated by Equation (2-20) ~ (2-22). Secondly, the sliding status will be judged. Thirdly, the friction characteristics will be calculated based on the friction model introduced in Section 2.4 and the mechanical model of DCFPB introduced in Figure 2-34. Finally, the total restoring force of the bearing will be obtained.

$gaccx(i); accx(i\text{-}1); velx(i\text{-}1); disx(i\text{-}1)$
$k(i\text{-}1); QFX(i\text{-}1)$

$accx(i); velx(i); disx(i)$

$ddisx=disx(i)\text{-}disx(i\text{-}1)$

$\alpha(i)=1\text{-}0.55*\exp(\text{-}0.019*|velx(i)|)$

$OPX(i)=|disx(i)\text{-}OX(i\text{-}1)|$

Slide or not

$OPX(i)>rf(i\text{-}1) \&$
$OPX(i)\geq|disx(i\text{-}1)\text{-}OX(i\text{-}1)|$

(Slide) Y   N (Don't slide)

$k(i)=N/2R_S$ $k(i)=kf$

$q(i,n)=\mu(i\text{-}1)*\sigma*|velx(i)|/2$ if $|OX(i\text{-}1)/2\text{-}mp(n)|\leq r$
=0   otherwise

$q(i,n)=0$

$T_{ave}(i)$ $T_{ave}(i)$

$\beta(i)$ $\beta(i)$

$\mu(i)=\mu_o* \gamma*\alpha(i)* \beta(i)$ $\mu(i)=\mu_o* \gamma*\alpha(i)* \beta(i)$

$Ffx(i)=\mu(i)*N*ddisx/|ddisx|$ $OX(i)=OX(i\text{-}1)$

$OX(i)=disx(i)\text{-}Ffx(i)/kf$ $Ffx(i)=(disx(i)\text{-}OX(i))*kf$

$rf(i)=|Ffx(i)/kf|$

$OPX(i)> |disx(i\text{-}1)\text{-}OX(i\text{-}1)|$

Y   N

$rf(i)= \mu(i)*N/kf$ $rf(i)=rf(i\text{-}1)$

$QFX(i)=OX(i)*kra+Ffx(i)$

Figure 2-35. Flow chart of the response analysis of a SDOF system based on precise model

2.5.3 Influence of velocity and temperature dependencies on the maximum restoring force

Response analysis under earthquake inputs were conducted to study the effect of friction dependencies on the response of the isolation system. Based on Equation (2-7), If all the friction dependencies are considered, the friction coefficient at time t can be expressed as:

$$\mu(t) = \mu_0 \times \gamma(\sigma(t)) \times \alpha(v(t)) \times \beta(T^{\circ}C(t)) \tag{2-7}$$

To ignore velocity dependency, the velocity dependency factor α will be considered as 1 and the following expression will be used for calculating friction coefficient in the response analysis:

$$\mu(t) = \mu_0 \times \gamma(\sigma(t)) \times 1 \times \beta(T^{\circ}C(t)) \tag{2-23}$$

To ignore temperature dependency, the temperature dependency factor β will be considered as 1 and the following expression of friction coefficient will be used:

$$\mu(t) = \mu_0 \times \gamma(\sigma(t)) \times \alpha(v(t)) \times 1 \tag{2-24}$$
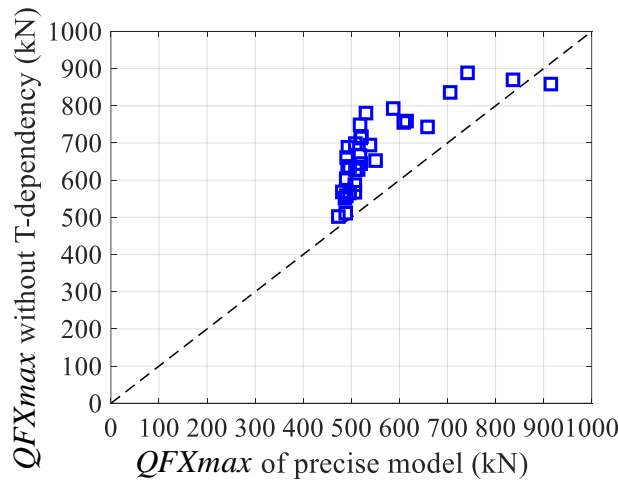
Based on this method, Figure 2-36 shows the accuracy of the maximum restoring force using the precise model without velocity dependency and that without temperature dependency under earthquake records with various PGV. It can be seen from Figure 2-36 (c) that if the temperature dependency is not considered, there is a high possibility that the analysis results will obviously overestimate the maximum restoring force under any earthquake intensity. On the other hand, as shown in Figure 2-36 (b), if the velocity dependency is not considered, even though the analysis results will also tend to overestimate the maximum restoring force, the error is relatively small.
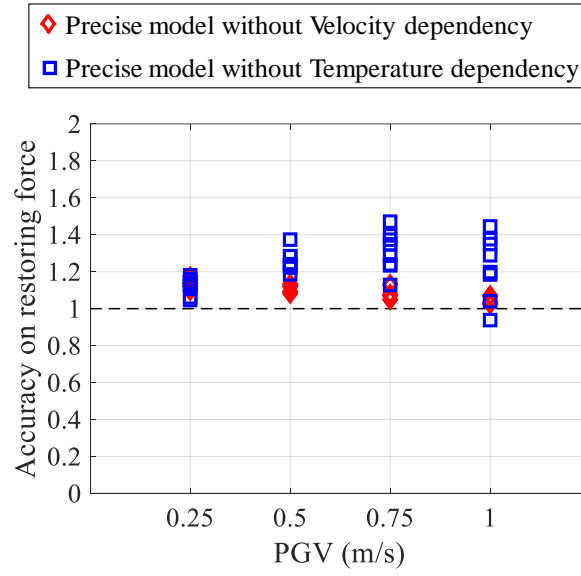
(a) Effect of velocity and temperature dependency the maximum restoring force
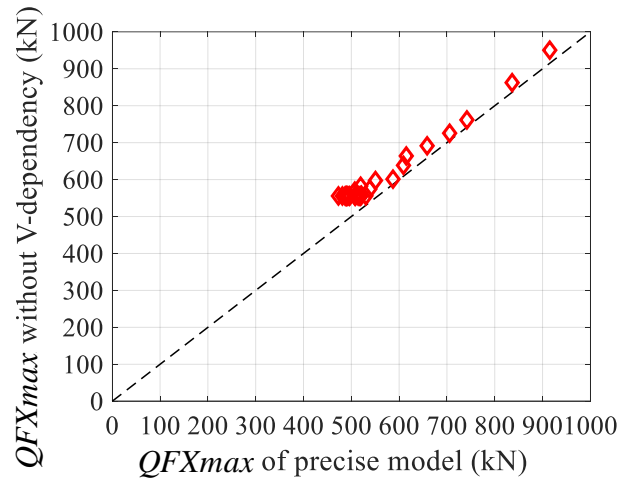
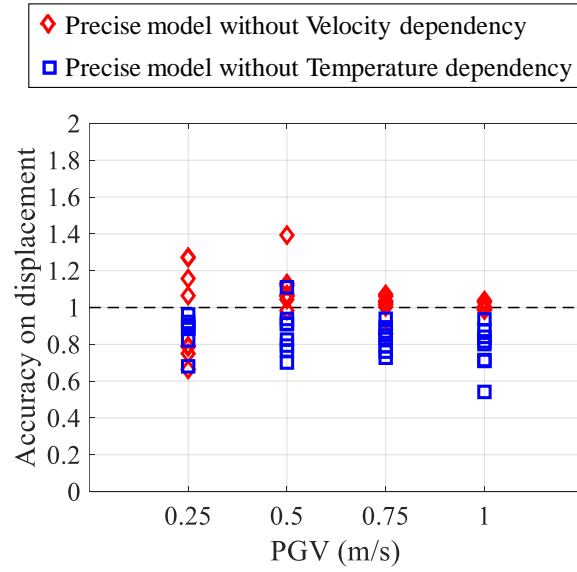(b) Effect of velocity dependency on the maximum restoring force

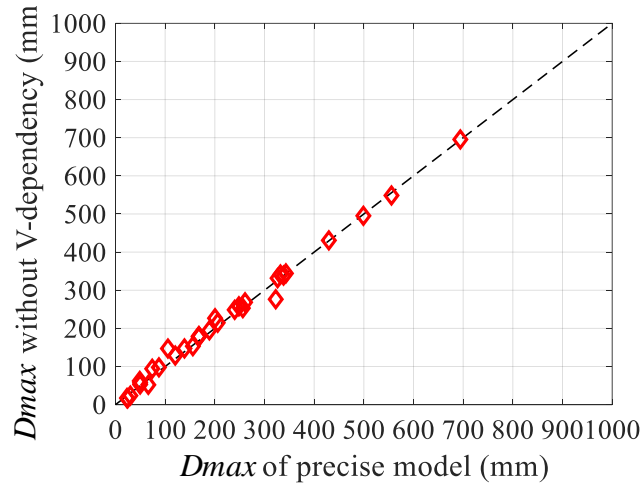(c) Effect of temperature dependency on the maximum restoring force

Figure 2-36. Influence of the velocity and temperature dependency on the maximum restoring force

2.5.4 Influence of velocity and temperature dependencies on the maximum displacement

Figure 2-37 shows the accuracy of the maximum displacement using the precise model without velocity dependency and that without temperature dependency under earthquake records with various PGV. It can be seen from Figure 2-37 (a) that, for DCFPBs installed in isolated structures, if the temperature dependency is not considered, there is a huge chance that the maximum response displacement of the DCFPBs under earthquakes is underestimate. Furthermore, from Figure 2-37 (c), it can be seen that, when the maximum displacement becomes larger, the value of the underestimation on maximum response displacement will also be larger. As a result, it is very dangerous to ignore the temperature dependency in the seismic isolation system design. If the temperature dependency is ignored, the maximum response displacement of the isolation system will be underestimated by an average of 20%. When the velocity dependency is ignored, Figure 2-37 (a) shows that the accuracy on the maximum response displacement will be low when PGV is lower than 0.5 m/s. However, Figure 2-37 (b) shows that the velocity dependency does not have serious influence on the behavior of DCFPBs especially when the maximum response displacement is large.

(a) Effect of velocity and temperature dependency the maximum isolator displacement

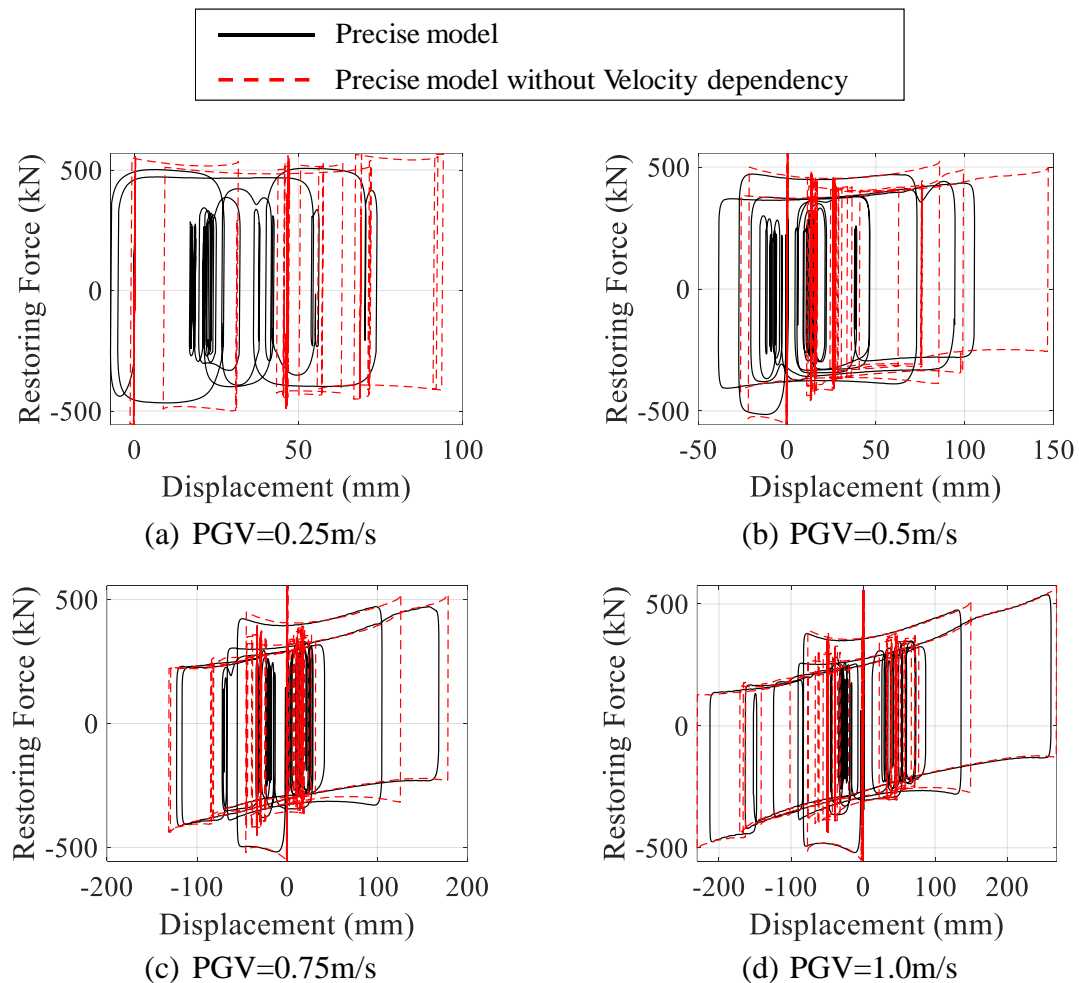(a) Effect of velocity dependency on the maximum isolator displacement
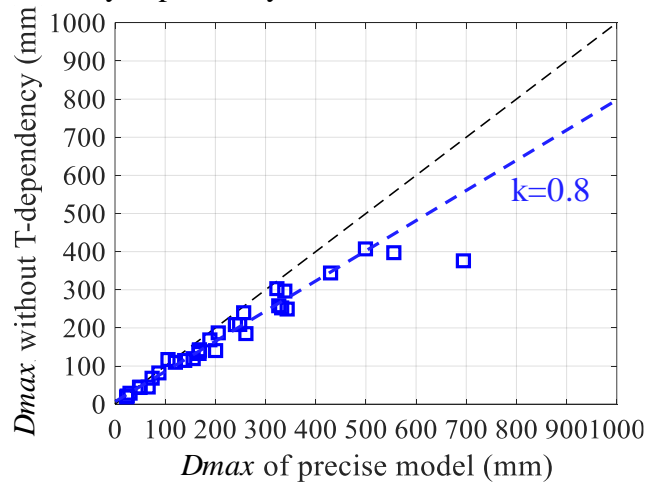
(b) Effect of temperature dependency on the maximum isolator displacement

Figure 2-37. Influence of the velocity and temperature dependency on the maximum displacement

2.5.5 Influence of velocity and temperature dependencies on response of the DCFP bearing under ground motion JKB

Figure 2-38 shows the restoring force – displacement curve of the response analysis using the precise model without the velocity dependency and that considering the velocity dependency under JKB ground motions with different peak ground velocity as one of the detailed example of Figure 2-36 and 2-37. This figure is aimed to exhibit the detail of the restoring force and displacement difference between the precise model without velocity dependency and the precise model. It can be seen that the larger the PGV, the smaller the influence of velocity dependency, especially on the response displacement. It can also be seen that the error caused by ignoring the velocity dependency mainly occurs at the turning points of displacement, where velocity is relatively small. This is because the velocity dependency factor has larger changing rate at small velocities.

Figure 2-38. Effect of velocity dependency on the hysteresis curve of (JKB)

A detailed example on the restoring force – displacement curve of the response analysis using the precise model without the temperature dependency and that considering the temperature dependency under JKB ground motions with different peak ground velocity is also given as shown in Figure 2-39. Figure 2-39 (c) and (d) show the overestimation of restoring force and the underestimation of displacement if the temperature dependency is ignored in case of JKB record. When PGV equals 1.0 m/s, the maximum response displacement of the analysis result using the precise model is 261 mm, however, the analysis result using the precise model without temperature dependency is 185 mm. If the temperature dependency is ignored in the seismic isolation design and 185 mm is considered as the maximum displacement, it will be very dangerous.
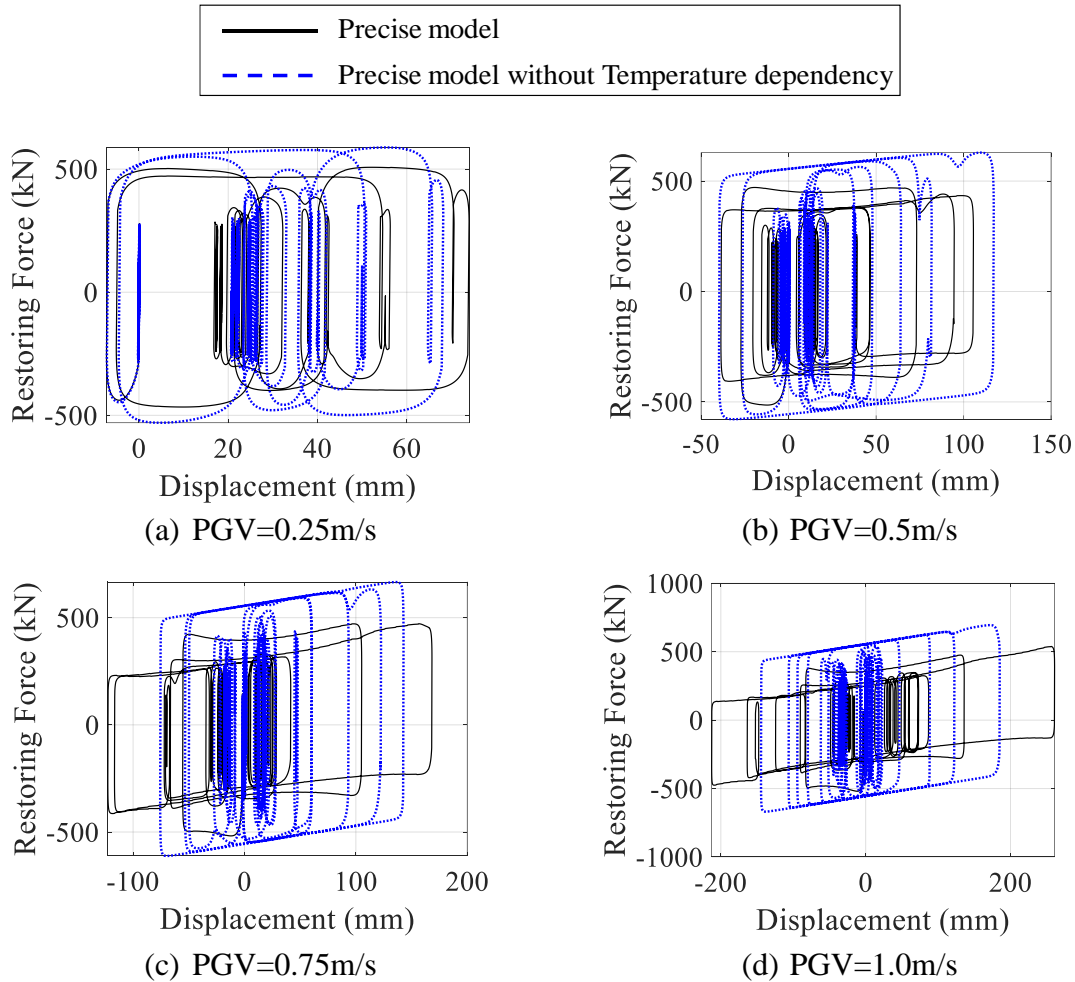
Figure 2-39. Effect of temperature dependency on the hysteresis curve of (JKB)

2.6 Conclusions

Friction dependency equations of a type of DCFP bearing using PTFE-related material were obtained by small-scale material tests by precious studies. In this Chapter, these dependencies were first validated separately by prototype specimens under dynamic excitations with a large region of speed and displacement (dependency test). As the temperature dependency will significantly affect the experimental results of the pressure and the velocity dependencies, the effect of temperature dependency was eliminated from the experimental data. Then, by comparing the revised experimental results with the proposed friction dependencies, it can be concluded that the friction dependency equations obtained by small-scale material tests is still available under real-size specimens and dynamic excitations, regardless of the size of the slider.

Further, Full-scale dynamic tests were conducted under various pressures, velocities, amplitude, and number of cycles based on the ASCE procedure (ASCE test) to evaluate the effects of surface pressure, velocity and the temperature rise due to friction heat on the dynamic behavior of DCFP bearings for seismic isolation structures. Then, based on the friction dependency equations and two temperature simulation models, two friction models (the precise model and the simplified model) were proposed. After verifying the friction models by the ASCE test, it was found that the two models can provide accurate simulation of the response under both strong and weak dynamic excitations. And the simplified model could simulate the DCFP bearing to the same standard as the precise model with much less calculation time. Moreover, the friction coefficient can be taken as an appropriate constant value by considering the effect of temperature on the friction coefficient under strong ground motions as constant with sufficient accuracy in estimating the response force of the isolation layer under strong ground motions. In this study, the constant friction coefficient was defined as the nominal friction coefficient, μ_n. It should be mentioned that, μ_n is only available under strong excitations.

Moreover, parametric studies were also held on the unidirectional response analysis using the precise model to investigate the influence of the velocity and temperature

67

dependency on the behavior of DCFPB and upper structures under earthquakes. The result indicates that if the temperature dependency is neglected, large error in the displacement and the restoring force of the DCFP bearing may occur. For instance, the maximum displacement of the bearing will be underestimated by around 20%, which is very dangerous for the seismic isolation design. However, if the velocity dependency is not considered, there will be no large difference on the response.

References.

[2-1].   Quaglini, V.; Dubini, P.; Poggi, C. Experimental assessment of sliding materials for seismic isolation systems. Bull. Earthq. Eng. **2012**, 10, 717–740.

[2-2].   Lomiento, G.; Bonessio, N.; Benzoni, G. Friction Model for Sliding Bearings under Seismic Excitation. *J. Earthq. Eng.* **2013**, *17*, 1162–1191.

[2-3].   Quaglini, V.; Bocciarelli, M.; Gandelli, E.; Dubini, P. Numerical Assessment of Frictional Heating in Sliding Bearings for Seismic Isolation. *J. Earthq. Eng.* **2014**, *18*, 1198–1216.

[2-4].   Kumar, M.; Whittaker, A.S.; Constantinou, M.C. Characterizing friction in sliding isolation bearings. *Earthquake Engng Struct. Dyn.* **2015**, *44*, 1409–1425.

[2-5].   Bianco, V.; Bernarddini, D.; Mollaioli, F.; Monti, G. Modeling of the temperature rises in multiple friction pendulum bearings by means of thermomechanical rheological elements. *Arch. Civ. Mech. Eng.* **2018**, *19*, 171–185.

[2-6].   Nakamura, H.; Nishimoto, K.; Hasegawa, H.; Nakamura, H. Predictive Method of a Temperature Rise and the Friction Coefficient of Spherical Sliding Bearing (Part 3), Paper No. 21232. AIJ, Kanto, Japan, 4–6 September **2015**.

[2-7].   Nishimoto, K.; Nakamura, H.; Hasegawa, H.; Wakita, N. Bearing Stress and Velocity Dependency of Spherical Sliding Bearing through Full-scale tests, Paper No. 21223. AIJ, Fukuoka, Japan, 24–26 August **2016**.

[2-8].   American Society of Civil Engineers (ASCE), **2016**. Minimum Design Loads and Associated Criteria for Buildings and Other Structures, ASCE/SEI 7-16, Reston, VA.

[2-9].   Shortreed JS, Seible F, Filiatrault A, Benzoni G. Characterization and testing of the Caltrans seismic response modification device test system. Philosophical Transactions of the Royal Society of London. Series A: Mathematical, Physical and Engineering Sciences. 2001 Sep 15;359(1786):1829-50.

[2-10]. S. Yamazaki, K. Nishimoto and A. Watanabe, 2019. Experimental and Analytical Study of Spherical Sliding Bearing for Long Period Ground Motion, in press, Summaries

of Technical Papers of Annual Meeting, Architectural Institute of Japan, 3-6 September, 2019, Hokuriku, Japan. (in Japanese).

[2-11]. MC. Constantinou, AS. Whittaker, Y. Kalpakidis, DM. Fenz, GP. Warn, **2007**. Performance of seismic isolation hardware under service and seismic loading. Multidisciplinary Center for Earthquake Engineering Research, Report No. MCEER-07-0012, Buffalo, NY.

[2-12]. Japan Society of Mechanical Engineers (JSME), 2009. Heat Transfer, 5th edition, JSME Data Books, Tokyo, JP, 284-285.

[2-13]. Kikuchi, M., Ishii, K., Yamamoto, M., Higashino, M., Kamoshita, N., Nakamura, T., and Kouchiyama, O., 2012. Experimental study on horizontal Bi-axial mechanical properties of sliding supports with rubber-pad (Part 3: Simulation Analysis), Paper No. 21160, Summaries of Technical Papers of Annual Meeting, Architectural Institute of Japan, 12-14 September, 2012, Nagoya, Japan. (in Japanese).

[2-14]. Kamoshita, N., Yamamoto, M., Minewaki, S., Kikuchi, M., Ishii, K., Kouchiyama, O., and Nakamura, T., 2014. Horizontal bidirectional characteristics of elastic sliding bearings under various fluctuant vertical condition, AIJ Journal of Structural and Construction Engineering, 79, 453-461 (in Japanese).

3. Behavior of DCFP bearings under bidirectional excitations (2D)

3.1 Introduction

3.1.1 Dependencies of isolation systems under bidirectional excitations

The mechanical properties of friction pendulum bearings (FPBs) depend mainly on the effect of pressure, velocity and temperature on the friction coefficient. In the previous study of the considered DCFP bearing, the pressure, velocity, and temperature dependencies were first tested by small-scale material friction tests [3-1][3-2], and then validated by full-scale unidirectional dynamic tests in a high speed and displacement region as introduced in Chapter 2 [3-3]. In this Chapter, the dependencies were combined in a bidirectional friction model and further validated under bidirectional artificial orbits and earthquake response orbits.

The mechanical properties of the BIS may also affected by the bidirectional effects (effects caused by bidirectional excitation compared with unidirectional excitation). In the previous studies, considerable experiments were conducted on the bidirectional behavior of FPBs. Bidirectional displacement-controlled tests conducted by Mokha et al. in 1993 was aimed at studying the importance of the bidirectional effects of the friction force in FPBs [3-4]. Thereafter, bidirectional displacement-controlled tests conducted by Gilberto Mosqueda et al. in 2004 studied the influence of the coupling between the two orthogonal components on the behavior of FPBs [3-5]. Following the development of testing facilities around 2011, the bidirectional sliding behavior of FPBs were tested on full-scale devices across a range of realistic vertical loads and sliding velocities for bidirectional excitations [3-6]. Then, with the increasing realization with the fact that for typical velocity ranges, the temperature appeared to be the overall dominant parameter on the friction coefficient around 2014 [3-7], more bidirectional tests were conducted to study the effect of temperature dependency [3-8] or, in another way, the cyclic effect [3-9] on the mechanical properties of the bearing. However, all the mentioned bidirectional dynamic tests of FPBs were conducted under artificial multidirectional graphics consisting of circles, ellipses, rectangles, and triangles. These graphics aimed at simulating the loop with the maximum displacement in the

earthquake response orbits and the dissipated energy during the earthquake was controlled by the number of loops. However, in realistic orbits, the loop with the maximum displacement has no duplicates. Even similar loops barely exist. Typically, the other loops in the duration are around small displacements. Consequently, this difference may influence the temperature of the isolation system and further affect the friction coefficient. Moreover, the loading period of the testing procedure using artificial graphics is typically designed based on the return period of the FPBs, which may result in much smaller accelerations than that in real earthquakes. Thus, the destructive load pulses imposed on the system under real earthquakes cannot be appropriately simulated. Therefore, to further understand the behavior of FPBs and validate the credibility of the friction dependencies under real earthquakes, full-scale experiments under earthquake response orbits are were conducted.

3.1.2 Influence of dependencies on the maximum displacement of FPBs

Simplified prediction methods were generally introduced in various structural codes, such as ASCE (American Society of Civil Engineering) [3-10], AASHTO (American Association State and Highway Transportation Officials) [3-11], Euro Code [3-12] and AIJ (Architectural Institute of Japan) [3-13], to obtain the design displacement of the isolation system, which were considered under unidirectional excitations with constant friction coefficients. However, Warn GP et al. proposed that the influence of bidirectional excitation and coupling on the maximum displacement cannot be ignored [3-14]. The coupling effect exists between the responses of the FPBs in each orthogonal direction [3-5][3-14] [3-15], which if ignored results in an underestimation of the maximum isolator displacement by approximately 20%. Moreover, Manish Kumar et al. demonstrate that a friction model of a FPB that ignores the effects of temperature rise may underestimate the median maximum displacement by 10% and 30%, for static axial pressures of 10 and 50MPa, respectively, based on 30 sets of three-component ground motions (GMs). And the effects of changes in velocity and axial pressure on the friction coefficient are small and may not need to be included in a friction model [3-16]. Li Jiaxi et al. did similar response analysis of a different DCFPB under 48 sets of three-component GMs, and concluded that the effect of bearing stress and velocity dependency on the maximum displacement is less than 10%, for static axial pressures of 60MPa. And, in most situation, the larger the intensity of the earthquake the less the effect [3-17]. Moreover, Chapter 2 proposed that if the temperature dependency of friction is ignored, the maximum response displacement of the isolation system under unidirectional GMs will be underestimated by an average of 20%, for static axial pressures of 60Mpa. And the effect of velocity dependency can be ignored [3-18].

As most existing codes and the determination of mechanical properties (mainly refer to the friction coefficient of the bearing in this study) were considered under unidirectional excitations, the effect of the velocity and temperature change caused by the additional perpendicular excitation (bidirectional effect) on the friction coefficient and further on the maximum response displacement needs to be clarified. Therefore, an approach to determine

the design displacement in preliminary design that considers these effects remains a research topic [3-19].

In this chapter, the mechanism of how the additional perpendicular GM component affect the temperature, in turn on the friction coefficient, and finally on the maximum response displacement was clarified. And the effect was discussed under various classification of GMs.

3.2 Performed expreiments

3.2.1 Specimens and testing setup

The information of the tested specimen is shown in Figure 3-1. The sliding material on the upper and lower surface of slider is composite PTFE material while the two concave plates are fabricated using stainless steel, which are squares with their radius of the concave equals to 4500 mm. φ and Φ denote the diameter of the slider and spherical surface respectively. Two types of specimens were tested: medium-frictional specimen (Spec. M) and low-frictional specimen (Spec. L). The interface of Spec. L is the same composite PTFE material as the Spec. M with lubricating oil on it.

(a) 3D plan

(b) Sectional Plan

(c) Interface of Spec. M

(d) Interface of Spec. L
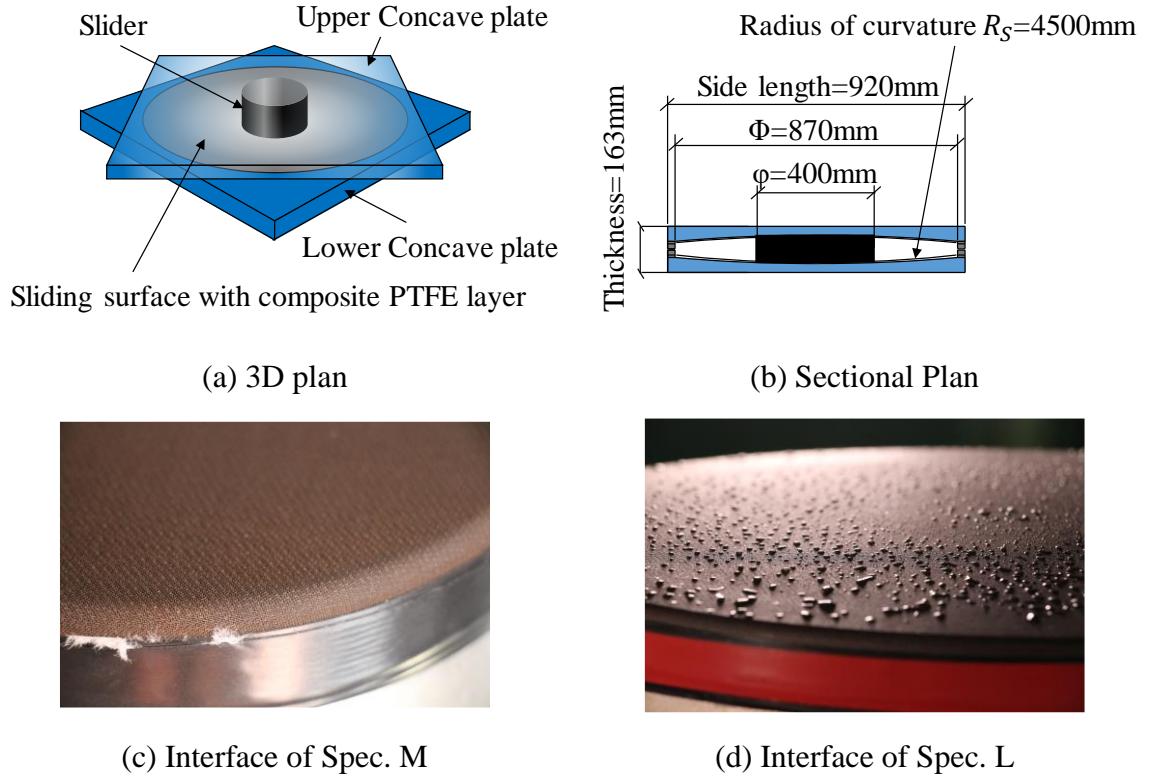
Figure 3-1. Dimension and the interface of the specimen

The experiments were conducted at the University of California, San Diego, in the Caltrans Seismic Response Modification Device (SRMD) Test Facility [3-20]. The testing setup was similar to the previous unidirectional tests introduced in Section 2.2.1; however, the test input was different. In this experiment, four actuators provided bidirectional displacement inputs.

3.2.2 Test procedure

A total of 2 artificial multidirectional graphics and 5 ground motion pairs were utilized for both Spec. M and Spec. L as shown in Table 3-1 and 3-2 respectively. The information of the ground motions is extracted from two sources: The Pacific Earthquake Engineering Research (PEER) data base [3-21] of America and the Kyoshin Network (K-NET) [3-22] of Japan. As shown in Table 3-1 and Table 3-2, C1 indicates one of the orthogonal components of the earthquake records with the larger peak ground velocity (PGV) in the horizontal plane and C2 means the component with the smaller PGV. For a simpler description, the directions of C1 and C2 are referred to as the longitudinal and lateral directions, respectively. The abbreviation (abv.) of the input orbits are also shown in Table 3-1, in which M represents Spec. M and L represents Spec. L. Except for PGV, the selection of the input earthquakes also considered the duration (Dur.), distance to fault and the orbit shape of the earthquake. In this table, large-magnitude earthquakes with both long-duration and short-duration, near-fault and far-field, line-like orbit and circle-like orbit were included, in order to contain as much situations as possible. The method used to evaluate the orbit shape will be introduced in Section 3.2.3. As for the artificial multidirectional graphics, the radius of the circular orbit and the major radius (a) and minor radius (b) of the ellipse were provided. In addition, the pressure on the contact surface of the slider and the concave plates was set as 60 MPa for all tests. To simulate the response under destructive earthquakes, the input data shown in Table 3-1 and Table 3-2 are the scaled data of the original ground motion, which were scaled to satisfy the limitation of the testing machine in limited total displacement and acceleration and the limitation of specimens in the maximum displacement. Consequently, the scaled orbit inputs of Spec. M and Spec. L are shown in Figure 3-2. They were obtained using the response analysis model of DCFP bearings proposed by Ishida Takanori etc. [3-23] assuming that the friction coefficients of Spec. M and Spec. L are 0.043 and 0.013 respectively.

Table 3-1. Orbit Inputs for Spec. M

Num.	1. Artificial graphics							
	Geometry				PGV-C1 (m/s)	PGV-C2 (m/s)	Dur. (s)	Radius / [a, b] (mm)	Orbit shape
M1	Circular				0.400	0.400	24	400	C=0.91
M2	Ellipse				0.400	0.143	30	[400, 133]	C=0.47
	2. Input Earthquakes of the Response Orbits								
	Year	Earthquake	Station	Abv.	Scaled factor	PGV-C1 (m/s)	PGV-C2 (m/s)	Dur. (s)	Distance to fault (km)[a]	Orbit shape
M3	1979	Imperial Valley	Delta	IVD-M	1.70	0.561	0.442	100	22	C=0.22
M4	1994	Northridge	Canyon Country-WLC	NCC-M	1.66	0.745	0.714	20	12	C=0.34
M5	1995	Kobe	Nishi-Akashi	KNA-M	1.94	0.724	0.710	41	7	C=0.42
M6	2011	Tohoku	JMA Sendai	TSD-M	1.38	0.752	0.751	180	172*	C=0.67
M7	2011	Tohoku	JMA Ishinomaki	TIM-M	2.08	0.782	0.559	300	145*	C=0.26

Table 3-2. Orbit Inputs for Spec. L

Num.	1. Artificial graphics							
	Geometry			PGV-C1 (m/s)	PGV-C2 (m/s)	Dur. (s)	Radius / [a, b] (mm)	Orbit shape
L1	Circular			0.400	0.400	24	400	C=0.91
L2	Ellipse			0.400	0.143	30	[400, 133]	C=0.47
	2. Input Earthquakes of the Response Orbits							
	Year	Earthquake	Station	Abv.	Scaled factor	PGV-C1 (m/s)	PGV-C2 (m/s)	Dur. (s)	Distance to fault (km)[a]	Orbit shape
L3	1979	Imperial Valley	Delta	IVD-L	0.98	0.323	0.255	100	22	C=0.22
L4	1994	Northridge	Canyon Country-WLC	NCC-L	1.53	0.687	0.658	20	12	C=0.32
L5	1995	Kobe	Nishi-Akashi	KNA-L	1.91	0.712	0.699	41	7	C=0.27
L6	2011	Tohoku	JMA Sendai	TSD-L	0.90	0.491	0.490	180	172*	C=0.59
L7	2011	Tohoku	JMA Ishinomaki	TIM-L	1.61	0.605	0.433	300	145*	C=0.25

Note: [a] Rupture distance based on PEER [3-21]; * denotes hypocentral distance based on K-NET [3-22]
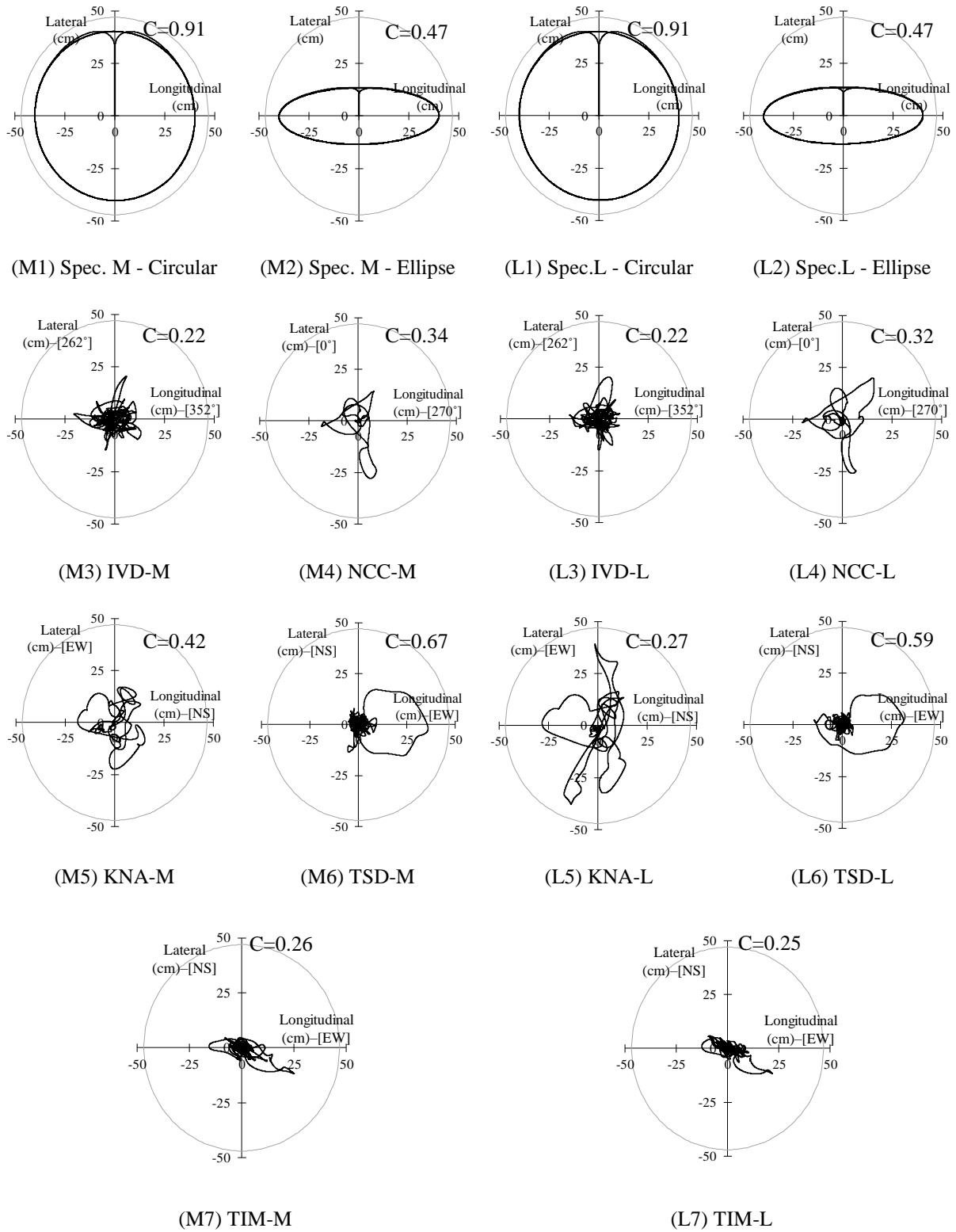
Figure 3-2. Orbit inputs of Spec. M and Spec. L

3.2.3 Category of orbit shape

The category of orbit shape is one of the major characteristics during the selection of the input orbit. To digitize the shape of the orbit, two coefficients are introduced: the average radius r_a and the circular degree factor C.
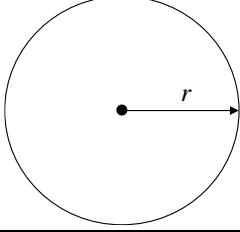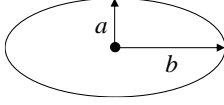
$$A = \sum_{i=0} \frac{1}{2} \times |x_i \times y_{i+1} - x_{i+1} \times y_i| \qquad (3\text{-}1)$$

$$r_a = \frac{2 \times A}{D_t} \qquad (3\text{-}2)$$

$$C = \frac{r_a}{d_{max}/2} \qquad (3\text{-}3)$$

In the equations, A denotes the cumulative area of the orbit; (x_i, y_i) is the coordinate of the ith point on the orbit; D_t is the total displacement of the orbit and d_{max} means the maximum distance between two random points on the orbit. Because the outer part of the response orbit reflects the response under strong excitations of the earthquake and the inner part will cause negative effect on the judgment of the shape of the outer part, the points whose distance from the origin is within 20% of D_{max} will not be considered during the calculation of C. Where D_{max} is the maximum distance from the orbit to the origin. It can be seen from Table 3-3 that the orbit is more like a circle if C is closer to 1 and more like a line if C is closer to 0. The orbit shape factors of all the input orbits are shown in Figure 3-3.

Table 3-3. Calculation of the circular degree factor under different orbit

(a) Circular orbit	(b) Ellipse orbit	(c) Linear orbit
$A = \pi r^2$	$A = \pi ab$	$A = 0$
$r_a = 2A/D_t = 2\pi r^2/2\pi r = r$	$b > r_a > a$	$r_a = 0$
$C = r_a/(d_{max}/2) = r/r = 1$	$1 > C > 0$	$C = 0$

(a) (a) Spec. H

(b) (b) Spec. L
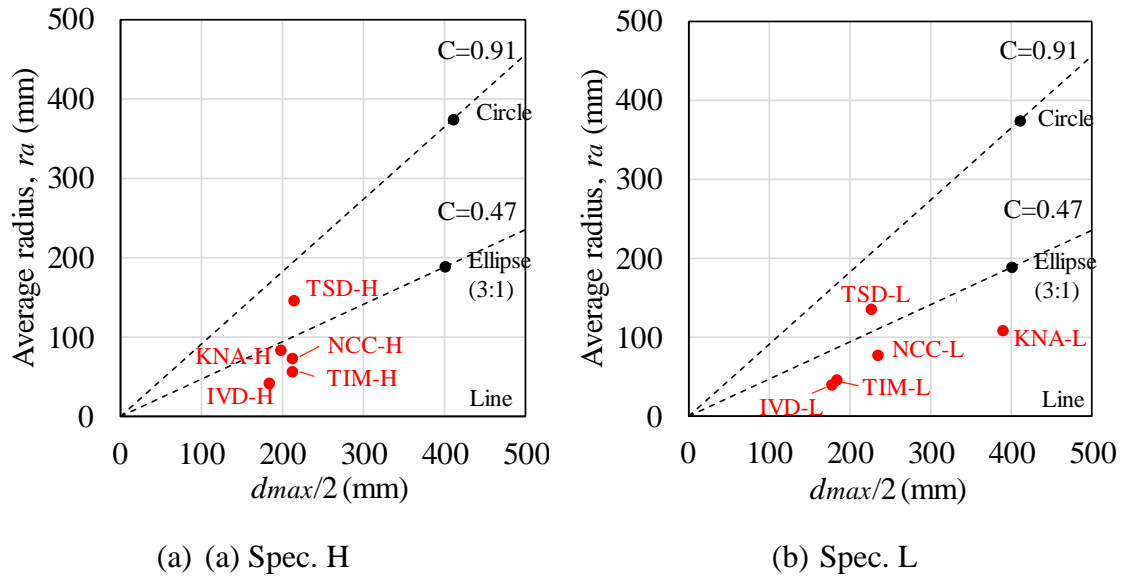
Figure 3-3. Orbit shape factors of the input orbits

3.3 Numerical simulation of the experiments

3.3.1 Numerical simulation using constant friction coefficient

Based on previous experiments on the behavior confirmation of the specimen, the response force-deflection diagram of Spec. M and Spec. L under strong excitations can be roughly simulated by using constant friction coefficients [3-24][3-25]:

$$\mu_n = 0.043 \quad (0.013) \quad \text{for Spec. M (L)} \tag{3-4}$$

where μ_n is the nominal friction coefficient, which is a constant value suitable for most seismic situations validated by previous unidirectional dynamic tests introduced in Chapter 2. This value was defined at the velocity of 400 mm/s, under the pressure of 60 MPa, and the interception of the y-axis of horizontal/vertical force at the average of the 3rd fully reversed cycle as introduced in Section 2.4.4. The selection of the 3rd cycle considered the effect of the increase of temperature caused by friction on the friction coefficient during strong excitations.

3.3.2 Precise model and simplified model of simulating friction coefficient

In this study, the accuracy of a simplified model and precise model were studied under bidirectional excitations. Their accuracy under unidirectional excitations was validated in Chapter 2. The only difference between the models for bidirectional and unidirectional excitations is the arrangement of monitor points for temperature simulation as shown in Figure 3-4 [3-16]: the precise model has 6×6 monitor points covering the sliding surface of the concave plates in two orthogonal directions. In contrast, the simplified model applies only one monitor point in the center of the concave plate, which facilitates much faster calculation.

| (a) | (b) |
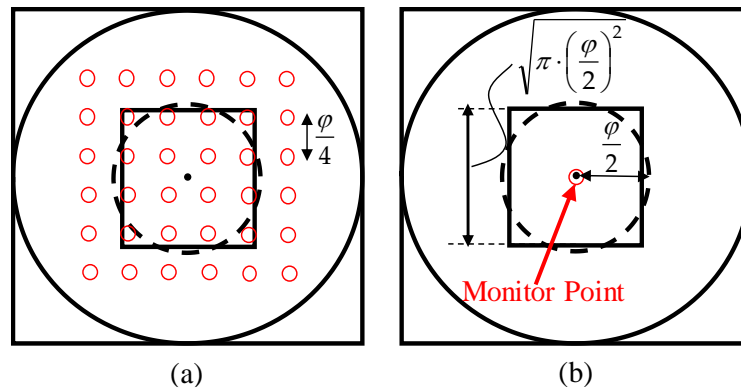
Figure 3-4. Calculation model of temperature for (**a**) precise and (**b**) simplified model.

The temperature simulation method of the monitor points is based on the previous study of Constantinou et al.: First, two well-known concepts that refer to the ability of a given material to transfer or conduct heat should be introduced: k, the thermal conductivity, which relate the temperature distribution in the material to the heat flux (energy per area); and D, the thermal diffusivity, which shows the rate of temperature spread through material. Based on previous study of Constantinou et al. [3-19], if the heat flux history on a surface is known, the temperature history of a point on this surface can be obtained by the following equation:

$$\Delta T(t) = \frac{1}{k} \times \int_0^t \frac{\sqrt{D}}{\sqrt{\pi\tau}} \times q(t-\tau)d\tau$$

<div style="margin-left:4em">Transfer Energy   How much   Energy input
to T°C   remain</div>

(3-5)

where τ is a time parameter that varies between 0 and time t, q is the heat flux at the surface, ΔT is the temperature change of the contact surface. Figure 3-5 shows the generate and spread of heat in case of DCFP Bearing. Where, Ds and Dp is the thermal diffusivity of the stainless steel and the PTFE layer respectively, ks and kp is the thermal conductivity of the stainless steel and the PTFE layer respectively, and $r_{contact}$ is the radius of the slider. As shown in Figure 3-5, in case of DCFP Bearing, heat flux is generated between the slider and the concave plate and the temperature will affect the friction coefficient. Comparing the value of k and D of the composite PTFE layer on the slider and the stainless steel surface of the concave plate, it was found that the thermal conductivity and diffusivity of stainless steel is much higher. This means that basically all the heat will enter the concave plate. Therefore, as shown in Figure 3-4, monitor points were set on the surface of the concave plate to calculate temperature by using the k and D of stainless steel, which equals 0.016 W/(mm·°C) and 4.07 mm^2/s respectively [3-26]. For the precise model of calculating temperature, many monitor points were set. In the excitation, heat will be generated at the points within the contact surface of the slider and the contact plates, and the effective temperature of the contact surface was obtained by calculating the average temperature of these points. As for the simplified model, only a monitor point at the center of the concave plate is set and the temperature of the contact surface is always simulated by the temperature of this point.
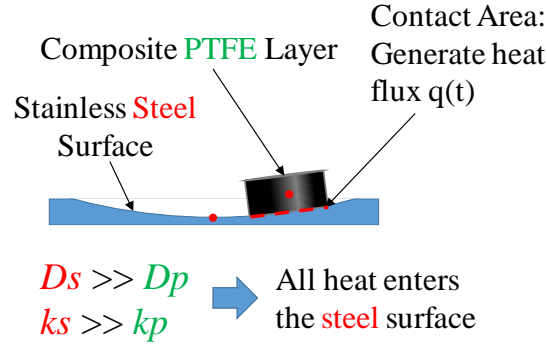
Figure 3-5. Generate and Spread of heat in case of DCFP Bearing

As for the calculation method of heat flux for each monitor point, it can be calculated by the following equations according to the position of the slider to the considered monitor point [3-16][3-19]:

$$q(t) = \begin{cases} \mu(t)p(t)\dfrac{v(t)}{2} & \text{if } \delta_m \leq \sqrt{\pi \cdot \left(\dfrac{\varphi}{2}\right)^2} / 2 \\ 0 & \text{otherwise} \end{cases} \tag{3-6}$$

where μ is the friction coefficient, p is the pressure at the contact area, v is the relative velocity between the upper and lower concave plates, and δ_m is the lateral distance from the center of the slider to the monitor point of interest. The calculation of heat flux of the monitor point at the center of the concave plate is shown as an example in Figure 3-6.
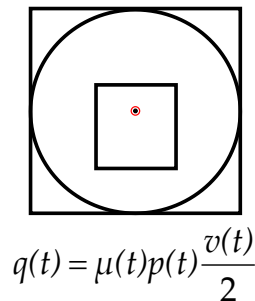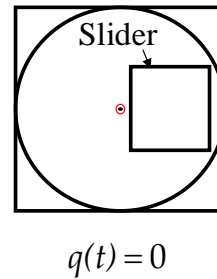
Figure 3-6. Calculation of the heat flux of a monitor point based on the position of the slider

Applying Equation (3-5) and (3-6), the temperature history of each monitor point can be simulated based on the input orbit. The analytical temperature distribution of the monitor points under the ellipse orbit for Spec. M (M2) is shown in Figure 3-7 and 3-8 as an example. The temperature distribution shown in these two figures happens in the first cycle of the ellipse orbit. It can be seen that the temperature simulated by the simplified model is a little higher than that simulated by the precise model, but the difference is not large.

(a) Precise model   (b) Simplified model
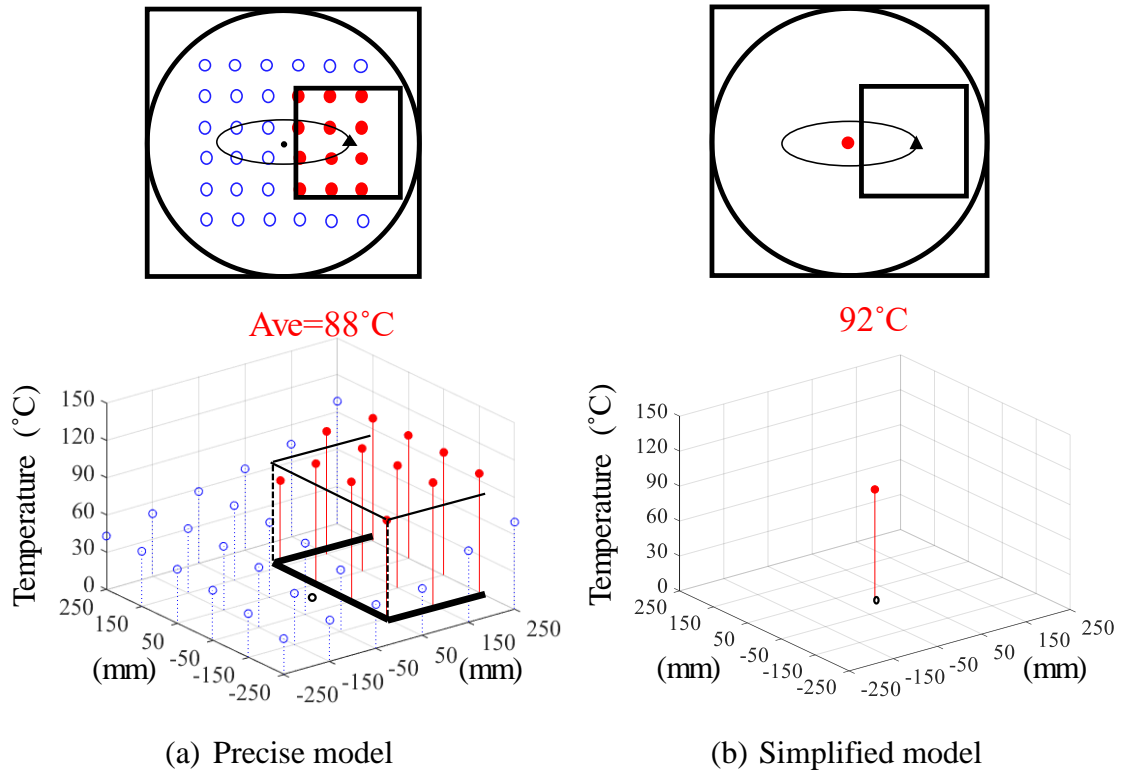
Figure 3-7. Temperature distribution of the monitor points under orbit M2 (Position 1)
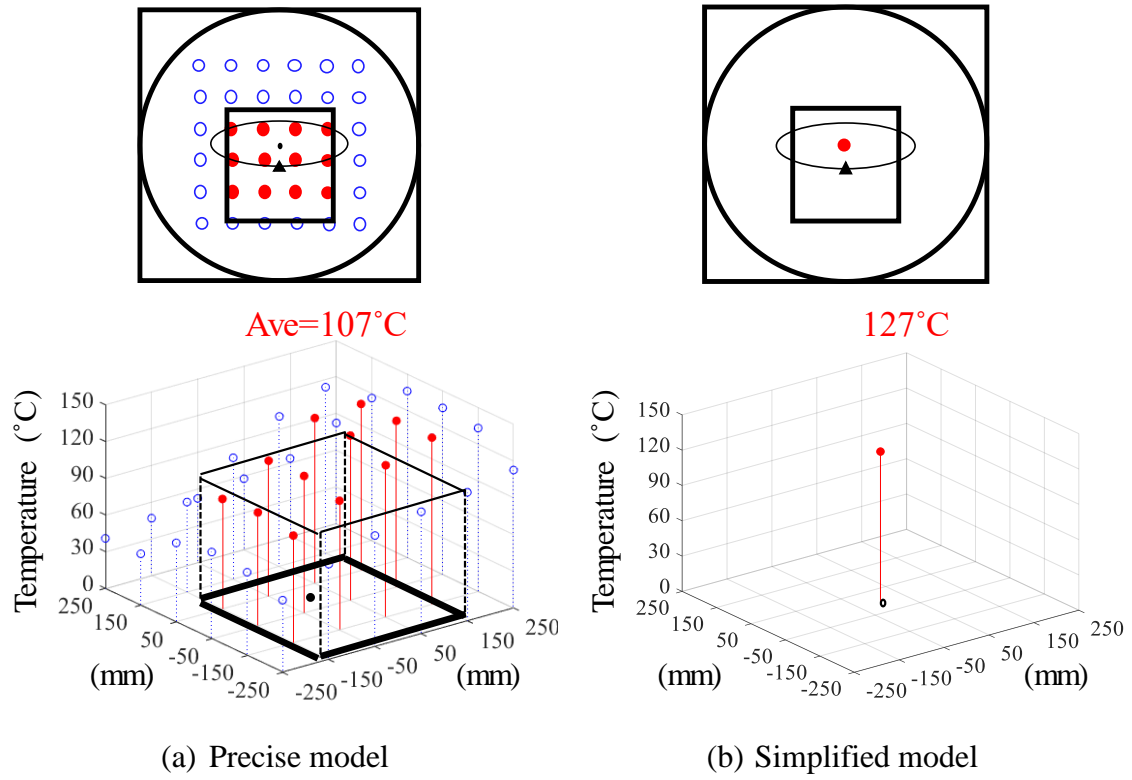
Figure 3-8. Temperature distribution of the monitor points under orbit M2 (Position 2)

Further, the friction dependency factors can be obtained and the friction coefficient can be calculated:

$$\mu(\sigma, v, T^{\circ}C) = \mu_0 \times \gamma(\sigma) \times \alpha(v) \times \beta(T^{\circ}C) \tag{3-7}$$

$$\gamma(\sigma) = 2.03 \times \sigma^{-0.19} + 0.068 \tag{3-8}$$

$$\alpha(v) = 1 - 0.55 \times e^{-0.019v} \tag{3-9}$$

$$\beta(T^{\circ}C) = 1.13 \times \exp(-0.007T^{\circ}C) \tag{3-10}$$

where γ is the pressure dependency factor, σ is the bearing stress at the contact area, α is the velocity dependency factor, β is the temperature dependency factor, and T is the temperature of the contact area in Celsius [3-27][3-28]. The dependencies introduced in Equation (3-8) ~ (3-10) is also show in Figure 3-9. It should be mentioned that the

temperature dependency of Spec. M and Spec. L is the same, and the difference of the pressure and velocity dependencies between Spec. M and Spec. L is not large. Therefore, the listed friction dependency equations for Spec. M were also used for Spec. L.

(a) Pressure dependency   (b) Velocity dependency   (c) T°C dependency
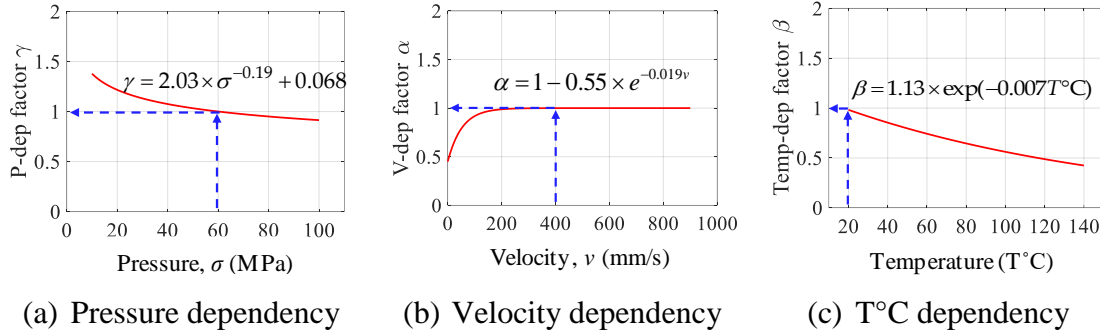
Figure 3-9. Friction dependencies obtained by small-scale material friction tests

Further, μ_o is the friction coefficient at 60 N/mm^2 ($\gamma = 1$), 400 mm/s ($\alpha = 1$) and an initial atmosphere temperature of 20 ˚C ($\beta = 1$). It was set as 0.075 for Spec. M and as 0.013 for Spec. L based on the method introduced in Section 2.4.2. Here, in the case of Spec. L, the value of μ_o is the same as that of μ_n, because the friction coefficient is minimally influenced by temperature for low-friction-type specimens.

3.4 Experimental and numerical results under artificial graphics and earthquake response orbits

The precise and simplified models considered all three friction dependencies throughout analysis procedure. In contrast, the constant model applied constant friction coefficient introduced in Equation (3-4). Coupling effect was also considered for all the models. Coupling effect is the effect of the response of two orthogonal directions on each other [3-5]. Figure 3-10 shows the definition of coupling effect. Where, *dis* is the displacement of the bearing in a short time interval, *disx* and *disy* are the component of *dis* on the *x* direction and the orthogonal direction, *y*, respectively, *μN* is the restoring friction force generated in the bearing, and *Ffx* and *Ffy* are the component of *μN* on the *x* direction and the orthogonal direction, *y*, respectively. If the coupling effect is considered, the restoring force, *μN*, of the bearing is considered to response in the opposite direction of *dis* and then divided into two orthogonal directions, *x* and *y*, as shown in Figure 3-10 (a). If the coupling effect is not considered, the response in the two orthogonal direction will be considered separately as *μN* as shown in Figure 3-10 (b).

(a) Coupling effect considered   (b) Coupling effect not considered
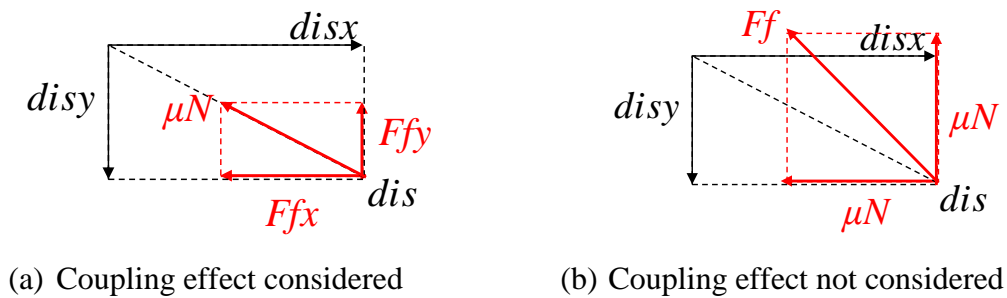
Figure 3-10. Definition of coupling effect

The accuracy of the friction models can be seen by comparing their force-displacement diagrams under artificial graphics with the experimental results. The comparisons under elliptical orbit for Spec. M and Spec. L is shown in Figures 3-11 and 3-12, respectively.
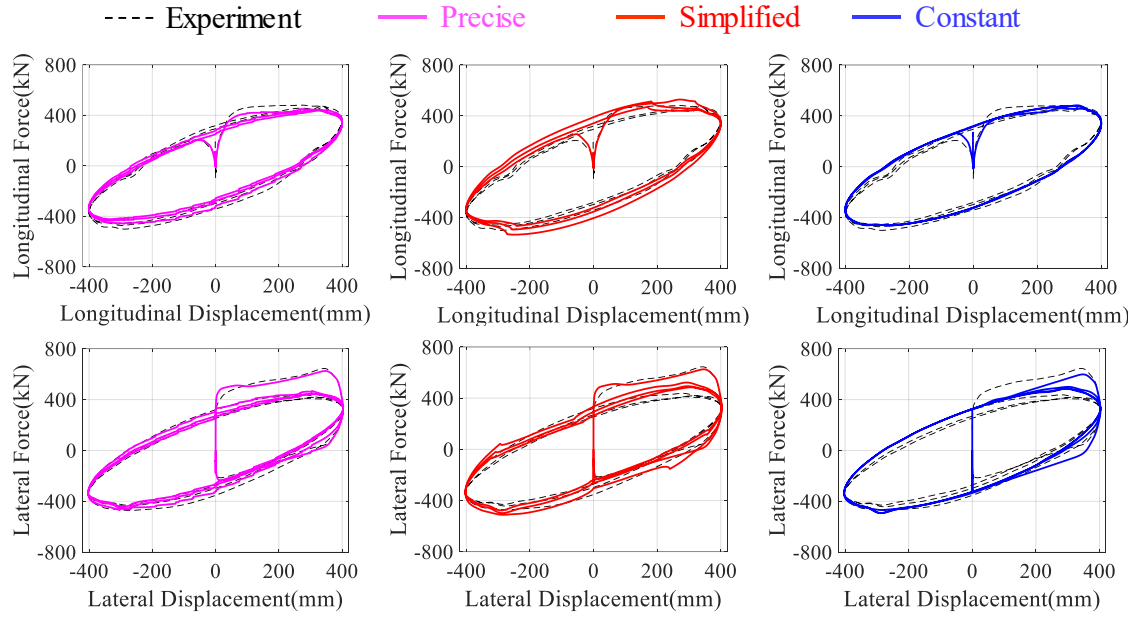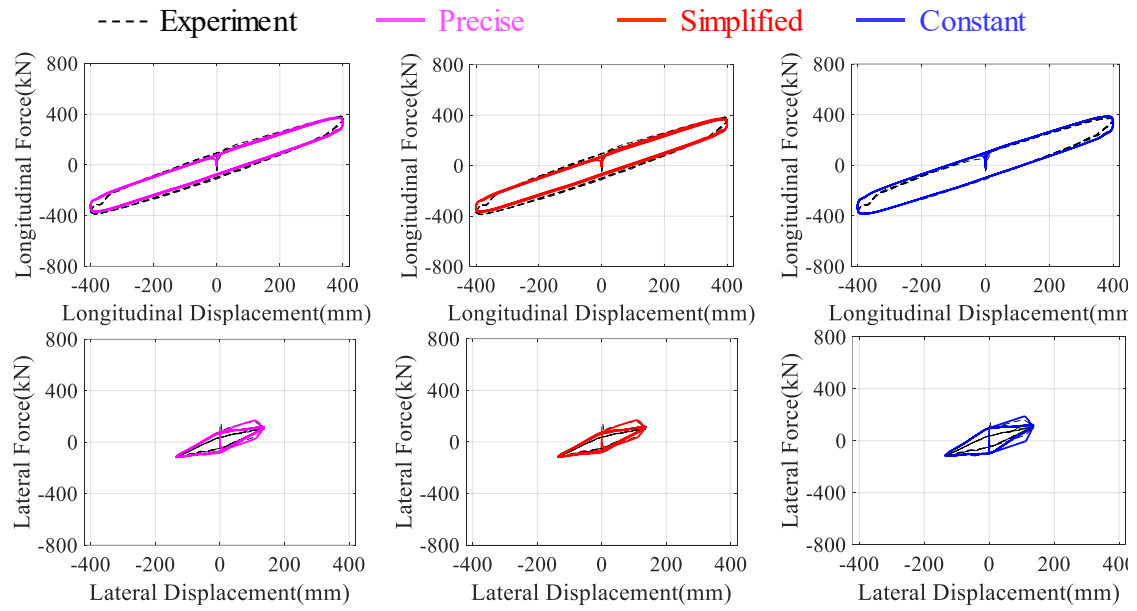
(a) Spec. M under circular orbit
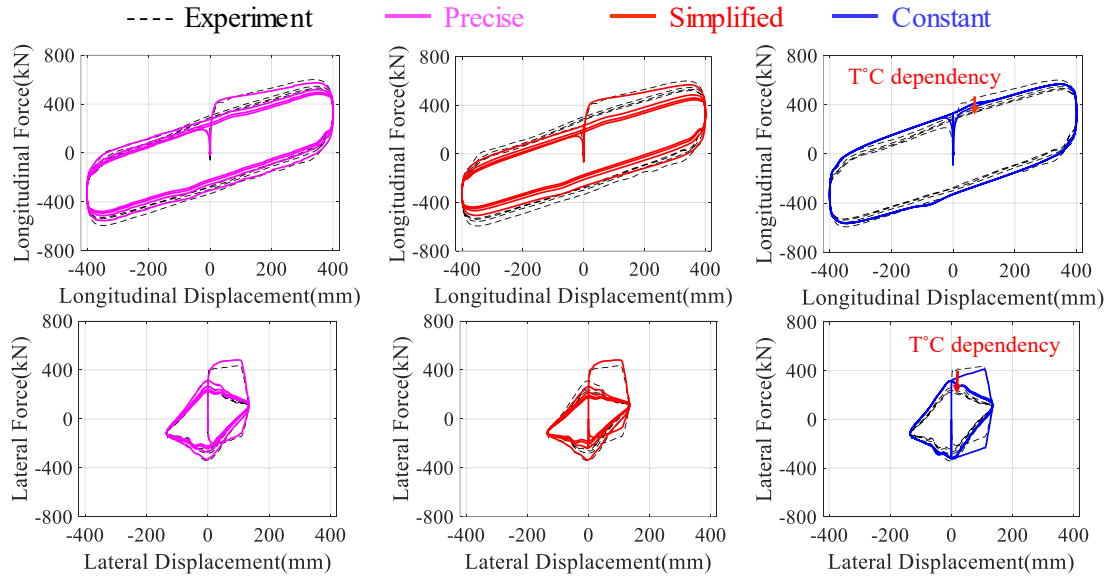
(b) Spec. M under ellipse orbit

Figure 3-11. Force-displacement diagrams of Spec. M under artificial graphics
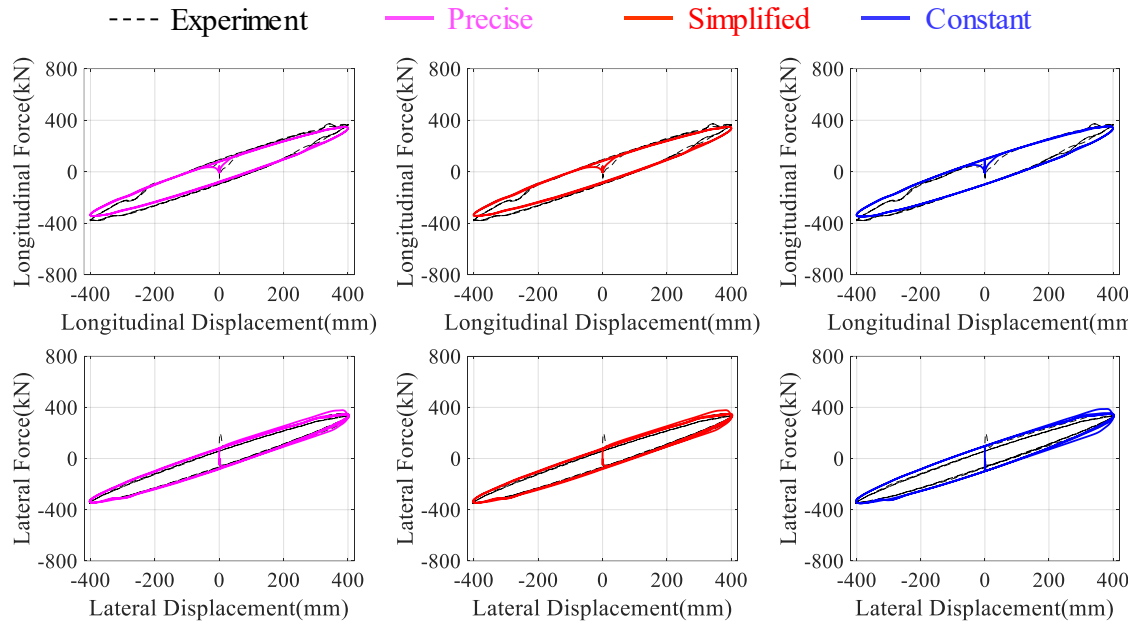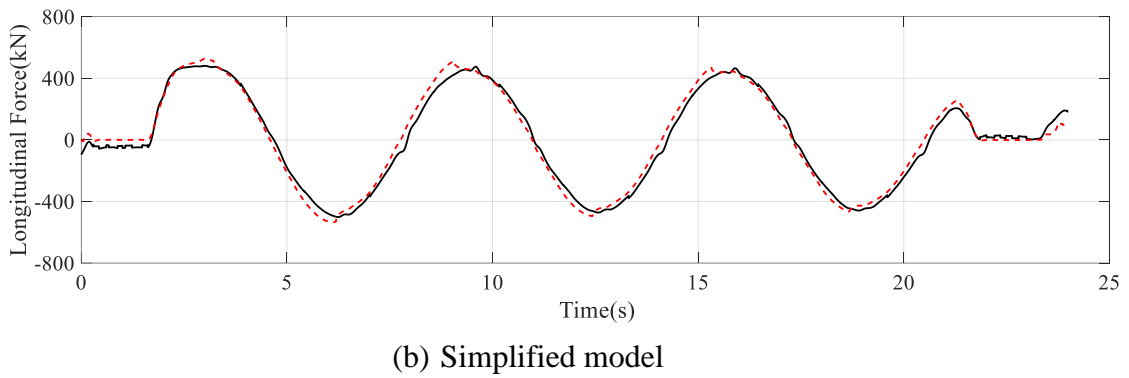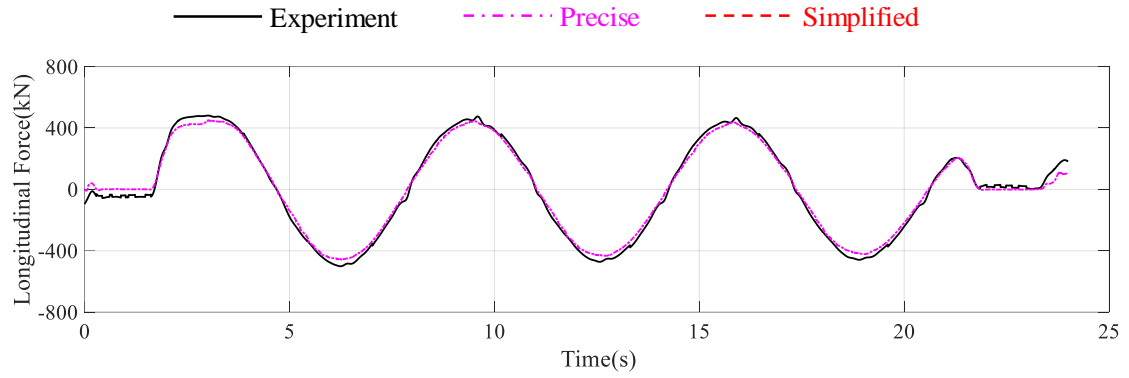
(a) Spec. L under circular orbit

(b) Spec. L under ellipse orbit

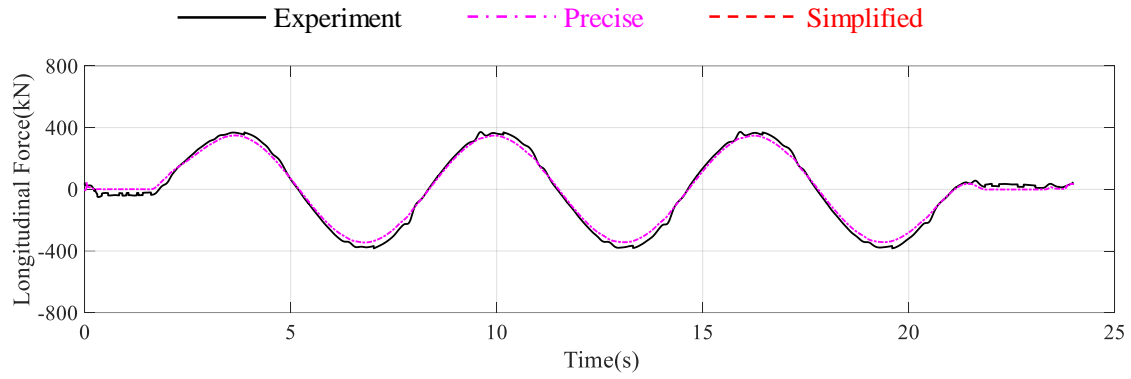**Figure 3-12.** Force-displacement diagrams of Spec. L under artificial graphics

In order to see the accuracy of the simplified model and the precise model clearer, the time history of the longitudinal response force of them under circular orbit are compared for both Spec. M and Spec. L as shown in Figure 3-13 and 3-14. It can be seen

that the response force simulated by the precise model and the simplified model show

high consistency with the experimental results under both Spec. M and Spec. L.

(a) Precise model

(b) Simplified model

Figure 3-13. Time history of longitudinal force of Spec. M under circular orbit

(a) Precise model
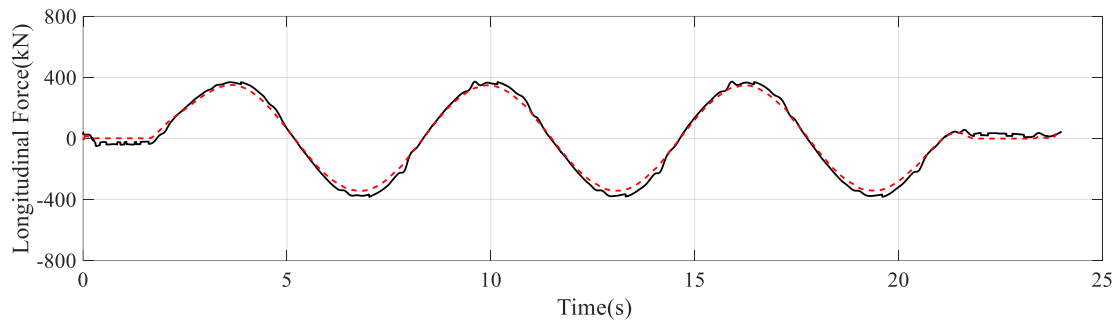
(b) Simplified model

Figure 3-14. Time history of longitudinal force of Spec. L under circular orbit

Figures 3-15 and 3-16 show the experimental and analytical results of force-displacement diagrams under earthquake response orbits for Spec. M and Spec. L, respectively. Then, from Figures 3-11 and 3-15, the followings can be concluded about the difference between the experimental results under artificial graphics and response orbits. Generally, all the experimental force-displacement loops have no large difference from the constant model (blue curve), which indicates that the magnitude of friction coefficient has no large difference between the artificial graphics and the response orbits. On the other hand, a large force pulse that breaks out the blue curve did occur for the case under response orbits compared to that under artificial graphics. This is caused by a rapidly increase of velocity at the beginning of the earthquake, which causes high velocity and low temperature happened simultaneously at the contact surface of the DCFP bearing. Based on Equation (3-7) ~ (3-10) and Figure 3-9, this will lead to a large friction
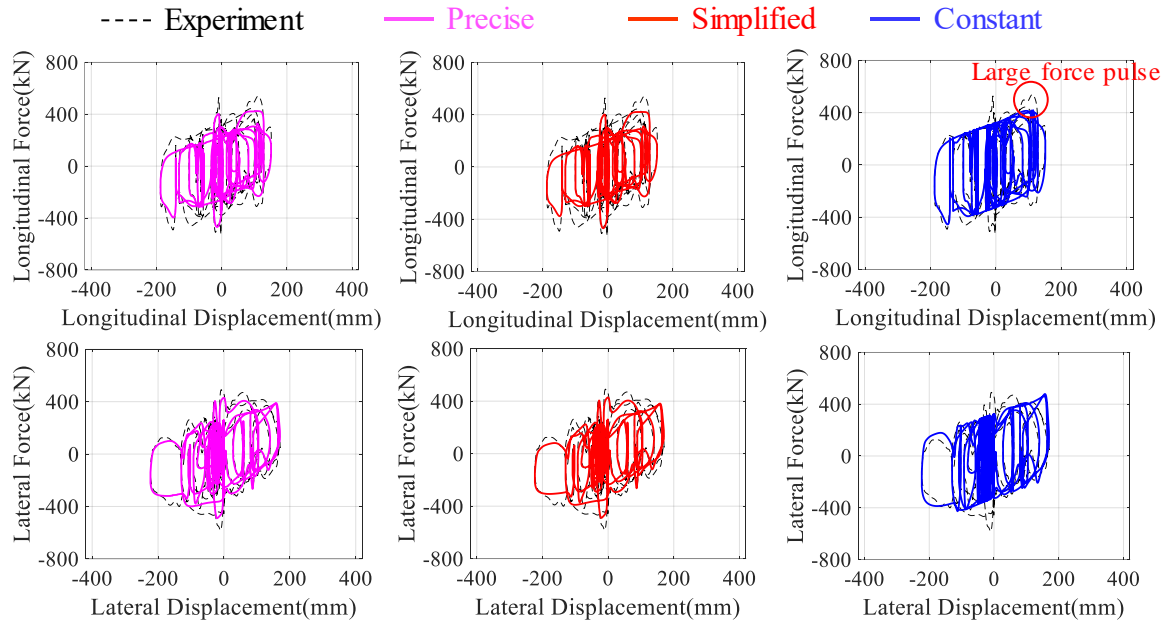
coefficient and in turn a large force. It can be seen from Figure 3-15 that both the precise and simplified model can simulate this force pulse. However, the nominal friction coefficient introduced in Section 3.3.1 cannot, because the constant value cannot simulate the change of friction coefficient.
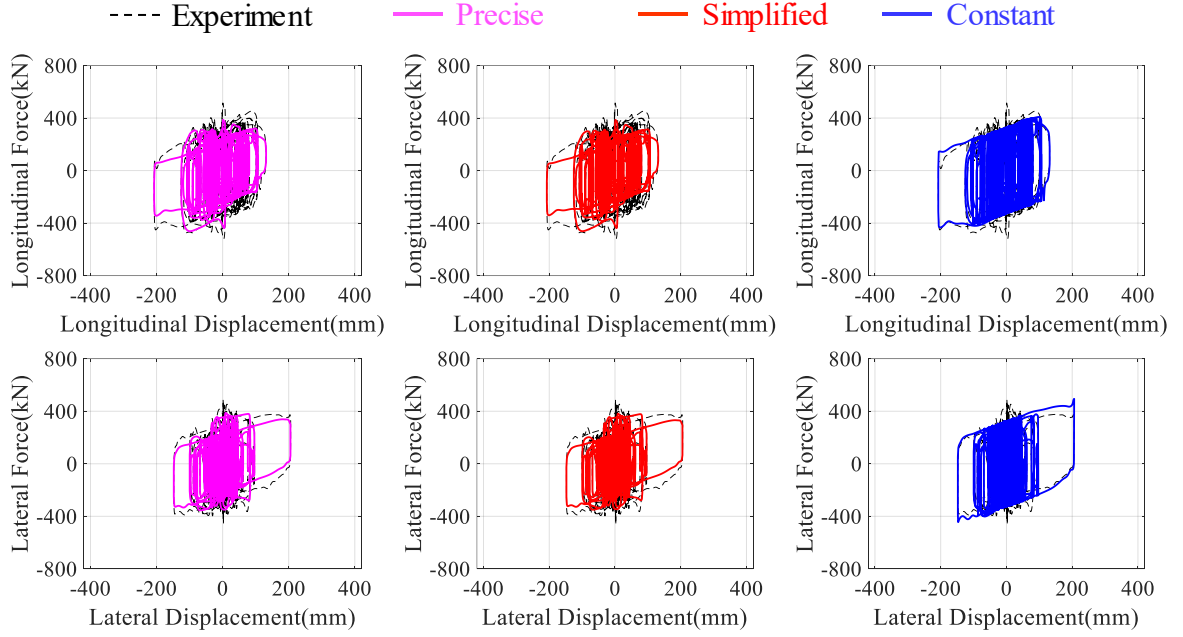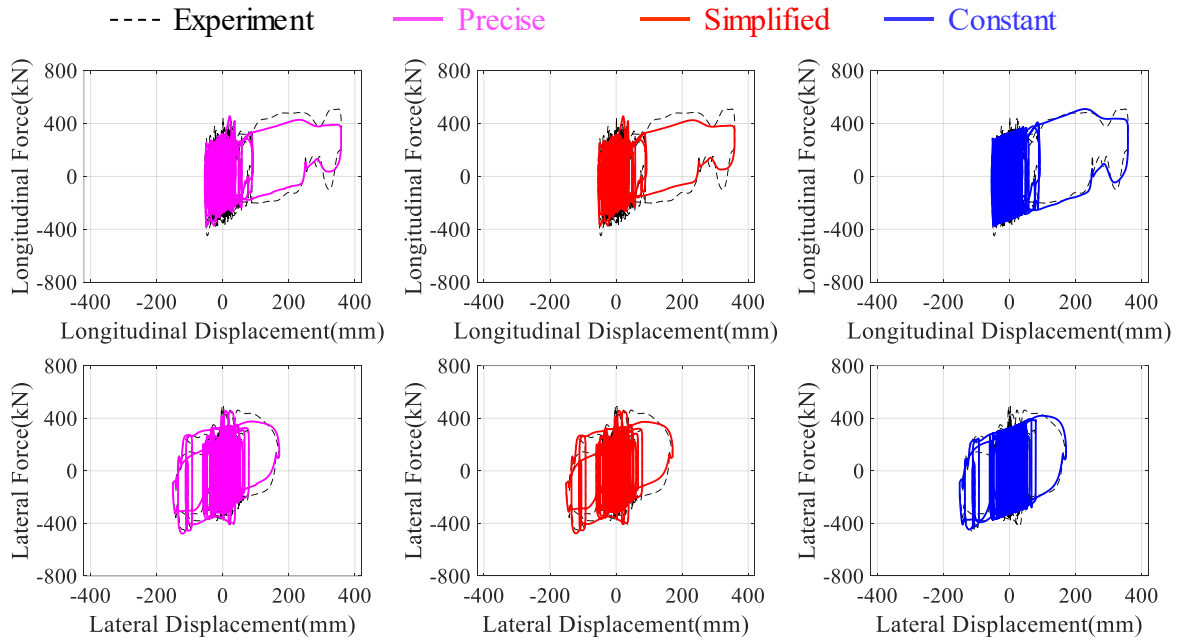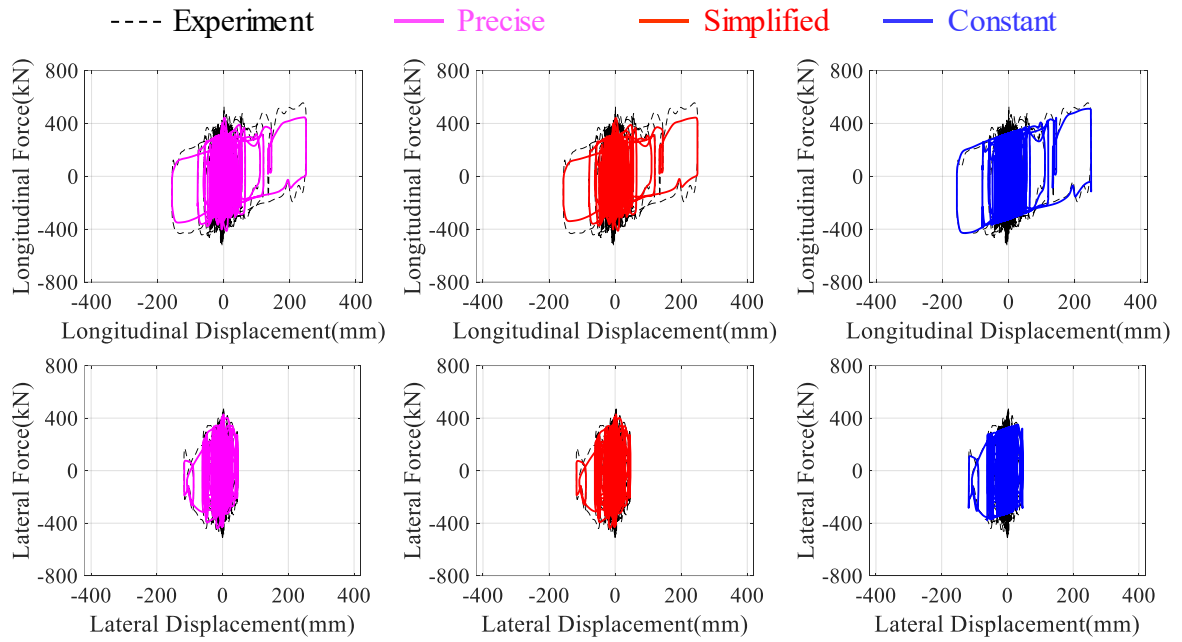

(a) Spec. M under IVD-M orbit
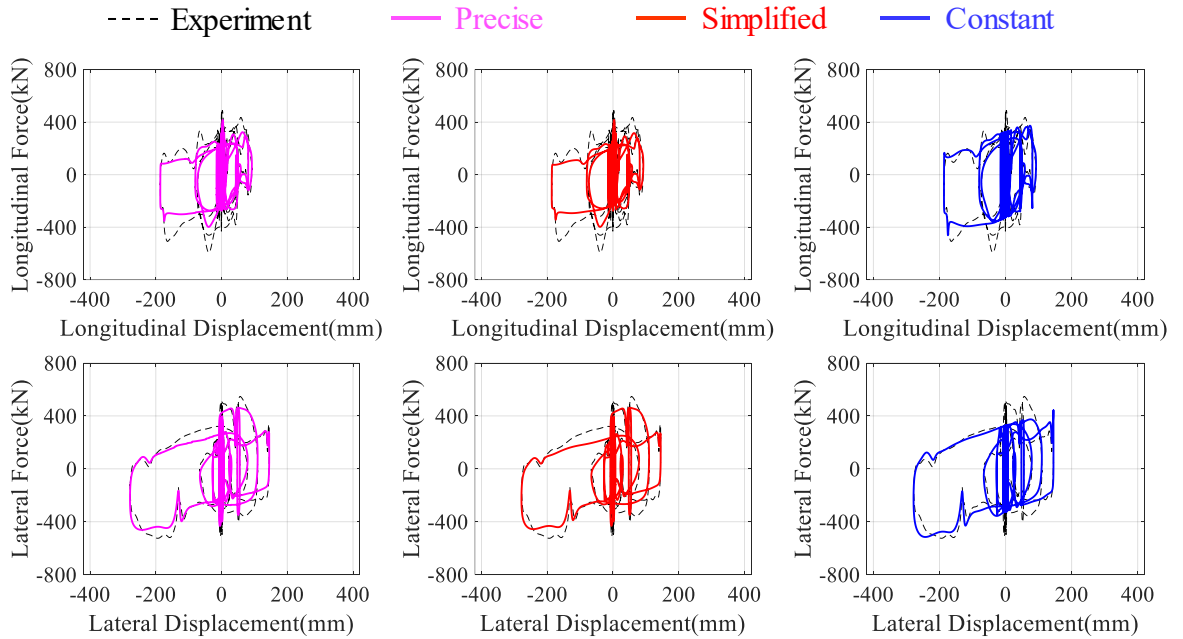
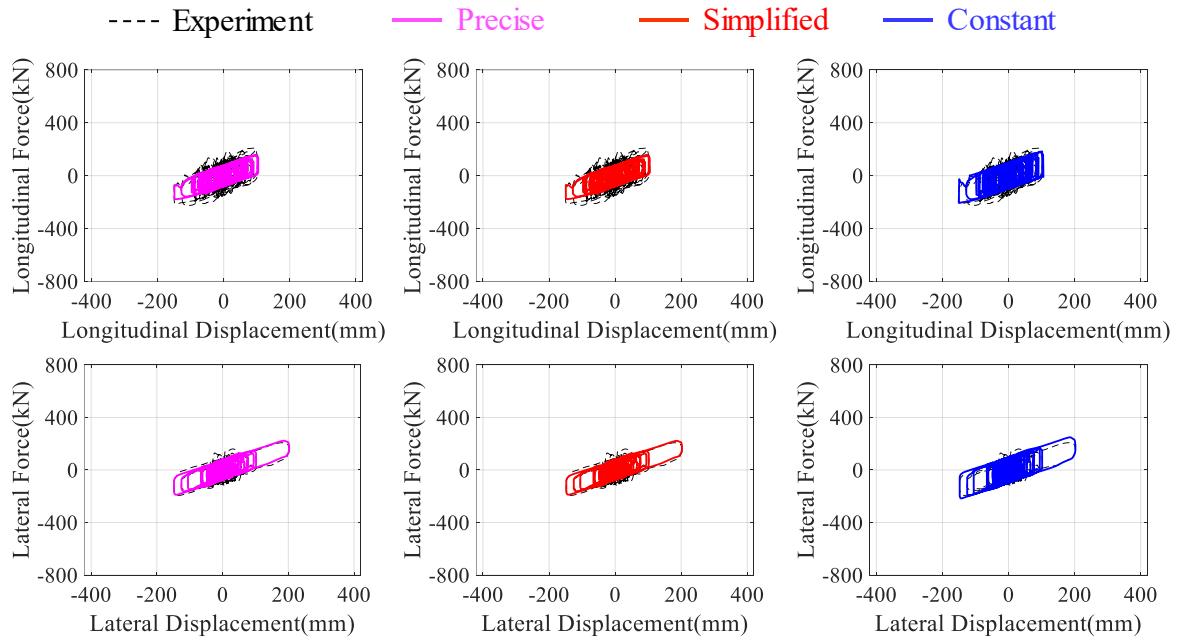(b) Spec. M under NCC-M orbit

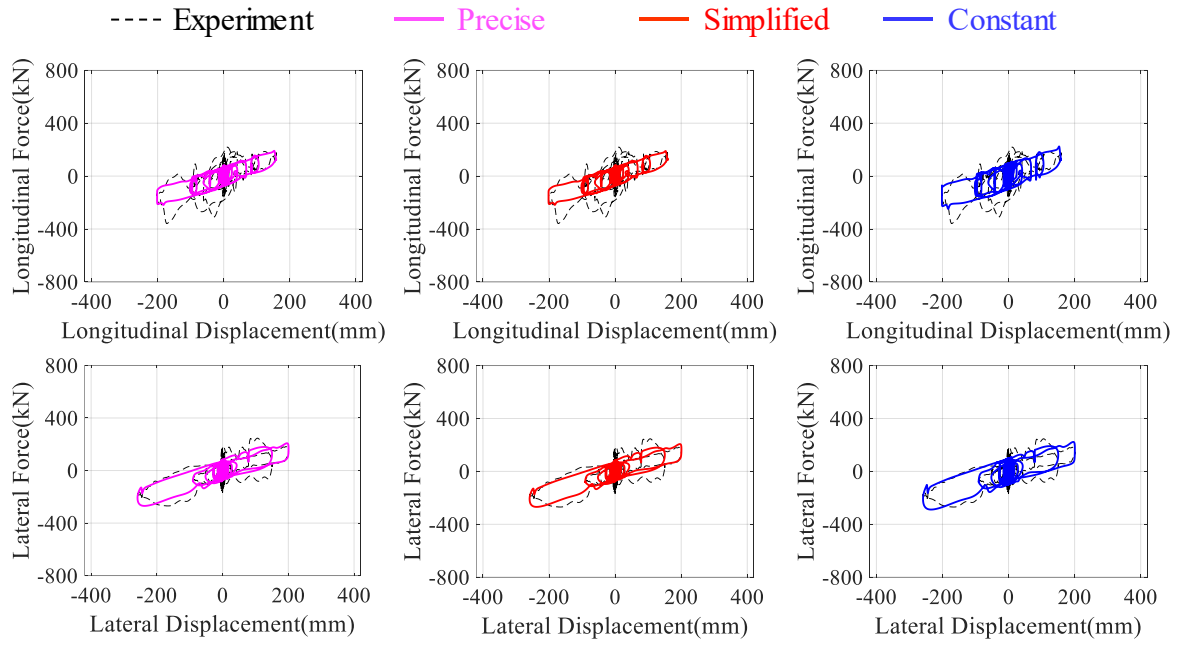(c) Spec. M under KNA-M orbit

(d) Spec. M under TSD-M orbit

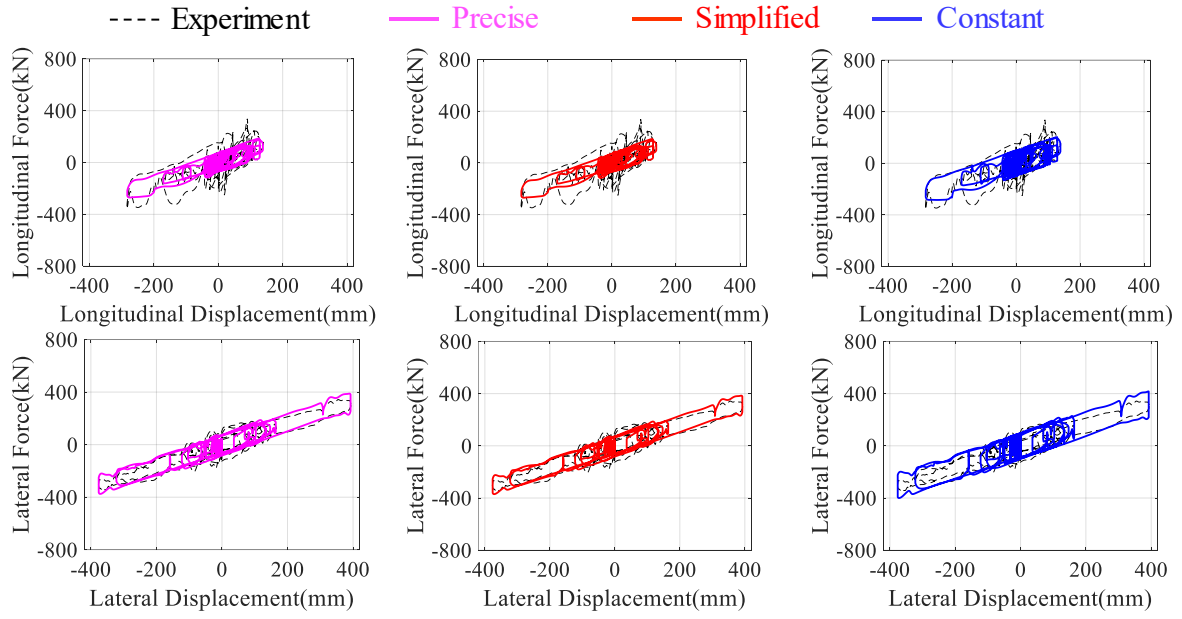(e) Spec. M under TIM-M orbit

Figure 3-15. Force-displacement diagrams of Spec. M under earthquake response orbits
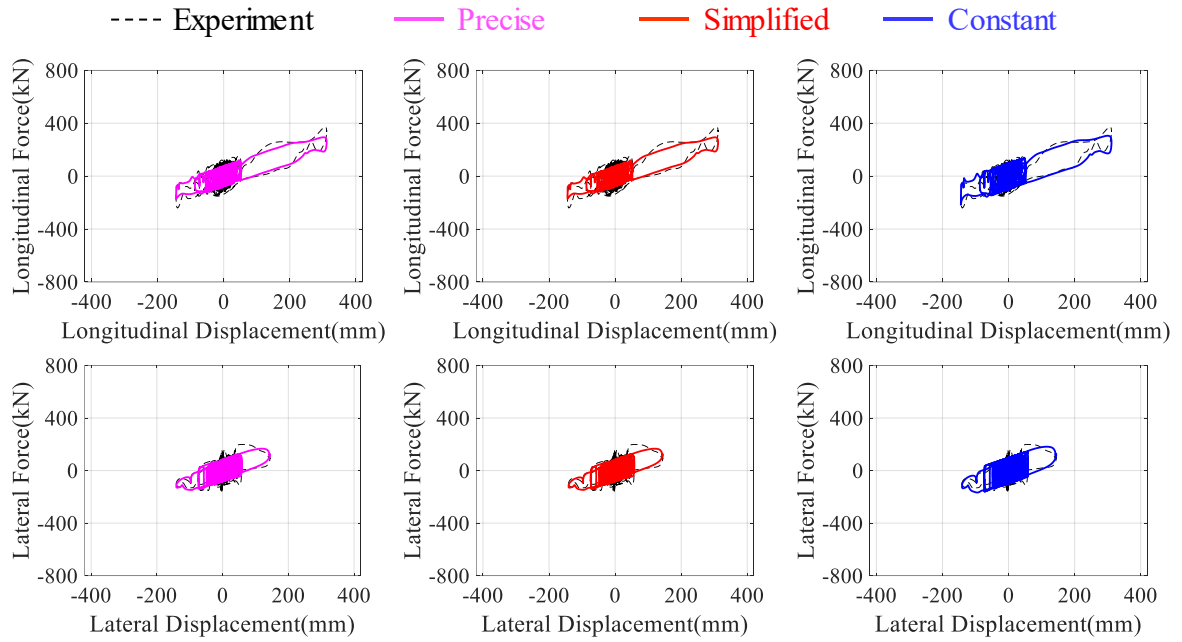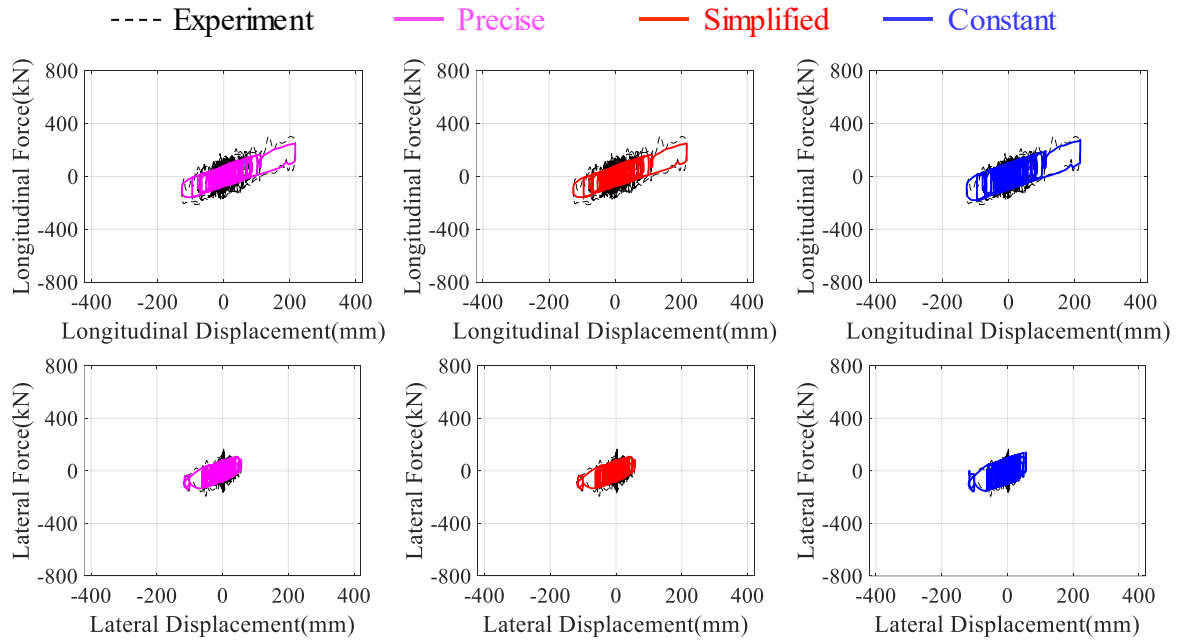

(a) Spec. L under IVD-L orbit

(b) Spec. L under NCC-L orbit

(c) Spec. L under KNA-L orbit

(d) Spec. L under TSD-L orbit


(e) Spec. L under TIM-L orbit

Figure 3-16. Force-displacement diagrams of Spec. L under earthquake response orbits

In order to see the accuracy of the simplified model and the precise model under earthquake response orbits clearer, the time history of the longitudinal response force of

them under KNA orbit are compared for both Spec. M and Spec. L as shown in Figure 3-17 and 3-18. It can be seen that the response force simulated by the precise model and the simplified model show high consistency with the experimental results under both Spec. M and Spec. L.
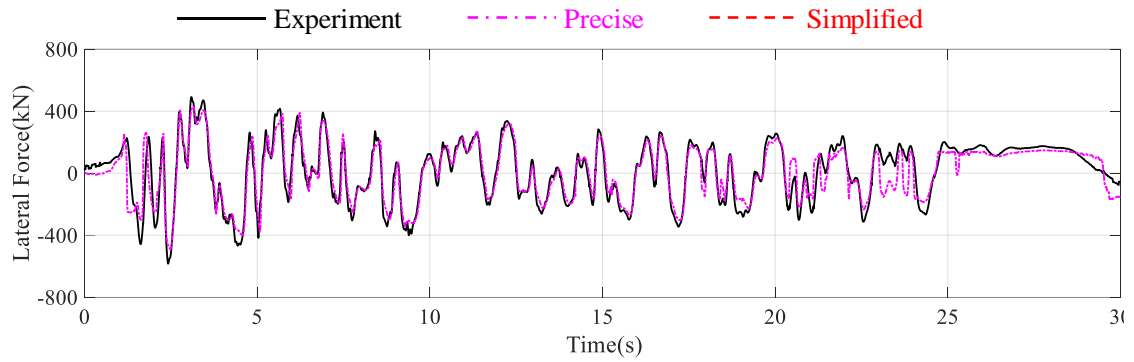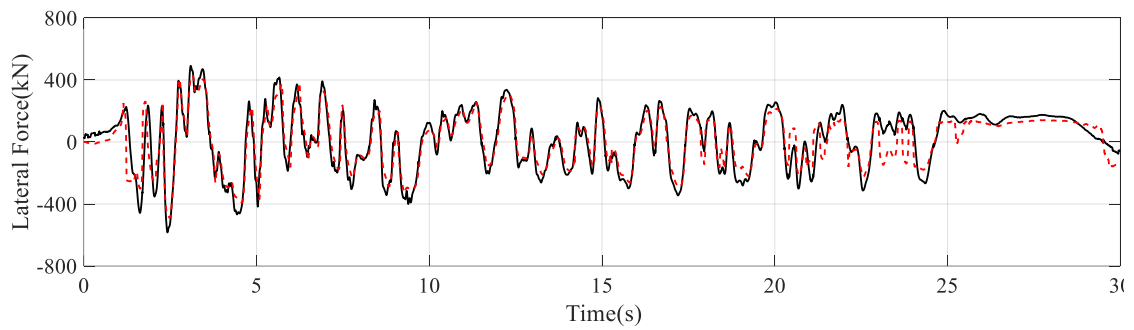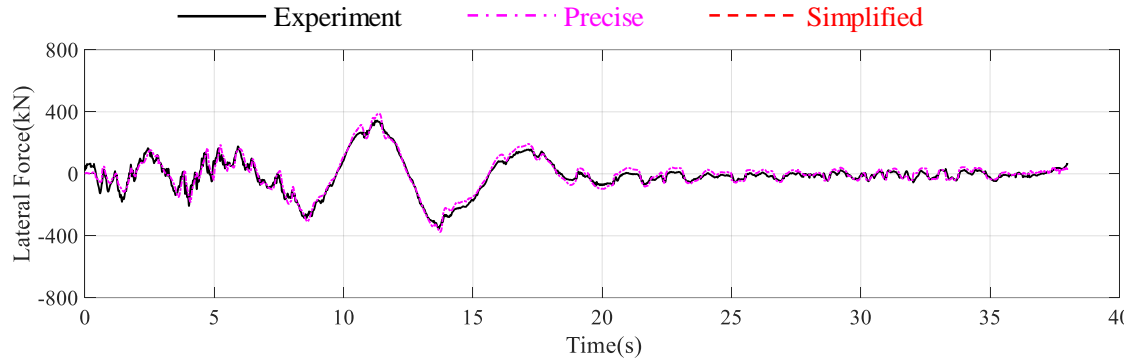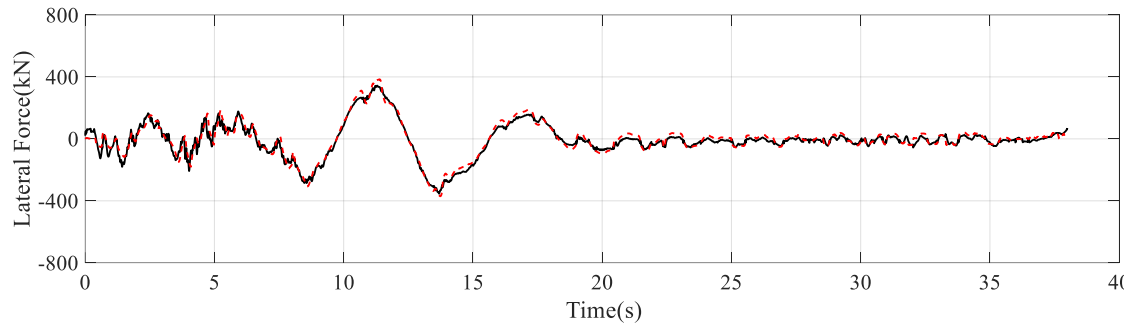

(a) Precise model

(b) Simplified model

Figure 3-17. Time history of longitudinal force of Spec. M under KNA-M orbit
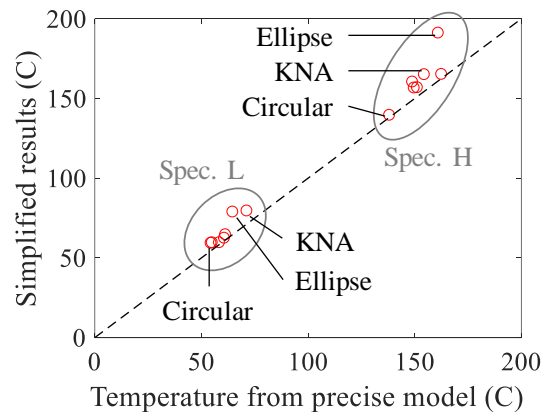
(a) Precise model

(b) Simplified model

Figure 3-18. Time history of longitudinal force of Spec. L under KNA-L orbit

In addition, the results under all the inputs are shown in Figure 3-19 in terms of the accuracy of the maximum horizontal response force and total dissipated energy of the bearing. Based on Figures 3-11 ~ 3-19, the simplified model exhibits nearly the same results as the precise model for both Spec. M and L. They slightly underestimated the response force and the dissipated energy in real earthquakes for the considered specimens, but the simulation accuracy is still high. Therefore, the simplified model can be used instead of the precise model for faster calculation. Further, from Figures 3-11 ~ 3-19, it is evident that using the nominal friction coefficient, μ_n, results in a slight overestimation of the maximum response force and dissipated energy. This difference is not large, but it implies that μ_n obtained from unidirectional experiments needs to be decreased a little bit under bidirectional excitations.
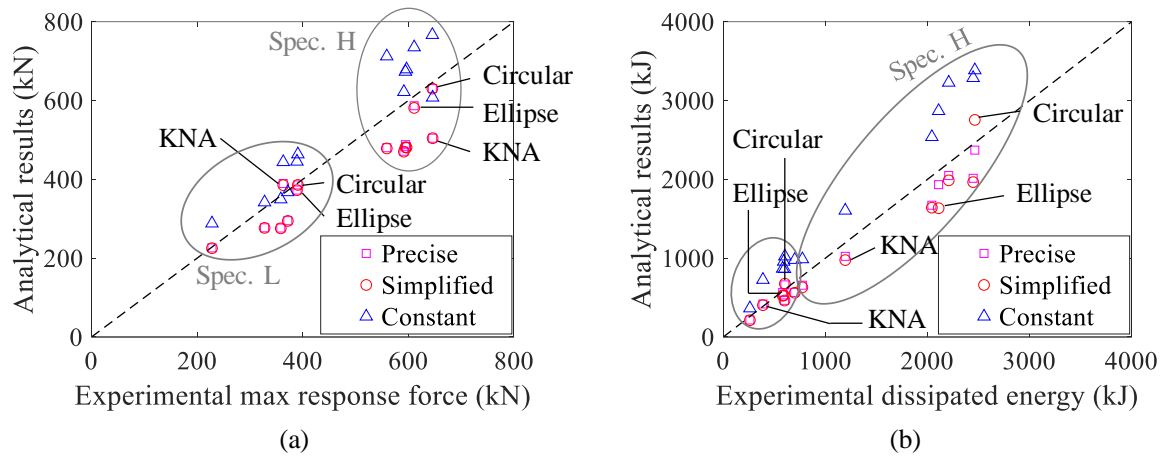
Figure 3-19. Accuracy of friction models on (a) maximum response force and (b) total dissipated energy under bidirectional excitations

Furthermore, Figure 3-20 shows the comparison of the simulated temperature on the contact surface of the bearing calculated by the precise model and the simplified model. It can be seen that the simplified model will overestimate the temperature a little bit, but the difference is not large. Together with the comparison shown in Figure 3-19, it can be concluded that the simplified model can be used instead of the precise model for both Spec. M and Spec. L.

Figure 3-20. Comparison of simplified model and precise model on the temperature of the contact surface

3.5 Influence of friction dependencies on the response displacement

3.5.1 Input ground motions

Eight earthquakes with various intensities, durations, and distances to fault were selected to incorporate most types of strong ground motions, as shown in Table 3-4. In the previous study of unidirectional response analysis as introduced in Chapter 2, component C1 was considered as input, whereas, in this study, both C1 and C2 were input. To be comparable, the C1 components of both studies were amplified to have PGV equal to 250, 500, 750, and 1000mm/s.

Table 3-4. Input earthquake motion

Abv.	Earthquake	Station	PGV-C1 (mm/s)	PGV-C2 (mm/s)	Dur. (s)	Rjb (km)[a]
IVD	Imperial Valley	Delta	330	260	100	22
LPG	Loma Prieta	Gilroy Array	447	357	40	9
NCC	Northridge	Canyon Country	449	430	20	11
JKB	Kobe	JMA Kobe	893	780	30	1
KNA	Kobe	Nishi-Akashi	373	366	41	7
TC1	Chi-Chi	TCU129	554	510	90	2
TSD	Tohoku	JMA Sendai	545	544	180	172*
TIM	Tohoku	JMA Ishinomaki	376	269	300	145*

Note: [a] Joyner-Boore distance in PEER [3-21]; * hypocentral distance in K-NET [3-22]

3.5.2 Mechanical model

It has been reported that it is effective to assume a rigid superstructure in predicting the isolator displacement [3-29][3-30]. Hence, in this study, the isolation system was simplified as a single degree of freedom (SDOF) system as shown in Figure 3-21. The mechanical model and process of the response analysis under bidirectional excitations are similar with that under unidirectional excitations as introduced in Section 2.5.1 and 2.5.2. Similar to the unidirectional model, the bidirectional model in this study considered both sliding and non-sliding states [3-23]. In addition of it, the coupling effect between the two horizontal directions was considered in this model. The states were judged by a circle with a radius of r_f, referred to as the "yield surface" and the internal forces are considered in terms of springs (a), (b), and (c): Spring (a) represents the restoring force of the pendulum movement. A vertical load that can provide 60 MPa of pressure on the slider surface was applied. Spring (b) represents the friction force between the slider and two concave plates. The bearing was set as the Spec. M simulated by the simplified model to study the effect of the temperature caused by friction heating. Finally, spring (c) represents the elastic stiffness of the entire system. Under bidirectional excitations, the direction of springs (b) and (c) is opposite to the moving direction of the displacement point. In addition, equations of motion at step i is shown as Equation (3-11) ~ (3-16), in which the method of releasing the unbalanced force is used.
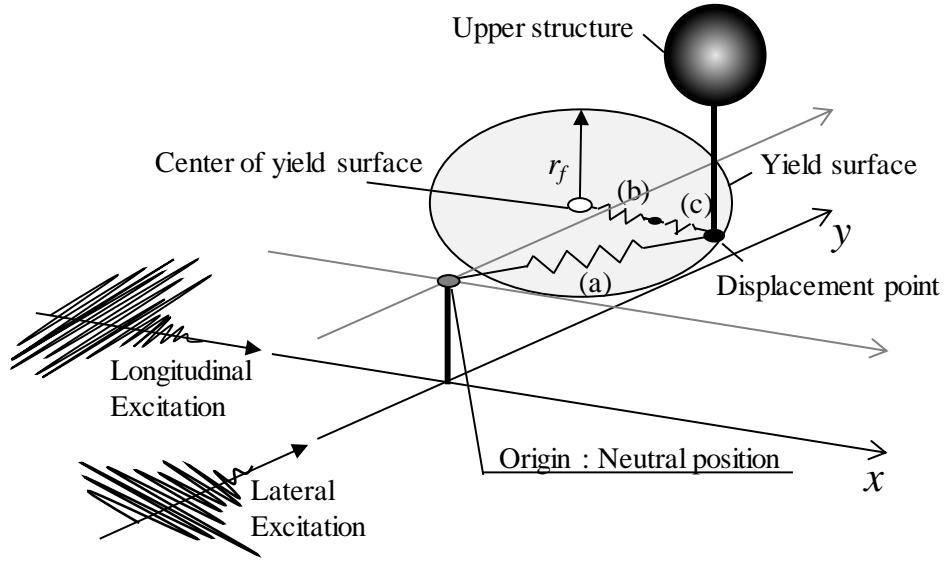
Figure 3-21. Bidirectional mechanical model of a structure with DCFP bearings.

$$accx(i) = -\frac{gaccx(i) + \dfrac{QFX(i-1)}{mass} + c \times (velx(i-1) + 0.5 \times accx(i-1) \times dt) + \dfrac{k(i-1)}{mass} \times (velx(i-1) \times dt + (0.5 - \beta_c) \times accx(i-1) \times dt^2)}{1 + 0.5 \times c \times dt + \dfrac{\beta_c \times k(i-1) \times dt^2}{mass}}$$

(3-11)

$$velx(i) = velx(i-1) + 0.5 \times (accx(i-1) + accx(i)) \times dt$$

(3-12)

$$disx(i) = disx(i-1) + velx(i-1) \times dt + (0.5 - \beta_c) \times accx(i-1) \times dt^2 + \beta_c \times accx(i) \times dt^2$$

(3-13)

$$accy(i) = -\frac{gaccy(i) + \dfrac{QFY(i-1)}{mass} + c \times (vely(i-1) + 0.5 \times accy(i-1) \times dt) + \dfrac{k(i-1)}{mass} \times (vely(i-1) \times dt + (0.5 - \beta_c) \times accy(i-1) \times dt^2)}{1 + 0.5 \times c \times dt + \dfrac{\beta_c \times k(i-1) \times dt^2}{mass}}$$

(3-14)

$$vely(i) = vely(i-1) + 0.5 \times (accy(i-1) + accy(i)) \times dt$$

(3-15)

$$disy(i) = disy(i-1) + vely(i-1) \times dt + (0.5 - \beta_c) \times accy(i-1) \times dt^2 + \beta_c \times accy(i) \times dt^2$$

(3-16)

Where *accx*(*i*) and *accxy*(*i*) are the acceleration of the upper structure relatives to the lower concave plate in x and y direction respectively, *gaccx*(*i*) and *gaccy*(*i*) is the ground acceleration at step *i* in x and y direction respectively, *QFX*(*i*) and *QFY*(*i*) is the total restoring force of the DCFPB in x and y direction respectively, *mass* is the mass of the rigid body which equals the mass that can provide 60MPa pressure on the slider surface, *c* is the damping coefficient which is set as 0, *velx*(*i*) and *vely*(*i*) is the velocity of the upper structure relatives to the lower concave plate in x and y direction respectively, *dt* is the time interval of each step which equals 0.0025s (this value is selected based on the error validation and the time consumption), *k*(*i*) is the stiffness of the system at step *i* and β_c is the constant value which equals 0.25.

A flow chart of the response analysis a SDOF (single degree of freedom) system based on precise model is shown in Figure 3-22 for a rigid-body structure with DCFPB. In which, (*OX*, *OY*) is coordinate of the center of the yield surface, *disx* and *disy* are the displacement of the upper structure relatives to the center of the lower concave plate in x and y direction respectively, *OPX* and *OPY* are the distance in between, k_f is the elastic stiffness of the entire DCFPB which equals 1900kN/mm based on experimental results, *n* is the serial number of the monitor points, (*mpx*(*n*), *mpy*(*n*)) is the coordinate of monitor point n on the lower concave plate, *r* is the side length of a square that has the same area as the slider surface, *q*(*i,n*) is the heat flux generated by friction heating at monitor point *n* at step *i* and σ is the average pressure at the slider surface which is set as 60 Mpa during excitation. T_{ave} is the average temperature of the contact surface, *Ffx* and *Ffy* are the components of the friction force in x and y direction respectively, and *QFX* and *QFY* are the components of the total horizontal force in x and y direction respectively.
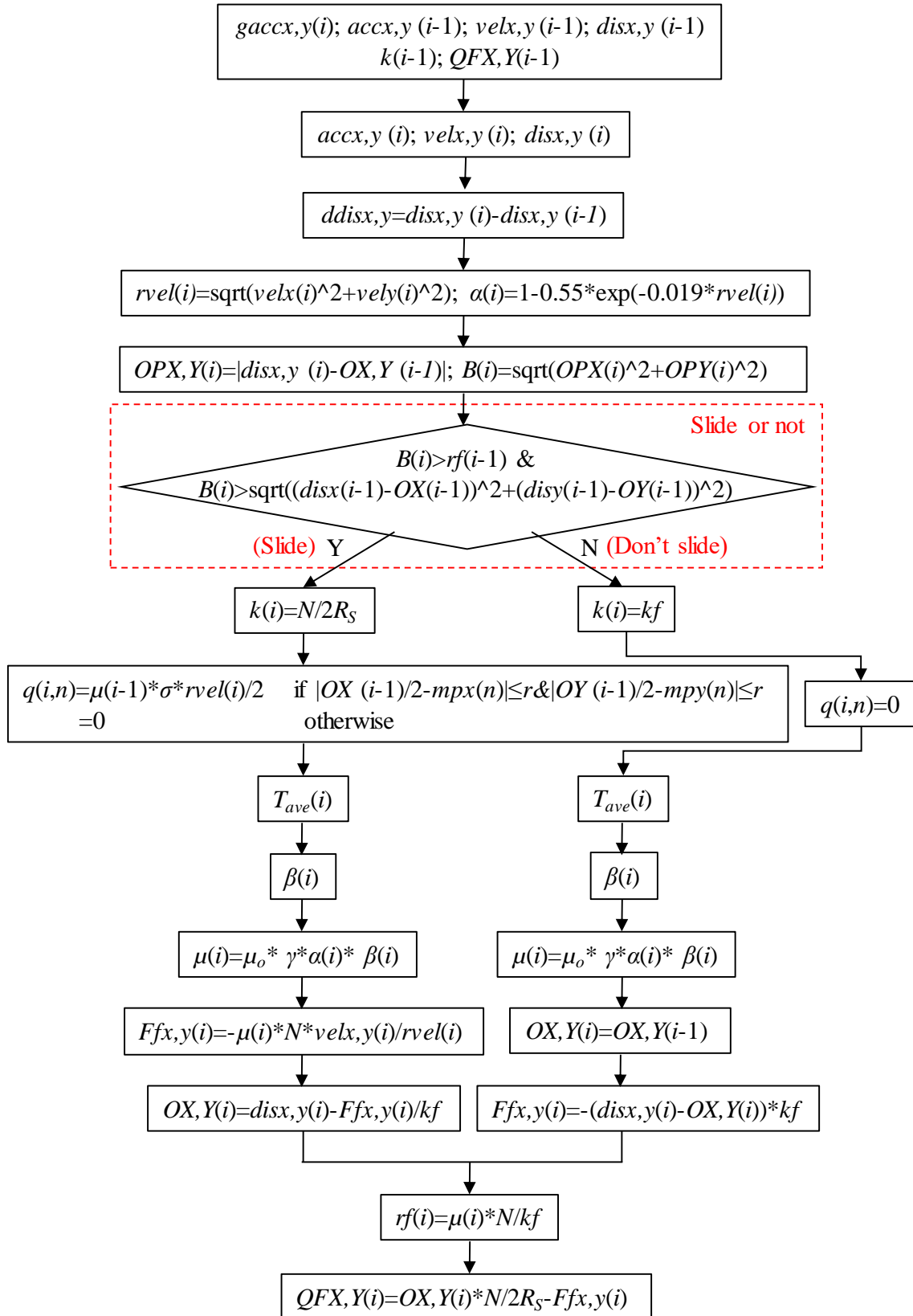
Figure 3-22. Flow chart of the bidirectional response analysis of a SDOF system

To further confirm the accuracy of the simplified model on predicting the maximum response displacement (D_{max}), the comparison of D_{max} of response analysis using the precise model, simplified model, and the constant friction coefficient is shown in Figure 3-23 (a). The simplified model provides a similar but slightly higher simulation on D_{max} compared to the precise model. In contrast, the response analysis using the nominal friction coefficient, μ_n, slightly underestimated D_{max}. Similar as the results shown in Figure 3-19, this difference is not large, but it implies that μ_n obtained from unidirectional experiments needs to be decreased a little bit under bidirectional excitations. Further, Figure 3-23 (b) shows the comparison of the representative temperature calculated using the precise and simplified models. Similar as the results shown in Figure 3-20, the simplified model overestimates the temperature slightly, however, the difference is not significant. To clearly observe the difference, the displacement response and corresponding increase of temperature during NCC (PGV in longitudinal direction is amplified as 750 mm/s) is shown in Figure 3-24 as an example. Consequently, it can be concluded that the simplified model can be used instead of the precise model with no large difference.
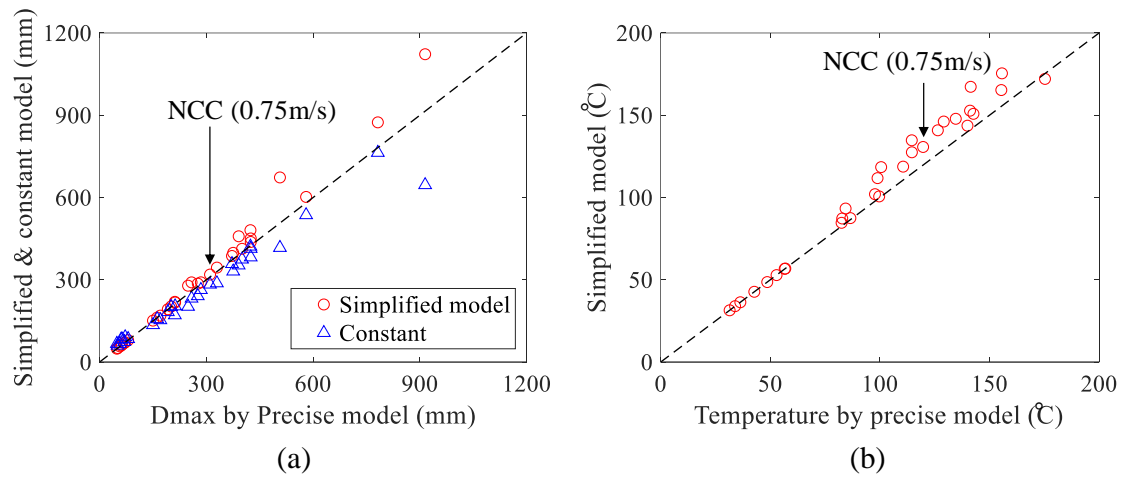
Figure 3-23. Comparison of the three models on the maximum displacement and temperature
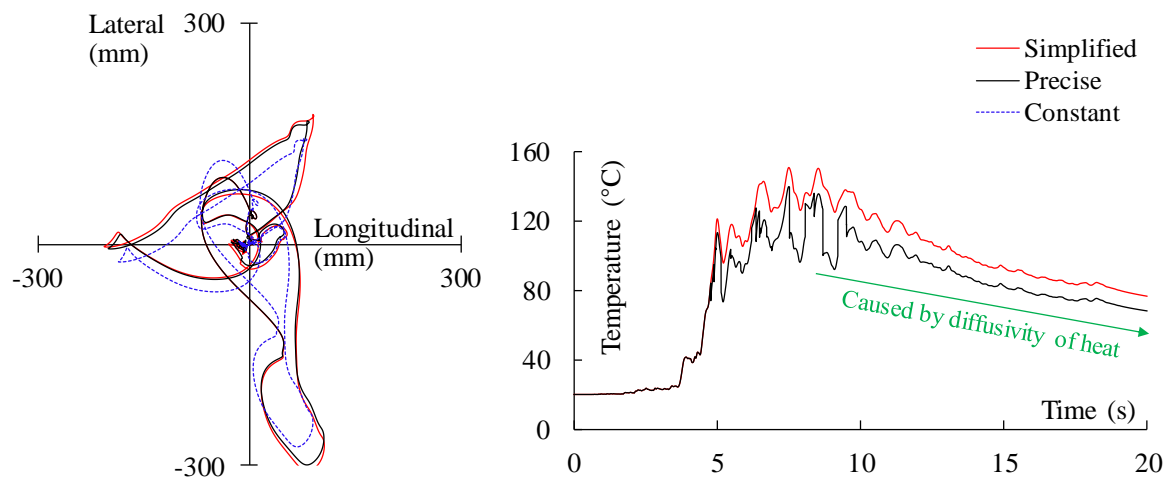
Figure 3-24. Response displacement and temperature history during NCC (750 mm/s)

3.5.3 Influence of friction dependencies on the response displacement

As introduced in Section 3.3.2, a larger velocity results in a larger friction coefficient (μ), while a larger temperature results in a smaller μ, which in turn causes change in the response displacement. As shown in Figure 3-25, d_{1D} is the maximum displacement of the DCFP bearing under C1 component of a ground motion pair and d_{2D} is the maximum displacement under the ground motion pair. Denoting the response temperature and velocity of the DCFP bearing under the C1 component of the ground motion pair as T_x and V_x, respectively, and the response velocity and temperature under the ground motion pair as V_{xy} and T_{xy}, respectively, two special displacements can be defined to investigate the influence of velocity and temperature dependency on the bidirectional response displacement respectively: d_{Vxy}, the maximum horizontal displacement under the C1 component of the ground motion pair using V_{xy} and T_x to calculate μ, and d_{Txy}, the maximum horizontal displacement under C1 using T_{xy} and V_x to calculate μ.
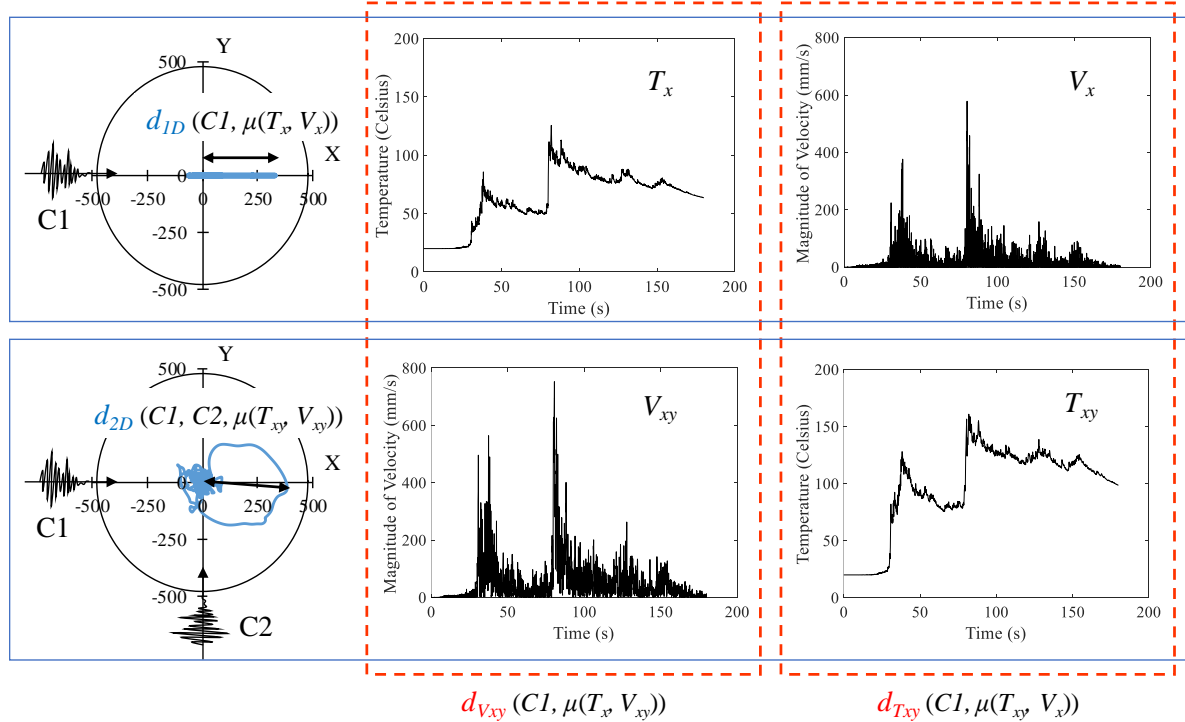

Figure 3-25. Definition of d_{Vxy} and d_{Txy}

Subsequently, the contribution of the change in the velocity dependency and temperature dependency caused by the addition of the C2 component on the increase of the maximum response displacement can be expressed as η_V and η_T, respectively:

$$\eta_V = \frac{d_{Vxy}}{d} \tag{3-17}$$

$$\eta_T = \frac{d_{Txy}}{d} \tag{3-18}$$

The analysis results of d_{1D}, d_{Vxy} d_{Txy}, and d_{2D} calculated with the amplified input waves are shown in Figure 3-26. Figures 3-26 (a) & (b) indicate that under strong seismic excitations, the temperature dependency contributes an increase of approximately 1.1 calculated by the least squares means (LSM) method to the change of the response displacement, while the influence of velocity dependency is relatively negligible.

(a) Contribution of η_V (b) Contribution of η_T
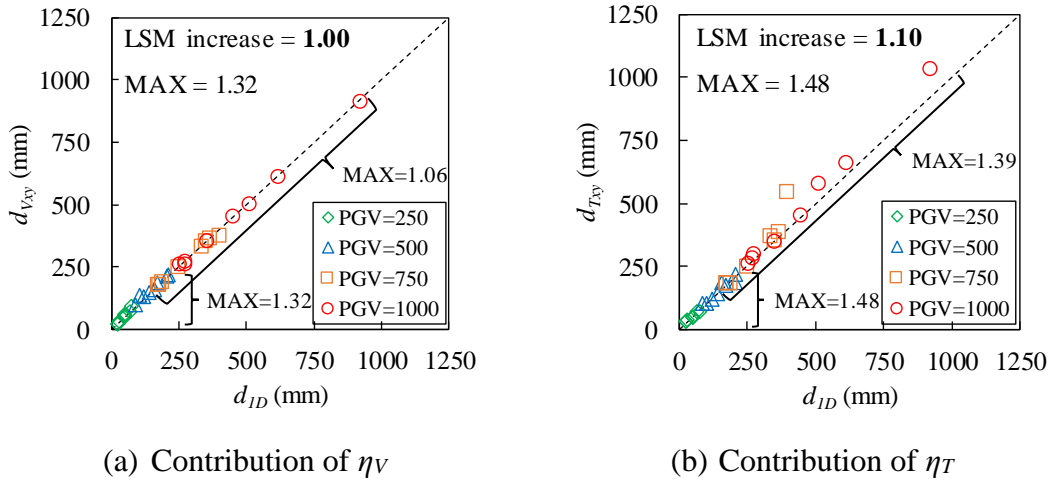
**Figure 3-26.** Influence of velocity and temperature change on the maximum displacement

As the influence of velocity dependency (η_V) is negligible, the major factors affect the displacement increase from unidirectional to bidirectional excitations will be remained as the temperature dependency (η_T), the bidirectional effect (η_0) and the coupled

behavior (η_C). Therefore, the increase caused by the contribution of the bidirectional effect (η_0) and the coupled behavior (η_C) can be expressed by:

$$\eta_0 \times \eta_C = \frac{d_{2D}}{d_{Txy}} \tag{3-19}$$

As shown in Figure 3-27 (a), from d_{Txy} to d_{2D}, the LSM increase of displacement caused by the the bidirectional effect (η_0) and the coupled behavior (η_C) is 1.18. Further, Figure 3-27 (b) shows that the change from d_{1D} to d_{2D} is an LSM increase of 1.29 with the maximum increase of PGV=250 and 500mm/s as 2.66 and PGV=750 and 1000 mm/s as 1.87, which is too large to be ignored. Consequently, it can be concluded that the influence of temperature (η_T) is as important as the bidirectional effect (η_0) and coupled behavior (η_C) on the contribution to the increase of the maximum displacement (temperature contributes almost one-third of the increase) and cannot be ignored.

(a) Contribution of η_0 & η_C (b) Relation between d and D
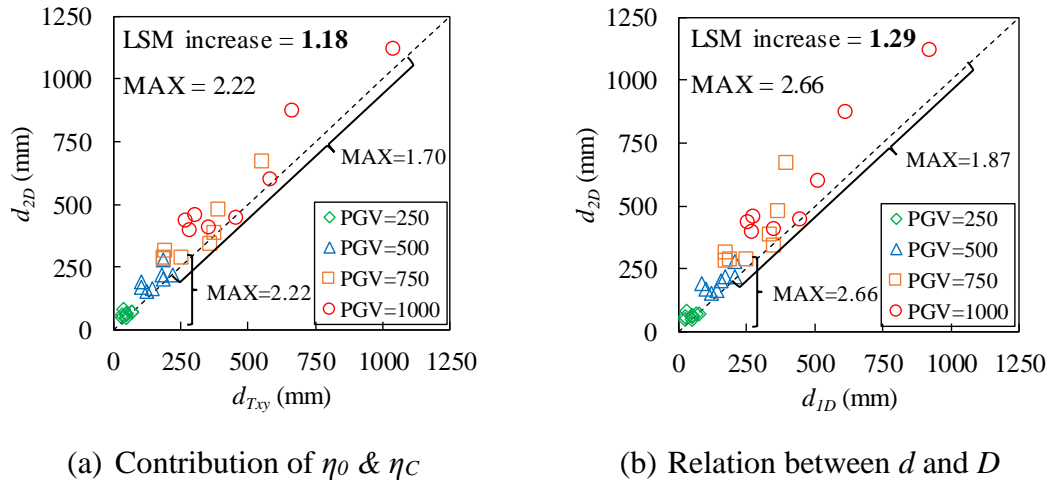
Figure 3-27. Relations between maximum displacements under amplified ground motions

3.5.4 Change of friction related factors after adding the second component

In order to assess the change of temperature, velocity and friction coefficient after adding the second component (C2) of a ground motion pair, three coefficients bT, bv and $b\mu$ were proposed respectively through the method of least squares based on the results of response analysis:
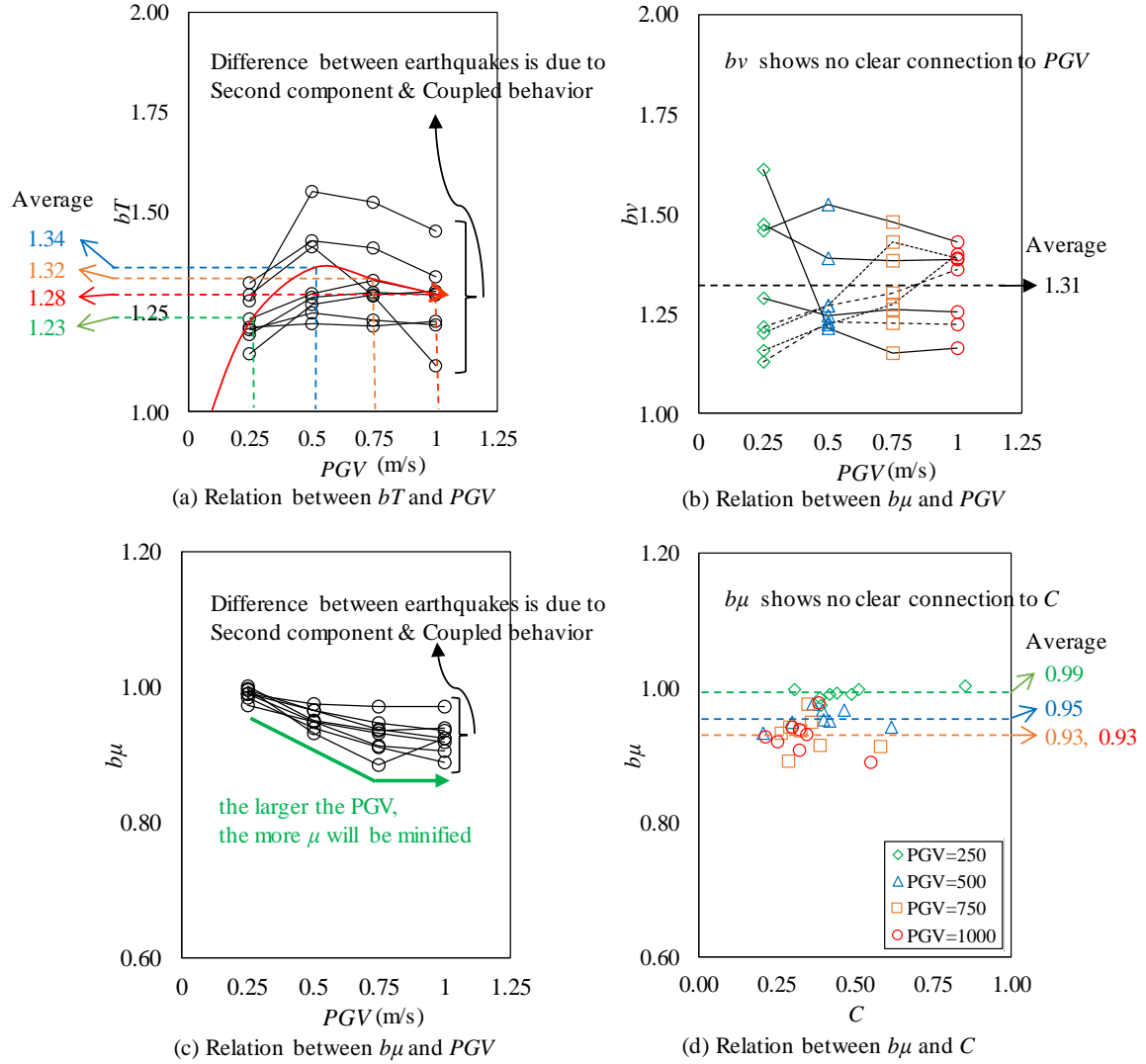
$$bT = \frac{\sum\limits_{t=0}^{Dur.} T_{1D}(t) \times T_{2D}(t)}{\sum\limits_{t=0}^{Dur.} T_{1D}(t)^2} \tag{3-20}$$

$$bv = \frac{\sum\limits_{t=0}^{Dur.} v_{1D}(t) \times v_{2D}(t)}{\sum\limits_{t=0}^{Dur.} v_{1D}(t)^2} \tag{3-21}$$

$$b\mu = \frac{\sum\limits_{t=0}^{Dur.} \mu_{1D}(t) \times \mu_{2D}(t)}{\sum\limits_{t=0}^{Dur.} \mu_{1D}(t)^2} \tag{3-22}$$

Where t is time, $Dur.$ is the duration of the earthquake; T_{1D}, v_{1D} and μ_{1D} are the temperature, response velocity and the friction coefficient of the bearing under the C1 component of the ground motion pair respectively; T_{2D}, v_{2D} and μ_{2D} are the temperature, response velocity and friction coefficient of the bearing under the ground motion pair respectively. The value of coefficients bT, bv and $b\mu$ can give an overview about the change of temperature, velocity and friction coefficient through the earthquake after considering the second component. However, they cannot represent the change around the maximum response displacement, which will be further studied through time histories in Section 3.6. The analysis results of bT, bv and $b\mu$ under the eight earthquakes in Table 3-4 with their longitudinal PGV amplified as 0.25m/s, 0.5m/s, 0.75m/s and 1m/s related

to the PGV and the circle degree factor of the response orbit (*C*) are shown in Figure 3-28.

(a) Relation between *bT* and *PGV*

(b) Relation between *bμ* and *PGV*

(c) Relation between *bμ* and *PGV*

(d) Relation between *bμ* and *C*

**Figure 3-28.** Analysis results of *bT*, *bv* and *bμ* under different PGV and different orbit shape

It is clear in Figure 3-28 that *bT* and *bv* is always larger than 1 and *bμ* is always less than 1. It means that, comparing with the response under unidirectional excitations, the temperature and velocity of the bearing under bidirectional excitations will be higher and the friction coefficient will be smaller. More specifically, it can be seen from Figure 3-28 (a) that, from unidirectional to bidirectional analysis, as the PGV becomes larger, the

value of bT increase rapidly when PGV is less than 0.5 m/s and decease slowly when PGV is larger than 0.5 m/s. The temperature is magnified by an average value of 1.23 times when PGV equals 0.25m/s, 1.34 times when PGV equals 0.5m/s, 1.32 times when PGV equals 0.75m/s and 1.28 times when PGV equals 1m/s. Figure 3-28 (b) shows that the velocity amplification is around 1.31 and it shows no clear connection to PGV. While Figure 3-28 (c) shows that, basically, the larger the PGV the more the friction coefficient will be minified. The friction coefficient is reduced by an average value of 0.99 times when PGV equals 0.25m/s, 0.95 times when PGV equals 0.5m/s and 0.93 times when PGV equals 0.75m/s and 1m/s. Also, it can be noticed that large difference exists between each earthquake in Figure 3-28 (a) and (c). This difference is caused by the second component and coupled behavior of the ground motion pair. Since the shape of the response orbit can partly reflect this factor, whether the circular degree factor C can be used to show the effect of it on $b\mu$ is further studied by plotting the relations between $b\mu$ and C, as shown in Figure 3-28 (d). However, $b\mu$ shows no clear connection to C. Based on previous study, second component and the coupled behavior are quite random for different earthquakes and can be considered by the classification of earthquake ground motions according to intensity, distance-to-fault and site condition [3-14]. In this study, the influence of temperature change will be the main focus and the influence of second component and the coupled behavior will only be calculated according to the selected earthquakes as a reference.

3.6 Mechanism of how the temperature change under bidirectional excitations affects the maximum displacement

To study the difference of the maximum displacement of DCFP bearings between bidirectional and unidirectional response, the comparison of the response time history under unidirectional and bidirectional NCC excitations (the PGV of the C1 components are amplified as 750 mm/s) is shown in Figure 3-29. When the maximum displacement occurs, the value of friction coefficient during this displacement pulse determines the magnitude of the maximum displacement. For easier comparison of the parameters, the first peak friction coefficient after the maximum displacement and the first peak temperature increase before the maximum displacement were selected. Where d_{1D} is the maximum displacement under unidirectional excitation, ΔT_{1D} and ΔT_{2D} are the corresponding peak temperature increase under unidirectional excitation and bidirectional excitation respectively, and μ_{1D} and μ_{2D} are corresponding peak friction coefficient under unidirectional and bidirectional excitation respectively. t_s is the duration of the strong motion and Δt_s is the duration of strong motion before d_{1D}.
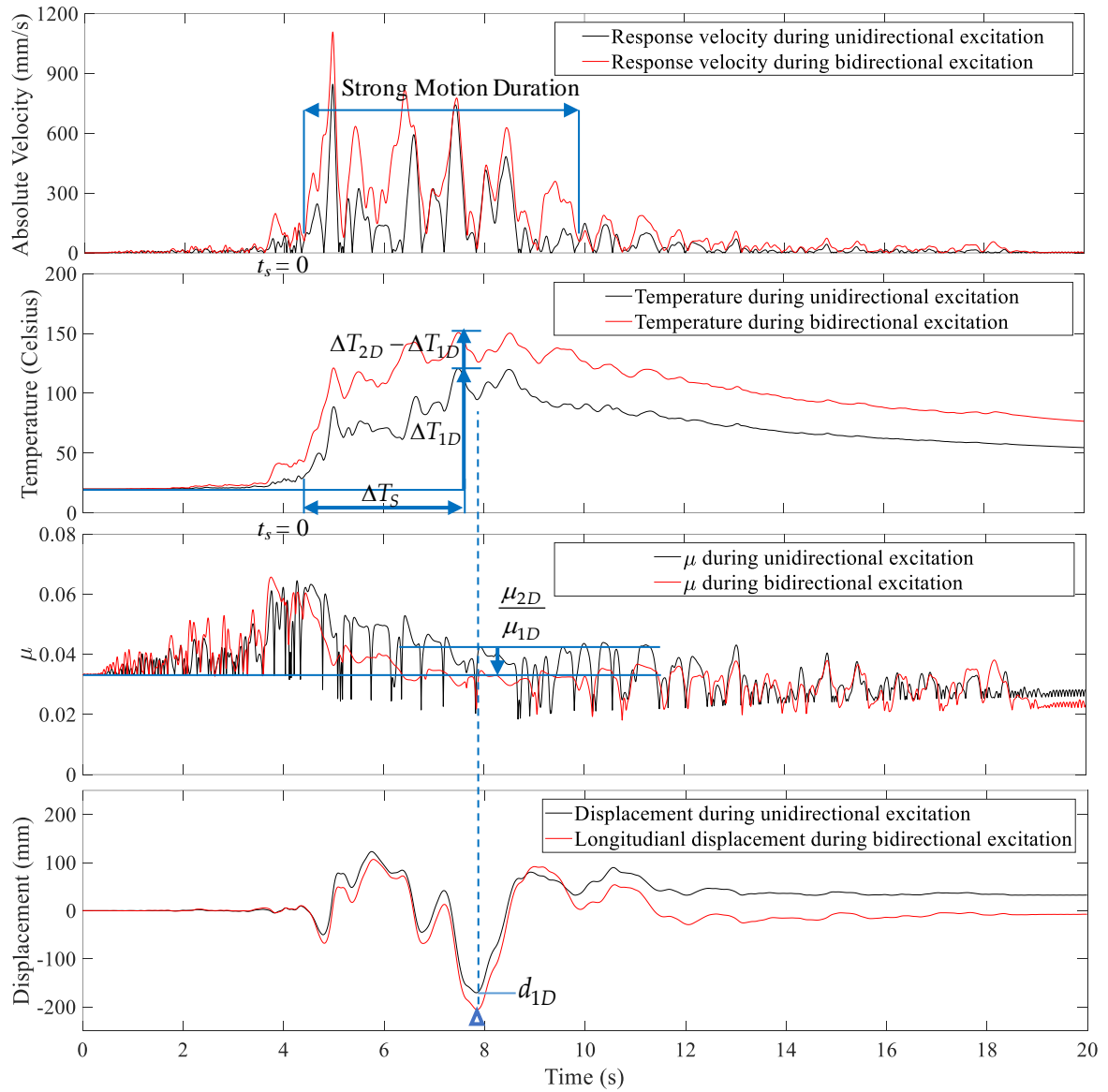
Figure 3-29. Time history of the response of DCFP bearing under NCC input (PGV=750 mm/s)

### 3.6.1 Influence of the ground velocity history on the temperature change

Based on Equation (3-6), by assuming the friction coefficient as the nominal value μ_n, the value of pressure as a constant value P, and the velocity during the strong motion duration shown in Figure 3-29 as a constant value $a_s \times PGV$. Then, the instantaneous heat flux during the strong motion duration can be estimated as:

$$q(t) = \mu(t) \times p(t) \times \frac{v(t)}{2} = \mu_n \times P \times \frac{a_s \times PGV}{2} \tag{3-23}$$

As shown in Figure 3-29, the strong motion duration before the maximum displacement is assumed as Δt_s. Then, as the energy absorption before the strong motion duration is relatively small, the energy absorption before the strong motion duration is neglected, and temperature change is calculated from the starting time of the strong motion duration ($t_s = 0$). Therefore, the regression model of ΔT_{1D} can be determined based on Equation (3-5) as:

$$\Delta T_{1D} = \frac{\sqrt{D}}{k\sqrt{\pi}} \int_0^{\Delta t_S} \frac{\mu_n \times P \times \dfrac{a_S \times PGV}{2}}{\sqrt{\tau}} d\tau = \frac{\sqrt{D}}{k\sqrt{\pi}} \times \mu_n \times P \times a_S \times PGV \times \sqrt{\Delta t_S} \tag{3-24}$$

where $d\tau$ is the time interval of the strong motion duration. The analytical data of ΔT_{1D} is shown in Figure 3-30, in which Spec. M is applied, μ_n is set as 0.043, and P is selected as 60 Mpa. Using LSM method, the value of $a_s \times \sqrt{\Delta t_s}$ was determined as 0.78, where the value 0.78 can only represent this selected group of ground motions. In Figure 3-30, the coefficient of correlation (R) of the data is 0.87, and the coefficient of determination (R^2) of the trend line is 0.75.
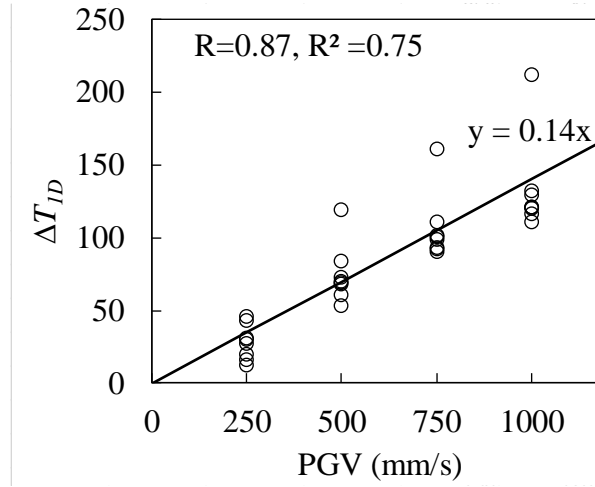
Figure 3-30. Relation between ΔT_{1D} and PGV

3.6.2 Influence of the addtion of the second earthquake component on the temperature change

Further, based on Equation (3-5), ΔT_{2D} - ΔT_{1D} can be expressed as:

$$\Delta T_{2D}(t) - \Delta T_{1D}(t) = \frac{\sqrt{D}}{k\sqrt{\pi}} \int_0^t \frac{[q_{2D}(t-\tau) - q_{1D}(t-\tau)]d\tau}{\sqrt{\tau}} \tag{3-25}$$

It is assumed that the response velocity of the bearing under bidirectional (v_{2D}) and unidirectional excitations (v_{1D}) are linear correlated as $v_{2D}(t) = a_2v_{1D}(t) + b_2$, where a_2 is the slope and b_2 is the interval. Then,

$$q_{2D}(t) - q_{1D}(t) = \mu(t)p(t)\frac{(a_2-1)v_{1D}(t)+b_2}{2} = (a_2-1)q_{1D}(t) + \frac{b_2\mu(t)p(t)}{2} \tag{3-26}$$

On substituting Equation (3-26) into Equation (3-25), the following regression model is obtained:

$$\begin{aligned}\Delta T_{2D}(t) - \Delta T_{1D}(t) \quad &= \frac{\sqrt{D}}{k\sqrt{\pi}} \int_0^t \frac{((a_2-1)q_{1D}(t-\tau) + \frac{b_2\mu(t)p(t)}{2})d\tau}{\sqrt{\tau}} \\ &= (a_2-1)\Delta T_{1D}(t) + \frac{\sqrt{D}}{k\sqrt{\pi}}b_2\mu(t)p(t)\sqrt{t}\end{aligned} \tag{3-27}$$

118

During the duration of strong motion before the maximum displacement, by assuming the friction coefficient and the pressure as constant, the regression model of ΔT_{2D} - ΔT_{1D} can be derived from Equation (3-27) as:

$$\Delta T_{2D}(t) - \Delta T_{1D}(t) = (a_2 - 1)\Delta T_{1D}(t) + c_2 \tag{3-28}$$

Where, c_2 is the value of the last item in Equation (3-27). The analytical data of ΔT_{2D} - ΔT_{1D} and ΔT_{1D} are shown in Figure 3-31. Using LSM method, a_2 and c_2 was determined as 1.10 and 13 respectively for this group of ground motions. In Figure 3-31, R is 0.46, and R^2 is 0.21, which means that there is no strong linear correlation between ΔT_{2D} - ΔT_{1D} and ΔT_{1D}, and the regression model does not match the data well. This is because the magnitude of the velocity of the second component is very random, which cause the value of v_{2D} cannot be accurately predicted from v_{1D}. However, a general trend can be simulated. For further validation of the availability of this regression model, it will be discussed under other real earthquake excitations in the next section.
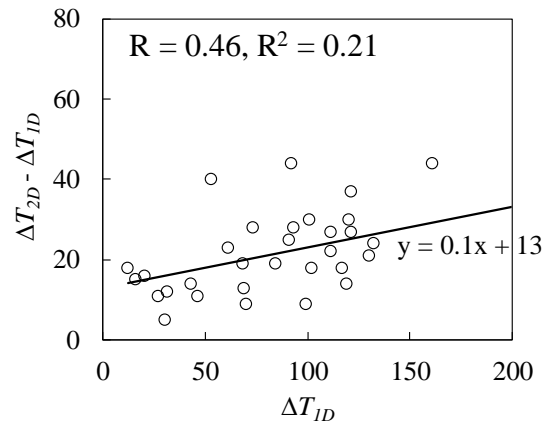

Figure 3-31. Relation between ΔT_{2D} - ΔT_{1D} and ΔT_{1D}

3.6.3 Influence of temperature change on the change of friction coefficient

Further, based on Equation (3-7) and Equation (3-10), as the temperature is the overall dominant dependency of friction validated in Section 3.5.3, μ_{2D} / μ_{1D} can be expressed as:

$$\frac{\mu_{2D}}{\mu_{1D}} = \frac{\beta_{2D}}{\beta_{1D}} = \frac{e^{-0.007T_{2D}}}{e^{-0.007T_{1D}}} = e^{-0.007(\Delta T_{2D} - \Delta T_{1D})} \tag{3-29}$$

The analytical data of μ_{2D} / μ_{1D} and $\Delta T_{2D} - \Delta T_{1D}$ are shown in Figure 3-32. The prediction result is closely in agreement with the experimental data.
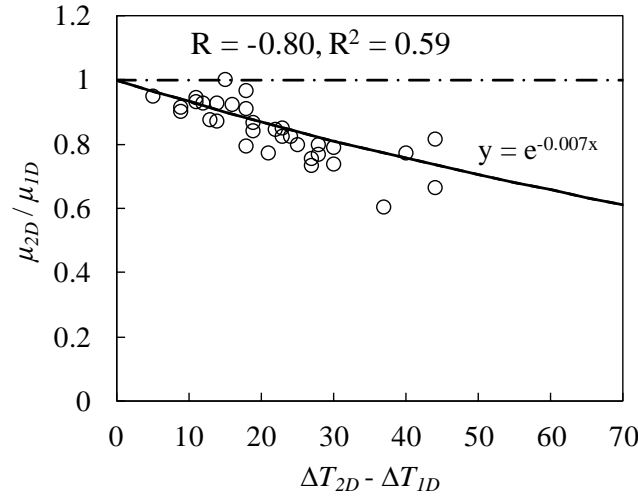
Figure 3-32. Relation between μ_{2D} / μ_{1D} and $\Delta T_{2D} - \Delta T_{1D}$

Then, on substituting Equations (3-23) and (3-28) into Equation (3-29), μ_{2D} / μ_{1D} can be expressed as:

$$\frac{\mu_{2D}}{\mu_{1D}} = e^{-0.007 \times \left((a_2 - 1) \times a_s \times \sqrt{\Delta t_s} \times \frac{\sqrt{D}}{k\sqrt{\pi}} \times \mu_n \times P \times PGV + c_2 \right)} \tag{3-30}$$

In this study, μ_{1D} can be considered as μ_n, which equals 0.043 for Spec. M. And Equation (3-30) shows how μ_n should be modified under bidirectional excitations.

3.6.4 Influence of the change of friction coefficient on the maximum displacement

On combining Equations (3-19) and (3-30), existing prediction methods of the unidirectional maximum displacement can be refined to provide a rough estimation on the maximum displacement under corresponding ground motion pairs. For instance, based on a previous study [3-3] on the energy-based prediction of the displacement under unidirectional excitation, the maximum response displacement under the C1 component (d_{1D}) can be conservatively predicted directly through PGV, as the line shown in Figure 3-33 (a) [3-3]. The markers are the analysis value of d_{1D} under the selected group of ground motions in this study. Further, based on Equations (3-19) and (3-30), the maximum bidirectional response displacement (d_{2D}) under the corresponding ground motion pairs can be predicted using μ_{1D} or μ_{2D}, shown in Figure 3-33 (b) as the dashed line and the solid line respectively. The markers are the analysis value of d_{2D} under the same group of scaled ground motions. It is evident that using μ_{1D} is no longer as conservative for predicting d_{2D} as for predicting d_{1D}. In contrast, the bidirectional prediction method using μ_{2D} can be considered to be relatively conservative. It further implies that, except for the effect of the bidirectional effect and the coupling behavior, the change of friction coefficient by considering temperature dependency also has major influence on the maximum response displacement of the DCFP bearing under bidirectional excitations.
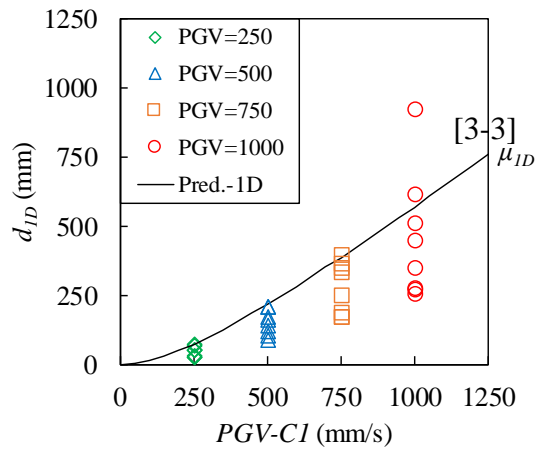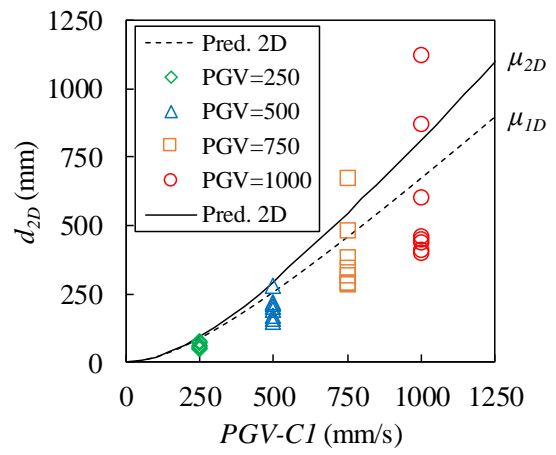
(a) Unidirectional excitation (b) Bidirectional excitation

Figure 3-33. Influence of the change of friction coefficient on the maximum displacement

3.7 Influence of characteristic parameters of ground motions and base isolation systems on the response increase from 1D to 2D

It has been concluded from Section 3.5.3 that the influence of velocity dependency on the displacement increase from unidirectional to bidirectional excitations (η_V) is negligible, especially when the maximum displacement is larger than 200mm. While, the temperature dependency (η_T), the bidirectional effect (η_0) and the coupled behavior (η_C) have major effect on the displacement increase. Further, the regression equations introduced in Chapter 3.6 illustrate the mechanism of how the temperature change caused by bidirectional excitations affect friction coefficient and in turn affect the maximum displacement. However, similar as the fact that the effect of the bidirectional effect and the coupling behavior on the maximum displacement is related to the characteristics of ground motions (GMs) [3-14] and the characteristics of the base isolation systems (BISs), the effect of temperature dependency may also be highly related to the selection of GMs and BISs. Therefore, the influence of temperature dependency on the maximum displacement under bidirectional motions will be discussed under various GM classifications and BISs in this Chapter.

3.7.1 Ground motion classification

Strong ground motions were considered to study the increase of the maximum displacement. Two basic filters were set during the selection of the ground motions: First, the moment magnitude of the earthquake (Mag.) should be larger than 6.5. Second, the peak ground velocity of ground motions should be larger than 200mm/s.

Based on these filters, 386 GM pairs were selected from PEER earthquake data base [3-21], and the distribution of them on different earthquake characteristics is shown in

Figure 3-34. Figure 3-34 (a) is organized by fault mechanism. SS is the abbreviation of strike-slip, N and R represent normal type and reverse type of dip-slip respectively. The number in the parentheses is the number of ground motions contained in the categories. Figure 3-34 (b) is organized by the moment magnitude of earthquakes. Figure 3-34 (c) is organized by the distance of the construction site to fault. NF, SD, and LD are the abbreviations of near fault ($R_{jb} \leq 10km$), small distance ($10km < R_{jb} \leq 30km$), and long distance ($30km < R_{jb}$) respectively, where R_{jb} is the Joyner-Boore distance to rupture plane. Figure 3-34 (d) is organized by the soil type of the construction site. A, B, C, and D are the classification of site condition based on NEHRP [3-12]. Where, class A & B represent firm and hard rock with V_{S30} (the average shear velocity of top 30 m of the site soil) larger than 760m/s, class C represent dense soil and soft rock with V_{S30} between 360 and 760 m/s, class D represent stiff soil with V_{S30} between 180 and 360 m/s.

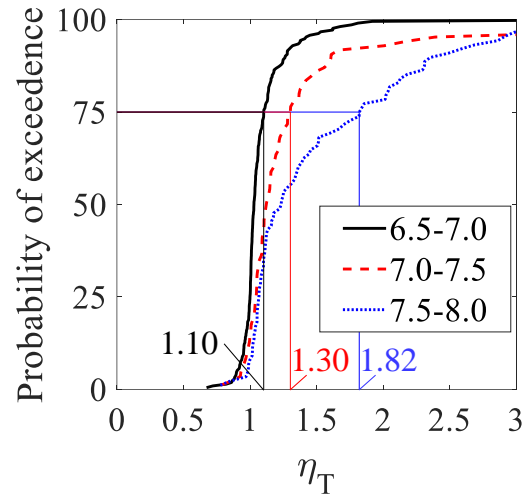(a) Mechanism (b) Magnitude

(c) Distance to fault (d) Soil type
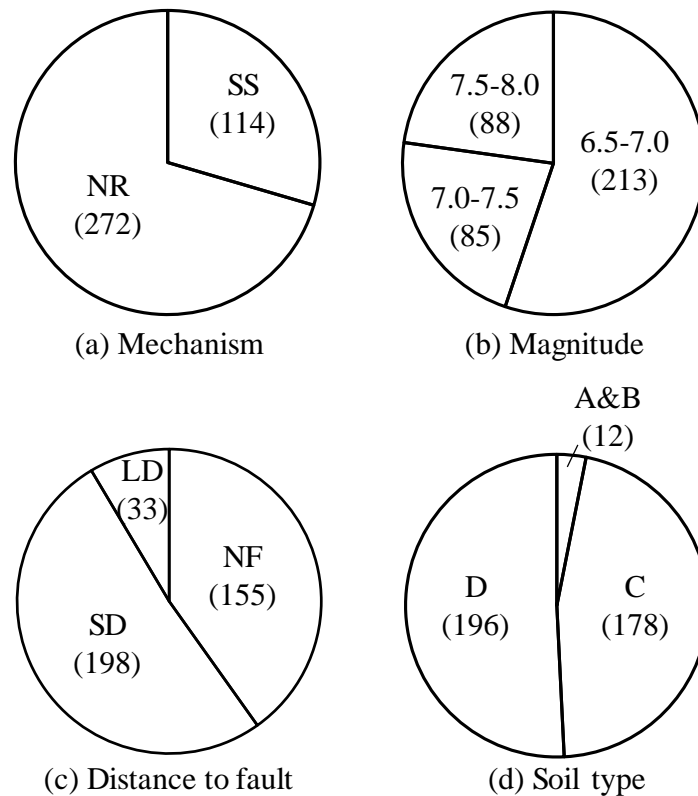
Figure 3-34. Characteristic parameters of GMs

### 3.7.2 Influence of earthquake characteristics on η_T

According to Equation (3-18), the contribution of the change in temperature dependency caused by the addition of the C2 component on the increase of the maximum response displacement (η_T) can be calculated for the selected earthquakes under different classifications as shown in Figure 3-34. Same as that in Section 3.5 and 3.6, a DCFP bearing with μ_n equals 0.043, slider diameter equals 400mm, and the radius of curvature equals 4500mm is applied in the analysis. Then, the cumulative distribution of η_T for various earthquake classifications is shown in Figure 3-35. In the figure, a relatively conservative percentage, 75% is selected for comparison. The value of η_T corresponding to 75% means that there is 25% possibility that the real result is larger than this value. Figure 3-35 (a) implies that the mechanism of the earthquake has no obvious influence on η_T. The value at 75% is around 1.22. However, when the magnitude of the earthquake increase, the influence of temperature dependency on the maximum bidirectional displacement will apparently increase, as shown in Figure 3-35 (b). The value of η_T is 1.30 for ground motions with earthquake magnitude between 7.0 and 7.5 and arrives 1.82 when the magnitude increase over 7.5. Also, η_T will be relatively larger under small distance to fault rather than near fault and long distance based on Figure 3-35 (c), whose value at 75% will arrive at 1.34. As for the soil type shown in Figure 3-35 (d), the softer the construction soil, the larger value of η_T will be, but the difference is not significant. Based on Figure 3-35, it can be concluded that earthquake characteristics will significantly affect the value of η_T, therefore, it should be considered under simulations. In specific, the value of η_T will be significantly increased under large earthquake magnitude (>7.0) and small distance to fault (10km < $R_{jb} \leq$ 30km).
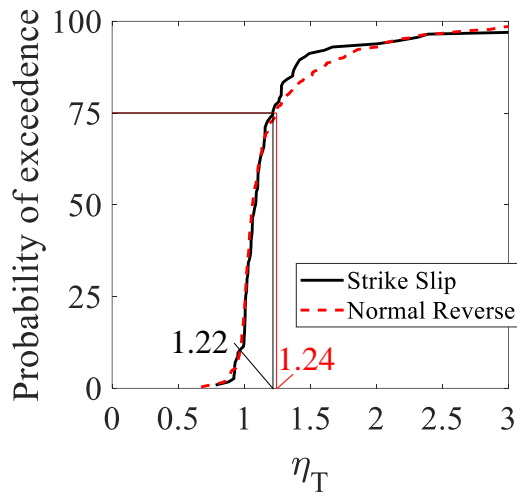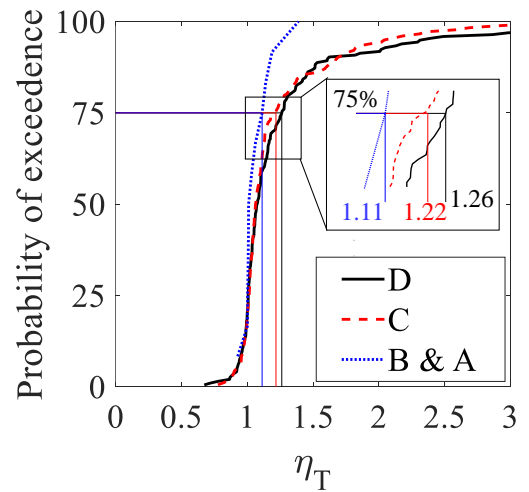
(a) Earthquake mechanism

(b) Magnitude
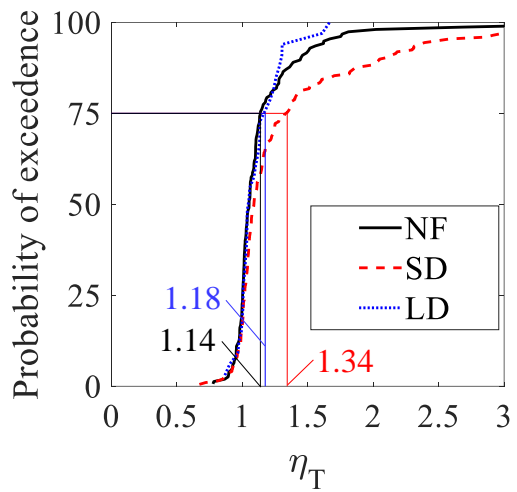
(c) Distance to fault

(d) Soil type of the site

Figure 3-35. Correlation between the characteristic parameters of GMs and η_T

To see the value of the probability of exceedance at various percentage clearly, box figures were introduced as shown in Figure 3-36. The value of 5th, 25th, 50th, 75th, and 95th percentile of the contribution is marked in this figure.
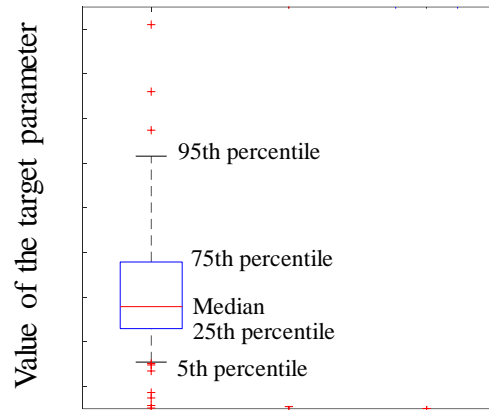
Figure 3-36. Definition of the box figure

Then, Figure 3-35 is plot in form of the box figure as shown in Figure 3-37.

(a) Earthquake mechanism

(b) Magnitude

(c) Distance to fault

(d) Soil type of the site
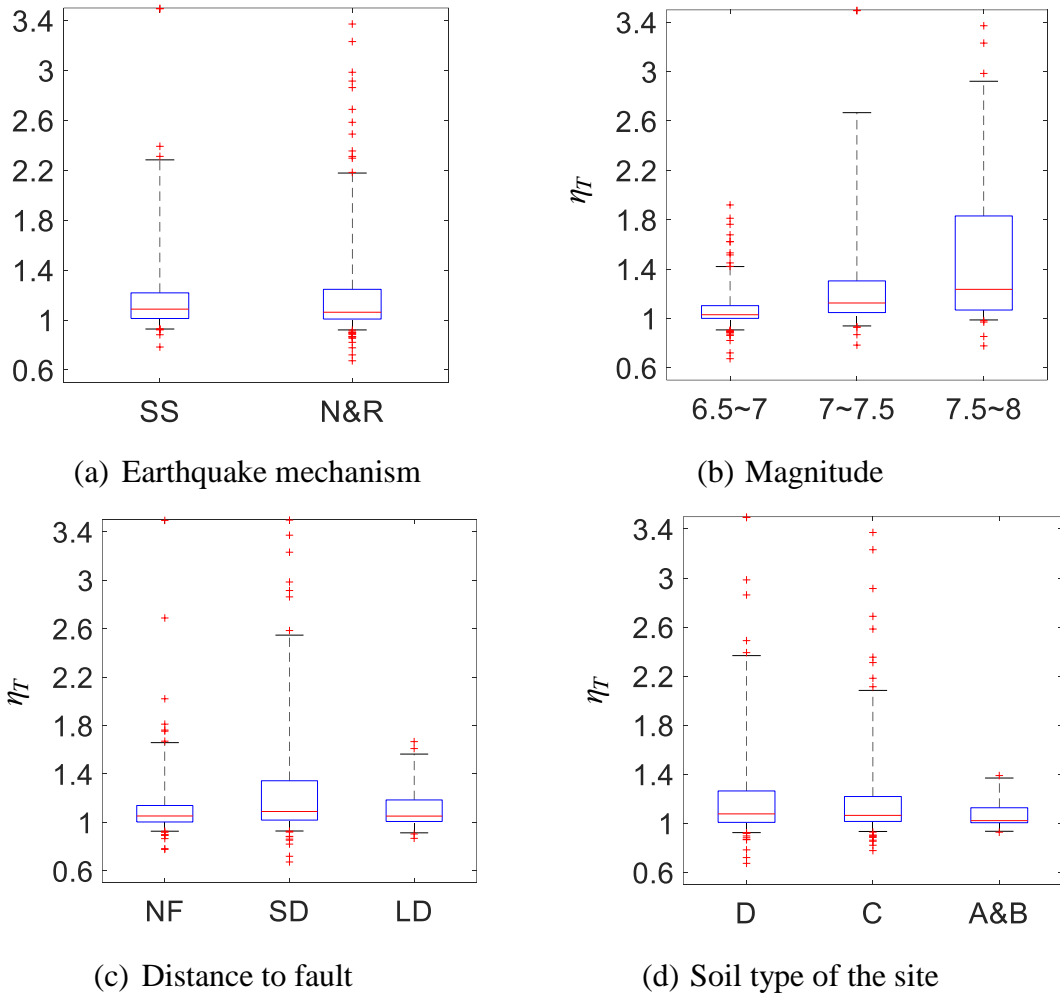
Figure 3-37. Correlation between the characteristic parameters of GMs and η_T

### 3.7.3 Influence of earthquake characteristics on $\eta_0 * \eta_c$

The cumulative distribution of $\eta_0 * \eta_c$ for various earthquake classifications is shown in Figure 3-38. In the figure, the value of $\eta_0 * \eta_c$ corresponding to 75% means that there is 25% possibility that the real result is larger than this value. Figure 3-38 (a) and (b) implies that the mechanism and magnitude of the earthquake has no obvious influence on $\eta_0 * \eta_c$. The value at 75% is all around 1.4. However, $\eta_0 * \eta_c$ will increase with the increase of the distance to fault and arrive at around 1.6 (75%) under GMs with long distance to fault ($R_{jb} > 30km$). As for the soil type shown in Figure 3-38 (d), the softer the construction soil, the larger value of $\eta_0 * \eta_c$ will be, but the difference is not significant. Based on Figure 3-38, it can be concluded that earthquake characteristics have no large influence on the value of $\eta_0 * \eta_c$. The value of $\eta_0 * \eta_c$ can be considered as around 1.4 (75%) for most GMs for the DCFP bearing with μ_n equals 0.043, slider diameter equals 400mm, and the radius of curvature equals 4500mm. However, for GMs with long distance to fault ($R_{jb} > 30km$), the value of $\eta_0 * \eta_c$ will be around 1.6 (75%).

(a) Earthquake mechanism

(b) Magnitude

(c) Distance to fault

(d) Soil type of the site
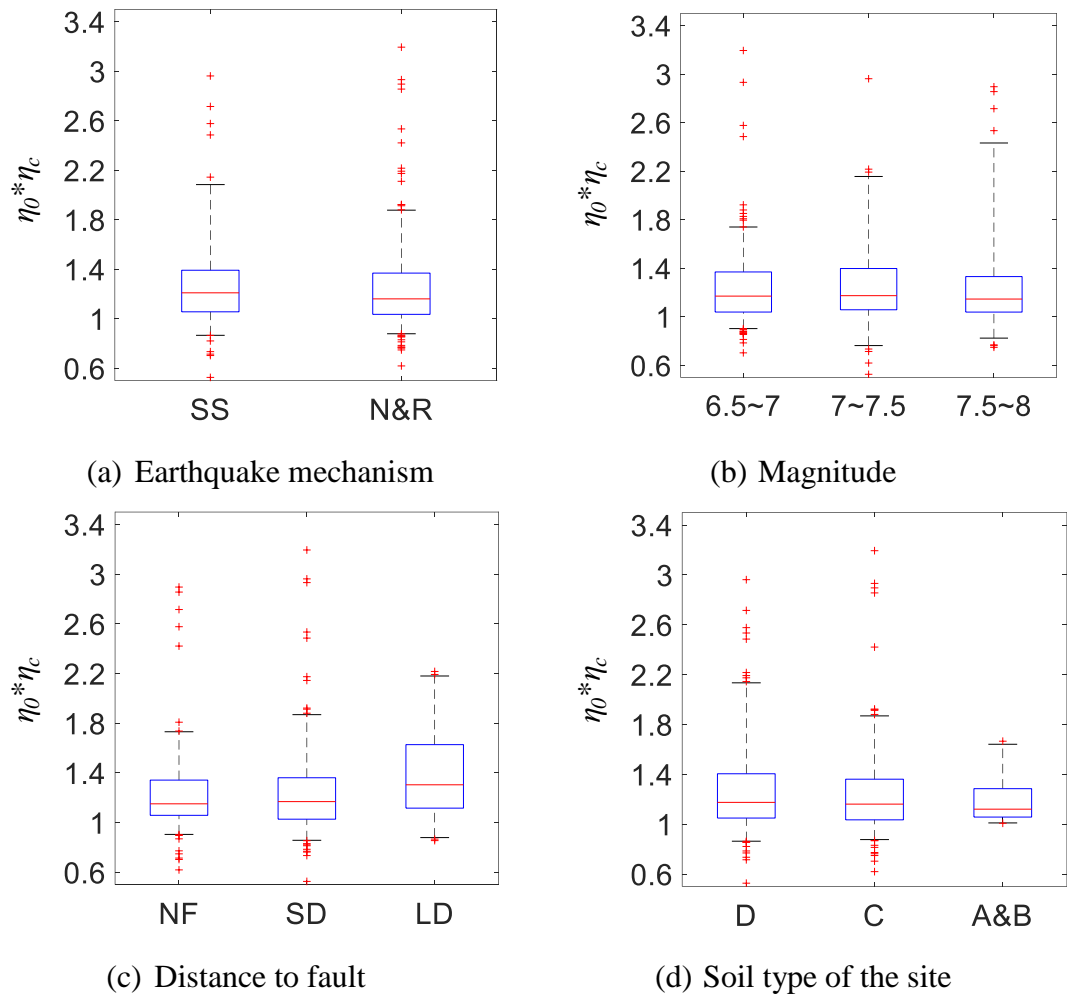
Figure 3-38. Correlation between the characteristic parameters of GMs and $\eta_0 * \eta_c$

3.7.4 Influence of peak ground velocity on $\eta_0 * \eta_c$ and η_T

The peak ground velocity (PGV) of the GM is determined by the earthquake characteristics introduced in Section 3.7.1, which are the earthquake mechanism, magnitude of the earthquake, distance of the construction site to the fault, and the soil condition of the construction site. The influence of PGV on $\eta_0 * \eta_c$ and η_T is shown in Figure 3-39. It can be seen from Figure 3-39 (a) that, for the considered DCFP bearing, the larger the PGV, the smaller the value of $\eta_0 * \eta_c$. When the PGV is smaller than 1000mm/s, the value of $\eta_0 * \eta_c$ is normal as around 1.4 (75%). However, when the PGV is larger than 1000mm/s, the value of $\eta_0 * \eta_c$ will decrease to around 1.2 (75%). On the other hand, Figure 3-39 (b) shows that the value of η_T is normal as around 1.2 (75%) when PGV is between 200 and 500 mm/s. However, η_T will be significantly increased to around 1.4 (75%) when PGV is between 500 and 1000 mm/s and significantly decrease to around 1 (75%) when PGV is larger than 1000 mm/s.

(a) Cumulative distribution of $\eta_0 * \eta_C$ (b) Cumulative distribution of η_T
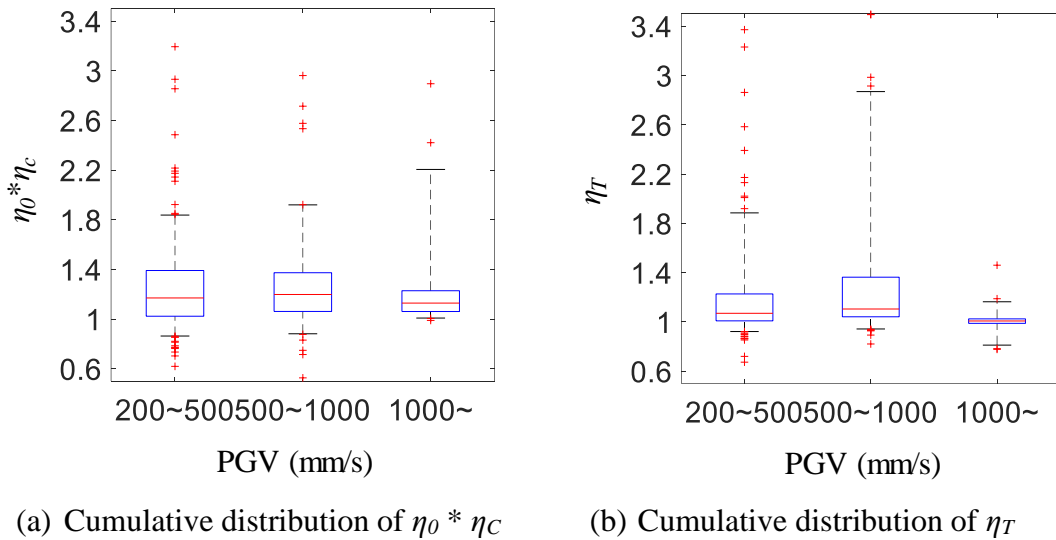
Figure 3-39. Correlation between PGV (mm/s) of GMs and $\eta_0 * \eta_c$ and η_T

3.7.5 Parameters of base isolation systems

The selected parameters of BIS and their range is shown in Table 3-5, where μ_0 is the friction coefficient at 60 N/mm^2, 400 mm/s and an initial atmosphere temperature of around 20 ˚C, T_r is the returning period of the BIS, R_S is the radii of the curvature of the concave plate, and φ is the diameter of the slider. Then, "IS-μ_0-T_r-φ" can refer to a certain BIS. φ is considered because it will affect the temperature at the contact surface of the slider and the concave plates and further affect the friction coefficient. Section 3.7.2 ~ 3.7.4 are all discussed under IS-0.075-6-400.

Table 3-5. Parameters of BISs

μ_0	T_r (s) / R_S (mm)	φ (mm)
0.015	4 / 2000	200
0.075	6 / 4500	400
0.135	8 / 8000	600

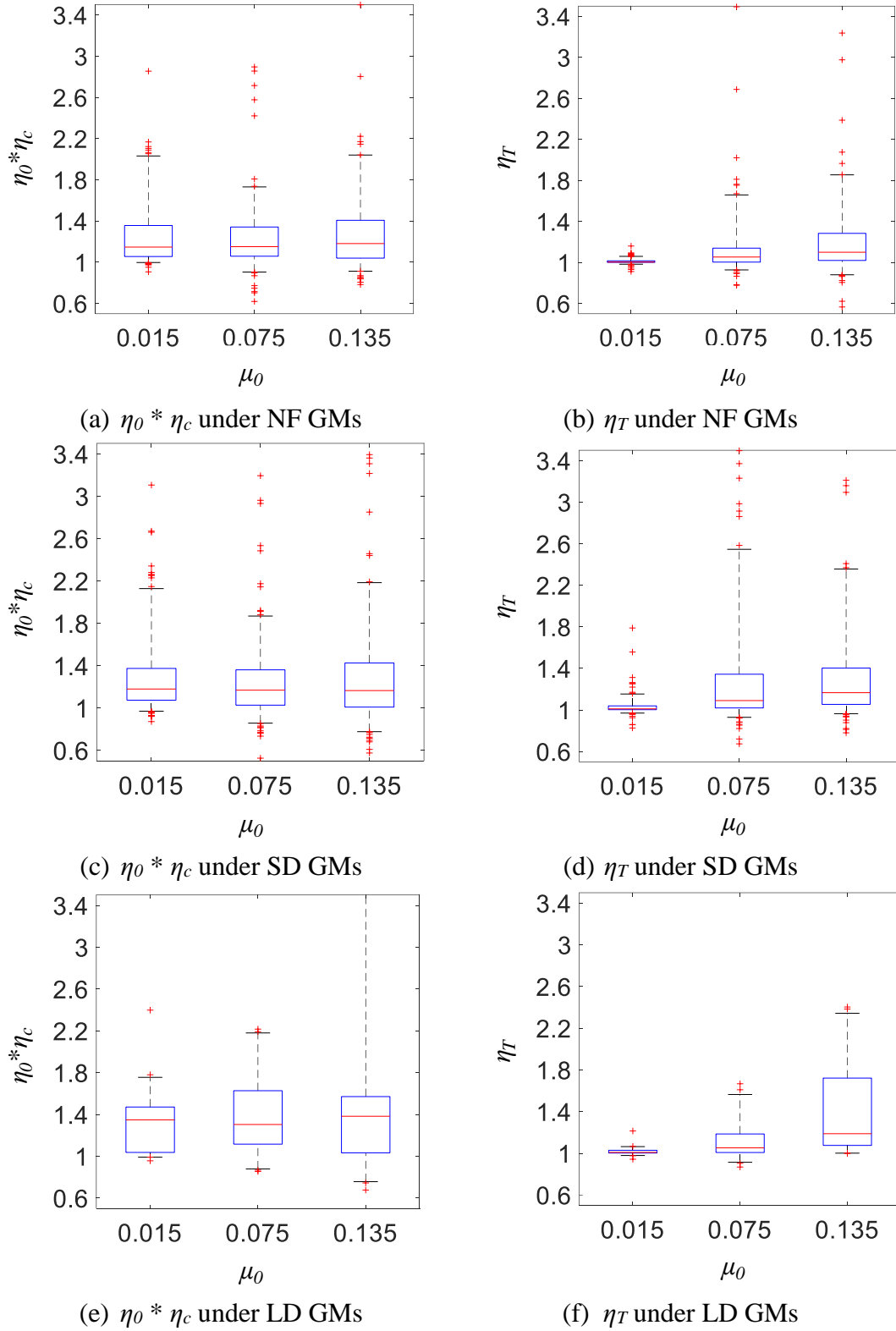### 3.7.6 Influence of friction coefficient (μ_0) on $\eta_0 * \eta_c$ and η_T

IS-0.015-6-400, IS-0.075-6-400, and IS-0.135-6-400 were considered in this section to study the influence of friction coefficient (μ_0) on the cumulative distribution of $\eta_0 * \eta_c$ and η_T under various GMs classified by distance to fault as shown in Figure 3-40. It can be seen that, under various distance to fault, the value of $\eta_0 * \eta_c$ will not change significantly under different value of friction coefficients. However, the value of η_T is highly related to the value of the friction coefficient. With the increase of the friction coefficient, the value of η_T will also increase significantly regardless of the distance to fault.

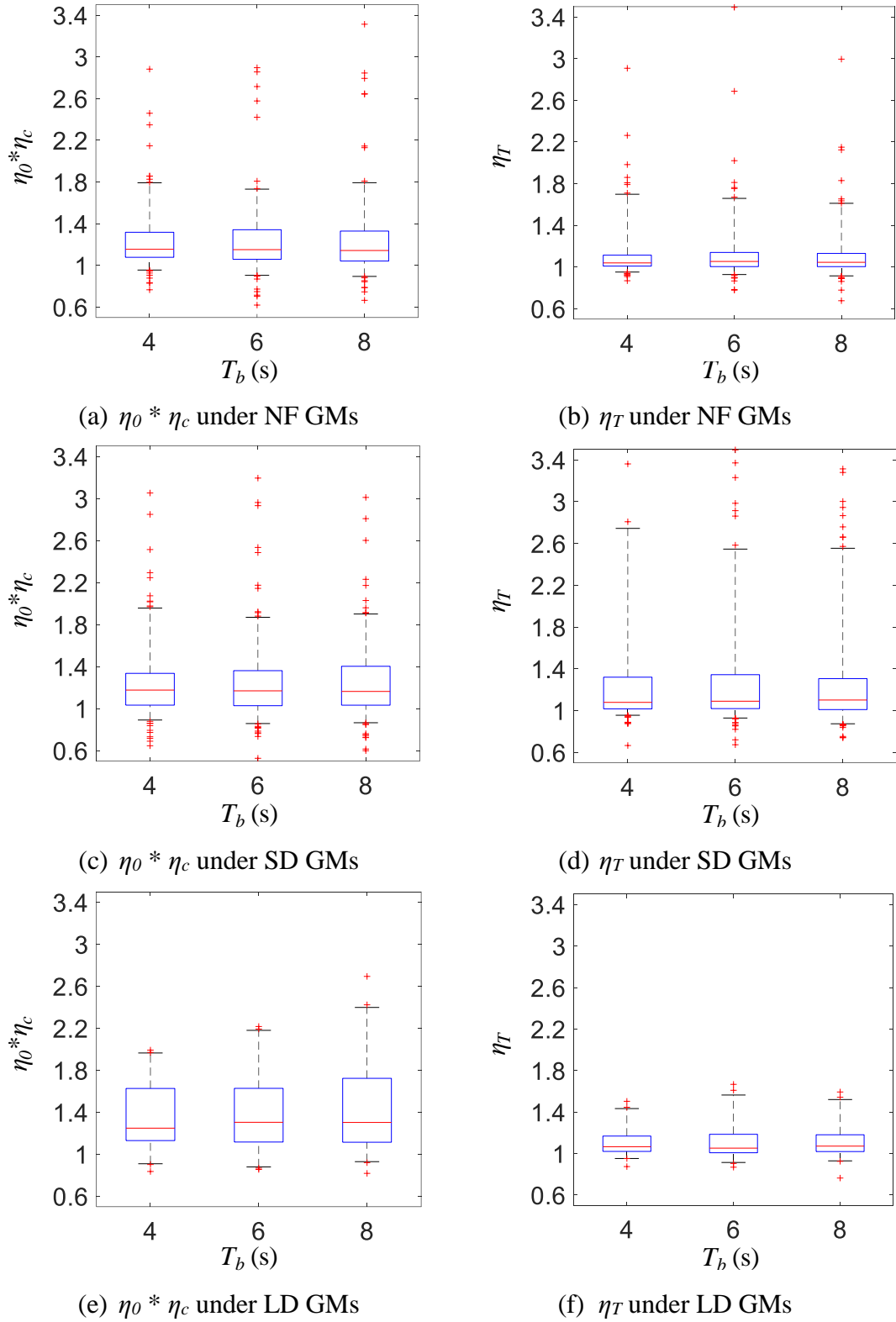### 3.7.7 Influence of natural period of the BIS (T_r) on $\eta_0 * \eta_c$ and η_T

IS-0.075-4-400, IS-0.075-6-400, and IS-0.075-8-400 were considered in this section to study the influence of natural period of the BIS, T_b (s), on the cumulative distribution of $\eta_0 * \eta_c$ and η_T under various GMs classified by distance to fault as shown in Figure 3-41. It can be seen that, regardless of distance to fault, both $\eta_0 * \eta_c$ and η_T will not change significantly under various T_b.

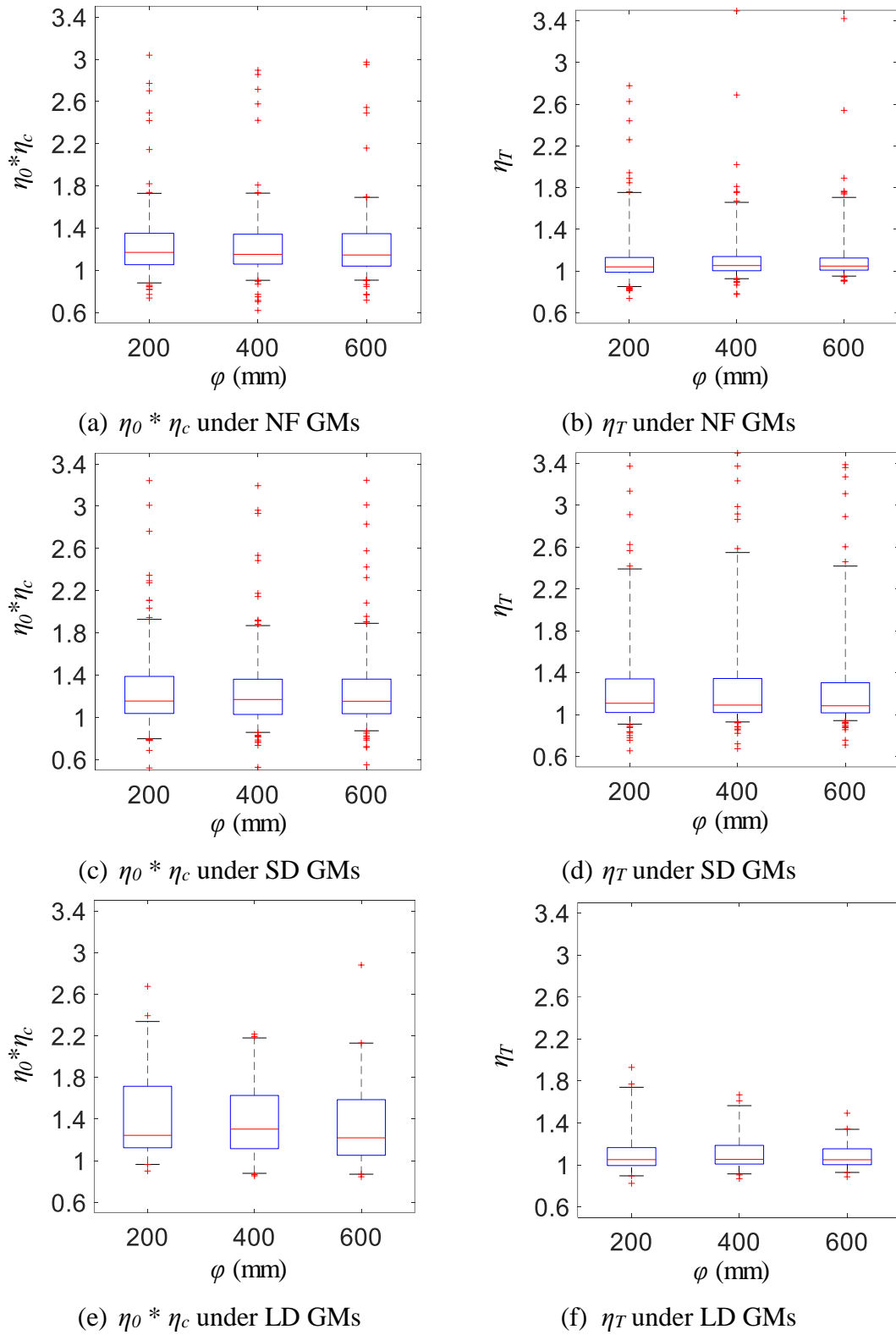### 3.7.8 Influence of slider diameter (φ) on $\eta_0 * \eta_c$ and η_T

IS-0.075-6-200, IS-0.075-6-400, and IS-0.075-6-600 were considered in this section to study the influence of slider diameter, φ (mm), on the cumulative distribution of $\eta_0 * \eta_c$ and η_T under various GMs classified by distance to fault as shown in Figure 3-42. It can be seen that, regardless of distance to fault, both $\eta_0 * \eta_c$ and η_T will not change significantly under various φ.

Figure 3-40. Influence of friction coefficient (μ_0) on the cumulative distribution of η_0 * η_c and η_T under various GMs classified by distance to fault

(a) $\eta_0 * \eta_c$ under NF GMs

(b) η_T under NF GMs

(c) $\eta_0 * \eta_c$ under SD GMs

(d) η_T under SD GMs

(e) $\eta_0 * \eta_c$ under LD GMs

(f) η_T under LD GMs

Figure 3-41. Influence of natural period of the BIS, T_b (s), on the cumulative distribution

of $\eta_0 * \eta_c$ and η_T under various GMs classified by distance to fault

(a) $\eta_0 * \eta_c$ under NF GMs

(b) η_T under NF GMs

(c) $\eta_0 * \eta_c$ under SD GMs

(d) η_T under SD GMs

(e) $\eta_0 * \eta_c$ under LD GMs

(f) η_T under LD GMs

Figure 3-42. Influence of Slider diameter, φ (mm), on the cumulative distribution of $\eta_0 *$ η_c and η_T under various GMs classified by distance to fault

135

3.8 Conclusions

To further understand the behavior of FPBs and validate the credibility of friction dependencies under real earthquakes, the velocity and temperature dependencies were combined in friction models and further validated by full-scale dynamic tests under multidirectional artificial graphics and earthquake response orbits. It was found that large force pulses that break out the conventional bilinear force-displacement relation may occur for the cases under response orbits compared to that under artificial graphics. These pulses are caused by rapidly increases of the velocity, which will cause high velocity and low temperature happened simultaneously and lead to a large friction coefficient. In addition, we evaluated a friction model of DCFP bearings using an appropriate constant friction coefficient (nominal friction coefficient) which considers the effect of temperature dependency under strong GMs as a constant, a bidirectional precise model that considers pressure, velocity, and temperature dependencies of the friction, and a simplified model. It was found that both the precise and simplified model can simulate the break-out force pulse. However, the constant friction coefficient cannot. Further, by comparing the simulation results of the precise model with the experimental results, it can be concluded that the proposed friction dependencies are still available under real-size specimen and real earthquakes.

Also, the accuracy of the friction models on simulating the response displacement were also discussed. It was found that regardless of friction types, strength of input waves, and shape of the response orbit, the simplified model is closely in agreement with the precise model for both response force and response displacement; thus, it can be used instead for faster calculation. Moreover, the simulation method using the nominal friction coefficient determined from unidirectional experiments slightly overestimated the

maximum response force and underestimated the maximum response displacement under bidirectional ground motion pairs. It indicates that the constant value of the constant friction coefficient should be refined under bidirectional GMs.

To clarify the effect of the velocity and temperature change caused by the additional perpendicular excitation on the friction coefficient and further on the maximum response displacement, response analysis under one-component GMs and corresponding two-component GMs were conducted. It was found that, except for the bidirectional effect of the ground motion pair and coupled behavior, the displacement increase from unidirectional excitation to bidirectional excitation was mainly caused by the contribution of the temperature dependency. In contrast, the influence of velocity dependency was relatively negligible under strong ground motion pairs. The temperature dependency contributed an average of 1.1 times amplification to the increase of the maximum displacement for the selected group of ground motions, which is one-third of the total increase (the other two-third is contributed by the bidirectional effect and the coupling behaviour).

During the study of the internal mechanism of this displacement increase, it was found that the addition of the second component will lead to a larger temperature increase, and in turn a smaller friction coefficient and finally a larger response displacement.

As the fact that the effect of the bidirectional effect and the coupling behavior on the maximum displacement is highly related to the characteristics of ground motions and base isolation systems, how the influence of temperature change caused by the bidirectional effect on the maximum displacement is affected by various earthquake characteristics was further investigated under 386 two-component GMs. It was found that this influence is highly related to the magnitude of the earthquake and the distance to fault. This influence

will be significantly increased under large earthquake magnitude (>7.0) and small distance to fault (10km $<$ R$_{jb}$ $\leq$ 30km). Soft soil condition will increase the influence slightly, and no clear relation was found with the earthquake mechanisms. Moreover, the influence of temperature change caused by the bidirectional effect on the maximum displacement is also affected by the friction coefficient of base isolation system. With the increase of the friction coefficient, this influence will also increase significantly. However, this influence is not related to the natural period of the base isolation system and the diameter of the slider.

References.

[3-1].   Nakamura, H.; Nishimoto, K.; Hasegawa, H.; Nakamura, H. Predictive Method of a Temperature Rise and the Friction Coefficient of Spherical Sliding Bearing (Part 3), Paper No. 21232. AIJ, Kanto, Japan, 4–6 September 2015.

[3-2].   Nishimoto, K.; Nakamura, H.; Hasegawa, H.; Wakita, N. Bearing Stress and Velocity Dependency of Spherical Sliding Bearing through Full-scale tests, Paper No. 21223. AIJ, Fukuoka, Japan, 24–26 August 2016.

[3-3].   Li J, Kishiki S, Yamada S, Yamazaki S, Watanabe A, Terashima M. Energy-Based Prediction of the Displacement of DCFP Bearings. Appl Sci 2020;10:5259. http://dx.doi.org/10.3390/app10155259

[3-4].   Mokha A, Constantinou MC, Reinhorn AM. Verification of friction model of teflon bearings under triaxial load. J Struct Eng 1993;119(1):240–261. https://doi.org/10.1061/(ASCE)0733-9445(1993)119:1(240)

[3-5].   Mosqueda G, Whittaker A S, Fenves G L. Characterization and modeling of friction pendulum bearings subjected to multiple components of excitation. J Struct Eng 2004;130(3):433-442. https://doi.org/10.1061/(ASCE)0733-9445(2004)130:3(433)

[3-6].   Lomiento G, Bonessio N, Benzoni G. Concave sliding isolator's performance under multi-directional excitation. Ingegneria Sismica, 2013;30(3):17-32.

[3-7].   Quaglini V, Gandelli E, Dubini P, Vazzana G, Farina G. Re-centring capability of friction pendulum system: experimental investigation. In: Proceedings of the 2nd European conference on earthquake engineering and seismology. Istanbul, TK; 2014.

[3-8]. De Domenico, D., G. Ricciardi, and G. Benzoni. "Analytical and finite element investigation on the thermo-mechanical coupled response of friction isolators under bidirectional excitation." Soil Dynamics and Earthquake Engineering 106 (2018): 131-147.

[3-9]. Furinghetti, M., Pavese, A., Quaglini, V., & Dubini, P. (2019). Experimental investigation of the cyclic response of double curved surface sliders subjected to radial and bidirectional sliding motions. Soil Dynamics and Earthquake Engineering, 117, 190-202.

[3-10]. ASCE/SEI 7-16. Minimum Design Loads and Associated Criteria for Buildings and Other Structures; American Society of Civil Engineers (ASCE): Reston, VA, USA, 2016.

[3-11]. Transportation Officials. AASHTO Guide for Design of Pavement Structures, 1993; Aashto.

[3-12]. General rules, Eurocode 8. Design provisions for earthquake resistance of structures; Part 1: seismic actions and rules for buildings. BS EN 1998-1; European Committee for Standardization, Brussels, Belgium, 2004.

[3-13]. Design Recommendations for Seismically Isolated Buildings; ISBN 978-4-8189-5000-9, Architectural Institute of Japan: Tokyo, Japan, 2016.

[3-14]. Warn G P, Whittaker A S. Performance estimates in seismically isolated bridge structures. Eng Struct, 2004;26(9):1261-1278.

[3-15]. Lomiento G, Bonessio N, Benzoni G. Concave sliding isolator's performance under multi-directional excitation. Ingegneria Sismica, 2013;30(3):17-32.

[3-16]. Kumar M, Whittaker AS, Constantinou MC. Characterizing friction in sliding isolation bearings. Earthq Eng Struct Dyn 2015;44:1409–1425. https://doi.org/10.1002/eqe.2524

[3-17]. Li Jiaxi, Nitawaki Masashi, Kishiki Shoichi, Ishida Takanori, Nishimoto Koji, Watanabe Atsushi and Yamada Satoshi, Analytical Study on Spherical Sliding Bearing (SSB) Subjected to Tri-directional Excitation ---- Effect of Bearing Stress and Velocity dependency of SSB on the response of isolation system, Summaries of Technical Papers of Annual Meeting, Architectural Institute of Japan, Paper No. 21490, Tohoku, Japan, 4-6 September 2018.

[3-18]. Jiaxi Li, S. Yamada, S. Kishiki, S. Yamazaki, A. Watanabe and M. Terashima, Experimental and numerical study of spherical sliding bearing (SSB) - part 3: seismic response, 17th World Conference on Earthquake Engineering, 17WCEE, Paper N° C000736, Session No. O01C01, Sendai, Japan, September 28th to October 2nd 2021.

[3-19]. Constantinou MC, Whittaker AS, Kalpakidis Y, Fenz DM, Warn GP. Performance of seismic isolation hardware under service and seismic loading. Multidisciplinary Center for Earthquake Engineering Research: Buffalo, NY, USA, 2007;Report No. MCEER-07-0012.

[3-20]. Benzoni G, Seible F, Design of the Caltrans Seismic Response Modification Device (SRMD) test facility (IWGFR–96). International Atomic Energy Agency (IAEA); International Working Group on Fast Reactors: Vienna, Austria, 1998; 325p, pp. 101–115.

[3-21]. PEER, https://ngawest2.berkeley.edu/; 2022/08/23

[3-22]. K-NET, https://www.kyoshin.bosai.go.jp/; 2022/08/23

[3-23]. Takanori I, Masashi N, Shoichi K. 21491 Experimental and Analytical Study on Spherical Sliding Bearing Subjected to Bidirectional Excitation Part 1 Bidirectional loading tests and verification of mechanical model. Architectural Institute of Japan, Construction II, 2018: 981-982.

[3-24]. Hideji N, Koji N, Atsushi T. 21241 Development of Spherical Sliding Bearing Resisting High Bearing Pressure (Part 1) [in Japanese]. Architectural Institute of Japan, Construction II 2014:481-482.

[3-25]. Koji N, Naoya W, Hasegawa K. 21479 Full-scale experiment of low-friction-type spherical sliding bearing on behavior confirmation [in Japanese]. Architectural Institute of Japan, Construction II, 2017: 957-958.

[3-26]. Japan Society of Mechanical Engineers (JSME), 2009. Heat Transfer, 5th edition, JSME Data Books, Tokyo, JP, 284-285.

[3-27]. Nakamura, H.; Nishimoto, K.; Hasegawa, H.; Nakamura, H. Predictive Method of a Temperature Rise and the Friction Coefficient of Spherical Sliding Bearing (Part 3), Paper No. 21232. AIJ, Kanto, Japan, 4–6 September 2015.

[3-28]. Nishimoto, K.; Nakamura, H.; Hasegawa, H.; Wakita, N. Bearing Stress and Velocity Dependency of Spherical Sliding Bearing through Full-scale tests, Paper No. 21223. AIJ, Fukuoka, Japan, 24–26 August 2016.

[3-29]. Kelly JM. Base isolation: linear theory and design. Earthq Spectra 1990;6(2):223–44. https://doi.org/10.1193%2F1.1585566

[3-30]. Bhagat S, Wijeyewickrema AC. Seismic response evaluation of base-isolated reinforced concrete buildings under bidirectional excitation. Earthq Eng Eng Vib 2017;16(2):365-382. https://doi.org/10.1007/s11803-017-0387-8

4. Response spectra of various DCFP bearings under various GM classifications

This chapter introduced the parametric study and preliminary design of DCFP systems under various ground motions.

4.1 Introduction

There are many parameters in simulating the earthquake response of a structure isolated by DCFP Bearings as shown in Table 4-1. Based on previous studies, parameters with the mark "*" are the major parameters that affect the response of the BIS and the superstructure. R.S. Jangid proposed that, in the design of a BIS, the selection of the friction coefficient of the FPB (μ) and the natural period of the BIS (T_b) is of vital importance [4-1]. Manish Kumar et al. demonstrate that the effects of changes in velocity and axial pressure on the friction coefficient are small and may not need to be included in a friction model. And the effect of temperature rise cannot be ignored [4-2]. The unidirectional and bidirectional analysis conducted in this study also implied that the temperature dependency should be carefully considered in the response analysis and the influence of velocity dependency on the earthquake response of the BIS can be neglected. Warn GP et al. proposed that the influence of bidirectional excitation and coupling on the maximum displacement cannot be ignored [4-3]. Midorikawa et al. proposed that the characteristics of ground motion is affected by the source characteristics (Magnitude and fault type of the earthquake), path (distance to fault), and site condition (Soil type) [4-4]. Jangid et al. and Providakis et al. demonstrate that the distance to fault of ground motions will affect the earthquake performance of BISs [4-5][4-6]. Also, in Section 3.7, it was concluded that, the magnitude of the earthquake and the distance to fault will affect the earthquake response of the BIS. Based on these studies, the major parameters which play

important roles in the earthquake response of DCFP bearings was clarified. To generate effective response spectra, BISs with various μ and T_b were considered, two-component ground motions were classified based on distance to fault and magnitude, and besides pressure and velocity dependencies, temperature dependency and coupling effect were also considered in the friction model. It should be mentioned that, the effect of temperature dependency and the magnitude of the earthquake were rarely considered in the previously proposed response spectra. In the existing studies of the response spectra of structures isolated with FPBs, the friction coefficient is always considered as constant and the earthquakes were generally classified by distance to fault [4-1][4-5]. Therefore, in this chapter, all the major parameters will be considered in conducting the response spectra. Further, how each major parameter affect the earthquake response will also be discussed.

Table 4-1 Major parameters in the earthquake response analysis of DCFP bearings

BIS	Analysis Model	Earthquake Selection
* μ (friction coefficient)	Pressure dependency	* Distance to fault
* T_b (Isolation Period)	Velocity dependency	* Magnitude
	* Temperature dependency	Soil type
	* Coupling effect	Fault type
	* Second Component	

* implies major parameters

4.2 Input ground motions

As the magnitude of the earthquake and the distance to fault are the major parameters that affect the earthquake response of a BIS, two-component ground motions were selected and classified based on these two parameters as five groups shown in Table 4-2 ~ 4-6. Where RSN is the Record Sequence Number in PEER [4-7]. Tp is the period of the velocity pulse, and no number is assigned for a non-pulse record. Station shows the unique name of strong-motion station. Mag. is the moment magnitude of earthquake. Mechanism is the type of fault mechanism. Rjb is the Joyner-Boore distance to rupture plane. In this study, GMs with Rjb less than 10km are defined as near-fault GMs, those with Rjb between 10km and 30km are defined as small distance GMs, and those with Rjb larger than 30km are defined as long distance GMs. V_{S30} is the average shear velocity of top 30m. PGA, PGV, and PGD are the peak ground acceleration, the peak ground velocity, and the peak ground displacement of the C1 component of the GM pair respectively.

Table 4-2. Near fault ground motions (less than 10km) with the magnitude of earthquake between 6.5 and 7.0 (Abv. NF65)

RSN	Tp (s)	Earthquake	Station	Mag.	Mechanism	Rjb (km)	V_{S30} (m/s)	PGA-C1 (m/s^2)	PGV-C1 (m/s)	PGD-C1 (m)
180	4.13	Imperial Valley-06	El Centro Array #5	6.53	strike slip	1.76	206	3.76	0.97	0.75
182	4.38	Imperial Valley-06	El Centro Array #7	6.53	strike slip	0.56	211	4.60	1.13	0.47
1044	1.37	Northridge-01	Newhall - Fire Sta	6.69	Reverse	3.16	269	5.79	0.97	0.34
1063	1.25	Northridge-01	Rinaldi Receiving Sta	6.69	Reverse	0	282	8.57	1.48	0.42
1106	1.09	Kobe_ Japan	KJMA	6.9	strike slip	0.94	312	8.18	0.92	0.21
1120	1.55	Kobe_ Japan	Takatori	6.9	strike slip	1.46	256	6.58	1.23	0.30

Table 4-3. Near fault ground motions (less than 10km) with the magnitude of earthquake between 7.0 and 7.5 (Abv. NF70)

RSN	Tp (s)	Earthquake	Station	Mag.	Mechanism	Rjb (km)	Vs30 (m/s)	PGA-C1 (m/s^2)	PGV-C1 (m/s)	PGD-C1 (m)
6906	6.23	"Darfield_NZ"	"GDLC"	7	strike slip	1.22	344	7.50	1.16	1.00
6962	7.14	"Darfield_NZ"	"ROLC"	7	strike slip	0	296	3.83	0.86	1.07
825	-	"Cape Mendocino"	"Cape Mendocino"	7.01	Reverse	0	568	14.65	1.23	0.32
828	3.00	"Cape Mendocino"	"Petrolia"	7.01	Reverse	0	422	6.49	0.89	0.33
1605	-	"Duzce_Turkey"	"Duzce"	7.14	strike slip	0	282	5.05	0.84	0.48
143	6.19	"Tabas_Iran"	"Tabas"	7.35	Reverse	1.79	767	8.45	1.23	0.94

Table 4-4. Near fault ground motions (less than 10km) with the magnitude of earthquake between 7.5 and 8.0 (Abv. NF75)

RSN	Tp (s)	Earthquake	Station	Mag.	Mechanism	Rjb (km)	Vs30 (m/s)	PGA-C1 (m/s^2)	PGV-C1 (m/s)	PGD-C1 (m)
1176	4.95	Kocaeli_Turkey	Yarimca	7.51	strike slip	1.38	297	3.16	0.72	0.47
1231	-	Chi-Chi_ Taiwan	CHY080	7.62	Reverse Oblique	0.11	496	7.94	1.07	0.16
1504	-	Chi-Chi_ Taiwan	TCU067	7.62	Reverse Oblique	0.62	434	4.89	0.92	1.01
1492	11.96	Chi-Chi_ Taiwan	TCU052	7.62	Reverse Oblique	0	579	4.38	1.72	2.26
1503	5.74	Chi-Chi_ Taiwan	TCU065	7.62	Reverse Oblique	0.57	306	7.75	1.25	1.09
2114	3.16	Denali_ Alaska	TAPS Pump Sta #10	7.9	strike slip	0.18	329	3.26	1.16	0.53

Table 4-5. Strong ground motions with small distance to fault (between 10km and 30km) (Abv. SD)

RSN	Tp (s)	Earthquake	Station	Mag.	Mechanism	Rjb (km)	Vs30 (m/s)	PGA-C1 (m/s^2)	PGV-C1 (m/s)	PGD-C1 (m)
5482	-	Iwate_Japan	AKTH04	6.9	Reverse	13.07	459	24.21	0.82	0.55
5664	-	Iwate_ apan	MYG005	6.9	Reverse	10.71	361	4.37	0.70	0.36
6952	-	Darfield_NZ	Papanui High School	7	strike slip	18.73	263	1.79	0.78	0.49
6966	8.76	Darfield_NZ	Shirley Library	7	strike slip	22.33	207	1.89	0.58	0.48
1506	-	Chi-Chi_Taiwan	TCU070	7.62	Reverse Oblique	19	401	1.57	0.60	0.56
1536	-	Chi-Chi_Taiwan	TCU110	7.62	Reverse Oblique	11.58	213	1.77	0.57	0.37

Table 4-6. Strong ground motions with long distance to fault (larger than 30km) (Abv. LD)

RSN	Tp (s)	Earthquake	Station	Mag.	Mechanism	Rjb (km)	Vs30 (m/s)	PGA-C1 (m/s^2)	PGV-C1 (m/s)	PGD-C1 (m)
786	-	Loma Prieta	Palo Alto - 1900 Embarc.	6.93	Reverse Oblique	30.56	210	2.10	0.42	0.20
731	-	Loma Prieta	APEEL 10 - Skyline	6.93	Reverse Oblique	41.71	392	0.87	0.25	0.08
738	-	Loma Prieta	Alameda Naval Air Stn Hanger	6.93	Reverse Oblique	70.9	190	2.05	0.43	0.14
838	9.13	Landers	Barstow	7.28	strike slip	34.86	370	1.33	0.25	0.17
832	-	Landers	Amboy	7.28	strike slip	69.21	383	1.43	0.20	0.07
573	-	Taiwan smart1(45)	smart1 I01	7.3	Reverse	56.18	276	1.30	0.31	0.09

The important information of the earthquake database considered in this study is summarized in Figure 4-1. It should be mentioned that the conclusions are affected by the contents of the database (the database is limited to the earthquake data recorded in recent decades; the recorded data may not cover all the possible patterns of large earthquakes).
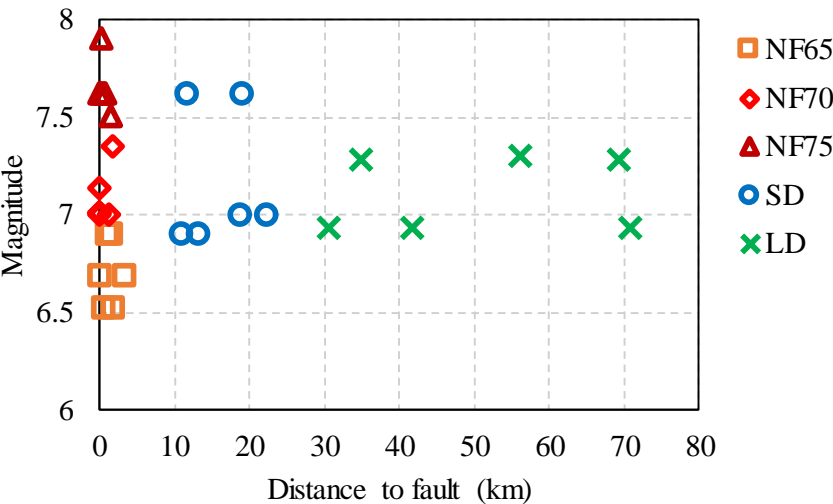
(a) Distribution of magnitude and distance to fault of the GMs in the database
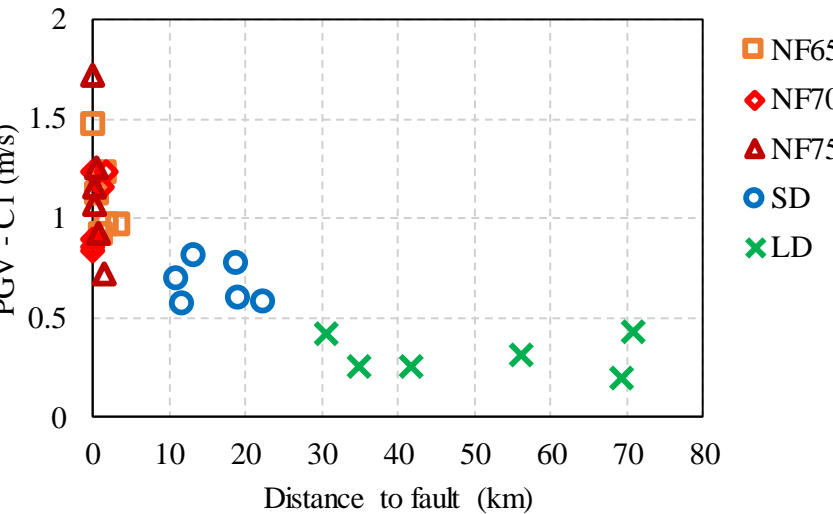
(b) Distribution of the PGV of the GMs in the database

Figure 4-1. Information of the earthquake database

4.3 Parameters of the DCFP systems

First, a reasonable range of friction coefficient is discussed for polished steel – PTFE sliding interface. This study will only focus on PTFE, because the friction dependency equations will be different for other low friction materials applied in isolation devices, like PE and PA. As for various PTFE-related materials with different friction coefficient, the friction dependency equations of them on the polished steel may be a little different from each other. However, it is simplified in this study that they share the same friction dependency equations. While, when simulating the temperature of the sliding interface, the results will have no large difference between various low friction materials, because most of the heat will be translated to the steel regardless of the type of the low friction material. Paolo et al. demonstrated that the friction coefficient of PTFE-related materials on polished steel is around 5-10% and the dynamic friction coefficient varies in the range 6-8% [4-8]. Moreover, Cardone et al. demonstrated that the friction coefficient of lubricated steel – PTFE sliding interface is around 2-5% under earthquake excitations [4-9]. Based on these studies and the PTFE material considered in this study, a range of 1.5-12% is selected for the dynamic friction coefficient of PTFE material, which can be represented by the nominal friction coefficient, μ_n, in this study. This range is little larger than the information collected by the author (2-8%) to theoretically study the influence of friction coefficient on the response in a large range and to consider more possible situations as well. The selection of μ_n and corresponding reference friction coefficient μ_o for DCFP bearings with slider diameter as 100 mm is shown in Table 4-7, which is calculated based on the method introduced in Section 2.4.4. Where, μ_o is the friction coefficient at 60 N/mm^2, 400 mm/s and an initial atmosphere temperature of 20˚C. The definition of μ_n and μ_o is also shown in Figure 4-2 and Equation (4-1), where μ is the friction coefficient at various condition, $T˚C_e$ and $T˚C_f$ are the temperature at point e and f respectively.

Table 4-7. Range of friction coefficient considered for the DCFP bearing (φ100)

μ_n	0.015	0.03	0.045	0.06	0.075	0.09	0.105	0.12
μ_o	0.018	0.041	0.072	0.113	0.164	0.23	0.319	0.431
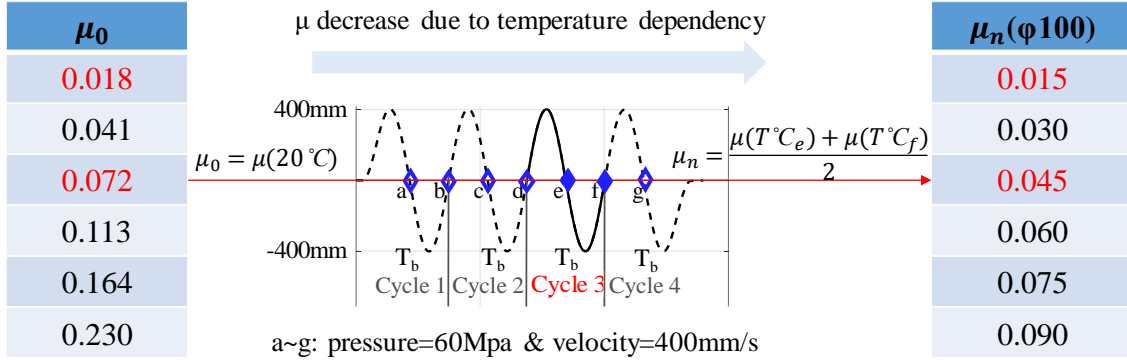
(a) Relation between μ_0 and μ_n
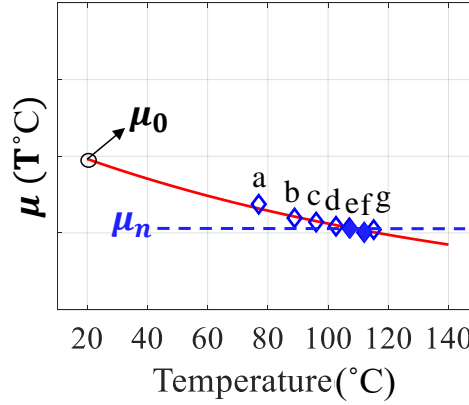
(b) An example of experimental friction coefficient

Figure 4-2. Definition of μ_0 and μ_n

$$\mu_n = \frac{\mu(60MPa,400mm/s,T^\circ C_e)+\mu(60MPa,400mm/s,T^\circ C_f)}{2} \tag{4-1}$$

Second, a reasonable range of natural period (T_b) is also selected for the DCFP bearing as 3-9 seconds. For a DCFP bearing, its natural period is determined by the radius of the curvature of the concave plates. The DCFP bearings considered in this study have the same radius for the curvature of the upper and lower concave plate, R_S. Then, the natural period can be expressed as:

$$T_b = 2\pi\sqrt{\frac{2R_S}{g}} \tag{4-2}$$

153

The considered T_b and corresponding R_S are shown in Table 4-8. Further, the horizontal displacement capacity of FPB is limited by the acceptability of the vertical displacement and residual horizontal displacement, both of which are a function of R_S. Dolce et al. proposed that the ratio of the design displacement (D_d) / R_S should be larger than the friction coefficient of the bearing for reasonable residual horizontal displacement [4-10] as shown in Figure 4-3 (a). Moreover, during horizontal excitations, displacement is produced in the vertical direction in the FPB due to the horizontal deformation as shown in Figure 4-3 (b). It is necessary to be careful about this effect when setting vertical clearances. When horizontal deformation occurs during an earthquake, the isolator must stably support the vertical load and minimize any settlement in the vertical direction associated with the horizontal deformation [4-11]. Therefore, the horizontal displacement capacity of FPB is conditioned by the acceptability of the corresponding vertical displacement. Which is a function of the radius of curvature R_S of the FPB. As a consequence, limitations to the ratio between the design displacement of the isolation layer (D_d) and the radius of curvature (R_S) are needed to limit vertical displacement. Reasonable values of the ratio D_d / R_S should be lower than 15% in order to avoid excessive vertical displacements [4-12] as shown in Figure 4-3 (b). Then, for the DCFP bearing considered in this study, the limitation should be expressed as: $\mu_n < D_d$ / $2R_S < 15\%$.

Table 4-8. Range of natural period of considered DCFP bearings

T_b (s)	3	4	5	6	7	8	9
R_S (mm)	1117	1986	3103	4468	6082	7943	10054
15%*2 R_S (mm)	335	596	931	1340	1825	2383	3016

$\mu_n*N < D_d/R_S*N$

Avoid large residual displacement

$\theta = \dfrac{D_d}{R_S}$

μ_n*N D_d/R_S*N

D_d

θ

N

$D_d/R_S < 15\%$

85% 50% **15%** R_S

Avoid large vertical displacement

D_d

(a) Residual horizontal displacement   (b) Vertical displacement
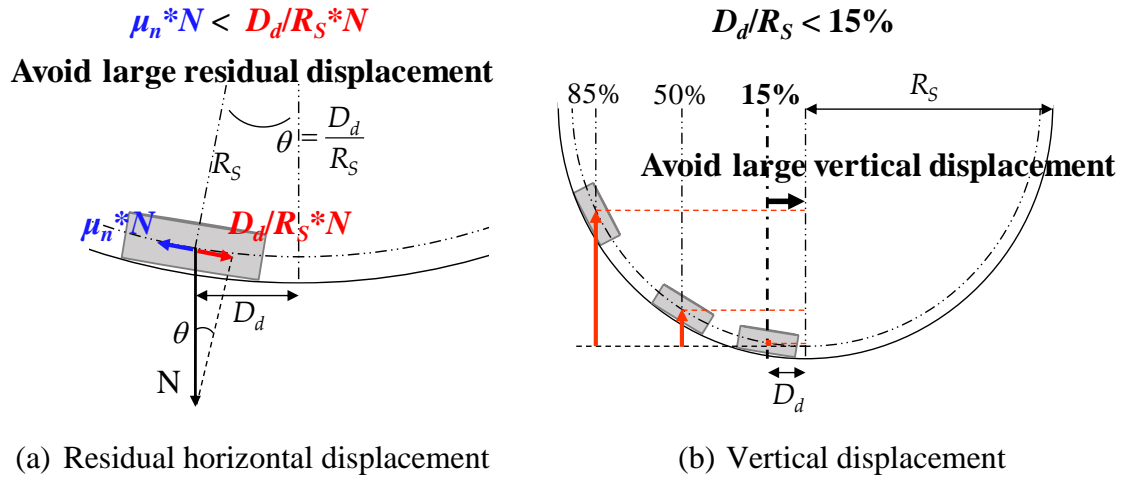
Figure 4-3 The horizontal displacement capacity of FPB limited by the acceptability of the residual horizontal and vertical displacements

To design an optimum isolation system for a superstructure and study the influence of different parameters on the response of the BIS, the mass of the superstructure is considered as a certain value. Further, as the effect of pressure is not considered in this study, the pressure of the sliding interface is selected as a constant of 60Mpa. As a consequence, the diameter of the slider is considered as the same for different situations. In this study, based on the range of R_S, a value of 100mm is selected as the slider diameter.

4.4 Numerical models

The difference between the simplified model and the precise model under various ground motion classifications and base isolation systems is clarified in this section. It has been validated in Chapter 2 and 3 that the simplified model can provide similar analysis results as the precise model for DCFP bearings with μ_n = 0.043 & 0.013 and T_b = 6s under 32 scaled ground motions. In this part, whether the simplified model can be applied to replace the precise model in simulating the response spectra is further validated under a much larger range of DCFP bearings and non-scaled earthquake records. The arrangement of monitor points for the precise model is -1500:10:1500 in the direction of excitation for the unidirectional precise model, and -1500:25:1500 in two orthogonal horizontal directions for the bidirectional precise model. Response spectra of the maximum superstructure acceleration and the maximum displacement of the isolation layer under NF65 was obtained by using the simplified model and the precise model, and the results is shown in Figure 4-4 and 4-5, respectively. Where, friction coefficient represents μ_n, isolation period represents the natural period of the isolation system, Acc(sup) and displacement increase ratio represents the increase of the maximum superstructure acceleration and the maximum displacement of the isolation layer from unidirectional excitation to corresponding bidirectional excitation, and the spectra is obtained by taking average of the results of all the earthquakes in the classification. The response spectra will be discussed later. Only the difference between the two models is focused in this section. Comparing the results using the simplified model and the precise model shown in these two figures, it can be seen that the simplified model can provide very similar results as the precise model for the response spectra of both the maximum superstructure acceleration and the maximum displacement of the isolation layer. And it is also true for all the other earthquake classifications. The only visible difference occurred at μ_n = 0.012 in Figure 4-5 (e) and (f), where the average

displacement increase ratio under T_b = 6s is 3.20 for simplified model and 2.04 for precise model. The difference is caused by the ground motion RSN 180 shown in Table 4-2. The maximum unidirectional displacement of the DCFP bearing under RSN 180 is 5mm for both the simplified model and the precise model. However, the corresponding maximum bidirectional displacement is 55mm for the simplified model and 33mm for the precise model. And it is also true for all the other earthquake classifications. Large increase ratio and visible difference between simplified and precise model are mainly caused by small response displacements. However, these cases are usually not considered in the design, because the small response in displacement always comes together with unacceptable residual displacement and large superstructure acceleration. Therefore, there is no large difference between the two models and the simplified model can be used instead of the precise model on obtaining the response spectra for faster calculation speed.
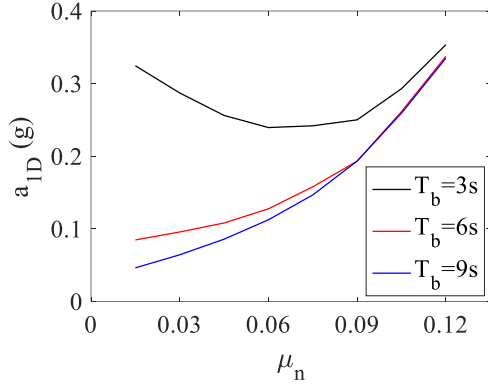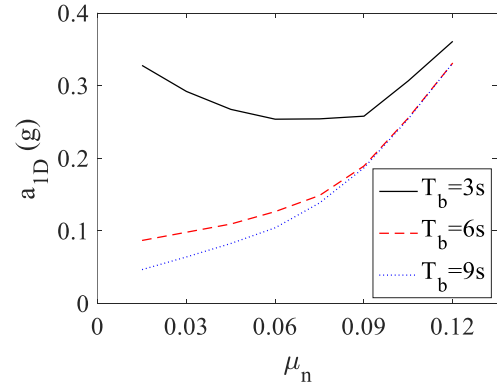
(a) Simplified model (b) Precise model
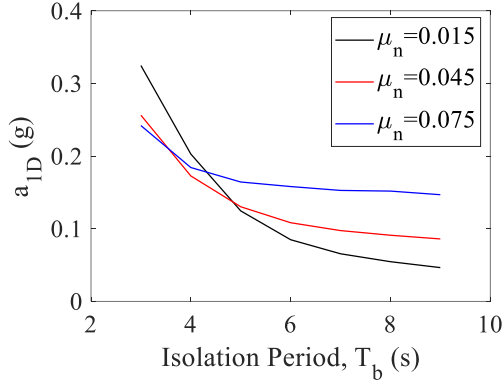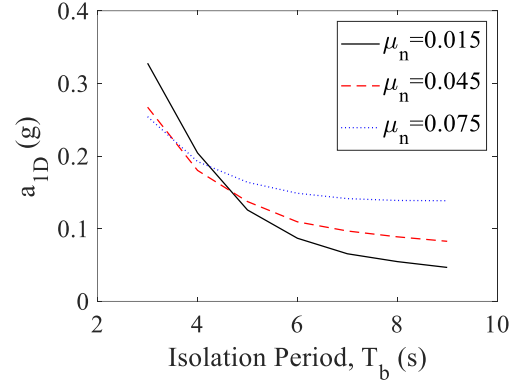
(c) Simplified model (d) Precise model
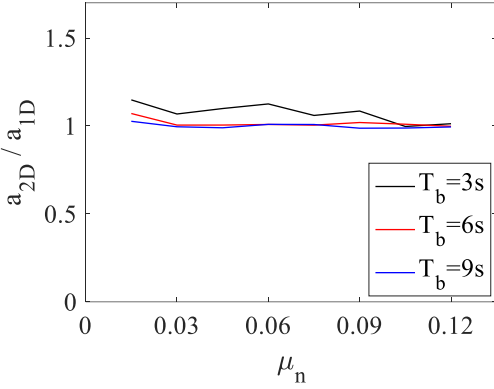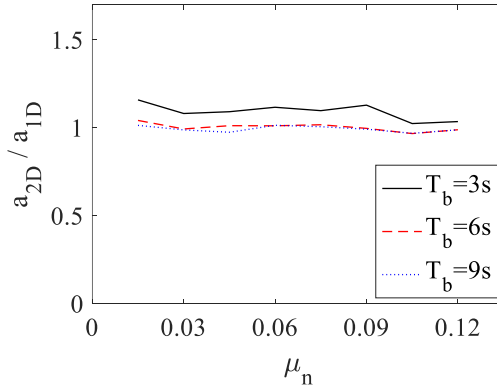
(e) Simplified model (f) Precise model
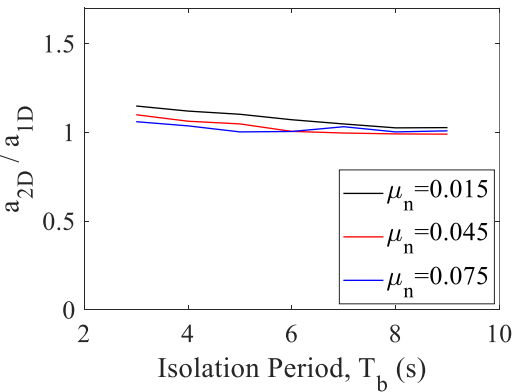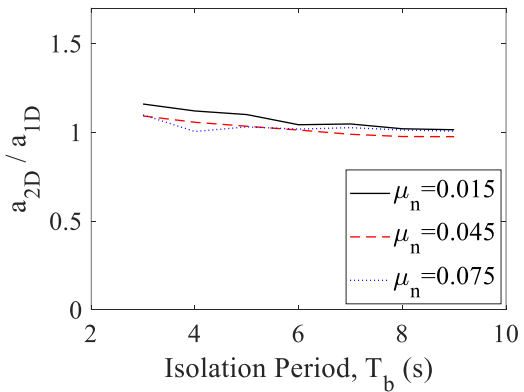
(g) Simplified model (h) Precise model

Figure 4-4. Response spectra of the maximum superstructure acceleration on μ_n and T_b using simplified model and precise model under NF65
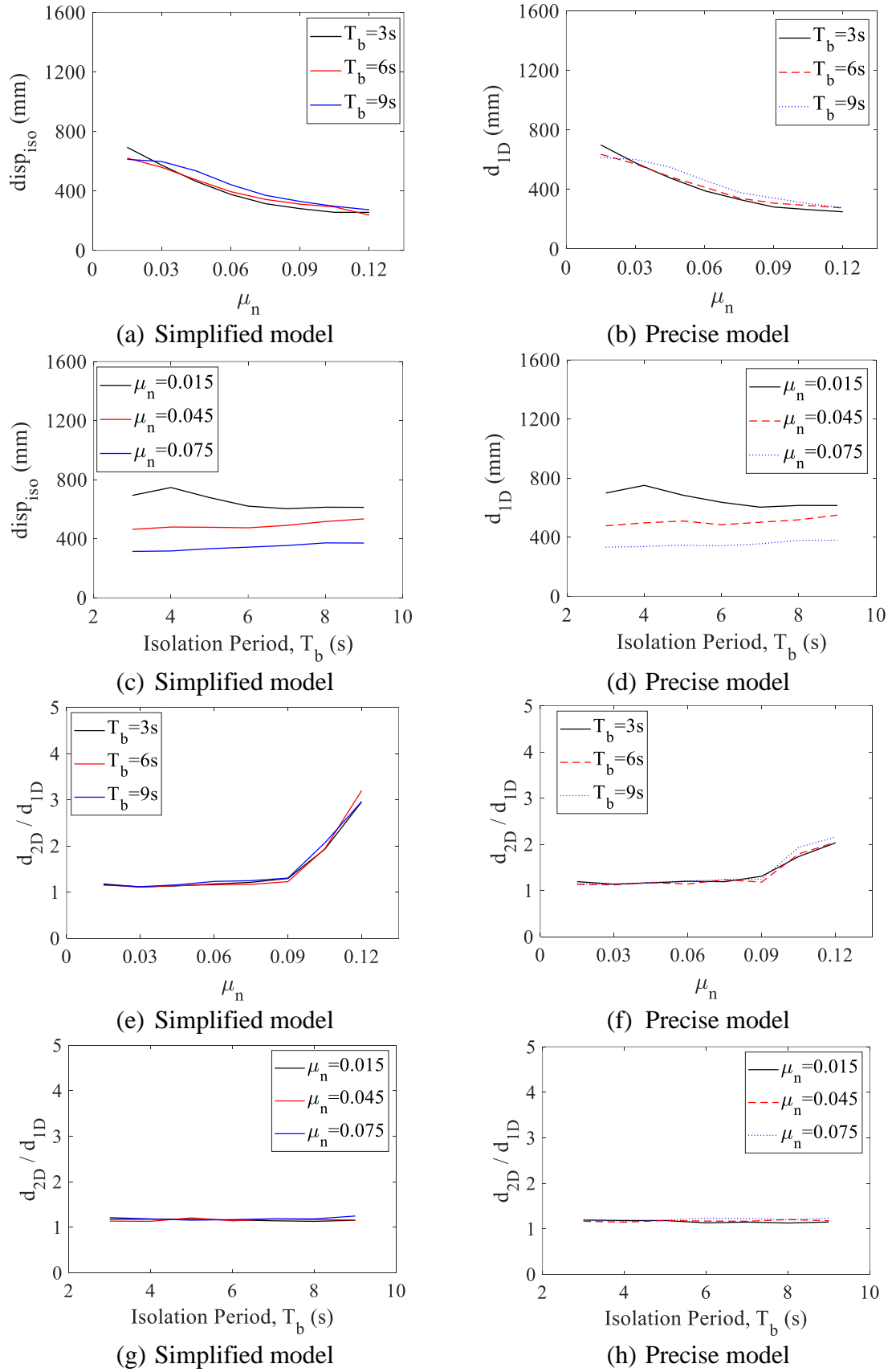
Figure 4-5. Response spectra of the maximum displacement of the isolated layer on μ_n and T_b using simplified model and precise model under NF65

4.5 Influence of the characteristics of the ground motion and the base isolation system on the response displacement history

As introduced in the last section, RSN 180 will lead to very small response displacement when μ_n is very large. This is actually because RSN 180 has large period of the velocity pulse (Tp = 4.13s). The ground velocity history and ground displacement history of it is shown in Figure 4-6 and 4-7 respectively. And the maximum response displacement of the DCFP bearing with various μ_n and T_b = 6s under NF65 classification is shown in Table 4-9. It can be seen that, for RSN 180 (Tp = 4.13s) and RSN 182 (Tp = 4.38s), the maximum unidirectional displacement (d_{1D}) decrease significantly with the increase of μ_n. This is because when Tp is large, the ground acceleration will be small, and it will be more and more difficult to make the bearing slide when the friction coefficient is increasing. Further, it can be seen that, for GMs with long period (Tp > 4s, e.g. RSN 180 & RSN 182), if the μ_n is small (e.g. 0.015 & 0.03), d_{1D} will be evenly larger than the PGD (peak ground displacement) of the ground motion. Therefore, it is necessary to be particularly careful if the isolation period is extended to 5 seconds or higher.
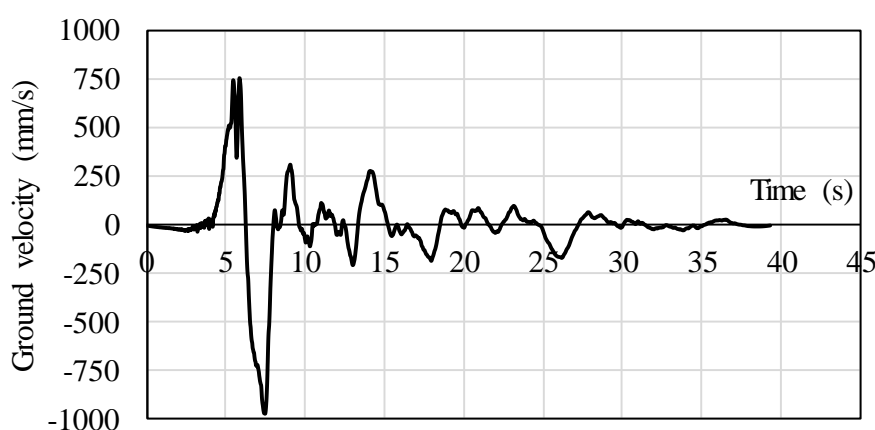
Figure 4-6. Ground velocity history of RSN 180
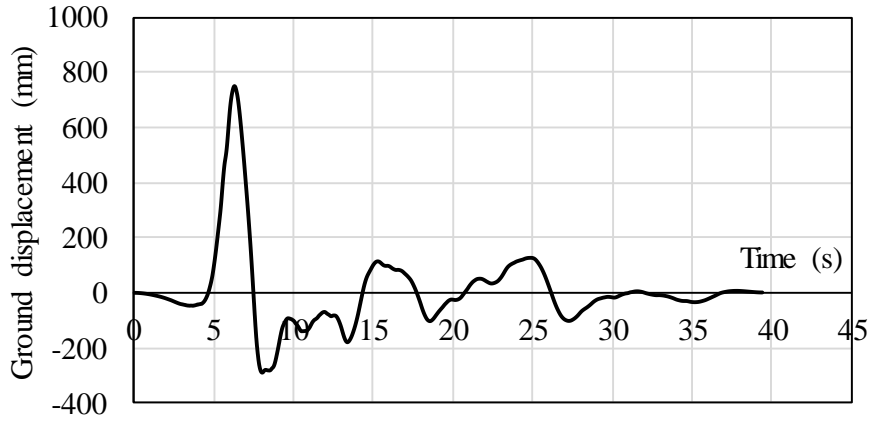
Figure 4-7. Ground displacement history of RSN 180

Table 4-9 Maximum unidirectional displacement of NF65 under various μ_n

T_b	6	6	6	6	6	6	6
μ_0	0.018	0.041	0.072	0.113	0.164	0.23	0.319
μ_n	0.015	0.03	0.045	0.06	0.075	0.09	0.105
d_{1D} (RSN 180, Tp=4.13s)	1136	988	788	550	366	208	35
d_{1D} (RSN 182, Tp=4.38s)	985	824	691	534	350	229	146
d_{1D} (RSN 1044, Tp=1.37s)	481	445	367	310	290	288	226
d_{1D} (RSN 1063, Tp=1.25s)	470	422	345	342	419	510	641
d_{1D} (RSN 1106, Tp=1.09s)	245	252	231	243	283	310	321
d_{1D} (RSN 1120, Tp=1.55s)	407	424	423	390	352	324	385

On the other hand, for the near fault ground motions with relatively small Tp like RSN 1063 (Tp = 1.25s), larger μ_n may slightly increase d_{1D}. This is because the ground acceleration is very large in this situation, which will make the displacement of the bearing during the velocity pulse close to the ground displacement of the ground motion. Therefore, when μ_n is larger, the displacement of the bearing will slide less in the first half of the velocity pulse (because the cumulated heat is little at the beginning of the velocity pulse, the friction coefficient is very large), then the friction coefficient will decrease because of heating and the displacement in the latter half of the velocity pulse will be close to the ground

161

displacement. The ground displacement history is shown in Figure 4-8 and the response displacement history under various μ_n is shown in Figure 4-9.
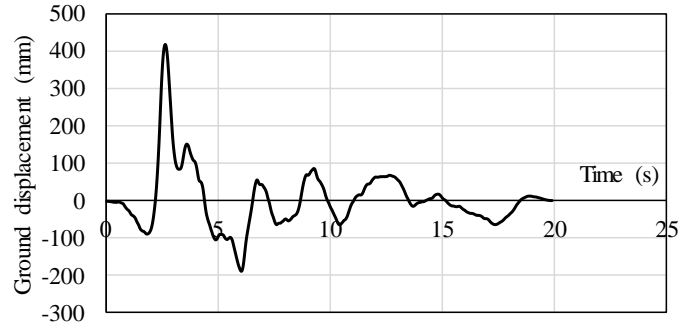
Figure 4-8. Ground displacement history of RSN 1063
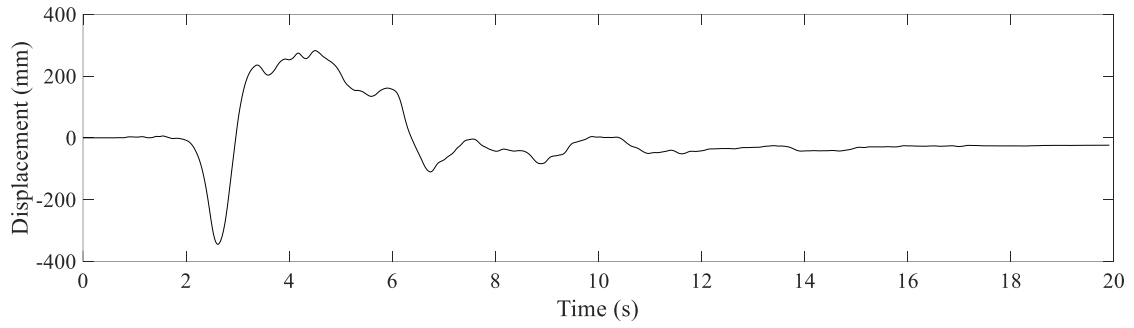
(a) $\mu_n = 0.045$
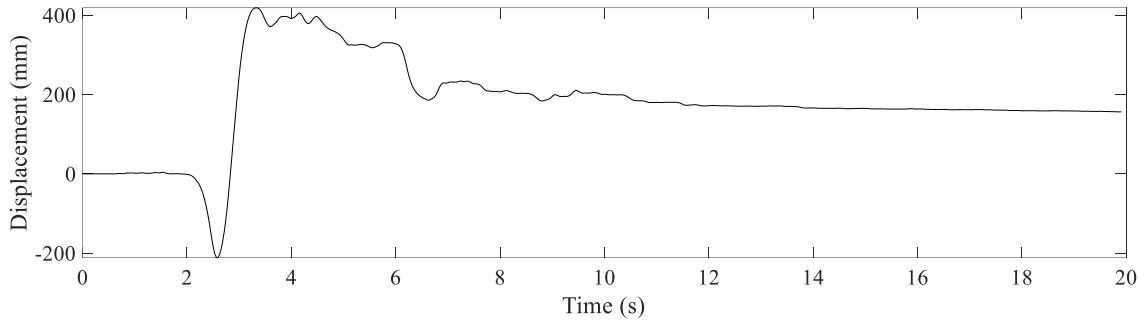
(b) $\mu_n = 0.075$
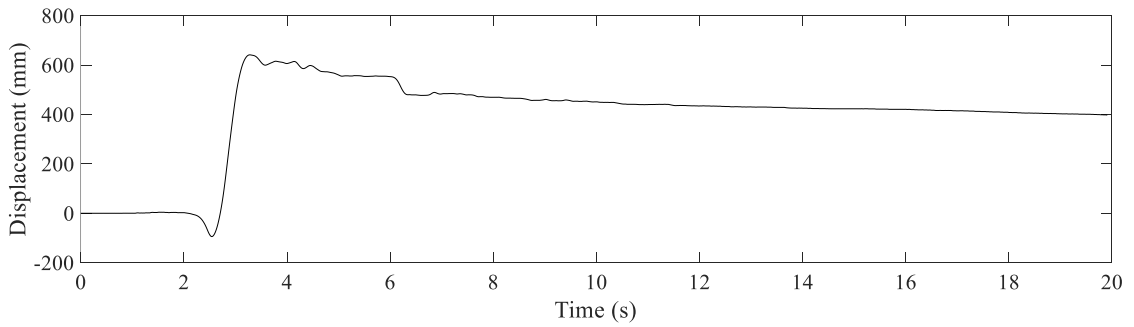
(c) $\mu_n = 0.105$

Figure 4-9. Response displacement history of RSN 1063 under various μ_n ($T_b = 6$s)

Moreover, the value of T_b will affect the frequency of the vibration after the velocity pulse as shown in Figure 4-10.
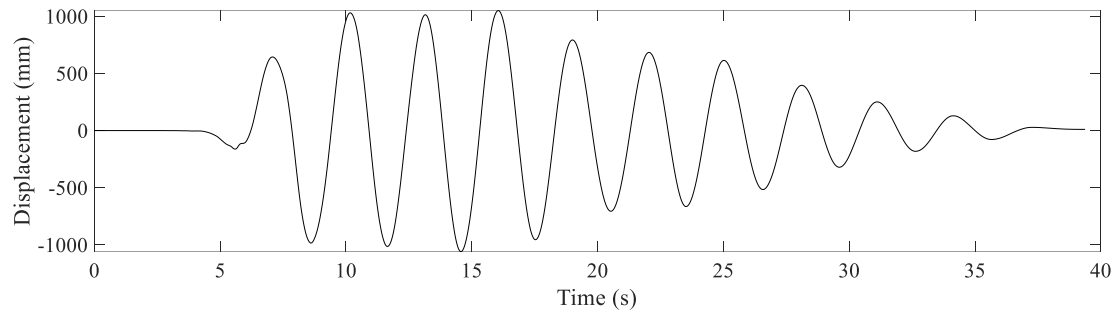
(a) $T_b = 3$s
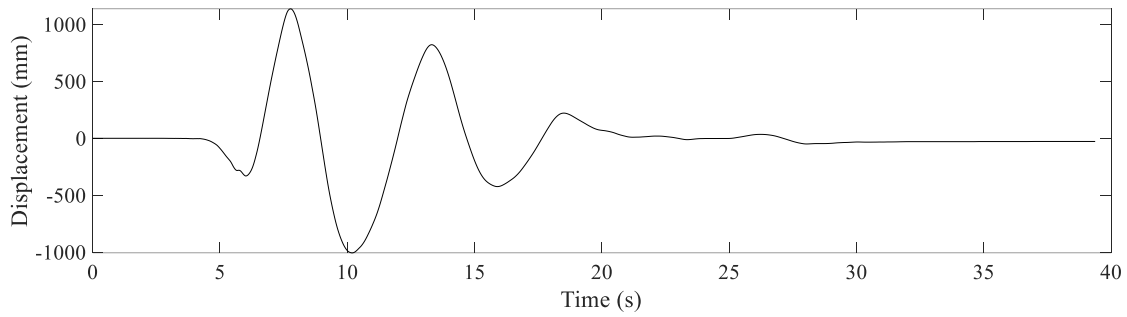
(b) $T_b = 6$s
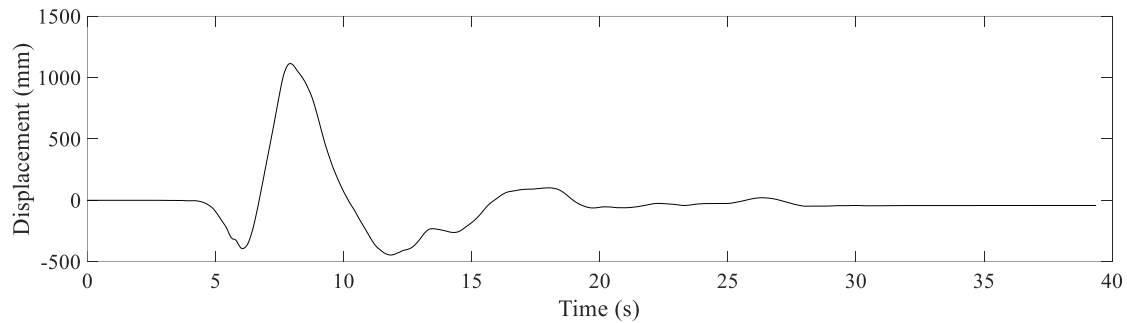
(c) $T_b = 9$s

Figure 4-10. Response displacement history of RSN 180 under various T_b ($\mu_n = 0.015$)

4.6 Parametric study and optimum selection of DCFP systems under various ground motions

4.6.1 Parametric study and optimum selection of DCFP systems under unidirectional GMs considering temperature effect (NF, SD, LD)

As introduced in Section 4.3, the horizontal displacement capacity of FPB is limited by the acceptability of the vertical displacement and residual horizontal displacement: the ratio of the design displacement of DCFP bearings $(D_d) / 2R_S$ should be larger than μ_n and less than 15%. These limits of displacement are shown in the unidirectional displacement spectra in form of dashed lines as shown in Figure 4-11, which shows the response spectra under the selected group of unidirectional GMs in NF65. Where d_{1D} and a_{1D} are the maximum displacement of the isolation layer and the maximum acceleration of the superstructure under 1D GMs respectively. For example, the blue dashed line shown in Figure 4-11 (a) is the lower displacement limit of the blue solid line, the BIS with d_{1D} under which will have large residual displacement under NF65 GMs. It shows that μ_n should be less than 0.03 for DCFP bearings with T_b equals 9s under near fault ground motions with the magnitude of the earthquake between 6.5 and 7.0 (NF65), less than 0.05 for DCFP bearings with T_b equals 6s, and less than 0.11 for DCFP bearings with T_b equals 3s to avoid unacceptable residual displacement. The upper limit of d_{1D} is shown in Figure 4-11 (b) to avoid excessive vertical displacement. It shows that T_b should be larger than 3s for DCFP bearings with μ_n equals 0.075 under near fault ground motions with the magnitude of the earthquake between 6.5 and 7.0 (NF65), larger than 3.5s for DCFP bearings with μ_n equals 0.045, and larger than 4.5s for DCFP bearings with μ_n equals 0.015 to avoid excessive vertical displacement. It should be mentioned at the beginning that, the response data which does not satisfy the displacement limits were also shown in the response spectra to discuss the influence of various parameters on the response of the BIS.
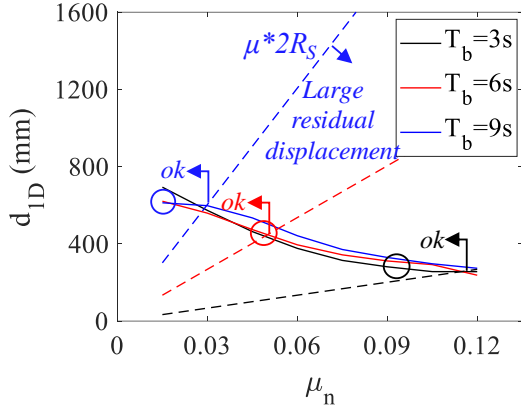
(a) Maximum displacement on μ_n (b) Maximum displacement on T_b
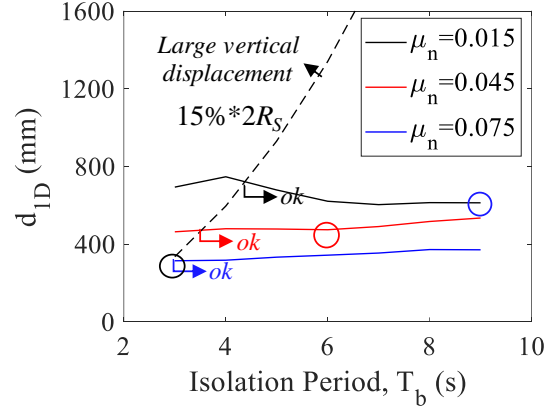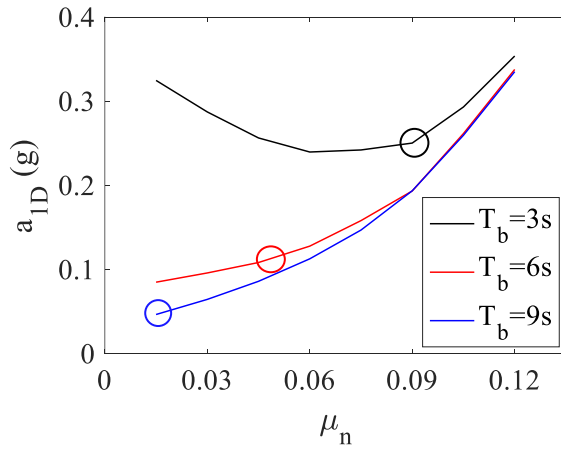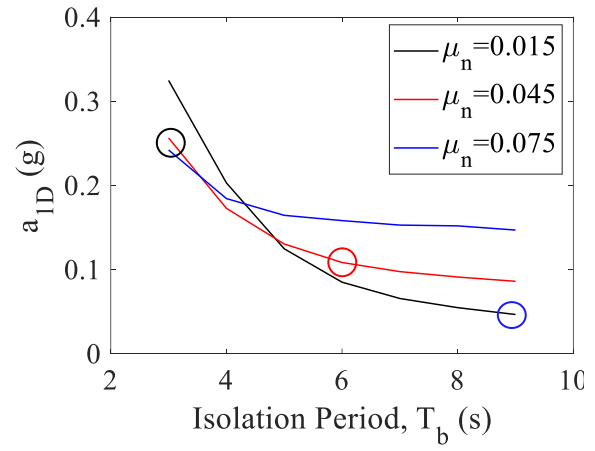
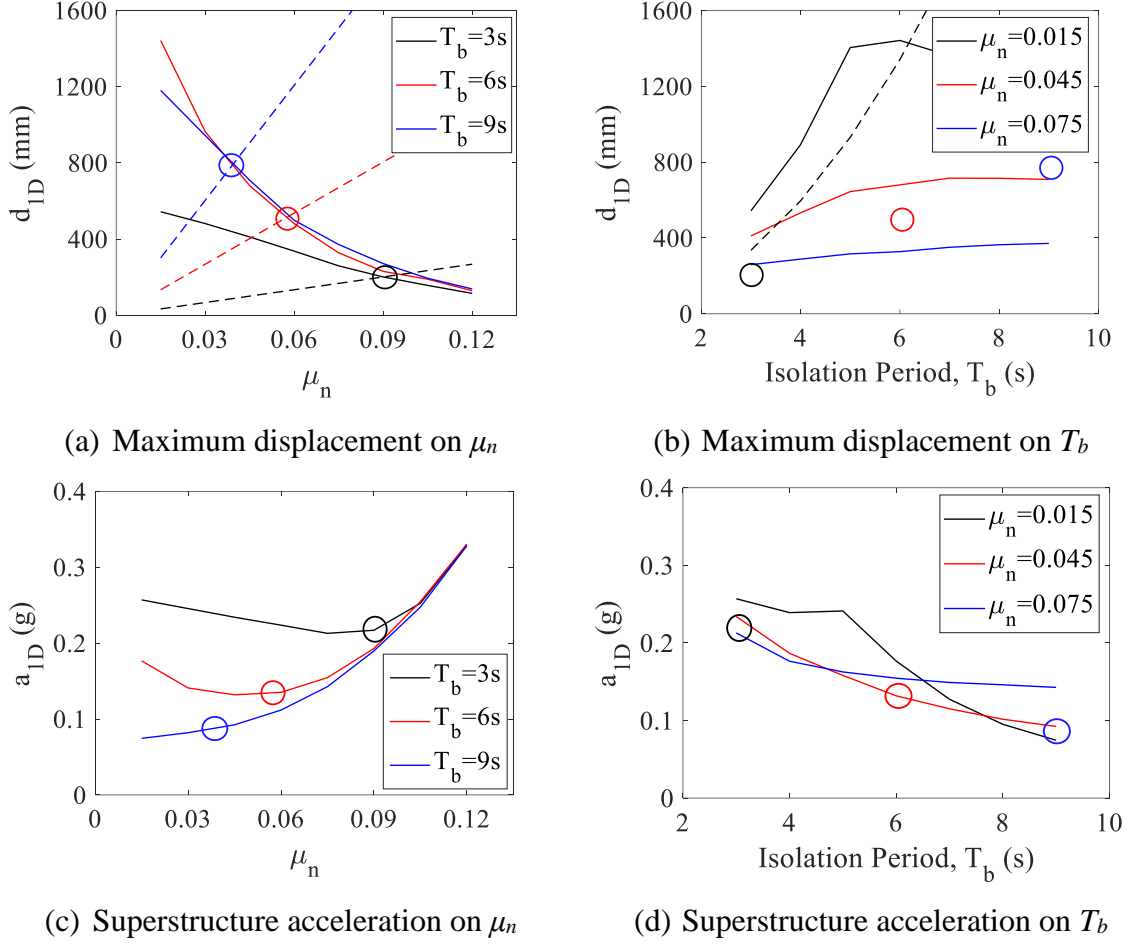(c) Superstructure acceleration on μ_n (d) Superstructure acceleration on T_b

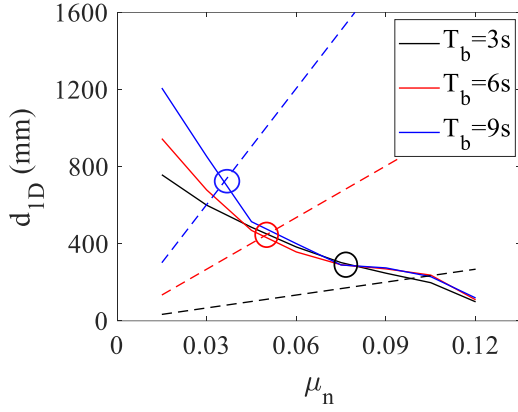**Figure 4-11.** Response spectra under unidirectional GMs in NF65

It can be seen from Figure 4-11 (a) that d_{1D} will significantly decrease with the increase of the friction coefficient regardless of the value of T_b. The mean value of d_{1D} decrease from around 700mm at $\mu_n = 0.015$ to around 300mm at $\mu_n = 0.12$. Figure 4-11 (b) shows that d_{1D} has no large difference under various T_b. Except for d_{1D}, a_{1D} is also very important in the design of a BIS. Figure 4-11 (c) and (d) show a_{1D} spectra on μ_n and T_b respectively. Figure 4-11 (c) shows that a_{1D} may achieve the minimum value at around $\mu_n = 0.06 \sim 0.09$ when T_b = 3s. While, for larger T_b (flatter concave), the minimum a_{1D} will be achieved at $\mu_n = 0.015$ (the minimum μ_n). Figure 4-11 (d) shows that a_{1D} will decrease with the increase of T_b, and the larger the value of μ_n, the smaller the ratio of decrease. Based on Figure 4-11 (a) and (c), the acceptable range of μ_n when T_b = 9s is from 0.015 to 0.03, with d_{1D} around 600mm and

a_{1D} around 0.05g. For T_b = 6s, the acceptable range of μ_n is from 0.015 to 0.045, with d_{1D}

decrease from 600mm to 400mm and the acceleration remained around 0.1g. As for T_b = 3s,

almost the whole range of μ_n is acceptable, with d_{1D} decrease from 700mm to 300mm and

a_{1D} decrease from 0.33g to 0.25g and then increase back to 0.35g. The optimum selections

of μ_n under each T_b were marked by circles in Figure 4-11. First, marked as the black circle,

T_b is around 3s and μ_n is around 0.09, which will result in a mean d_{1D} of 250mm and a mean

a_{1D} of 0.25g. Second, marked as the red circle, T_b is around 6s and μ_n is around 0.05, results

in d_{1D} around 400mm and a_{1D} around 0.1g. Third, marked as the blue circle, T_b is around 9s

and μ_n is around 0.015, results in d_{1D} around 600mm and a_{1D} around 0.05g. Then, the

selections were validated in Figure 4-11 (b) and excessive vertical displacement will not
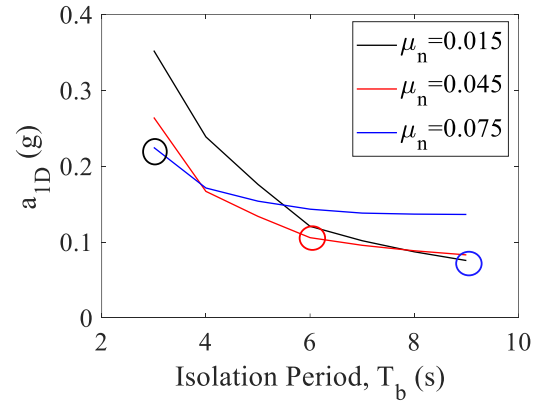
happen.

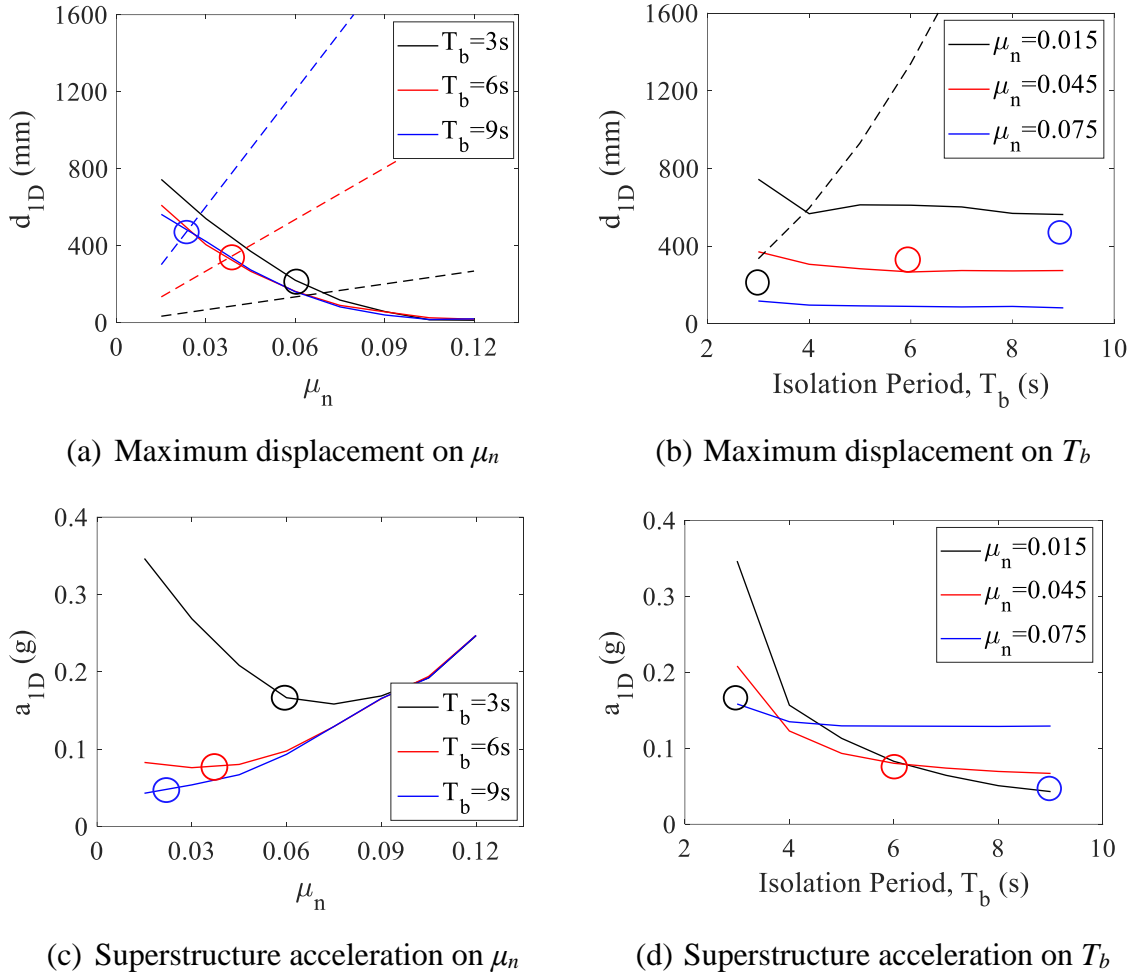(a) Maximum displacement on μ_n (b) Maximum displacement on T_b

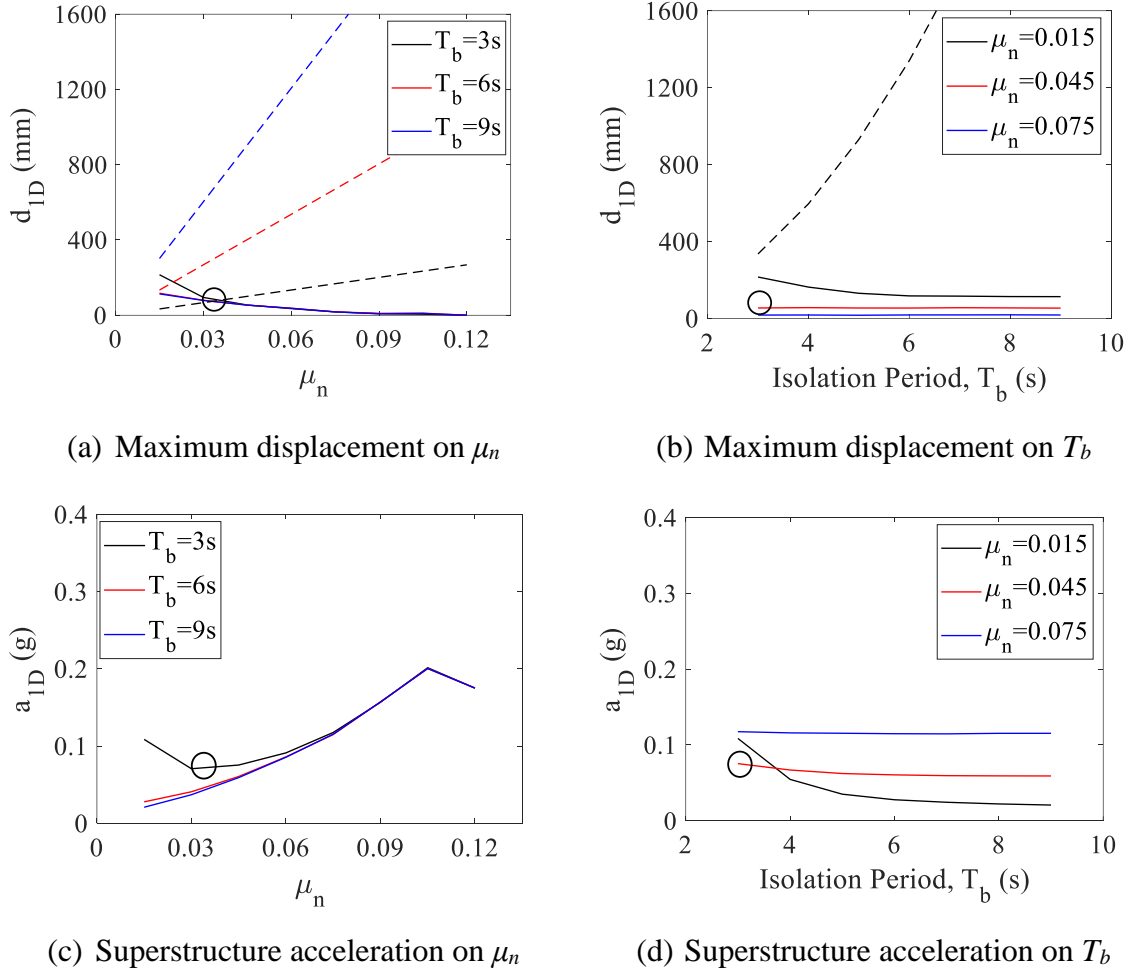(c) Superstructure acceleration on μ_n (d) Superstructure acceleration on T_b

Figure 4-12. Response spectra under unidirectional GMs in NF70

It can be seen from Figure 4-12 that the influence of μ_n and T_b on the response of the BIS under near fault ground motions with the magnitude of the earthquake between 7.0 and 7.5 (NF70) is similar as that under NF65: d_{1D} will significantly decrease with the increase of the friction coefficient regardless of the value of T_b; a_{1D} may achieve the minimum value at around $\mu_n = 0.06 \sim 0.09$ when $T_b = 3$s. While, for larger T_b (flatter concave), the minimum a_{1D} will be achieved at $\mu_n = 0.015$ (the minimum μ_n); a_{1D} will decrease with the increase of T_b, and the larger the value of μ_n, the smaller the ratio of decrease. The optimum selections of μ_n under each T_b under NF70 were also marked by circles. For example, marked as the black circle, T_b is around 3s and μ_n is around 0.09, which will result in a mean d_{1D} of 200mm and a mean a_{1D} of 0.23g. Second, marked as the red circle, T_b is around 6s and μ_n is around 0.06, results in d_{1D} around 500mm and a_{1D} around 0.14g. Third, marked as the blue circle, T_b is around 9s and μ_n is around 0.04, results in d_{1D} around 800mm and a_{1D} around 0.09g.
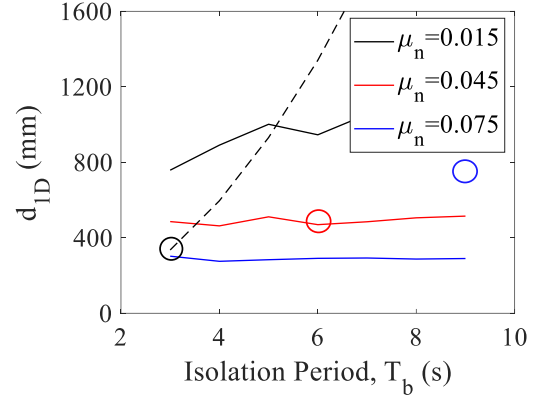
167

(a) Maximum displacement on μ_n

(b) Maximum displacement on T_b
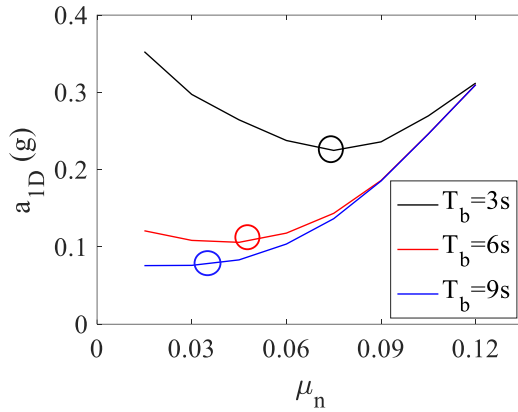
(c) Superstructure acceleration on μ_n

(d) Superstructure acceleration on T_b

Figure 4-13. Response spectra under unidirectional GMs in NF75

It can be seen from Figure 4-13 that the influence of μ_n and T_b on the response of the BIS under near fault ground motions with the magnitude of the earthquake between 7.5 and 8.0 (NF75) is also similar as that under NF65 and NF70. The optimum selections of μ_n under each T_b under NF75 were marked by circles in Figure 4-13. For example, marked as the black circle, T_b is around 3s and μ_n is around 0.075, which will result in a mean d_{1D} of 300mm and a mean a_{1D} of 0.23g. Second, marked as the red circle, T_b is around 6s and μ_n is around 0.045, results in d_{1D} around 500mm and a_{1D} around 0.1g. Third, marked as the blue circle, T_b is around 9s and μ_n is around 0.03, results in d_{1D} around 700mm and a_{1D} around 0.08g.

168

(a) Maximum displacement on μ_n (b) Maximum displacement on T_b

(c) Superstructure acceleration on μ_n (d) Superstructure acceleration on T_b

Figure 4-14. Response spectra under unidirectional GMs in SD

It can be seen from Figure 4-14 that the influence of μ_n and T_b on the response of the BIS under small-distance-to-fault ground motions with the magnitude of the earthquake between 6.5 and 8.0 (SD) is similar as that under near fault ground motions (NF65, NF70, NF75). The optimum selections of μ_n under each T_b under SD were also marked by circles in Figure 4-14. For example, marked as the black circle, T_b is around 3s and μ_n is around 0.06, which will result in a mean d_{1D} of 200mm and a mean a_{1D} of 0.17g. Second, marked as the red circle, T_b is around 6s and μ_n is around 0.04, results in d_{1D} around 300mm and a_{1D} around 0.08g. Third, marked as the blue circle, T_b is around 9s and μ_n is around 0.02, results in d_{1D} around 500mm and a_{1D} around 0.05g.

(a) Maximum displacement on μ_n (b) Maximum displacement on T_b

(c) Superstructure acceleration on μ_n (d) Superstructure acceleration on T_b

Figure 4-15. Response spectra under unidirectional GMs in LD

It can be seen from Figure 4-15 that the influence of μ_n and T_b on the response of the BIS under long-distance-to-fault ground motions with the magnitude of the earthquake between 6.5 and 8.0 (LD) is similar as that under NF65, NF70, NF75, and SD. Only except that a_{1D} may achieve the minimum value at around $\mu_n = 0.03 \sim 0.06$ when $T_b = 3$s. As for the optimum selections, only the DCFP bearing with T_b less than 6s can satisfy the requirement of residual displacement under LD. For example, the optimum selections of μ_n under $T_b = 3$s under LD were marked by black circles in Figure 4-15. T_b is around 3s and μ_n is around 0.03, which will result in a mean d_{1D} of 100mm and a mean a_{1D} of 0.08g.

4.6.2 Effect of bidirectional behavior on the response (NF, SD, LD)

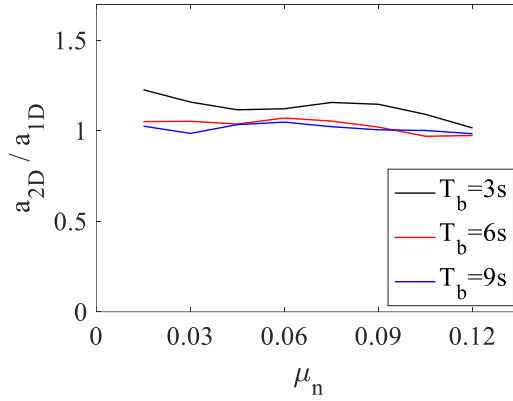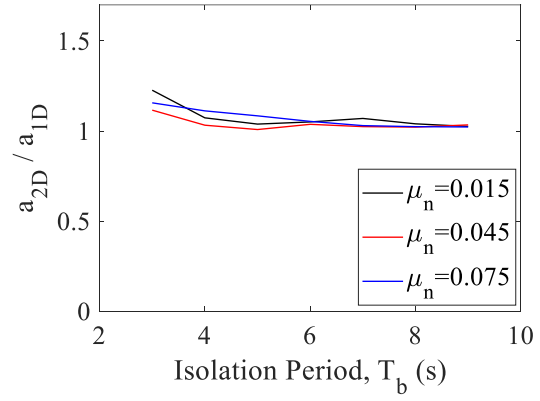As for the response under bidirectional excitation, Figure 4-16 shows the spectra of response increase under bidirectional GMs compared with corresponding unidirectional GMs in NF65. Where d_{2D} and a_{2D} are the maximum displacement of the isolation layer and the maximum acceleration of the superstructure under corresponding 2D GMs respectively. It shows that for optimum selections, T_b around 3s and μ_n around 0.09, the mean increase in the displacement (d_{2D}/d_{1D}) is around 1.29 and the mean increase in the acceleration (a_{2D}/a_{1D}) is around 1.08; for T_b around 6s and μ_n around 0.045, the mean value of d_{2D}/d_{1D} is around 1.14 and the mean value of a_{2D}/a_{1D} is around 1.01; for T_b around 9s and μ_n around 0.015, the mean value of d_{2D}/d_{1D} is around 1.15 and the mean value of a_{2D}/a_{1D} is around 1.00.

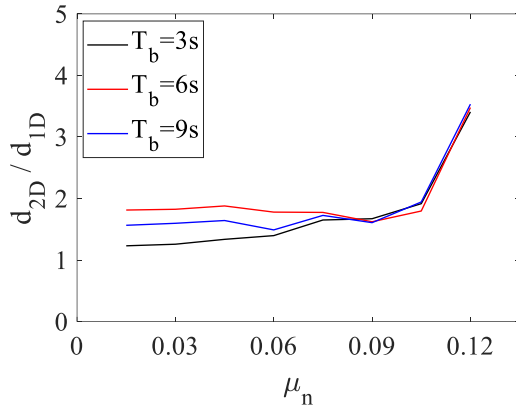(a) Maximum displacement on μ_n (b) Maximum displacement on T_b

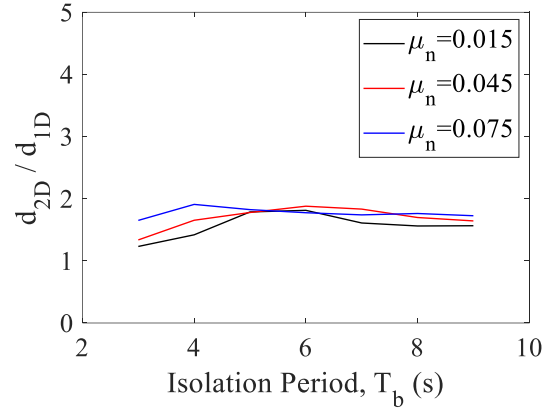(c) Superstructure acceleration on μ_n (d) Superstructure acceleration on T_b
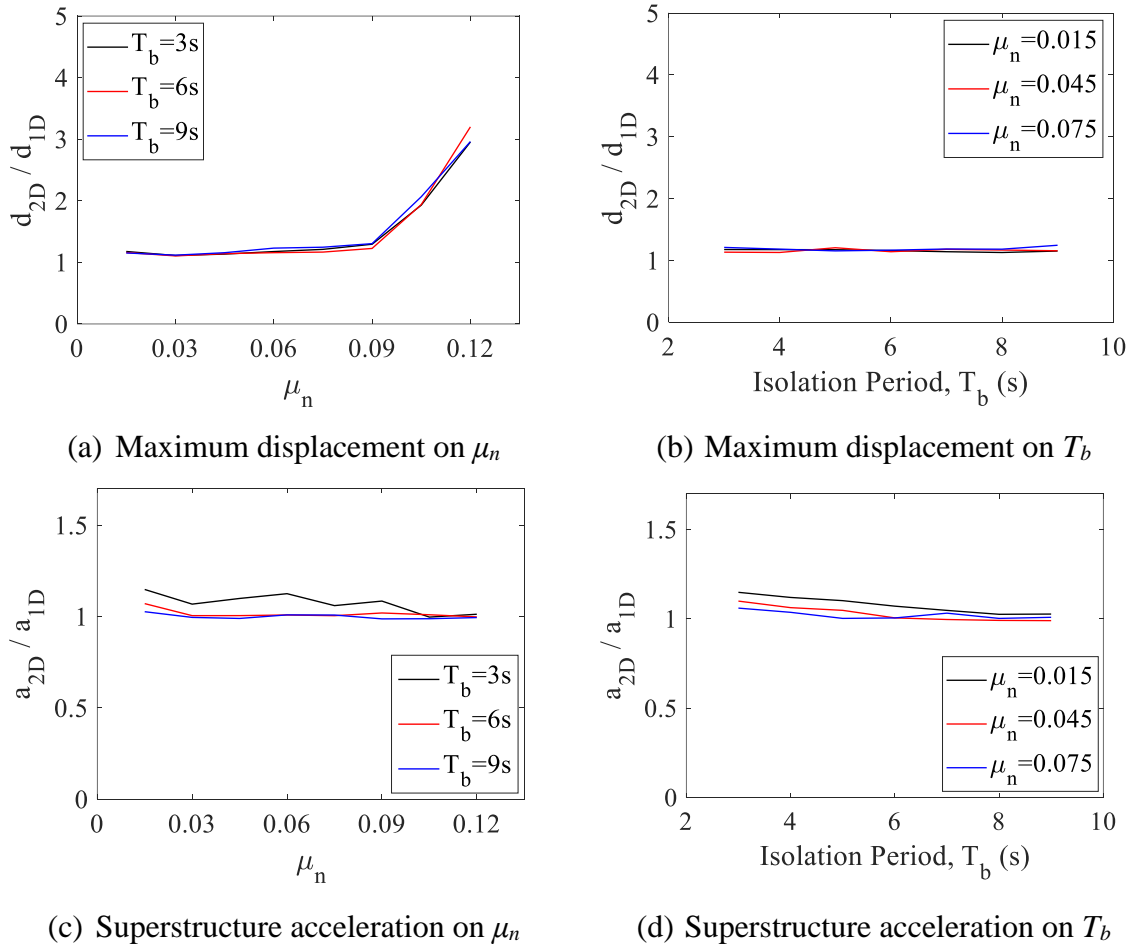
Figure 4-16. Spectra of response increase under bidirectional GMs compared with corresponding unidirectional GMs in NF65
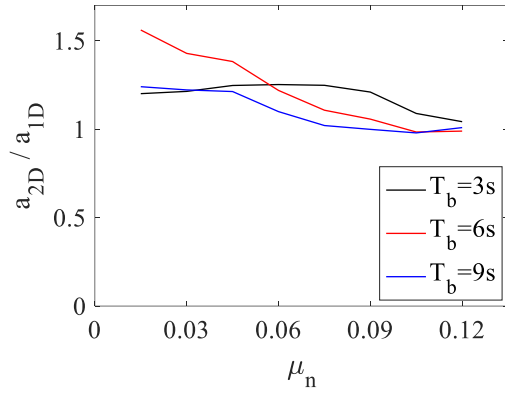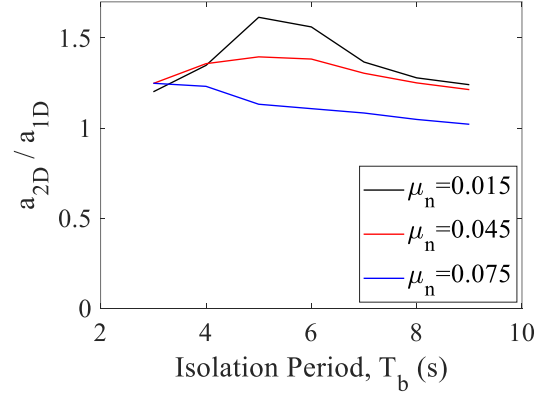
171

Figure 4-17 shows the spectra of response increase under bidirectional GMs compared with corresponding unidirectional GMs in NF70. It shows that for optimum selections, T_b around 3s and μ_n around 0.09, the mean value of d_{2D}/d_{1D} is around 1.48 and the mean value of a_{2D}/a_{1D} is around 1.15; for T_b around 6s and μ_n around 0.06, the mean value of d_{2D}/d_{1D} is around 1.24 and the mean value of a_{2D}/a_{1D} is around 1.07; for T_b around 9s and μ_n around 0.04, the mean value of d_{2D}/d_{1D} is around 1.09 and the mean value of a_{2D}/a_{1D} is around 1.03.
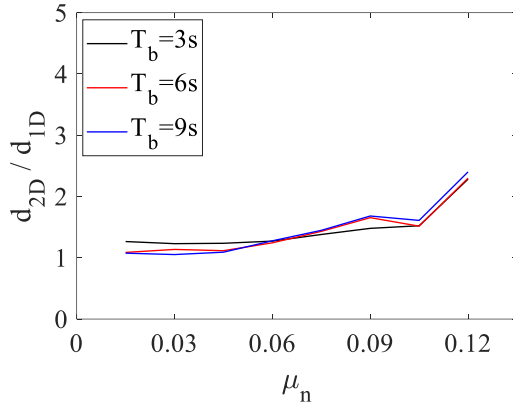
(a) Maximum displacement on μ_n (b) Maximum displacement on T_b
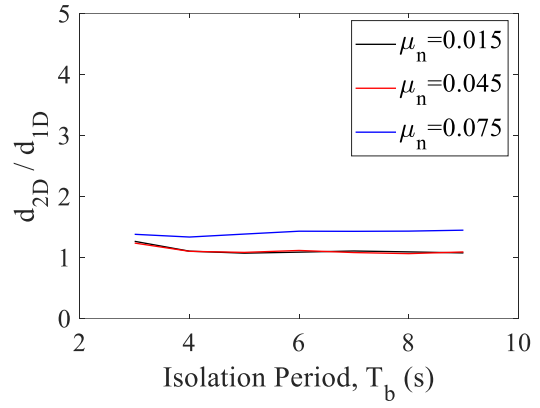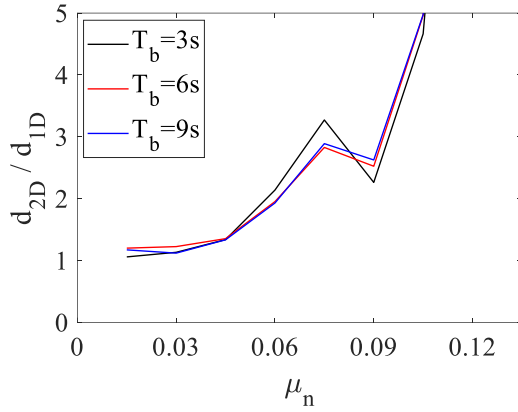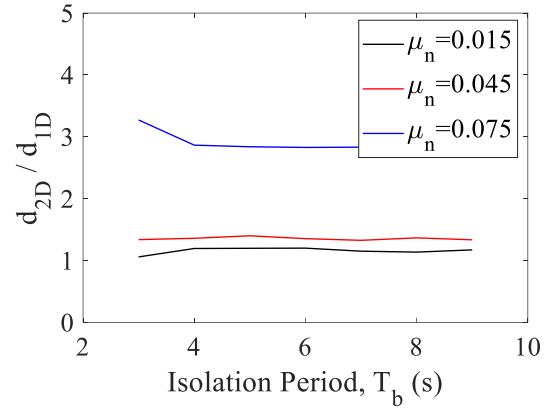
(c) Superstructure acceleration on μ_n (d) Superstructure acceleration on T_b

Figure 4-17. Spectra of response increase under bidirectional GMs compared with corresponding unidirectional GMs in NF70
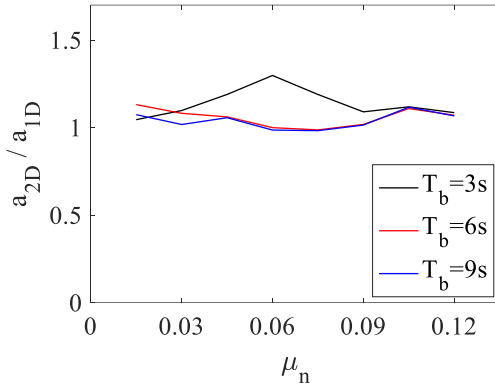
Figure 4-18 shows the spectra of response increase under bidirectional GMs compared with corresponding unidirectional GMs in NF75. It shows that for optimum selections, T_b around 3s and μ_n around 0.075, the mean value of d_{2D}/d_{1D} is around 1.65 and the mean value of a_{2D}/a_{1D} is around 1.25; for T_b around 6s and μ_n around 0.045, the mean value of d_{2D}/d_{1D} is around 1.88 and the mean value of a_{2D}/a_{1D} is around 1.38; for T_b around 9s and μ_n around 0.03, the mean value of d_{2D}/d_{1D} is around 1.60 and the mean value of a_{2D}/a_{1D} is around 1.22.
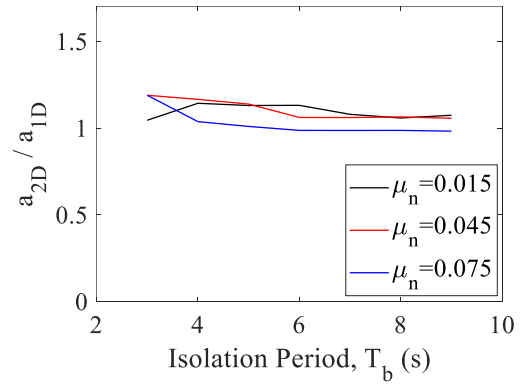

(a) Maximum displacement on μ_n

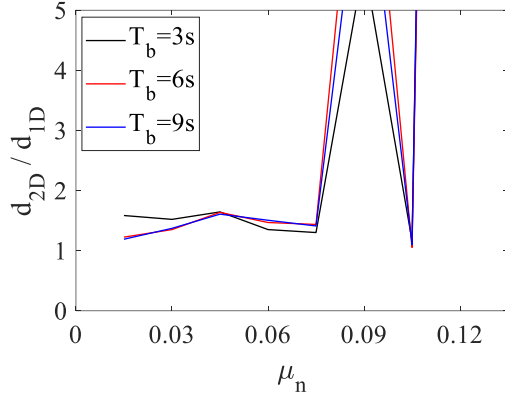(b) Maximum displacement on T_b
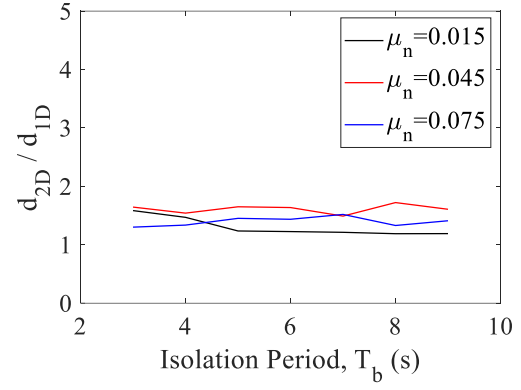
(c) Superstructure acceleration on μ_n

(d) Superstructure acceleration on T_b

Figure 4-18. Spectra of response increase under bidirectional GMs compared with corresponding unidirectional GMs in NF75

Figure 4-19 shows the spectra of response increase under bidirectional GMs compared with corresponding unidirectional GMs in SD. It shows that for optimum selections, T_b around 3s and μ_n around 0.06, the mean value of d_{2D}/d_{1D} is around 2.14 and the mean value of a_{2D}/a_{1D} is around 1.30; for T_b around 6s and μ_n around 0.04, the mean value of d_{2D}/d_{1D} is around 1.35 and the mean value of a_{2D}/a_{1D} is around 1.06; for T_b around 9s and μ_n around 0.02, the mean value of d_{2D}/d_{1D} is around 1.17 and the mean value of a_{2D}/a_{1D} is around 1.07.

(a) Maximum displacement on μ_n

(b) Maximum displacement on T_b

(c) Superstructure acceleration on μ_n

(d) Superstructure acceleration on T_b

Figure 4-19. Spectra of response increase under bidirectional GMs compared with corresponding unidirectional GMs in SD
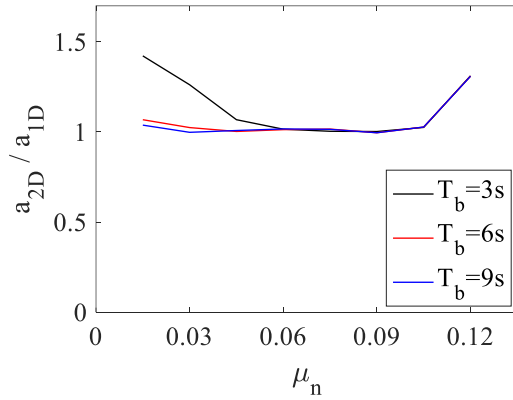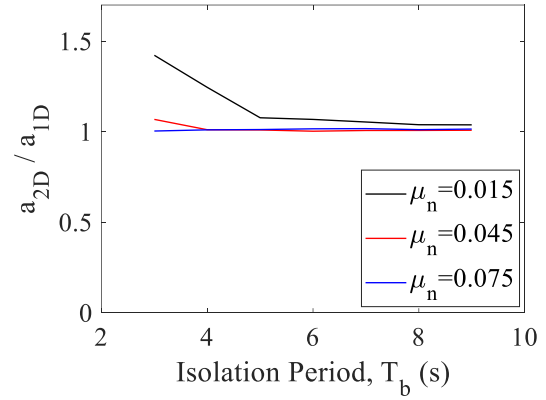
Figure 4-20 shows the spectra of response increase under bidirectional GMs compared with corresponding unidirectional GMs in LD. It shows that for optimum selections, T_b around 3s and μ_n around 0.03, the mean value of d_{2D}/d_{1D} is around 1.52 and the mean value of a_{2D}/a_{1D} is around 1.26.

(a) Maximum displacement on μ_n (b) Maximum displacement on T_b
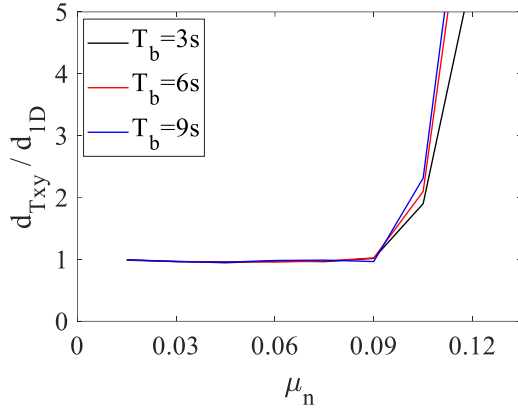
(c) Superstructure acceleration on μ_n (d) Superstructure acceleration on T_b

Figure 4-20. Spectra of response increase under bidirectional GMs compared with corresponding unidirectional GMs in LD

### *4.6.3 Effect of temperature change on the response (NF, SD, LD)*

Further, the contribution of the temperature change caused by the addition of the second component (from unidirectional GMs to corresponding bidirectional GMs) on the maximum response displacement of the isolation layer (η_T introduced in Section 3.5.3) and the maximum superstructure acceleration is shown in form of spectra in Figure 4-21. Where d_{Txy} and a_{Txy} are the maximum displacement of the isolation layer and the maximum acceleration of the superstructure under 1D GMs respectively, using the response temperature under corresponding 2D GMs to calculate μ as introduced in Section 3.5.3. It shows that for optimum selections, T_b around 3s and μ_n around 0.09, the contribution of the temperature change on the displacement (η_T) is around 1.02 and that on the acceleration is around 1.00; For T_b around 6s and μ_n around 0.05, the contribution of the temperature change on the displacement is around 0.96 and that on the acceleration is around 1.00; For T_b around 9s and μ_n around 0.015, the contribution of the temperature change on the displacement is around 1.00 and that on the acceleration is around 1.00. It can be noticed that the contribution of temperature is not always larger than 1. This is because the temperature of the contact surface under corresponding 2D GMs is not necessarily higher than that under 1D GMs (further introduced in Appendix B).
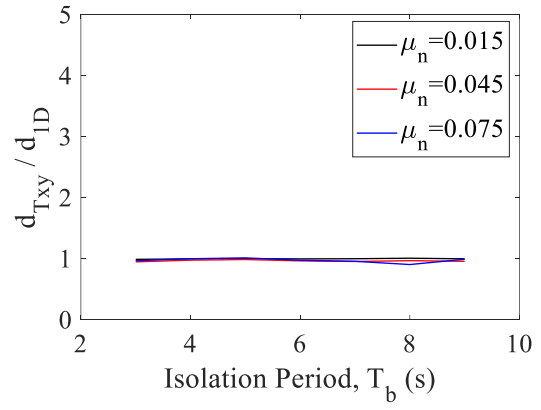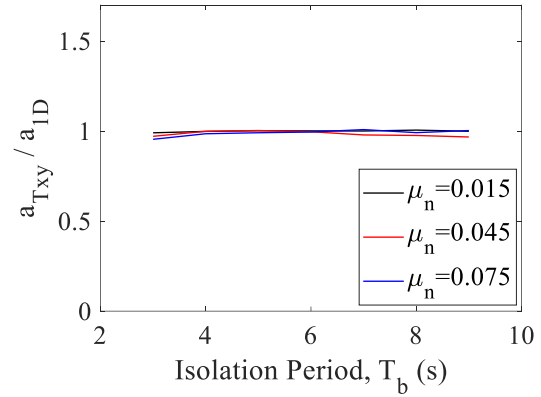
176

(a) Maximum displacement on μ_n
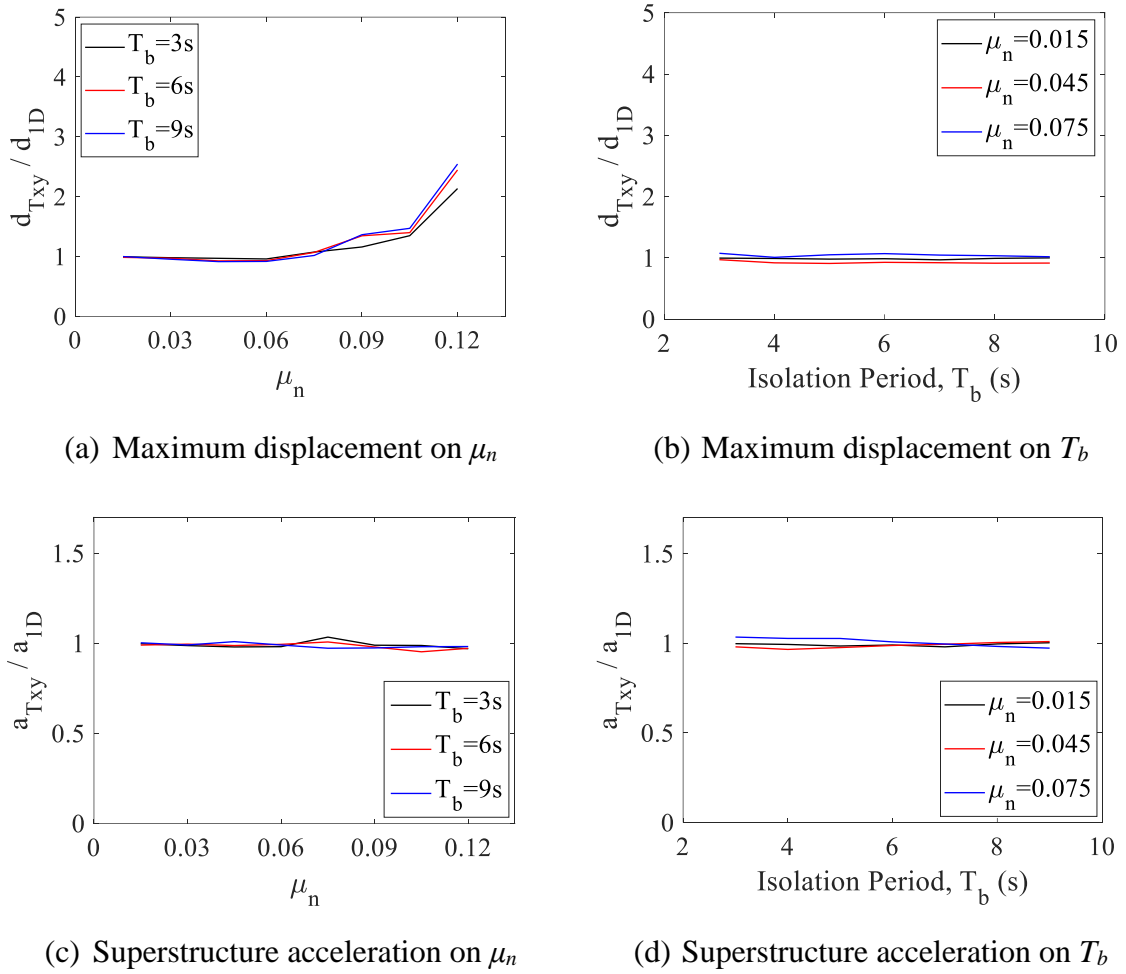
(b) Maximum displacement on T_b
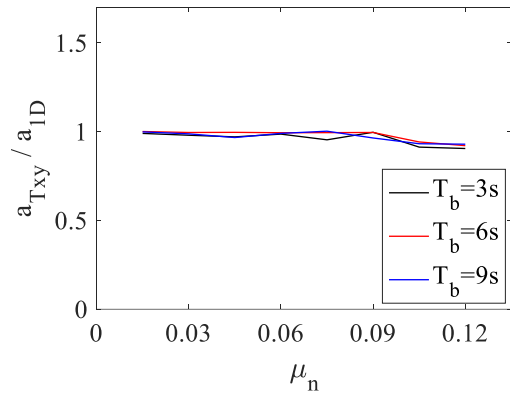
(c) Superstructure acceleration on μ_n
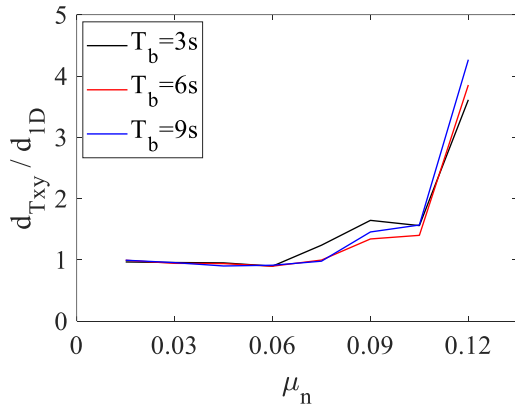
(d) Superstructure acceleration on T_b

Figure 4-21. Spectra of the contribution of the temperature dependency on the bidirectional response in NF65

Figure 4-22 shows the spectra of the contribution of the temperature dependency on the bidirectional response (d_{Txy} /d_{1D} and a_{Txy} /a_{1D}) in NF70. It shows that for optimum selections, T_b around 3s and μ_n around 0.09, the mean value of d_{Txy} /d_{1D} is around 1.16 and the mean value of a_{Txy} /a_{1D} is around 0.99; For T_b around 6s and μ_n around 0.06, the mean value of d_{Txy} /d_{1D} is around 0.93 and the mean value of a_{Txy} /a_{1D} is around 0.99; For T_b around 9s and μ_n around 0.04, the mean value of d_{Txy} /d_{1D} is around 0.91 and the mean value of a_{Txy} /a_{1D} is around 1.01.

(a) Maximum displacement on μ_n (b) Maximum displacement on T_b

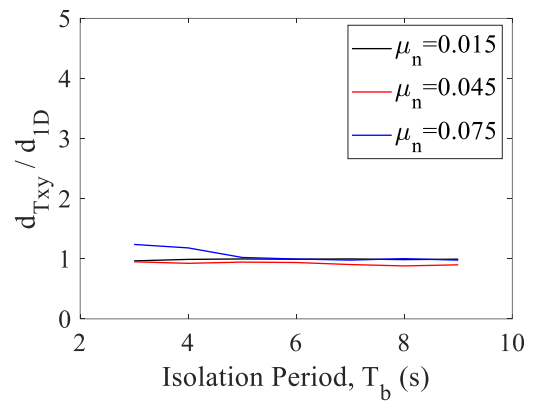(c) Superstructure acceleration on μ_n (d) Superstructure acceleration on T_b

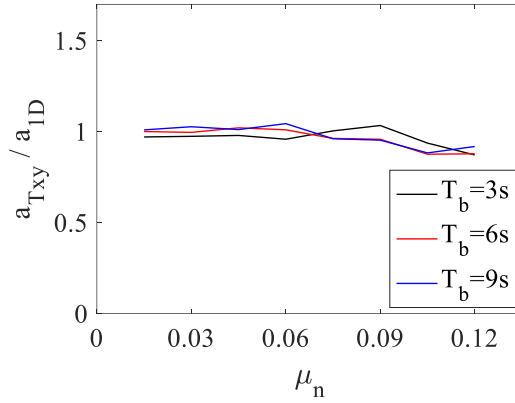**Figure 4-22.** Spectra of the contribution of the temperature dependency on the bidirectional response in NF70

Figure 4-23 shows the spectra of the contribution of the temperature dependency on the bidirectional response (d_{Txy}/d_{1D} and a_{Txy}/a_{1D}) in NF75. It shows that for optimum selections, T_b around 3s and μ_n around 0.075, the mean value of d_{Txy}/d_{1D} is around 1.24 and the mean value of a_{Txy}/a_{1D} is around 1.00; For T_b around 6s and μ_n around 0.045, the mean value of d_{Txy}/d_{1D} is around 0.94 and the mean value of a_{Txy}/a_{1D} is around 1.02; For T_b around 9s and μ_n around 0.03, the mean value of d_{Txy}/d_{1D} is around 0.95 and the mean value of a_{Txy}/a_{1D} is around 1.03.
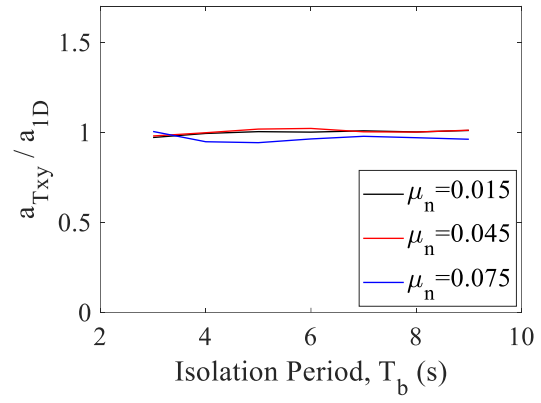

(a) Maximum displacement on μ_n (b) Maximum displacement on T_b

(c) Superstructure acceleration on μ_n (d) Superstructure acceleration on T_b

Figure 4-23. Spectra of the contribution of the temperature dependency on the bidirectional response in NF75

Figure 4-24 shows the spectra of the contribution of the temperature dependency on the bidirectional response (d_{Txy} /d_{1D} and a_{Txy} /a_{1D}) in SD. It shows that for optimum selections, T_b around 3s and μ_n around 0.06, the mean value of d_{Txy} /d_{1D} is around 1.88 and the mean value of a_{Txy} /a_{1D} is around 1.17; For T_b around 6s and μ_n around 0.04, the mean value of d_{Txy} /d_{1D} is around 1.10 and the mean value of a_{Txy} /a_{1D} is around 1.01; For T_b around 9s and μ_n around 0.02, the mean value of d_{Txy} /d_{1D} is around 1.00 and the mean value of a_{Txy} /a_{1D} is around 1.00.

(a) Maximum displacement on μ_n

(b) Maximum displacement on T_b

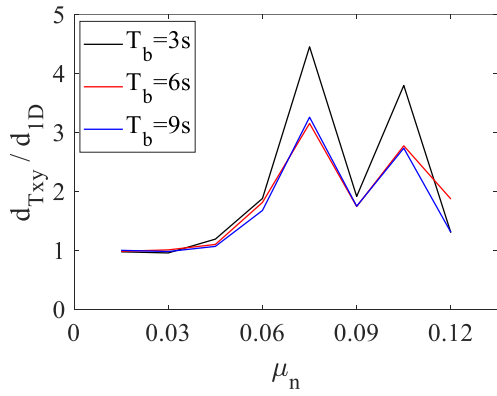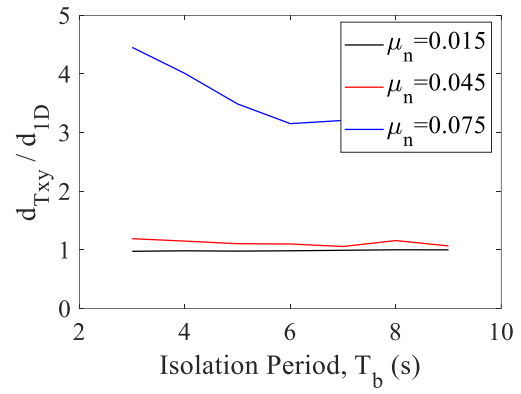(c) Superstructure acceleration on μ_n

(d) Superstructure acceleration on T_b

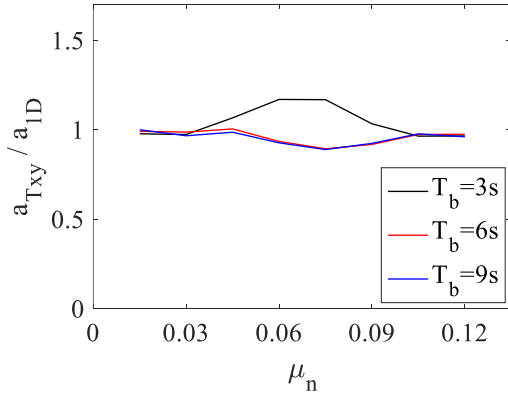**Figure 4-24.** Spectra of the contribution of the temperature dependency on the bidirectional response in SD

Figure 4-25 shows the spectra of the contribution of the temperature dependency on the bidirectional response (d_{Txy}/d_{1D} and a_{Txy}/a_{1D}) in LD. It shows that for optimum selections, T_b around 3s and μ_n around 0.03, the mean value of d_{Txy}/d_{1D} is around 1.07 and the mean value of a_{Txy}/a_{1D} is around 1.01.
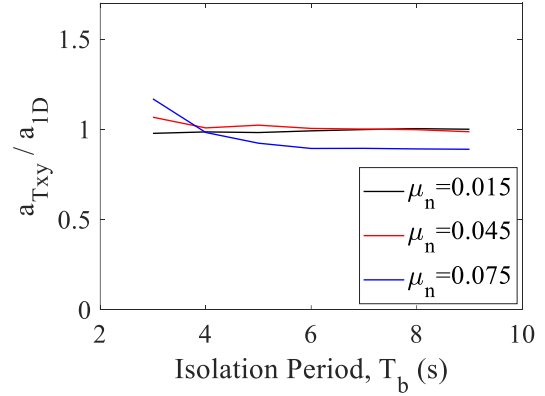

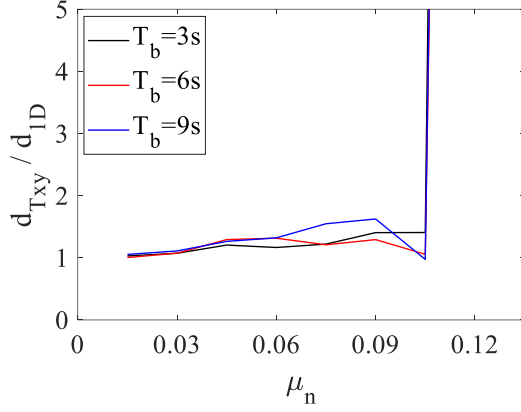(a) Maximum displacement on μ_n (b) Maximum displacement on T_b

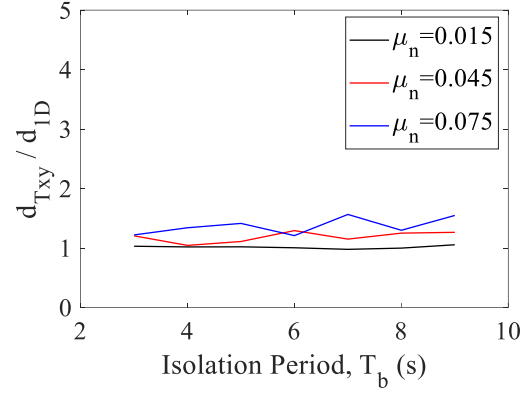(c) Superstructure acceleration on μ_n (d) Superstructure acceleration on T_b

Figure 4-25. Spectra of the contribution of the temperature dependency on the bidirectional response in LD
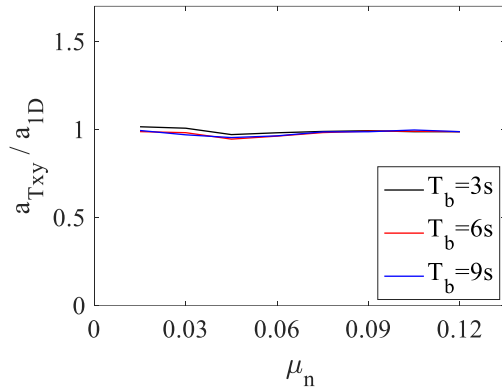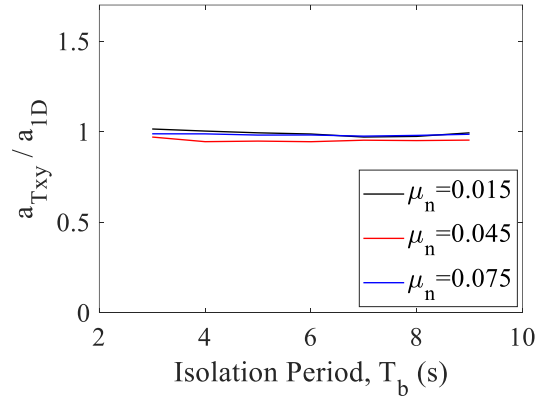
4.7 Preliminary design of DCFP systems under various GMs

4.7.1 Procedure of the preliminary design

In base isolation designs, because the superstructure is usually determined before the design of the isolation system, a lower limit of the isolation period can be obtained first based on the information of the superstructure (aspect ratio and the primary elastic period of the superstructure) to avoid uplifting and to ensure the effectiveness of seismic isolation. The detailed procedure of the optimum selection of the DCFP bearings in base isolation design is introduced as following steps:

a. *Determine the lower limitation of the isolation period based on the characteristics of the superstructure*

As mentioned by Sato Sensei, before the design of the base isolation system (BIS), the characteristics of the superstructure were generally determined. Usually, the rough values of the aspect ratio (H/B, building height / width of shortest side direction) and the primary elastic period of the superstructure (T_S) were known. Based on these information, a lower limitation of the seismic isolation period (T_b) can be obtained.

1) Figure 4-26, obtained from the response prediction based on the energy balance, shows the relation between H/B and T_b to prevent production of tensile forces in the seismic isolation device [4-11]. Where V_E is the equivalent velocity of the seismic input energy. It can be observed that the larger the value of H/B, the larger the value of T_b should be selected. For example, if $V_E \approx 120$cm/s and the superstructure has an aspect ratio of 2, the isolation period should be designed larger than 2 s to prevent uplifting.
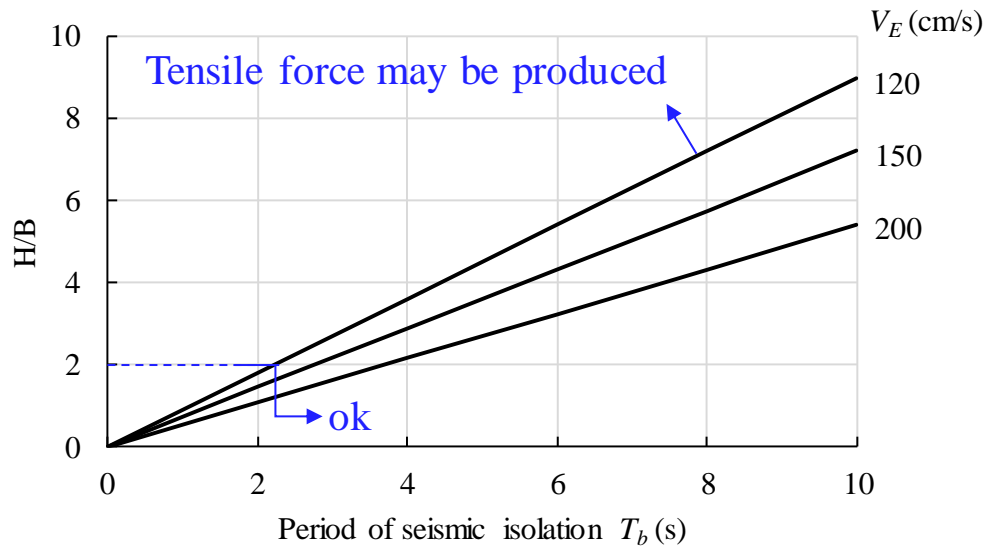
Figure 4-26. Relation of isolation period (T_b) and aspect ratio (H/B) [4-11]

2) T_b must be selected to ensure that resonance with T_S does not occur. Normally, when T_b (superstructure is assumed to be rigid) is more than double T_S, the effectiveness of seismic isolation can be expected [4-13]. Moreover, a rigid body can be substituted for the superstructure and the seismic isolation level, condition that T_b/T_S is about 2.5 or higher [4-14]. Therefore, if the superstructure has a primary elastic period of 0.5 s, the isolation period should be designed larger than 1.25 s to maintain the seismic isolation performance.

3) To maintain the seismic isolation performance, the determination of T_b is also highly related to the properties of the input ground motions (earthquake source properties, properties of the transmission path, and the soil properties near the building). This effect is very complicated, therefore, in this procedure, it will be considered meticulously in the response spectra by classifying ground motions (GMs) based on various characteristics as shown in the next step.

b. *Select a group of GMs based on the construction site and determine the upper limit of T_b according to the response spectra*

Response spectra were plot as design examples in Section 4.6 for five classifications of GMs introduced in Section 4.2. Applying these spectra, the upper limit of T_b can be determined according to the residual displacement limitation and the requirement of the maximum unidirectional displacement of the isolation layer (d_{1D}). For example, if the group of near-fault GMs with the earthquake magnitude between 6.5 and 7.0 (NF65) is considered and d_{1D} is expected to be less than 400 mm, then T_b should be selected less than 6 s according to Figure 4-11 (a) to avoid large residual displacement.

Combined with the lower limit of T_b determined in Step a, an applicable range of T_b can be obtained. For example, if the superstructure has a primary elastic period of 0.5 s and an aspect ratio of 2, and the maximum unidirectional displacement of the isolation layer is expected to be lower than 400 mm, then the isolation period of the DCFP bearing should be selected between 2 s and 6 s under GMs classified as NF65.

c. *Select various values of T_b in the applicable range and obtain the corresponding optimum μ_n based on the response spectra.*

Various values of T_b should be selected in the applicable range to obtain the corresponding optimum μ_n based on the response spectra. The criterion selected for the optimality is minimization of both superstructure acceleration and the displacement of the isolation layer. Then, the selection should be validated by Figure 4-11 (b) to prevent large vertical displacement. Based on this procedure, various groups of satisfied T_b and corresponding μ_n can be obtained. Generally, the larger the value of T_b, the larger the displacement, and the smaller the superstructure acceleration. In isolation design, designers should select based on practical needs.

d. An amplification of the response under bidirectional excitations should also be considered for the optimum selection based on the response increase spectra

Response increase under bidirectional GMs compared with corresponding unidirectional GMs for the optimum selection can be obtained from the response increase spectra. For example, for the group of GMs in NF65, the amplified ratio of the response can be obtained from Figure 4-16.

4.7.2 Effect of bidirectional behavior and temperature change on the response of optimum DCFP systems under various GMs

In the study of the effect of bidirectional behavior and temperature change on the response of DCFP systems, their effect on the response of optimum DCFP systems is of vital importance, because they can reveal the effect of bidirectional behavior and temperature change in preliminary design.

Table 4-10 Optimum selection of T_b and μ_n and corresponding average response under various GM classifications

GMs	T_b (s)	μ_n	d_{1D} (mm)	a_{1D} (g)	d_{2D}/d_{1D}	a_{2D}/a_{1D}	d_{Txy}/d_{1D}	a_{Txy}/a_{1D}
NF65	3	0.09	250	0.25	1.29	1.08	1.02	1.00
	6	0.05	400	0.10	1.14	1.01	0.96	1.00
	9	0.015	600	0.05	1.15	1.00	1.00	1.00
NF70	3	0.09	200	0.23	1.48	1.15	1.16	0.99
	6	0.06	500	0.14	1.24	1.07	0.93	0.99
	9	0.04	800	0.09	1.09	1.03	0.91	1.01
NF75	3	0.075	300	0.23	1.65	1.25	1.24	1.00
	6	0.045	500	0.10	1.88	1.38	0.94	1.02
	9	0.03	700	0.08	1.60	1.22	0.95	1.03
SD	3	0.06	200	0.17	2.14	1.30	1.88	1.17
	6	0.04	300	0.08	1.35	1.06	1.10	1.01
	9	0.02	500	0.05	1.17	1.07	1.00	1.00
LD	3	0.03	100	0.08	1.52	1.26	1.07	1.01
	6	NaN	NaN	NaN	NaN	NaN	NaN	NaN
	9	NaN	NaN	NaN	NaN	NaN	NaN	NaN

The optimum selection of T_b and μ_n under various GM classifications, corresponding average response, effect of bidirectional behavior, and the contribution of temperature change on the response introduced in Section 4.6 is summarized in Table 4-10. From Table 4-10, the following knowledge can be obtained.
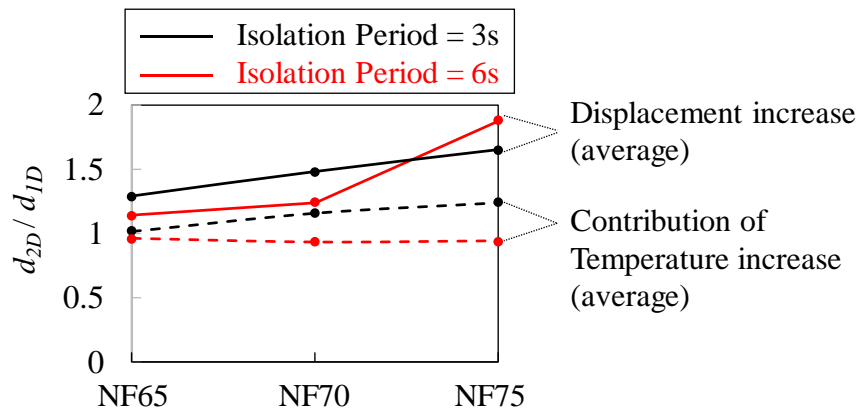
1. About the optimum selection of DCFP bearings: Larger T_b should be match with smaller μ_n; When the selection of T_b increase, the maximum response displacement will increase and maximum superstructure acceleration will decrease. However, no matter in what classification of GMs, the cost-effective ratio of $T_b > 6$s is high. Compared with $T_b = 6$s, $T_b = 9$s can only slightly decrease the acceleration, but the displacement will be significantly increased. The designer should balance the trade-off between higher superstructure acceleration and higher isolation displacement.

2. The optimum selection range of T_b and μ_n under 1D NF (near-fault) GMs with earthquake magnitude larger than 6.5 is similar as 3 ~ 6s and 0.045 ~ 0.09 respectively as shown in Figure 4-27, which will result in the maximum bidirectional response displacement of 300 ~ 900mm and the maximum superstructure acceleration of 0.1 ~ 0.3g in case of 60Mpa. And the response increase from unidirectional to bidirectional near-fault GMs is highly related to the magnitude of the earthquake as shown in Figure 4-28.
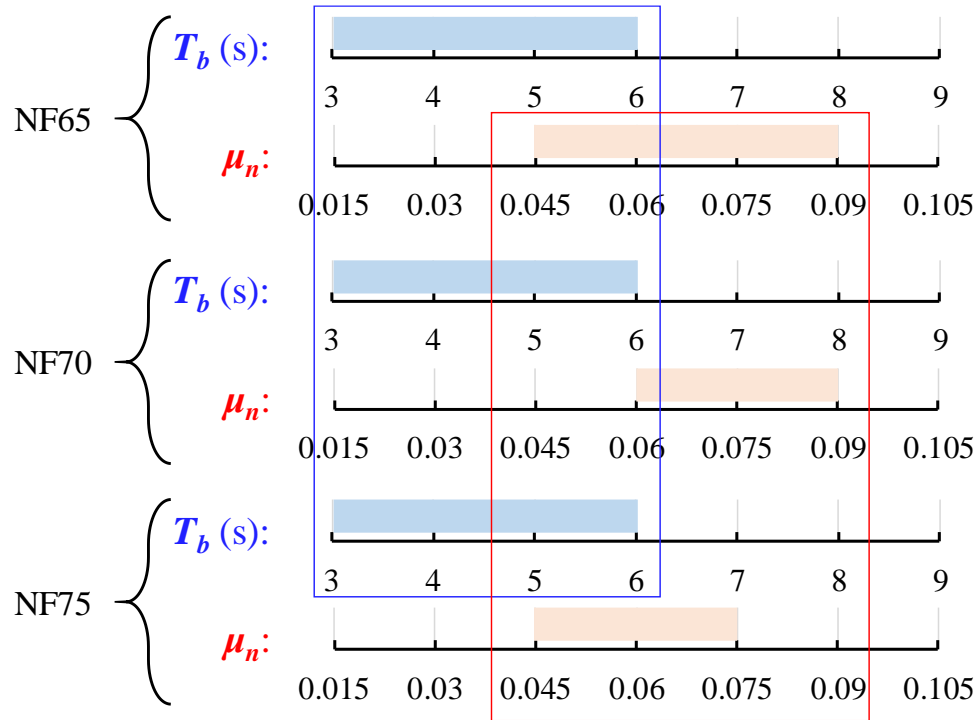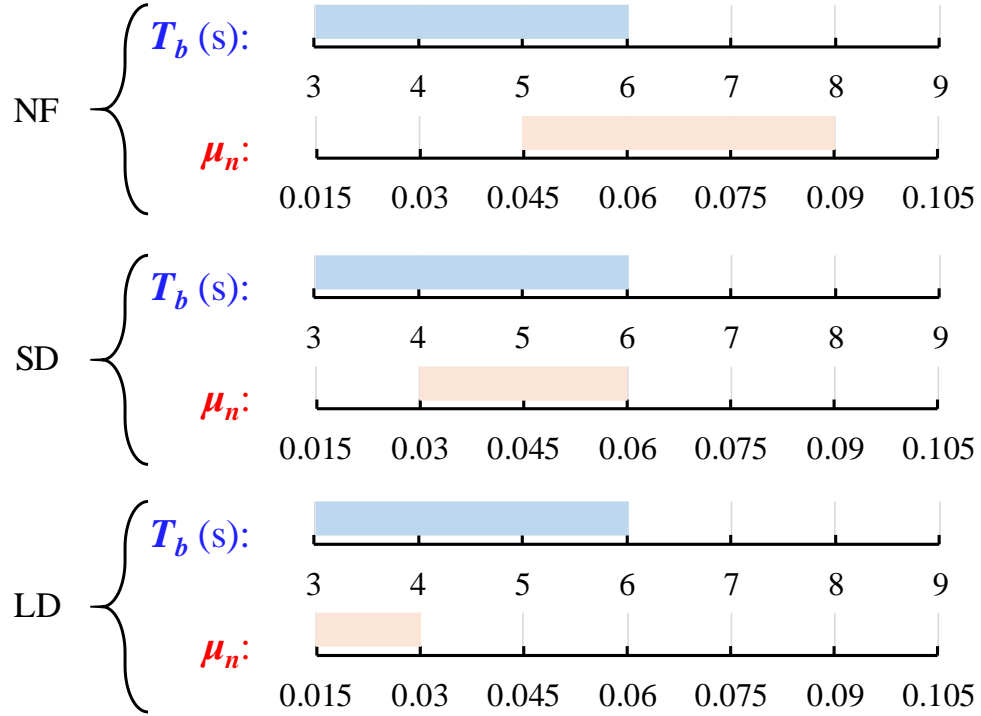

Figure 4-27 Optimum selection of DCFP bearings under different magnitude

Figure 4-28 Effect of earthquake magnitude on d_{2D}/d_{1D}

3. The optimum selection of DCFP bearings under GMs with various distance-to-fault is summarized in Figure 4-29. The optimum selection of T_b and μ_n under small-distance-to-fault GMs with earthquake magnitude larger than 6.5 are 3 ~ 6s and 0.03 ~ 0.06 respectively, which will result in the maximum bidirectional displacement of around 400mm and maximum acceleration of 0.1 ~ 0.2g in case of 60Mpa. If DCFP bearings are applied for long-distance-to-fault GMs, small T_b (<6s) and small μ_n (<0.03) should be selected and the bidirectional response displacement and acceleration will be around 150mm and 0.1g respectively.

Figure 4-29 Optimum selection of DCFP bearings under various distance-to-fault

4. The response (superstructure acceleration & isolator displacement) will be significantly amplified (by an average percentage of 110% & 130% respectively) from unidirectional GMs to corresponding bidirectional GMs under following situations (in the case that the pressure in the bearing is 60Mpa): Structures constructed at near-fault site with the design magnitude of earthquake larger than 7.0 and natural period of the DCFP bearing (T_b) smaller than 4s, near-fault site with the design magnitude of earthquake larger than 7.5, small-distance-to-fault site with

design magnitude of earthquake larger than 6.5 and T_b smaller than 4s, and long-distance-to-fault site with design magnitude of earthquake larger than 6.5 and T_b smaller than 5s;

5. The influence of temperature change on the bidirectional response displacement is significant (the average value of $\eta_T > 1.1$) and cannot be ignored under following situations (in the case that the pressure in the bearing is 60Mpa): Structures constructed at near-fault site with the design magnitude of earthquake larger than 7.0 and the friction coefficient of the DCFP bearing (μ_n) larger than 0.075, near-fault site with the design magnitude of earthquake larger than 7.5 and μ_n larger than 0.06, and small-distance-to-fault site with the design magnitude of earthquake larger than 6.5 and μ_n larger than 0.045;

In the future study, the response of the BISs will be analyzed under a much larger amount of GMs under each classification and cumulative distribution of the response can be obtained, which will be more applicable in actual design.

4.8 Conclusions

Based on previous studies and the up-mentioned studies, the major parameters in the earthquake response analysis of DCFP bearings are marked by '*' in Table 4-1. In which, the effect of temperature dependency and earthquake magnitude were rarely considered in previous studies. By considering all the major parameters (the velocity dependency was also considered) introduced in Table 4-1, response spectra were produced for studying the earthquake response of BISs using PTFE-related materials under a larger range of BISs and various earthquake classifications (based on distance to fault and magnitude). The considered range of the friction coefficient of the BIS is determined by the possible range that the PTFE-related material can provide. Moreover, the horizontal displacement capacity of FPBs limited by the acceptability of the vertical displacement and residual horizontal displacement is also considered. Based on the response spectra satisfying the limitation of the horizontal displacement, the following conclusions can be obtained:

1) Some general rules about the optimum selection of DCFP bearings: Larger T_b should be matched with smaller μ_n; When the selection of T_b increase, the maximum response displacement will increase and maximum superstructure acceleration will decrease. The designer should choose it based on practical needs. However, no matter in what classification of GMs, the cost-effective ratio of $T_b > 9$s is high. Compared with $T_b = 6$s, $T_b = 9$s can only slightly decrease the acceleration, but the displacement will be significantly increased.

2) The optimum selection of T_b and μ_n under near-fault GMs with earthquake magnitude larger than 6.5 are 3 ~ 6s and 0.045 ~ 0.09 respectively, which will result in the maximum bidirectional response displacement of 300 ~ 900mm and the maximum superstructure acceleration of 0.1 ~ 0.3g in case of 60Mpa. And the response increase

191

from unidirectional to bidirectional near-fault GMs is highly related to the magnitude of the earthquake.

3) The optimum selection of T_b and μ_n under small-distance-to-fault GMs with earthquake magnitude larger than 6.5 are 3 ~ 6s and 0.03 ~ 0.06 respectively, which will result in the maximum bidirectional displacement of around 400mm and maximum acceleration of 0.1 ~ 0.2g in case of 60Mpa. If DCFP bearings are applied for long-distance-to-fault GMs, small T_b (<6s) and small μ_n (<0.03) should be selected and the bidirectional response displacement and acceleration will be around 150mm and 0.1g respectively.

4) The response (superstructure acceleration & isolator displacement) will be significantly amplified (by an average percentage of 110% & 130% respectively) from unidirectional GMs to corresponding bidirectional GMs if one of the following condition is satisfied (in the case that the pressure in the bearing is 60Mpa): (1) The natural period of the DCFP bearing (T_b) < 4s; (2) Near-fault ground motions with the moment magnitude of the earthquake larger than 7.5 is considered.

5) The influence of the temperature change under bidirectional ground motions on the bidirectional response displacement is significant (the average value of $\eta_T > 1.1$) and cannot be ignored under following situations (in the case that the pressure in the bearing is 60Mpa): (1) Structures constructed at near-fault site with the design magnitude of earthquake larger than 7.0 and the friction coefficient of the DCFP bearing (μ_n) larger than 0.075, (2) near-fault site with the design magnitude of earthquake larger than 7.5 and μ_n larger than 0.06, and (3) small-distance-to-fault site with the design magnitude of earthquake larger than 6.5 and μ_n larger than 0.045, which is very common in practice.

References.

[4-1].   Jangid RS. Optimum friction pendulum system for near-fault motions. Engineering
structures. 2005 Feb 1;27(3):349-59.

[4-2].   Kumar M, Whittaker AS, Constantinou MC. Characterizing friction in sliding
isolation   bearings.   Earthq   Eng   Struct   Dyn   2015;44:1409–1425.
https://doi.org/10.1002/eqe.2524

[4-3].   Warn G P, Whittaker A S. Performance estimates in seismically isolated bridge
structures. Eng Struct, 2004;26(9):1261-1278.

[4-4].   Si H, Midorikawa S. New attenuation relations for peak ground acceleration and
velocity considering effects of fault type and site condition. In Proceedings of 12th World
Conference on Earthquake Engineering 2000 Jan 30 (No. 0532).

[4-5].   Panchal VR, Jangid RS. Seismic behavior of variable frequency pendulum isolator.
Earthquake Engineering and Engineering Vibration. 2008 Jun;7(2):193-205.

[4-6].   Providakis CP. Effect of supplemental damping on LRB and FPS seismic isolators
under near-fault ground motions. Soil Dynamics and Earthquake Engineering. 2009 Jan
1;29(1):80-90.

[4-7].   PEER, https://ngawest2.berkeley.edu/

[4-8].   Calvi, Paolo M., and Gian Michele Calvi. "Historical development of friction-based
seismic isolation systems." Soil Dynamics and Earthquake Engineering 106 (2018): 14-
30.

[4-9].   Cardone D, Palermo G, Dolce M. Direct displacement-based design of buildings
with different seismic isolation systems. Journal of Earthquake Engineering. 2010 Jan
6;14(2):163-91.

[4-10]. Dolce M, Cardone D, Croatto F. Frictional behavior of steel-PTFE interfaces for seismic isolation. Bulletin of earthquake engineering. 2005 Jan;3(1):75-99.

[4-11]. Architectural Institute of Japan：Recommendation for the Design of Seismically Isolated buildings (2nd Ed.), 1993

[4-12]. Priestley, M.J.N., Calvi G.M. and Kowalsky M., (2007) Displacement-based seismic design of structures., Iuss Press.

[4-13]. R. I. Skinner, W. H. Robinson, G. H. McVery："An Introduction to Seismic Isolation", John Wiley & Sons, 1993

[4-14]. Architectural Institute of Japan：Design Recommendations for Seismically Isolated buildings, 2016

5. Conclusions

5.1 Conclusions

The friction dependency equations of a type of DCFP bearing using PTFE-related material obtained by previous small-scale material tests (combined as the precise model and the simplified model proposed in this study) were comprehensively validated by various prototype specimens under various dynamic excitations. They were validated available under 1) various diameters of the slider (200, 300, 400 mm); 2) a large range of velocity (15 ~ 800 mm/s); 3) a large range of pressure (30 ~ 90 MPa); 4) a large range of displacement (10 ~ 440 mm); 5) two types of interface, Spec. M (PTFE) and Spec. L (PTFE + oil); 6) various bidirectional artificial graphics and bidirectional earthquake response orbits.

This study focused on the behavior of the DCFP bearings applying PTFE-related materials under bidirectional ground motions. The effect of overturning, rotation and the vertical component of the ground motion on the earthquake response of the DCFP bearing was not considered. Therefore, the pressure at the contact surface of the bearing is considered as constant in the analysis. In this condition, parametric studies of the earthquake response indicate that ignoring velocity dependency will not cause large difference on the response of the base isolation system (BIS). However, ignoring temperature dependency will lead to significant influence on the superstructure acceleration and the displacement of the isolation layer. For the Spec. M under 60 MPa pressure, if the friction coefficient decrease caused by temperature increase is ignored, the maximum response displacement of the isolation layer under unidirectional ground motions will be underestimated by an average of 20%. Further, under bidirectional ground motions, if the temperature cahnge compared with that under unidirectional ground motions is not considered, the maximum response displacement of the isolation layer will be underestimated by an average of 10%, which is in the same level with the influence of bidirectional effect and coupling effect.

Moreover, the friction coefficient can be taken as a constant value (μ_n) by considering the effect of temperature on the friction coefficient under strong ground motions as constant, with sufficient accuracy in estimating the response of the isolation layer under strong ground motions. However, as the friction coefficient is considered as constant, the large break-out force pulse caused by the existence of the large velocity pulse at the beginning of the earthquake (T°C is small) that may happen in the earthquake excitations cannot be estimated. This may affect the design of maximum base shear and the maximum superstructure acceleration, therefore, it should be paid attention when using a constant friction coefficient in the response analysis. Moreover, the selection of the constant friction coefficient should be applicable for the expected load of the structure. The constant value, μ_n, proposed in this study is selected based on unidirectional strong ground motions. Therefore, its accuracy under unidirectional strong ground motions is satisfied, however, its simulation results under weak excitations shows large difference from the experimental results. Further, even though the accuracy of the simulated response using μ_n shows no large difference from the experimental results under corresponding bidirectional ground motions, the simulation results will be better if the temperature change under bidirectional excitations is considered to refine the value of μ_n.

As the fact that the effect of the bidirectional effect and the coupling behavior on the maximum displacement is highly related to the characteristics of ground motions and base isolation systems, how the influence of temperature change caused by the bidirectional effect on the maximum displacement is affected by various earthquake characteristics was further investigated under a large amount of GMs. For the considered type of PTFE-related material (Spec. M), regardless of the curvature of the concave plates and the diameter of the slider, the influence of the temperature change under bidirectional GMs on the maximum displacement will be significantly affected by the magnitude of the earthquake and the distance from the construction site to fault. The value of the influence at 75% cumulative

distribution is larger than 1.2 if one of the following conditions is satisfied: 1) the moment magnitude of the earthquake is larger than 7.0; 2) the distance from the construction site to fault is between 10 km and 30 km. Moreover, it was found that, if the friction coefficient increase, this influence will also increase significantly.

Based on previous studies and the up-mentioned studies, the major parameters in the earthquake response analysis of DCFP bearings are marked by '*' in Table 5-1. The major parameters in red were rarely considered in previous studies.

Table 5-1 Major parameters in the earthquake response analysis of DCFP bearings

BIS	Analysis Model	Earthquake Selection
* μ (friction coefficient)	Pressure dependency	* Distance to fault
* T_b (Isolation Period)	Velocity dependency	* Magnitude
	* Temperature dependency	Soil type
	* Coupling effect	Fault type
	* Second Component	

* implies major parameters

By considering all the major parameters (the velocity dependency was also considered) introduced in Table 5-1, response spectra were produced for studying the earthquake response of BISs using PTFE-related materials under a larger range of BISs and various earthquake classifications (based on distance to fault and magnitude). The considered range of the friction coefficient of the BIS is determined by the possible range that the PTFE-related material can provide. Moreover, the horizontal displacement capacity of FPBs limited by the acceptability of the vertical displacement and residual horizontal displacement is also considered. Based on the response spectra satisfying the limitation of the horizontal displacement, the following conclusions can be obtained:

1) Some general rules about the optimum selection of DCFP bearings: Larger T_b should be matched with smaller μ_n; When the selection of T_b increase, the maximum

response displacement will increase and maximum superstructure acceleration will decrease. The designer should choose it based on practical needs. However, no matter in what classification of GMs, the cost-effective ratio of $T_b > 9$s is high. Compared with $T_b = 6$s, $T_b = 9$s can only slightly decrease the acceleration, but the displacement will be significantly increased.

2) The optimum selection of T_b and μ_n under near-fault GMs with earthquake magnitude larger than 6.5 are 3 ~ 6s and 0.045 ~ 0.09 respectively, which will result in the maximum bidirectional response displacement of 300 ~ 900mm and the maximum superstructure acceleration of 0.1 ~ 0.3g in case of 60Mpa. And the response increase from unidirectional to bidirectional near-fault GMs is highly related to the magnitude of the earthquake.

3) The optimum selection of T_b and μ_n under small-distance-to-fault GMs with earthquake magnitude larger than 6.5 are 3 ~ 6s and 0.03 ~ 0.06 respectively, which will result in the maximum bidirectional displacement of around 400mm and maximum acceleration of 0.1 ~ 0.2g in case of 60Mpa. If DCFP bearings are applied for long-distance-to-fault GMs, small T_b (<6s) and small μ_n (<0.03) should be selected and the bidirectional response displacement and acceleration will be around 150mm and 0.1g respectively.

4) The response (superstructure acceleration & isolator displacement) will be significantly amplified (by an average percentage of 110% & 130% respectively) from unidirectional GMs to corresponding bidirectional GMs if one of the following condition is satisfied (in the case that the pressure in the bearing is 60Mpa): (1) The natural period of the DCFP bearing (T_b) < 4s; (2) Near-fault ground motions with the moment magnitude of the earthquake larger than 7.5 is considered.

5) The influence of the temperature change under bidirectional ground motions on the bidirectional response displacement is significant (the average value of $\eta_T > 1.1$) and

cannot be ignored under following situations (in the case that the pressure in the bearing is 60Mpa): (1) Structures constructed at near-fault site with the design magnitude of earthquake larger than 7.0 and the friction coefficient of the DCFP bearing (μ_n) larger than 0.075, (2) near-fault site with the design magnitude of earthquake larger than 7.5 and μ_n larger than 0.06, and (3) small-distance-to-fault site with the design magnitude of earthquake larger than 6.5 and μ_n larger than 0.045, which is very common in practice.

5.2 Future work

In the future study, the response of the BISs will be studied under a much larger amount of GMs under each GM classification so that cumulative distributions of the response can be obtained, which will be of vital importance in understanding the behavior of DCFP bearings under GMs and assisting seismic isolation design.

Further, as there are many possibilities for distance to fault and magnitude of earthquake, designers have to consider many type of earthquakes (distance to fault and magnitude) in practical design. In order to satisfy multiple objectives under many types of ground motions, advanced FPBs were recently developed from traditional FPBs. For example, the variable friction FPB (VFPB) and the variable curvature FPB (VCFPB). In the future, parametric analysis and optimum design method of VFPB and VCFPB will also be studied.

Appendix A - Effect of earthquake duration on the temperature of DCFP bearings

In order to study the effect of duration time of the earthquake on the temperature, unidirectional GMs with various durations but same PGV were set as inputs. Table A-1 shows the information of the GMs and the analytical maximum temperature of the contact surface of Spec. M under these excitations. It can be observed that the temperature shows no strong relationship with the duration time of the GMs.

Table A-1. Maximum temperatures of ground motions with various duration

GM	PGV (m/s)	Distance-to-fault (km)	Duration (s)	Temperature (˚C)
NCC-C1	0.75	11	20	121
JKB-C1	0.75	1	20	122
LPG-C1	0.75	9	25	127
KNA-C1	0.75	7	25	145
TC1-C1	0.75	2	50	122
IVD-C1	0.75	22	90	193
TSD-C1	0.75	172	150	126
TIM-C1	0.75	145	170	140

The temperature and earthquake input energy history under GMs in Table A-1 is shown in Figure A-1. The orange line and the blue line represent the history of temperature and total earthquake input energy respectively. It can be observed that the temperature will quickly increase when earthquake input energy quickly increase ("strong excitation duration", which is marked in the figure). This stage lasts for around 5s for the selected near-fault GMs (0 ~ 10 km: NCC, JKB, LPG, KNA, and TC1) and around 20s for the selected small distance-to-fault GMs (10 ~ 30 km: IVD). For the selected GMs with long distance-to-fault (> 30 km: TSD and TIM), this stage happens twice. However, for all the GMs, the increase of earthquake input energy will slow down after this stage, and the temperature will remain or

decrease gradually. Therefore, the temperature change is not highly related to the total duration of the GM, but may be related to the magnitude and distance-to-fault of the GM.
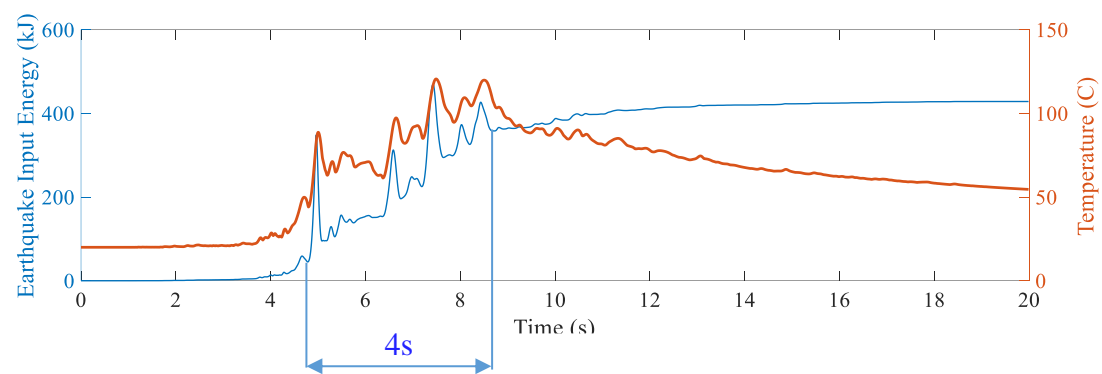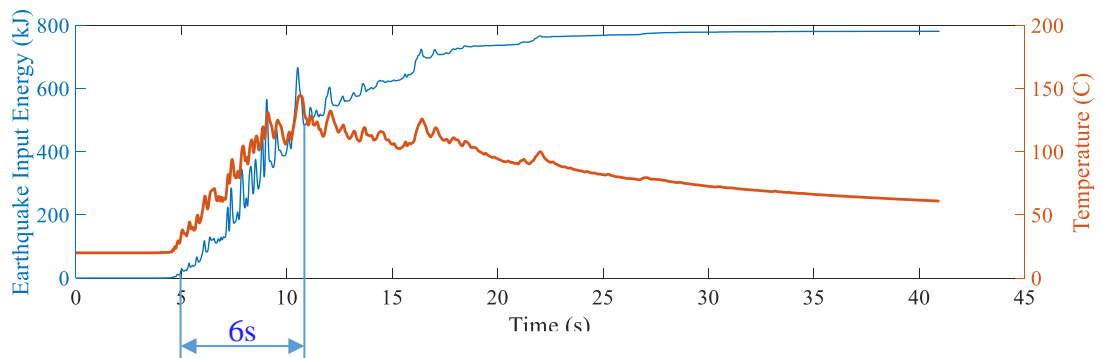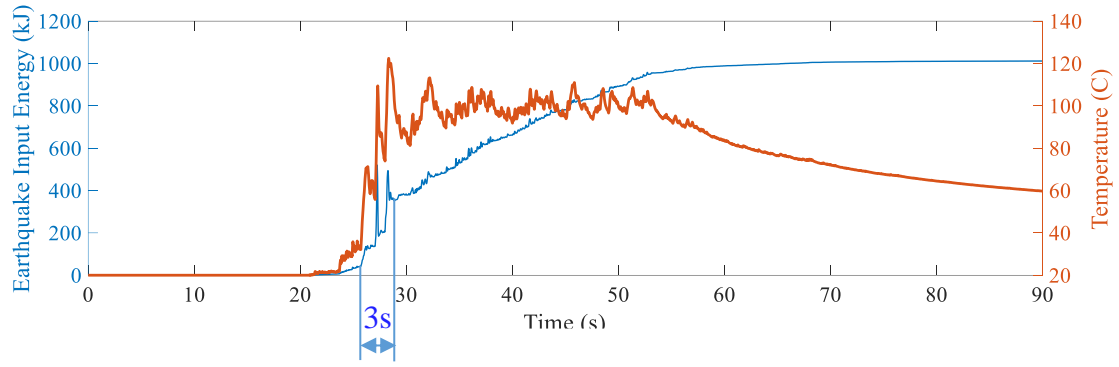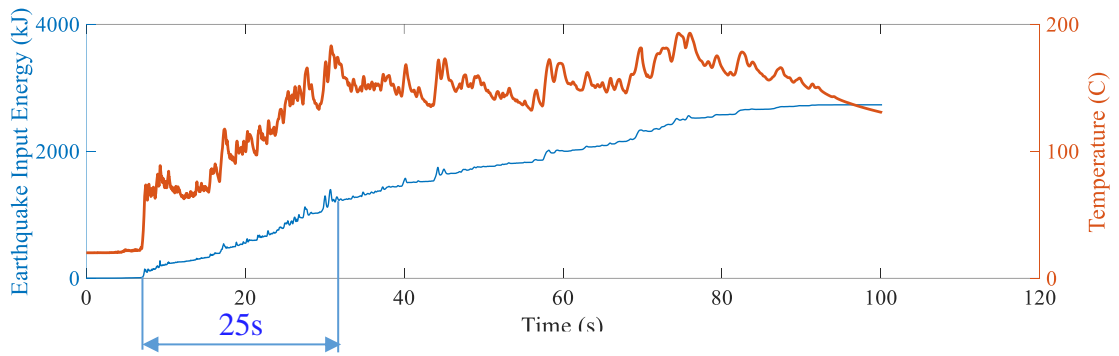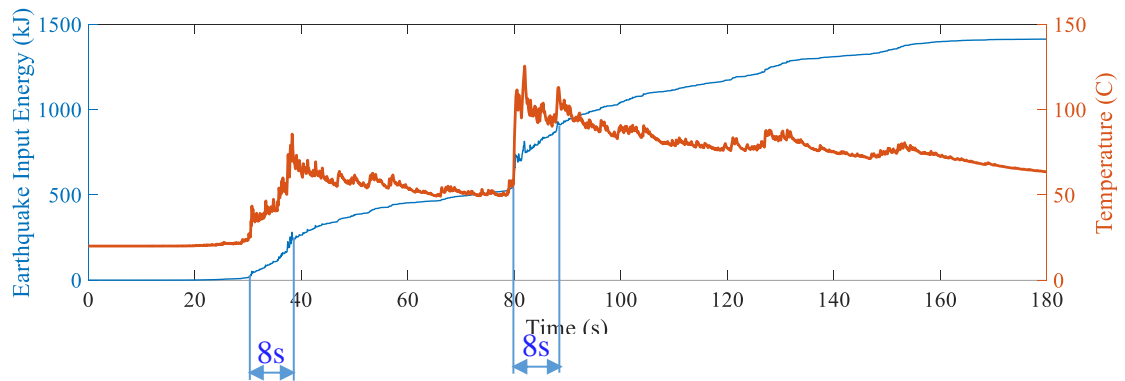

(a) NCC-C1
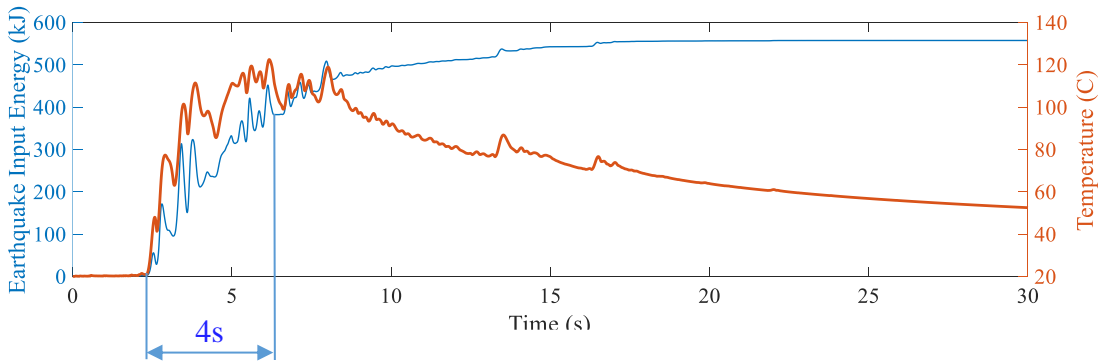
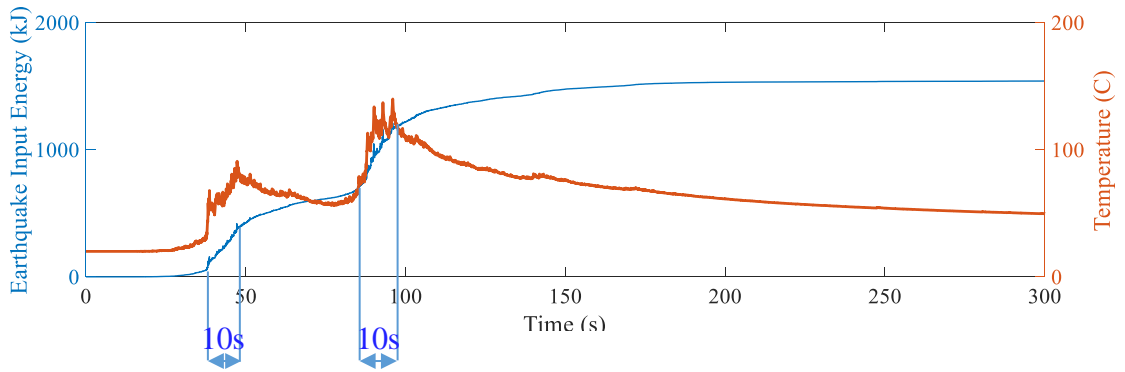(b) JKB-C1
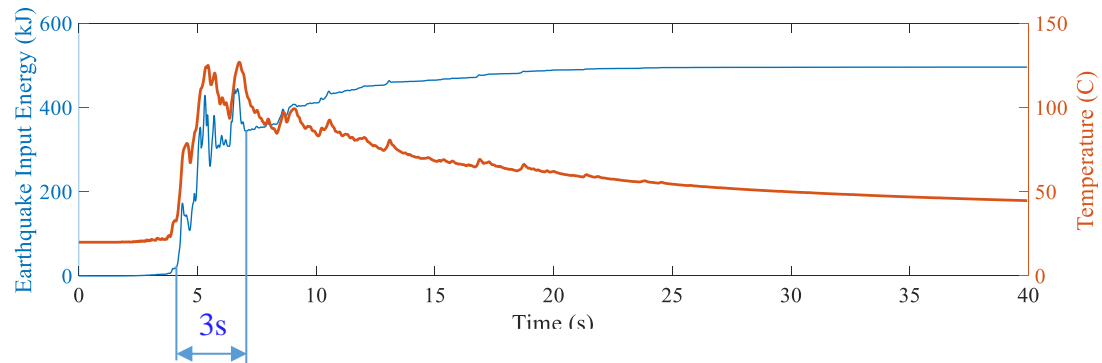
(c) LPG-C1

(d) KNA-C1

201

(e) TC1-C1

(f) IVD-C1

(g) TSD-C1

(h) TIM-C1

Figure A-1. Temperature and earthquake input energy history under C1 component of GMs with various durations (PGV-C1 is amplified as 750mm/s)

As shown in Figure A-1, differences exist in the "strong excitation duration" for GMs with various distance to fault. One of the reasons that may cause this phenomenon is considered to be the difference in the travel speed of the seismic waves. When an earthquake occurs, it releases waves of energy, which are known as seismic waves as shown in Figure A-2. It consists of P waves, S waves, and Surface waves, in which P waves travel in the speed range of 1.5 -13 km/s, S waves are almost 1.7 times slower than P waves, and Surface waves are much slower. Therefore, for NF GMs, the three seismic waves happened at the same time in a duration of around 5s; for SD GMs, the three seismic waves tend to happen next to each other according to their travel speeds, lasting a duration of around 20s. It should be mentioned that, to clarify the influence of distance to fault on the "strong excitation duration", further study is still necessary.
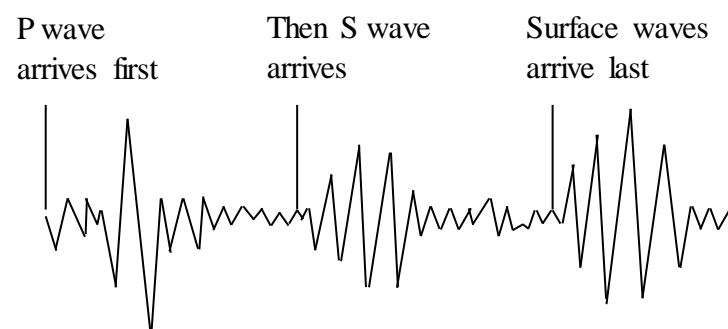
Figure A-2. Structure of an earthquake wave

For the temperature and earthquake input energy history of LD GMs radiated from the Tohoku earthquake (TSD and TIM) shown in Figure A-1, the quick earthquake input energy increase happened 2 times. This is considered to be caused by the characteristics of the 2011 Tohoku earthquake. Based on previous studies of W. Suzuki et al. [A-1], it was found out that the Tohoku earthquake seems to consist of several rupture events, which might be the main reason that the seismic waves radiated from the Tohoku earthquake contributes to the very long durations of strong shaking with multiple "strong excitation durations".

Reference

[A-1] Suzuki, Wataru, et al. "Source rupture process of the 2011 Tohoku-Oki earthquake derived from the strong-motion records." *Proceedings of the fifteenth world conference on earthquake engineering. Lisbon, Portugal*. 2012.

Appendix B - Relationship between the temperature under 2D and that under 1D

About the conducted experiments, there are no corresponding bidirectional and unidirectional tests. To answer this question, analytical results are used. Analytical results show that the temperature under 2D GMs are usually larger than that under corresponding 1D components, because the seismic energy input under 2D GMs are larger than that under corresponding 1D GMs. However, the temperature under 2D might be slightly lower than that under 1D if both of the following conditions are satisfied:

(1) the increase of seismic input energy under 2D from that under 1D is small

(2) the slider diameter is too small compared with the response orbit, so that cumulated contact area rarely repeat

Table B-1 shows some examples of the maximum analytical temperature of the contact surface under unidirectional and corresponding bidirectional GMs. The DCFP bearing considered in Table B-1 has a nominal friction coefficient (μ_n) of 0.045 and an isolation period of 6s. Two various slider diameters, 100 mm and 400 mm were considered and the pressure at the contact surface is considered as a constant value of 60 MPa. TSD, NCC, and KNA represents three of the GMs listed in Table 3-1 (GMs selected for bidirectional dynamic tests) with different distance-to-fault and their scaled factors were considered as "1". It can be observed from Table B-1 that, for the GMs considered in the bidirectional experiments (TSD, NCC, and KNA), the temperature under 2D is always higher than that under 1D. This is because the seismic input energy under 2D is always larger than that under 1D as shown in Figure B-1 (c) and Figure B-2 (c).

Table B-1 Maximum temperature of the contact surface under unidirectional and corresponding bidirectional GMs

GM	Max. T˚C of φ100			Max. T˚C of φ400		
(unscaled)	Unidirectional		Bidirectional	Unidirectional		Bidirectional
TSD (LD)	70.51˚C	<	95.39˚C	81.07˚C	<	112.18˚C
NCC (SD)	72.95˚C	<	82.47˚C	80.30˚C	<	105.40˚C
KNA (NF)	79.43˚C	<	87.93˚C	85.08˚C	<	98.78˚C
RSN180 (NF)	88.87˚C	>	86.40˚C	142.87˚C	<	143.24˚C

However, as the cumulated contact area of the slider and the concave plates under 2D is larger than that under 1D, sometimes the temperature under 2D might be smaller than that under 1D. One of the example is also shown in Table B-1, which is the temperature of a DCFP bearing with a slider of 100mm diameter under a near-fault (NF) GM listed in Table 4-2 (Section 4.2 in the doctoral thesis), RSN180. The response orbit, temperature history and seismic input history of this case is shown in Figure B-3. It can be seen that the seismic input energy under 2D is only slightly larger than that under 1D. Further, as shown in Table B-1, if a DCFP bearing with a larger slider diameter (400 mm) is considered, the temperature under 2D will be slightly higher than that under 1D. The response orbit, temperature history and seismic input history of this case is shown in Figure B-4.

Therefore, it can be concluded that, the temperature under bidirectional (2D) GMs are usually larger than that under corresponding unidirectional (1D) components. However, the temperature under 2D might be slightly lower than that under 1D if both of the following conditions are satisfied:
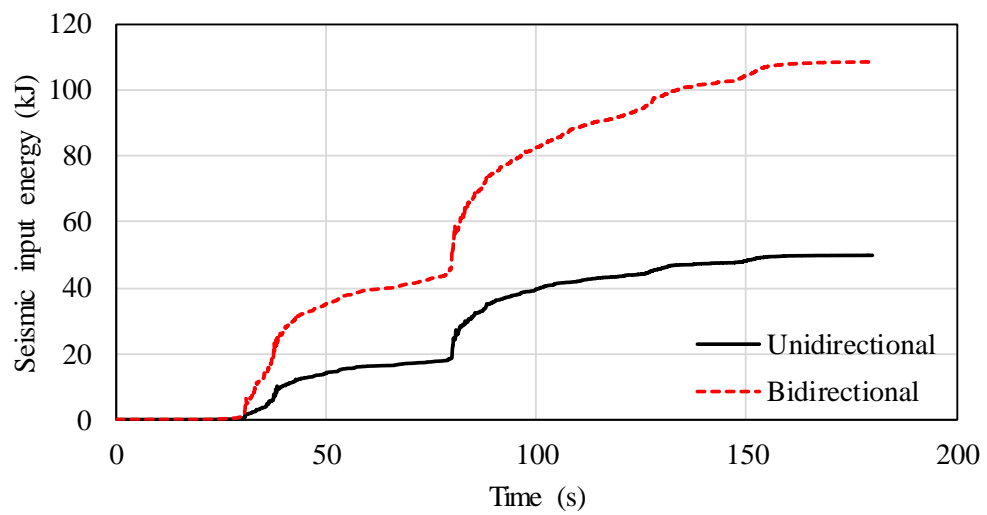
(1) the increase of seismic input energy under 2D from that under 1D is small

(2) the slider diameter is too small compared with the response orbit, so that cumulated contact area rarely repeat
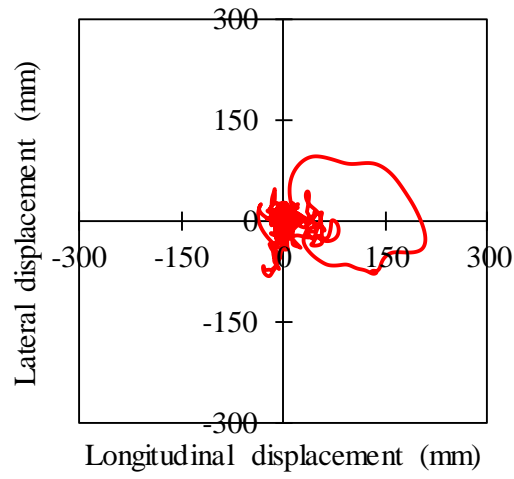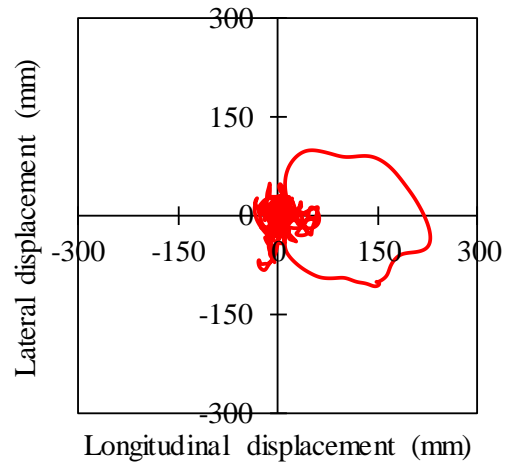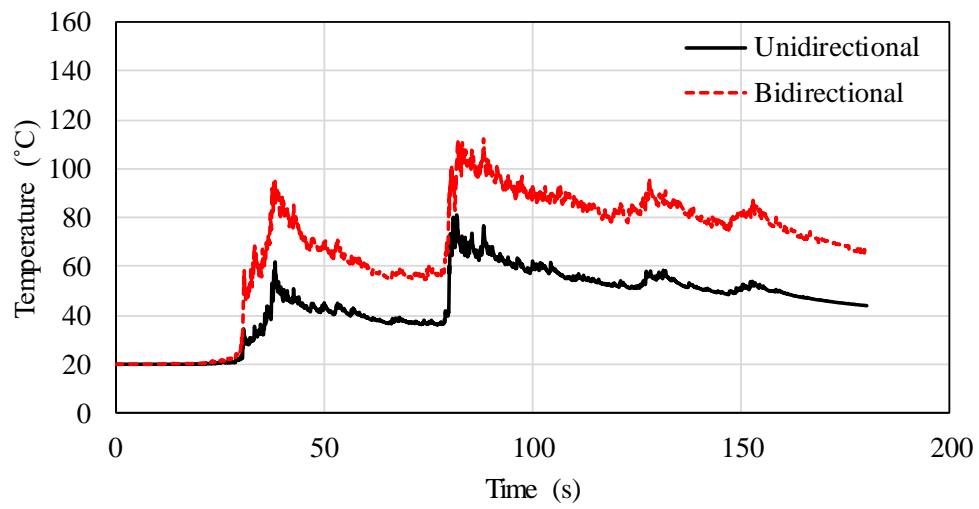
(a) Orbit
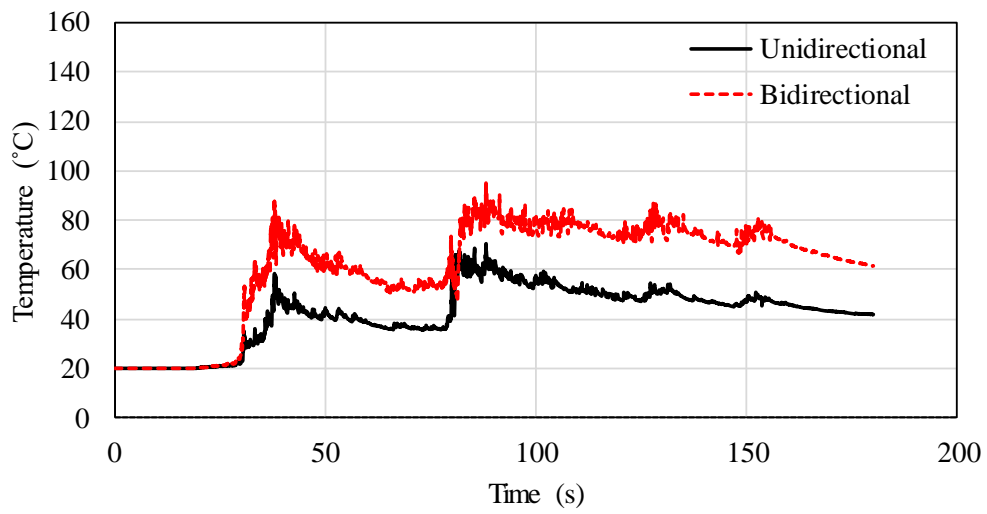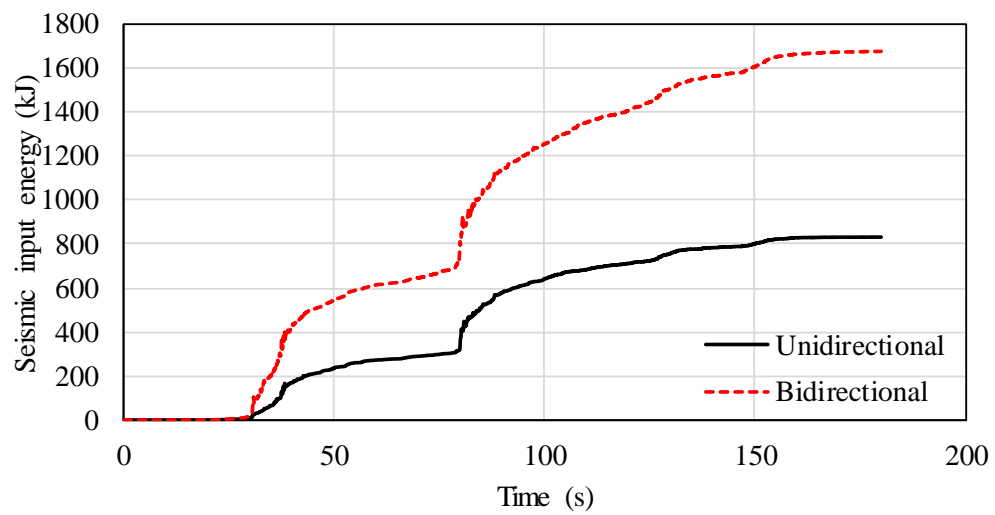

(b) Temperature

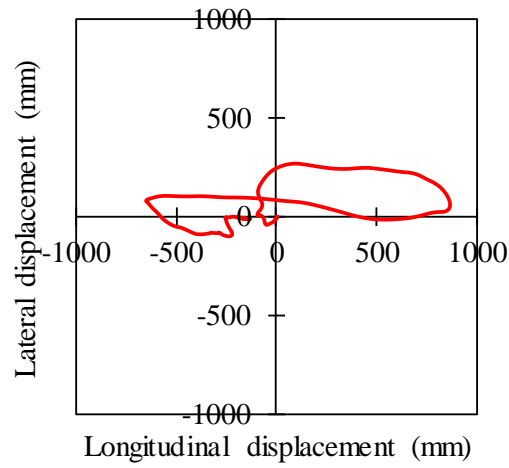(c) Seismic input energy
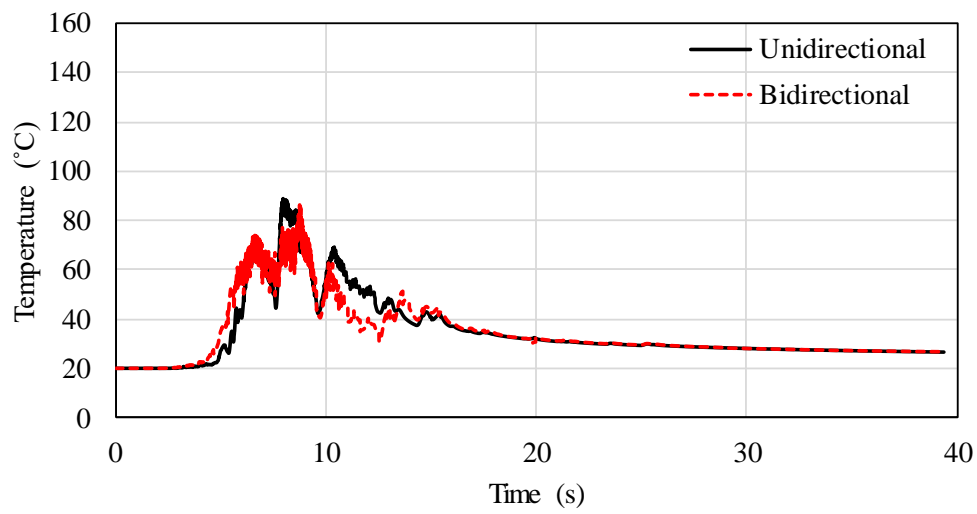
Figure B-1 TSD-φ100

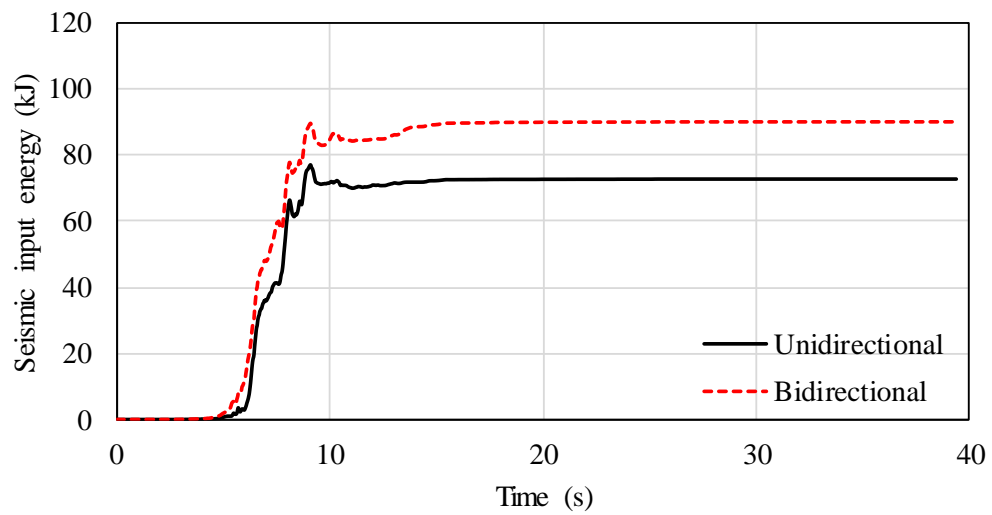(a) Orbit

(b) Temperature

(c) Seismic input energy

Figure B-2 TSD-φ400
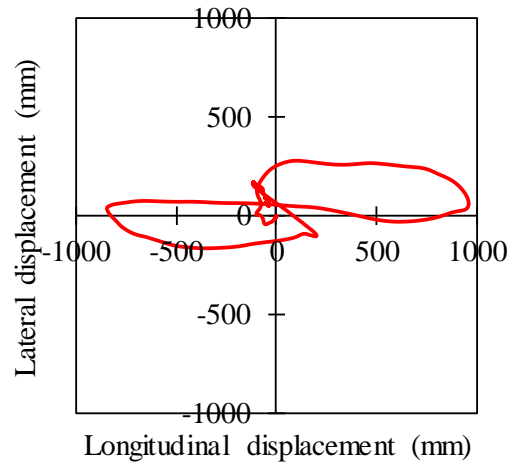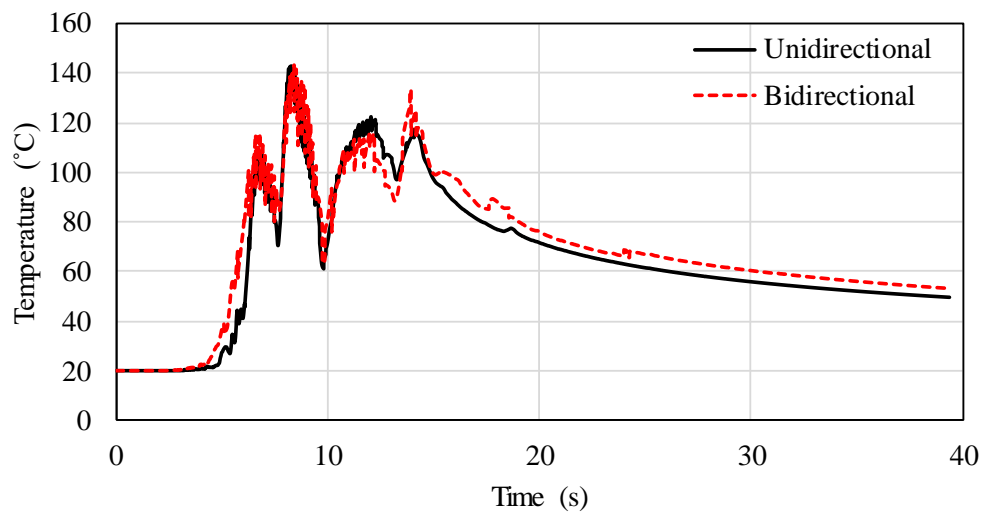
(a) Orbit

(b) Temperature
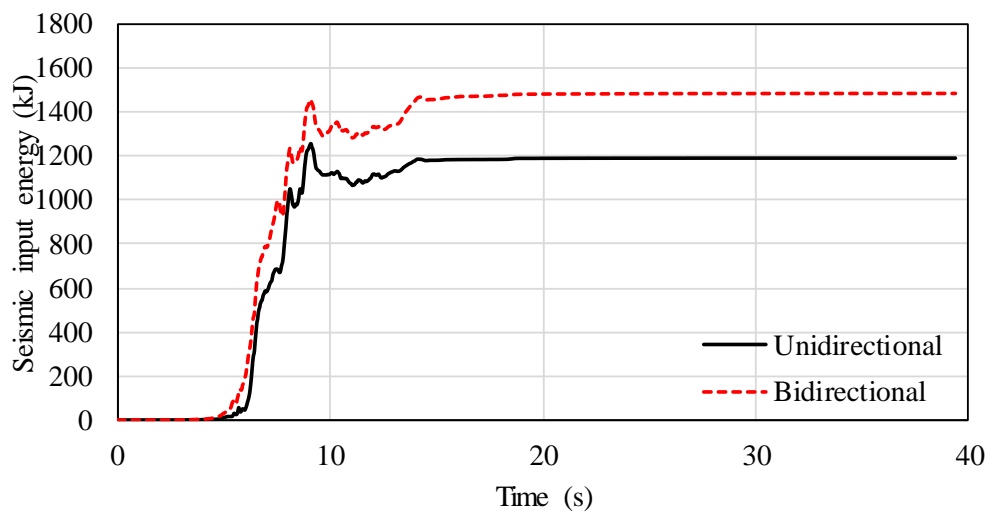

(c) Seismic input energy

Figure B-3 RSN180-φ100

(a) Orbit

(b) Temperature

(c) Seismic input energy

Figure B-4 RSN180-φ400